Mechanics of deformable glacier beds

Thesis by

Brent Minchew

In Partial Fulfillment of the Requirements
for the Degree of
Doctor of Philosophy

California Institute of Technology
Pasadena, California

2016
(Defended October 28, 2015)

For Ellie.

Acknowledgments

This work would not have been possible without insight, guidance, inspiration, and other assistance from many people. Listing all of the individuals and describing their contributions is a daunting task, but I will do my best to give everyone their due. Before doing so, I acknowledge funding from NASA's Earth and Space Sciences Fellowship program and NASA's Cryospheric Sciences program (Award NNX14AH80G), both of which provided the bulk of my funding throughout this work and afforded numerous opportunities to conduct field work and collect radar data in support of this research. Generous donations from the Albert Parvin and ARCS LA Chapter foundations were indispensable in the overall success of my PhD work and in improving the general quality of life for my family and myself.

Undoubtedly the person most responsible for the direction and results presented here is my advisor, Mark Simons. I first met Mark in June 2009 when he had just returned from collecting data with NASA's Uninhabited Aerial Vehicle Synthetic Aperture Radar (UAVSAR) in Iceland. His enthusiasm was, and still is, infectious and I was, and still am, impressed with the creativity in his approach to science. Mark wanted to do something that no one else was doing and that was promising, though not clearly doable. His original vision is manifested in Chapters 2 and 3 of this thesis and we will continue to exploit the data and general approach for many years to come. An obvious, and powerful, extension to Mark's original idea takes an early form in Chapter 5. Mark showed me what it is to have vision, at both grand and practical scales, and how to think outside the bounds of standard practice in order to reach for the questions whose answers lie just beyond our current reach. For all the things that Mark has done and taught me, I will always be grateful.

Mark was certainly not alone in shaping the work and approaches described in this thesis. I began thinking about the kinds of problems discussed herein while a master's student in Aerospace Engineering at the University of Texas at Austin. My master's thesis advisor, Sean Buckley, introduced me to synthetic aperture radar (SAR), particularly interferometric applications, and helped inspire me to follow my current path. Early on, it became clear that I was more interested in doing science with the data than engineering instruments to collect data and Sean graciously reached out to people he knew that could help bring my nascent interest in glaciology to fruition. Sean helped arrange my original interactions with the UAVSAR group at NASA's Jet Propulsion Laboratory (JPL), which marked a critical turning point in my career.

The bulk of the work described here likely would have never existed without support from the UAVSAR group. In particular, I owe immeasurable gratitude to Yunling Lou for providing me with my first opportunities to work with the radar group at JPL and UAVSAR in particular. Yunling has been a tireless moral and financial supporter of my work on glaciers, as well as wildfires and marine oil spills, neither of which are described in this thesis. Processing UAVSAR data would have been difficult on a practical level without assistance from Brian Hawkins, who helped ensure I always had the most up-to-date software and was always available to answer my questions and help me troubleshoot when things went wrong. Other members of the UAVSAR group that provided essential help are Naiara Pinto, Yang Zheng, Ian Tan, Roger Chao, Ron Muellerschoen, Bill Fiechter, and others. I also want to extend my deepest gratitude to Cathleen Jones and Ben Holt who encouraged and supported my early research efforts in marine oil spills. I learned so much from working with Ben, an oceanographer, and Cathleen, a physicist, on specialized applications of radar and I am proud to know that methods we helped develop are being applied and improved to help protect the global environment from contamination caused by spilled oil.

I owe special thanks to Scott Hensley, whose enthusiasm and knowledge about radar were instrumental in my understanding of SAR and the success of the work described herein. My master's thesis topic was Scott's idea and that work helped me gain a perspective on the interaction of radar and natural media that shaped nearly all of my early research and continues to inform my work. I am fortunate to have had the rare opportunity to work closely with one of the primary developers and master practitioners of a powerful method that has helped bring about a revolution in our understanding of many parts of the Earth and planetary systems.

I am also fortunate to have had so many knowledgable and helpful glaciologists as collaborators over the years. Our Icelandic colleagues—Helgi Björnsson, Finnur Pálsson, Eyjólfur Magnússon, and Alexander Jarosch—have always been welcoming and selfless with their time, patience, and knowledge while guiding me through the process of learning about glaciers. Their expertise in the field and knowledge of their country's glaciers have ensured successful field campaigns and airborne operations with UAVSAR. My knowledge of glaciology, particularly in West Antarctica, was, and continues to be, expanded by my interactions with Hilmar Gudmundsson, who will soon be my postdoctoral advisor at the British Antarctic Survey.

None of the ice flow modeling work presented in this thesis would have been possible without Eric Larour, Mathieu Morlighem, Helene Seroussi, and others with the Ice Sheet Systems Model (ISSM) group at JPL. Eric, Mathieu, and Helene have always been available to answer any of my questions and to simply provide a supportive local group to discuss glaciology. Helene, in particular, put a lot of work into organizing our quasi-regular glaciological reading groups where I learned so much about glaciers in general and the topics of contemporary research in the field. I look forward to many more years of collaborating with everyone on the ISSM team.

Many others at Caltech deserve acknowledgement. I owe thanks to everyone on my thesis committee: Victor Tsai, Andrew Thompson, Michael Lamb, and Jean-Paul Ampuero. Their feedback and support over the years helped inspire many avenues of research featured here and that will continue into the future. My various office mates over the years, including Asaf Inbal and Daniel Bowden, have always provided a motivating and productive work environment interspersed with light-hearted moments that keep the mental gears turning. Bryan Riel has been a great friend, gym partner, and collaborator for more than eight years, starting in our time as aerospace engineering students at the University of Texas at Austin.

I followed an unusual path to get this point and I have innumerable people to thank who played crucial roles along the way. Among them are Hans Mark and Dwayne Surls at the University of Texas who introduced me to research at the Institute for Advanced Technology; my mother who gave me her fire and determination; my father who instilled in me his work ethic; and my grandfather who fueled my insatiable curiosity. It is difficult to describe how much I owe to my friends and fellow Marines—Kenny, Jud, Ian, Jerky, Bob, Brad, Ryan, and others—with whom I served many years stateside and abroad, on land and at sea, during peacetime and war. We shared good times and hard realities. We grew up together, in some sense, and then went our separate ways. Though some are now gone and others I rarely see, their influences from years past continue to resonate. They are my brothers and it was a great honor to have stood with them.

Last, I extend my love and appreciation to Mari, who has given so much time, patience, love, and support during the long hours, difficult setbacks, and eventual triumphs that went into this work. She has cared for our daughter, Ellie, to whom this thesis is dedicated. Without Mari doing the things she did, I could not have done the work I did.

Abstract

My focus in this thesis is to contribute to a more thorough understanding of the mechanics of ice and deformable glacier beds. Glaciers flow under their own weight through a combination of deformation within the ice column and basal slip, which involves both sliding along and deformation within the bed. Deformable beds, which are made up of unfrozen sediment, are prevalent in nature and are often the primary contributors to ice flow wherever they are found. Their granular nature imbues them with unique mechanical properties that depend on the granular structure and hydrological properties of the bed. Despite their importance for understanding glacier flow and the response of glaciers to changing climate, the mechanics of deformable glacier beds are not well understood.

Our general approach to understanding the mechanics of bed deformation and their effect on glacier flow is to acquire synoptic observations of ice surface velocities and their changes over time and to use those observations to infer the mechanical properties of the bed. We focus on areas where changes in ice flow over time are due to known environmental forcings and where the processes of interest are largely isolated from other effects. To make this approach viable, we further develop observational methods that involve the use of mapping radar systems. Chapters 2 and 5 focus largely on the development of these methods and analysis of results from ice caps in central Iceland and an ice stream in West Antarctica. In Chapter 3, we use these observations to constrain numerical ice flow models in order to study the mechanics of the bed and the ice itself. We show that the bed in an Iceland ice cap deforms plastically and we derive an original mechanistic model of ice flow over plastically deforming beds that incorporates changes in bed strength caused by meltwater flux from the surface. Expanding on this work in Chapter 4, we develop a more detailed mechanistic model for till-covered beds that helps explain the mechanisms that cause some glaciers to surge quasi-periodically. In Antarctica, we observe and analyze the mechanisms that allow ocean tidal variations to modulate ice stream flow tens of kilometers inland. We find that the ice stream margins are significantly weakened immediately upstream of the area where ice begins to float and that this weakening likely allows changes in stress over the floating ice to propagate through the ice column.

Contents

List of Figures

List of Tables

Chapter 1

Introduction

Magnificent and imposing, glaciers are the heart of Earth's cryosphere. The relentless flow of glacier ice carves deep valleys, builds moraines, and transports rocks and minerals of all shapes and sizes. Minerals churned up and carried by glaciers produce some of the most biologically productive waters on the planet. Glacier meltwater supplies many of Earth's great rivers, providing freshwater to downstream communities and a source of energy in areas where the flow of water can be harnessed. Their slow flow rates and immense proportions can give the impression that glaciers are relatively stable features of the landscape but both geological evidence and modern observations show that glaciers are capable of appreciable change on timescales from multi-millennia to hours.

Glaciers have long been a focus of scientific inquiry but concerns about the implications of climate change have contributed to increased interest in glaciers in recent years. This attention encompasses small mountain glaciers and continental ice sheets alike and involves scientists from disparate disciplines. Everywhere we look, we see glaciers changing and learn more about the crucial roles glaciers play in local and global environments. Many changes are driven by variations in oceanic and climatic conditions, others by internal instabilities, and all play out over a variety of timescales. Separating natural variability from anthropogenic influences is a daunting task made more difficult by our incomplete understanding of all the processes involved in glacier changes and the timescales at which these processes occur. What is clear is that the response of glaciers to varying environmental conditions is highly nonlinear and developing reliable models of future glacier states requires sound understanding of the physics of ice flow and the physical mechanisms at play on the ice-ocean, ice-atmosphere, and ice-bed interfaces. The latter of these boundaries is the focus of this thesis and we pay particular attention to the special case where glaciers flow over beds composed of deformable sediment.

Deformable beds are found under large portions of many, if not all, of the fast flowing, and numerous slower flowing, glaciers. In areas where we observe the greatest levels of change and rates of change, glacier flow is facilitated predominately by slip along the glacier bed. Often this slip can arise from deformation of underlying till-covered beds. Existing computational models of ice flow do not explicitly consider the mechanics of deformable beds, preferring a form of the basal boundary condition that assumes a power-law relationship between basal slip rate and basal shear traction. The exponent in the power law is always nonnegative and has considerable influence on the temporal variability of ice flow. Understanding the actual mechanics of glacier beds is the first step in effectively including such mechanisms in numerical ice flow models.

In this thesis, we describe our efforts to understand the mechanics of deformable glacier beds through observations, numerical models, and theoretical development. The two main study sites in this thesis—central Iceland and West Antarctica—are separated by more than 16,000 kilometers of open ocean and inhabit very different climates while sharing the common trait of having beds known to be largely covered by deformable sediment. We chose these study sites because they act as natural laboratories, where the mechanisms of interest are largely isolated from other influences and are illuminated by known temporal variations. In central Iceland, temporal variations in ice flow are driven by seasonal surface melt. On Rutford Ice Stream, West Antarctica, temporal variations in ice flow are driven by ocean tides.

Chapter 2 contains methodological development and results from an airborne campaign in central Iceland to collect repeat-pass interferometric synthetic aperture radar (InSAR) data. These data provide measurements of ice surface displacement along the oblique radar line of site direction during the interim between repeated SAR acquisitions. Data were collected from NASA's Uninhabited Aerial Vehicle Synthetic Aperture Radar (UAVSAR) instrument. UAVSAR is one of the few airborne platforms capable of collecting repeat-pass InSAR data and provides us with the unique ability to dictate flight paths and repeat times; most InSAR data are collected by satellites whose orbital parameters are fixed by their governing space agencies, requiring researchers to work with the non-customizable acquisition geometries and schedules. The ability to determine the data acquisition strategy allowed us to collect usable InSAR data during the early melt season when most InSAR data collected by satellites are too noisy to use. To maintain high signal to noise ratios, we scheduled UAVSAR to repeat a given flight plan after 24-hours and for several days over the course of the experiment. We designed the flight plan so that UAVSAR imaged the complete surface of Hofsjökull and Lanjökull, two moderately sized ice caps in central Iceland, from at least three unique vantage points. Using low-noise, short-repeat-time InSAR data from multiple geometries, we reconstruct the 3D velocity field using a Bayesian approach that we developed for the task. GPS data collected on Lanjökull throughout the UAVSAR campaign corroborates our InSAR-derived velocity fields. During this work we quickly discovered that changes in the surface moisture content on the glacier between data acquisitions corrupted the vertical component of the velocity field, a noise source that had not been previously considered in glaciological applications. The vertical component of velocity is small relative to the horizontal components and moisture-induced offsets in the InSAR data are unlikely to map into the horizontal field, so we examine horizontal ice flow and show, through simple ice flow models, that at least half of the observed surface velocity in the faster moving ice is due to slip at the ice-bed interface. Given the weak, volcanic nature of the bedrock beneath both ice caps and the existence of sediment layers beneath many of the outlet glaciers, these observations of surface velocities on Hofsjökull and Lanjökull are the foundation of our work on the mechanics of deformable beds in Iceland.

In Chapter 3, we apply the technique described in Chapter 2 to a similar dataset collected in winter to study the mechanisms of seasonal ice flow variability on Hofsjökull. InSAR-derived velocity fields show significant speedup on most outlet glaciers during the early melt season. As the melt season progresses, some glaciers slow to their wintertime velocities, others slow partially but maintain elevated ice flow relative to wintertime speeds, while others do not slow at all. We focus on understanding this spatially heterogenous response to surface melt. Part of the answer lies in the well-studied, but not well understood, evolution of the hydrological system at the bed of the glaciers, which determines how a given volume of incoming surface meltwater influences basal water pressure at a given time. Our interest is in better understanding the mechanical link between basal water pressure and ice flow in areas with deformable beds. So we develop numerical ice flow models, using the known geometry of Hofsjökull and constrained by the observed surface velocity fields, to infer the mechanical properties of the bed that provide the best match between observed and modeled ice flow. We use the common power-law form of the basal boundary condition and infer the optimal value of the constant of proportionality, testing numerous values for the exponent in the process. We find that the inferred values of basal shear traction, i.e. basal resistance to ice flow, and basal slip rate are independent of our prior assumptions of the value of the exponent in the power-law basal boundary condition. Comparing inferred values of basal slip rate and basal shear traction for winter and different times during the melt season, we further show that basal shear traction is independent of basal slip rate, which is consistent with a plastically deforming bed. Using the inferred basal shear traction fields and assuming a Mohr-Coulomb model for the plastically deforming till, we estimate the spatial distribution of water pressure at the base of the ice cap and change in water pressure during the early melt season. Our results indicate that slight changes in water pressure ($\sim$ 2–3 %) can double glacier flow rates. Motivated by these findings, we develop a new model for basal slip rate over a plastically deforming bed and show that the sensitivity of ice flow to changes in basal water pressure is inversely proportional to the slope of the ice free surface. This means that glaciers with shallow sloping beds are more sensitive to changes in basal water pressure than steeper sloping glaciers, which helps explain much of the spatial heterogeneity in the response of outlet glaciers to seasonal surface melt.

We further develop the theory of basal mechanics in Chapter 4 where we present an original mechanistic model of incipient surge motion in glaciers with till-covered beds. Surges are quasi-periodic episodes of rapid flow interspersed in longer quiescent periods defined by more subtle ice flow rates. Surface velocities during surges can exceed 10–100 times quiescent phase velocities, a change in speed facilitated by increases in basal slip rate. Glaciers capable of surging are exceedingly rare, tend to cluster in space, and are underlain by deformable beds and highly erodible bedrock. Surges begin in winter or late fall when there is little or no meltwater flux from the surface, indicating that surges arise from internal instabilities at the bed. Our model shows the conditions of the instabilities and how a combination of local climate and specific mechanical properties of the bed create conditions favorable for surging. We propose four necessary conditions for glaciers to surge, explore the process of incipient surge motion, and discuss how our model applies to surge cessation as well as initiation. Half of our proposed conditions arise solely from the mechanical and hydrological properties of the bed, imposing potentially strict restrictions on the mechanical properties of surge-type glacier beds. The other conditions link local climate, glacier geometry, and the mechanics of deformable beds, providing a potential path to understanding the geographic distribution of surge-type glaciers.

In Chapter 5, we present an extension to the time domain of the method in Chapter 2. This approach leverages continuous SAR observations to construct a time series of 3D ice surface velocity fields at synoptic spatial scales. Observing temporal variability in all three spatial dimensions over broad spatial scales is an important step in the evolution of modern geodetic remote sensing techniques and we present first-of-their-kind 3D surface velocity field time-series (4D velocity fields) that highlight the potential for continuous synthetic radar observations to constrain spatiotemporal ice flow variability. We validate our technique through a series of rigorous tests on synthetic data designed to resemble our study area, Rutford Ice Stream, West Antarctica. We then apply our

method to SAR data collected over Rutford by COSMO-SkyMed, a constellation of four SAR satellites operated by ASI, the Italian space agency. The resulting 4D velocity fields elucidate the spatial characteristics of the response of ice flow to ocean tidal forcing. GPS data collected inland and immediately seaward of the grounding zone, which separates grounded ice from floating ice, indicate strong modulations (~ 20 %) in horizontal ice flow rates over fortnightly timescales. The primary period of these modulations is the beat frequency of the lunar and solar semi-dirunal tides, which feature the two largest tidal amplitudes. Our results indicate that the response of horizontal ice flow to ocean tidal forcing is most pronounced over the ice shelf, exhibiting amplitudes up to a factor of three larger than over grounded ice. Horizontal ice flow on the floating ice shelf responds to tidal forcing before the grounded ice and variations in horizontal ice flow propagate upstream at a mean rate of 29 km/day, decaying quasi-linearly over a distance of 85 km upstream of the grounding zone. Using ice flow models we show that ice in the margins for tens of kilometers upstream of the grounding zone are weak relative to ice in the central trunk of the ice stream. Weakened margins may allow changes in buttressing, or back stresses, from the ice shelf to be transmitted upstream directly through the ice column, which would not be possible if the margins were strong. Horizontal stress perturbations are likely generated by the grounding and ungrounding of the ice shelf at discrete pinning points and along a several-kilometer-long pinning zone located along the eastern ice shelf margin.

Chapter 2

Early melt-season velocity fields of Langjökull and Hofsjökull ice caps, central Iceland

This chapter has been published as:

B. M. Minchew, M. Simons, S. Hensley, H. Björnsson, and F. Pálsson. Early melt-season velocity fields of Langjökull and Hofsjökull ice caps, central Iceland. *Journal of Glaciology*, 61(226):253–266, 2015.

2.1 Abstract

We infer the horizontal velocity fields of Langjökull and Hofsjökull ice caps, central Iceland, using repeat-pass interferometric synthetic aperture radar (InSAR). NASA's Uninhabited Aerial Vehicle Synthetic Aperture Radar (UAVSAR) acquired airborne InSAR data from multiple vantage points during the early melt season, June 2012. We develop a Bayesian approach for inferring 3D velocity fields from multiple InSAR acquisitions. The horizontal components generally agree with available GPS measurements wherever ice motion is well constrained by InSAR observations. We provide evidence that changes in volumetric moisture content near the glacier surface induce phase offsets that obfuscate the vertical component of the surface velocity fields, an effect that could manifest itself on any glacier that experiences surface melt. Spatial patterns in the InSAR-derived horizontal speeds are broadly consistent with the results of a simple viscous flow model and the directionality of the InSAR-derived horizontal flow field is nearly everywhere consistent with the ice surface gradient. Significant differences between the InSAR-derived horizontal speed and the speed predicted by the viscous flow model suggest that basal slip accounts for more than half of the observed outlet glacier flow.

2.2 Introduction

Glaciers transport ice from areas of mass accumulation at high elevation to areas of mass loss at lower elevations through a combination of internal deformation and slip at the ice-bed interface. While the constitutive relation for viscous flow of glacier ice is relatively well-known (Glen, 1955; Nye, 1957; MacAyeal, 1989), understanding the mechanics of basal slip, which includes the sliding of ice relative to a stationary bed and deformation of the bed, remains an open problem (e.g., Howat et al., 2008; Schoof, 2010; Bartholomaus et al., 2011; Hewitt, 2013; Werder et al., 2013). Slip at the glacier bed is an important component of velocity fields of many glaciers (e.g., Boulton, 1979; Engelhardt and Kamb, 1998; Tulaczyk et al., 2000; Kamb, 2001), accounting for observed seasonal and diurnal velocity variations (e.g., Rignot and Kanagaratnam, 2006; Shepherd et al., 2009; Joughin et al., 2012), and is imperative for erosion to occur (Boulton, 1979; Hallet, 1996; Iverson, 2013). As a result, understanding subglacial mechanics is crucial to developing predictive models of the future states of glaciers, estimating the contribution of glacier melt to sea-level rise, and improving our knowledge of how glaciers shape the landscape.

Direct observations of glacier beds are often impractical whereas surface velocity fields are relatively easy to observe and are useful for inferring subglacial mechanical and hydrological properties (e.g., Iken and Bindschadler, 1986; Kamb, 1987; Tulaczyk et al., 2000; Zwally et al., 2002; Magnússon et al., 2007, 2010, 2011). Repeat-pass interferometric synthetic aperture radar (InSAR) can provide synoptic-scale observations of glacier surface velocities and has been used to map the velocity fields of many glaciers (e.g., Joughin et al., 2001; Rignot et al., 2011), often during winter. To gain a better understanding of the subglacial mechanics, and their interdependence with basal hydrology, it is desirable to observe glaciers during the melt season, in particular the early melt season (Schoof, 2010) when surface meltwater flux can induce variations in basal slip on hourly to monthly time scales (e.g., Zwally et al., 2002; Shepherd et al., 2009; Joughin et al., 2012). However, the amplitudes of velocity fluctuations can be small relative to the mean background velocity (Bartholomew et al., 2010), necessitating accurate and robust InSAR analysis techniques.

It is difficult to make useful InSAR measurements of glaciers during the early melt season because the surface often changes rapidly between SAR acquisitions, inducing high noise levels in InSAR data. Because most InSAR data are acquired by spaceborne systems, the time between repeated acquisitions is fixed and typically on the order of days to weeks, depending on the radar system. To overcome these limitations, we acquired repeat-pass InSAR data using NASA's Uninhabited Aerial Vehicle Synthetic Aperture Radar (UAVSAR), an airborne, L-band (24-cm wavelength) SAR system which allows us to choose the repeat-pass time interval and to design custom flightlines (e.g., Hensley et al., 2009b). In June 2012, we collected InSAR data over Langjökull and Hofsjökull ice caps, central Iceland (Figure 2.1), from multiple vantage points for six noncontinuous days over a 12-day period. We designed the flightlines to provide complete spatial coverage of both ice caps from at least three different look directions with 24-hour repeat-pass times. Short repeat-pass times and L-band radar provided data with acceptable signal-to-noise ratios (SNR) everywhere on both ice caps.

Langjökull and Hofsjökull are natural laboratories which we can use to investigate basal mechanics more easily and in much greater detail than is practical in many other regions. Both ice caps are land-terminating and cover areas of approximately 900 km^2 with typical ice thicknesses of more than 200 m (Björnsson and Pálsson, 2008). The beds of both ice caps have been near-completely mapped with ice-penetrating radar (Björnsson, 1986) and recently obtained surface DEMs are available, mostly from LiDAR surveys. Previous studies of the bedrock lithology show that porous lavas underly southern Langjökull whereas the remainder of Langjökull and all of Hofsjökull rest on impermeable bedrock (Björnsson et al., 2003). Both ice caps have been previously studied using InSAR data acquired with 3-day repeat-pass time by European Remote-sensing Satellite (ERS) in 1994 (Palmer et al., 2009; Gourmelen et al., 2011).

In this study, we present a Bayesian approach to inferring three-dimensional (3D) velocity fields from multiple InSAR acquisitions. Our approach incorporates a data correlation length to reduce large offsets in the velocity field, which often occur at InSAR scene boundaries. We use this Bayesian method to infer the horizontal velocity fields of Langjökull and Hofsjökull ice caps from UAVSAR data. We also present evidence that differential surface moisture content causes phase offsets that corrupt estimates of the vertical velocity component but do not cause significant errors in the inferred horizontal velocity components. We compare the inferred velocity field with a simple viscous flow model and collocated GPS data, discuss the observed characteristics of the outlet glaciers, and show that basal slip is likely to account for more than half of the observed surface velocities in many outlet glaciers.

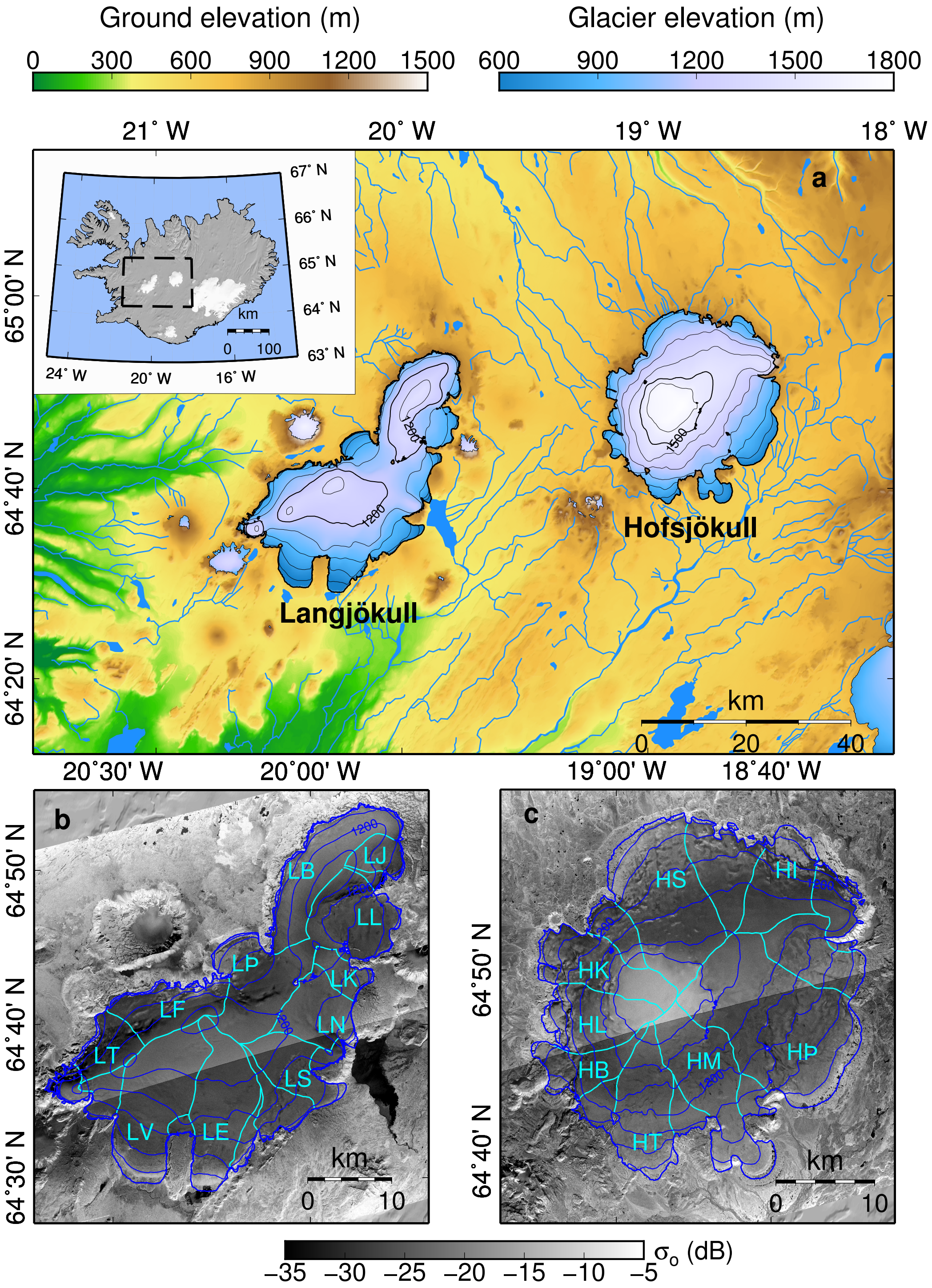

Figure 2.1: (a) Shaded relief map of central Iceland showing Langjökull and Hofsjökull ice caps. Inset map shows the location of the region of interest. (b) and (c) Horizontal transmit, horizontal receive (HH) amplitude images (expressed as normalized radar cross section σ_o) with ice divides (cyan lines) and major outlet glaciers of Langjökull and Hofsjökull (Björnsson, 1988), respectively. Contour lines indicate surface elevation in 150-m increments. The major outlet glaciers of Langjökull are: Þjófadalajökull (LJ), Leiðarjökull (LL), Kirkjujökull (LK), Norðurjökull (LN), Suðurjökull (LS), Eystri-Hagafellsjökull (LE), Vestari-Hagafellsjökull (LV), Svartárjökull (LT), Flosaskarðsjöklar (LF), Þrístapajökull (LÞ), and Baldjökull (LB). The major outlet glaciers of Hofsjökull are: Illviðrajökull (HI), Þjórsárjökull (HÞ), Múlajökull (HM), Blautukvislarjökull (HT), Blágnípujökull (HB), Blöndujökull (HL), Kvíslajökull (HK), and Sátujökull (HS).

2.3 Methodology

InSAR encompasses commonly used methods for measuring deformation or topography of an area that has been imaged at least twice by a SAR system. SAR data are complex-valued, providing information on both the amplitude and phase of the radar waves. InSAR processing takes two SAR scenes and aligns them such that sub-wavelength changes in the path distance between the radar antenna and a given target can be calculated using the difference in the phase of each image (e.g., Rosen et al., 2000). In this study we consider repeat-pass InSAR which requires two SAR images acquired over a given area at different times and from approximately the same sensor position. The final products, called interferograms, provide measurements of displacement along the radar line-of-sight (LOS) unit vector, $\hat{\boldsymbol{\ell}}_i\left(\mathbf{r},\mathbf{r}'_i\right)$, pointing from the sensor position $\mathbf{r}'_i$ to a ground position $\mathbf{r}$. The InSAR phase per unit time in interferogram i is given as:

$$\dot{\phi}_i\left(\mathbf{r}\right)=\frac{\hat{\boldsymbol{\ell}}_i\left(\mathbf{r},\mathbf{r}'_i\right)\cdot\mathbf{u}_i\left(\mathbf{r}\right)}{\Delta t_i} \tag{2.1}$$

where $\mathbf{u}_i\left(\mathbf{r}\right)$ is the displacement vector at $\mathbf{r}$ over repeat-pass time interval Δt_i.

We can write the InSAR measurements in matrix form as:

$$\mathbf{d}\left(\mathbf{r}\right)=\mathbf{G}\left(\mathbf{r},\mathbf{r}'\right)\bar{\mathbf{v}}\left(\mathbf{r}\right) \tag{2.2}$$

where $\bar{\mathbf{v}}\left(\mathbf{r}\right)$ is the mean velocity vector and $\mathbf{G}\left(\mathbf{r},\mathbf{r}'\right)$ is the design matrix. Rows in $\mathbf{G}$ consist of LOS unit vectors associated with the entries of the InSAR phase vector $\mathbf{d}\left(\mathbf{r}\right)$, which we take to be of the form in Eq. 2.1. If $\mathbf{G}$ contains three or more LOS vectors that are sufficiently different from one another, we can solve Eq. 2.2 for an estimate of the mean velocity vector $\bar{\mathbf{v}}$.

2.3.1 Velocity model

We approach the problem of estimating $\bar{\mathbf{v}}$ using a Bayesian formulation that follows Tarantola (2005). Inverse methods are, of course, well-known, epitomized by the least-squares method and its regularized variants. Our motivation for using a Bayesian formulation is to apply a probabilistic approach to derive a generalized model of the desired quantity, in this case $\bar{\mathbf{v}}$, and estimates of the uncertainties of the model parameters. There are three parameters that form the conceptual basis of this approach: The *a posteriori* conditional probability density function (PDF), or posterior, of the model, $\mathbf{m}$, given the observed data; the *a priori* PDF, or liklihood, which relates the observations with the model; and the *a priori* PDF of the model, known as the prior, which incorporates prior expectations of all model parameters. The basic strategy of Bayesian inversion is then to represent the posterior, $P(\mathbf{m}|\mathbf{d})$, as a combination of the likelihood, $P(\mathbf{d}|\mathbf{m})$, and prior, $P(\mathbf{m})$. Maximizing the posterior yields an expression for the model that is comparable to classical regularized least-squares formulations but includes prior model estimates and a prior model covariance matrix. Though we use Bayesian inversion to infer a relatively simple physical model, 3D velocity fields, we note that the formulation of the posterior model is generalized and can be used to infer most any linear or nonlinear model. Because Bayesian inverse methods are well developed (cf. Tarantola, 2005; Stuart, 2010), the following derivation of the posterior model for $\bar{\mathbf{v}}$ is concise, meant only as an overview for readers unfamiliar with Bayesian methods.

Let $\mathbf{m}$ be a model for $\bar{\mathbf{v}}$ such that $\mathbf{m} \in \mathfrak{M}$, where $\mathfrak{M}$ is the set of all realizable models. From Bayes' Theorem, the posterior probability distribution is given as (Tarantola, 2005):

$$P(\mathbf{m}|\mathbf{d}) \propto \quad P(\mathbf{d}|\mathbf{m})P(\mathbf{m}) \tag{2.3}$$

Assuming a Gaussian model, the likelihood and prior are defined as (Tarantola, 2005):

$$P(\mathbf{d}|\mathbf{m}) \propto \quad \exp\left\{-\tfrac{1}{2}\left(\mathbf{d}-\mathbf{G}\mathbf{m}\right)^T \mathbf{C}_d^{-1}\left(\mathbf{d}-\mathbf{G}\mathbf{m}\right)\right\} \tag{2.4}$$

$$P(\mathbf{m}) \propto \quad \exp\left\{-\tfrac{1}{2}\left(\mathbf{m}-\mathbf{m}_0\right)^T \mathbf{C}_m^{-1}\left(\mathbf{m}-\mathbf{m}_0\right)\right\} \tag{2.5}$$

respectively, where $\mathbf{m}_0$ is the prior model estimate, and $\mathbf{C}_m$ and $\mathbf{C}_d$ are the prior model and data covariance matrices, respectively. Plugging Eqs. 2.4 and 2.5 into Eq. 2.3 yields:

$$P(\mathbf{m}|\mathbf{d}) \propto \exp\left\{-\beta\left(\mathbf{m}\right)\right\} \tag{2.6}$$

where:

$$\begin{aligned}\beta\left(\mathbf{m}\right) = \frac{1}{2} \quad &\Big(\left(\mathbf{d}-\mathbf{G}\mathbf{m}\right)^T \mathbf{C}_d^{-1}\left(\mathbf{d}-\mathbf{G}\mathbf{m}\right) + \\ &\left(\mathbf{m}-\mathbf{m}_0\right)^T \mathbf{C}_m^{-1}\left(\mathbf{m}-\mathbf{m}_0\right)\Big)\end{aligned} \tag{2.7}$$

The best-fit posterior model $\widetilde{\mathbf{m}}$ maximizes the posterior probability (*i.e.* minimizes β) such that

(Tarantola, 2005):

$$\widetilde{\mathbf{m}} = \left(\mathbf{G}^T\mathbf{C}_d^{-1}\mathbf{G} + \mathbf{C}_m^{-1}\right)^{-1}\left(\mathbf{G}^T\mathbf{C}_d^{-1}\mathbf{d} + \mathbf{C}_m^{-1}\mathbf{m}_0\right) \tag{2.8}$$

The first term in Eq. 2.8 is the posterior model covariance matrix:

$$\widetilde{\mathbf{C}}_m = \left(\mathbf{G}^T\mathbf{C}_d^{-1}\mathbf{G} + \mathbf{C}_m^{-1}\right)^{-1} \tag{2.9}$$

which provides an estimate of the uncertainties in $\widetilde{\mathbf{m}}$ (Tarantola, 2005). Higher amplitudes in the components of $\widetilde{\mathbf{C}}_m$ indicate higher uncertainty in $\widetilde{\mathbf{m}}$. It is often desirable to encapsulate the error of the posterior model as:

$$\Lambda_m = \sqrt{tr[\widetilde{\mathbf{C}}_m]} \tag{2.10}$$

where tr is the trace operator.

Due to the size of most InSAR data, iterative approaches, which do not explicitly invert the parenthetical term in the righthand side of Eq. 5.21, may be the only computationally tractable way to estimate $\widetilde{\mathbf{m}}$. Therefore, when calculating $\widetilde{\mathbf{C}}_m$ it may be more practical to consider the case where $\mathbf{C}_m^{-1} \ll \mathbf{G}^T\mathbf{C}_d^{-1}\mathbf{G}$ such that Eq. 5.21 simplifies as:

$$\widetilde{\mathbf{C}}_m \approx \left(\mathbf{G}^T\mathbf{C}_d^{-1}\mathbf{G}\right)^{-1} \tag{2.11}$$

whose elements can be estimated for each independent pixel, assuming $\mathbf{C}_d$ is diagonal (see next section), instead of as an ensemble of interdependent pixels as required in Eq. 5.21. From Eq. 2.11, we can see that $\widetilde{\mathbf{C}}_m$ is a function of the viewing geometries (via $\mathbf{G}$) and interferometric noise (via $\mathbf{C}_d$).

Estimates of the uncertainty attributable to non-ideal viewing geometries are contained in the sensitivity matrix:

$$\mathbf{S} = \left(\mathbf{G}^T\mathbf{G}\right)^{-1} \tag{2.12}$$

The diagonal terms of $\mathbf{S}$ are the sums of the squares of the components of the LOS vector and the off-diagonal terms are the sums of the cross products of the LOS vector components. The off-diagonal components indicate the coupling between the respective inferred velocity field components that result from a non-ideal set of viewing geometries while the diagonal components quantify how InSAR measurement errors propagate into the components of $\widetilde{\mathbf{m}}$. An ideal set of viewing geometries can be generally described as having a constant, oblique incidence angle and full azimuthal coverage, with constant azimuthal spacing between flightlines. Differential incidence angles, inconsistent azimuthal spacing, or incomplete azimuthal coverage in the viewing geometries leads to non-zero off-diagonal components and increased sensitivity to measurement noise. Sensitivity to measurement noise decreases with increasing amounts of data. To characterize the contribution of the LOS geometry to the model uncertainty, we define the variance term:

$$\Lambda_g = \sqrt{tr[\mathbf{S}]} \tag{2.13}$$

Readers familiar with GPS analysis might recognize Λ_g as the position dilution of precision (PDOP), the spatial component of the geometric dilution of precision (GDOP) (Misra and Enge, 2006).

We can glean some intuition about the sensitivity of Λ_g to the number of independent data and a constant incidence angle by considering an idealized set of $p \geq 3$ viewing geometries. Let the members of a set of p LOS unit vectors be defined in a spherical coordinate system described by equispaced azimuth angles ($\psi_k = 2\pi k/p$, for $k = 1, ..., p$) and a constant incidence angle θ, measured relative to vertical. These simplifications yield:

$$\Lambda_g = \sqrt{\frac{1}{p}\left(\frac{4}{\sin^2\theta} + \frac{1}{\cos^2\theta}\right)} \tag{2.14}$$

Therefore, Λ_g decreases as the square root of the number of observations for a given θ and is approximately constant, for a given p, over the range of incidence angles common in InSAR data.

2.3.2 Data covariance matrix

The data covariance matrix, $\mathbf{C}_d$, can have contributions from atmospheric phase delay (e.g., Hanssen, 2001; Emardson et al., 2003; Lohman and Simons, 2005), interferometric decorrelation (e.g., Rodriguez and Martin, 1992; Hanssen, 2001; Zebker and Villasenor, 1992), and spatial dependences within the InSAR data. Because the spatial scales of our study areas are no more than a few kilometers while the spatial wavelength of atmospheric phase delays are $\sim$ 10 km (Emardson et al., 2003) and we do not know the *a priori* spatial dependencies in the InSAR data, we assume that the data covariance matrix $\mathbf{C}_d$ is a function of only the interferometric SNR and is defined as:

$$\mathbf{C}_{d_{ij}} = \begin{cases} \sigma^2_{d_i} & i = j \\ 0 & i \neq j \end{cases} \tag{2.15}$$

where $\sigma^2_{d_i}$ is the phase variance for a given pixel in scene i. If any of the interferograms considered in the estimation share a common SAR scene (*i.e.* acquisition), the data covariance matrix will have off-diagonal components (Emardson et al., 2003).

The phase variance can be estimated as a function of the interferometric correlation γ_i and N_i, the number of pixels in the incoherent averaging window (*i.e.* the number of independent looks) for scene i, using the Cramer-Rao bound (Rodriguez and Martin, 1992):

$$\sigma^2_{d_i} = \frac{1}{2N_i}\frac{1-|\gamma_i|^2}{|\gamma_i|^2} \tag{2.16}$$

The interferometric correlation γ_i is defined as (e.g., Rosen et al., 2000):

$$\gamma_i = \frac{\langle s_a s_b^* \rangle_i}{\sqrt{\langle s_a s_a^* \rangle \langle s_b s_b^* \rangle}} \qquad 0 \leq |\gamma_i| \leq 1 \tag{2.17}$$

where s_z is the complex scattered signal in SAR image z, $\langle \cdot \rangle$ indicates averaging over numerous realizations of the argument, and * represents the complex conjugate. The phase in Eq. 5.31 is the interferometric phase and the complement of the amplitude ($\varsigma_i = 1 - |\gamma_i|$) is commonly called the interferometric decorrelation.

The correlation amplitude, sometimes called the coherency, provides an estimate of the interferometric noise in a given interferogram. Values near unity indicate a small amount of interferometric noise whereas correlation values near zero mean that the data are dominated by noise. The interferometric correlation is generally defined as a product, $\gamma_i = [\gamma_n \gamma_b \gamma_z \gamma_t]_i$, where the four independent components are due to noise, viewing geometry (perpendicular baseline), volumetric effects, and temporal variations in the scatterers, respectively (e.g., Rosen et al., 2000).

2.3.3 Prior model covariance matrix

We should define the prior model covariance matrix for a given study area based on the physical processes being studied. Choosing $\mathbf{C}_m^{-1} = \mathbf{0}$ reduces Eq. 2.8 to the classical weighted least squares problem, the least computationally demanding approach. This choice implicitly assumes that points within the prior model are independent from all other points, which is not necessarily true for many geophysical problems.

In this study, we expect the surface velocity to vary smoothly in space such that $\nabla^2 \mathbf{m}_0 \approx \mathbf{0}$.

Therefore, we define the model prior covariance matrix as (Ortega, 2013):

$$\mathbf{C}_m^{-1} = \kappa(\nabla^2)^T \boldsymbol{\Omega}_d \nabla^2 \tag{2.18}$$

where κ is a scalar weighting parameter, whose value can be chosen to reduce high-frequency variations in the posterior model, and:

$$\Omega_{d_{ij}} = \begin{cases} \left[\mathbf{G}^T \mathbf{C}_d^{-1} \mathbf{G}\right]_{ij} & i = j \\ 0 & i \neq j \end{cases} \tag{2.19}$$

Because we assume $\mathbf{m}_0$ to be smoothly varying, it follows that $\mathbf{C}_m^{-1}\mathbf{m}_0 \approx \mathbf{0}$. We note that applying Eq. 2.18 to Eq. 2.8 reduces Eq. 2.8 to a form similar to Tikhonov-regularized least-squares.

Applying this form of $\boldsymbol{\Omega}_d$ results in a spatially varying damping factor and weights the elements of the Laplacian in terms of the interferometric phase variances, through $\mathbf{C}_d^{-1}$, and the viewing geometry, via $\mathbf{G}$. A key advantage to using the Laplacian form of $\mathbf{C}_m^{-1}$ is that we do not impose specific values for our prior model $\mathbf{m}_0$, as would be the case if we assumed $\mathbf{C}_m^{-1} = \mathbf{0}$. In other words, we implicitly apply a correlation length to $\mathbf{m}_0$ that effectively makes velocity models with unphysical discrete jumps less likely in areas with non-ideal data coverage.

2.3.4 Limitations of the Bayesian method

The primary limitations of the Bayesian method discussed above are attributable to limitations of the chosen form of the prior model, $\mathbf{m}_0$, its associated prior covariance, $\mathbf{C}_m$, and incomplete representations of errors described by the data covariance matrix $\mathbf{C}_d$. These limitations are consistent with any inverse problem but we discuss them here in the context of our formulation of $\widetilde{\mathbf{m}}$. For this study, we chose a posterior model that contains only an average velocity vector field because the temporal sampling of our dataset negates the possibility of resolving other model components. This model implicitly assumes that there is no acceleration. However, our data were collected over a finite time during the early melt season when diurnal variations in velocity driven by variable surface meltwater flux might be present. As a result, a time-invariant average velocity does not perfectly represent glacier motion and this shortcoming in the model introduces a prediction error (Duputel et al., 2014) for which we currently cannot account. Though beyond the scope of this study, we note that, in general, a model could be composed of a mean velocity, a secular acceleration, a series of harmonic functions, and any number of transient functions (cf. Hetland et al., 2012; Riel et al., 2014).

The most appropriate form of the prior data covariance matrix must be based on a number of factors. As previously discussed, we assume that the data covariance matrix used in this study is diagonal and thereby neglect off-diagonal components. Our main motivations for this assumption are simplicity and computational tractability. We recognize that the resulting posterior model covariance matrix does not fully capture the total, or true, errors, but we expect it to capture most of the formal errors because the off-diagonal components of $\mathbf{C}_d$ are small relative to the diagonal components for the reasons discussed above. It is important to note that formal errors are not necessarily a complete or accurate representation of total errors. In the model defined in Eq. 2.8, formal errors are described by the posterior model covariance matrix, a function of only viewing geometry and InSAR correlation. Any noise sources that do not impact either of these parameters are unaccounted for in the formal error. The classic example of such a noise source is tropospheric delay (e.g., Lohman and Simons, 2005). Phase shifts caused by differences in the volumetric moisture content at or near the surface of the glacier between radar acquisitions will also introduce errors that are not fully manifest in our current error estimation.

2.3.5 Moisture-induced error

Just as propagation through water vapor in the troposphere can cause erroneous deformation signals in interferograms (e.g., Zebker et al., 1997; Hanssen, 2001; Emardson et al., 2003; Lohman and Simons, 2005), moisture contained in a volume through which the signal propagates can cause phase offsets. There is even evidence to suggest that changes in the moisture content of natural media that are typically thought of as purely surface scatterers, such as bare agricultural fields, can cause phase shifts (Nolan and Fatland, 2003; Nolan et al., 2003; Khankhoje et al., 2012). Our interest is in accurate estimates of surface velocity during the early melt season, so it is important to consider the potential influence of moisture content on the radar signal in order to properly understand how InSAR phase estimates relate to actual glacier motions. Hereafter when discussing moisture content or surface moisture in the context of InSAR measurements and as they relate to moisture-induced errors, we are referring to the volumetric concentration of liquid water in the uppermost region of the glacier that extends down to at least the penetration depth of the radar signal.

Whenever air temperatures exceed the melting temperature, snow at or near a glacier's surface will be infused with liquid water and exhibit variations in moisture content over timescales shorter than repeat-pass time intervals. Changes in moisture content in the near-surface influence SAR phase values via the permittivity of the media. The real component of the permittivity of liquid water is approximately 80, which differs markedly from the real permittivity for dry snow, which is close to unity (Ulaby et al., 1986). As a result, even small changes in surface moisture content can significantly influence the electromagnetic properties of media observed with shallow-penetrating radar.

We use a simple empirical model to show the dependence of permittivity on the moisture content. Based on laboratory measurements of the scattered electric fields for snow samples with various moisture contents, Hallikainen et al. (1986) modeled the relative permittivity of wet snow ε as:

$$\varepsilon = \varepsilon' - i\varepsilon'' \tag{2.20}$$

$$\varepsilon' = 1 + c_\rho \rho_s + 2\nu_m + \psi \tag{2.21}$$

$$\varepsilon'' = (f_0/f_r)\,\psi \tag{2.22}$$

$$\psi = \frac{30\nu_m^{1.3}}{1+(f_0/f_r)^2} \tag{2.23}$$

where f_0 is the radar frequency in free-space, $f_r \approx 9$ GHz is the relaxation frequency of liquid water in snow, c_ρ is a constant equal to 1.83×10^{-3} m^3 kg^{-1}, ρ_s is the density of dry snow, and ν_m is the dimensionless volumetric concentration of liquid water. Eqs. 2.20–2.23 show that while both the real and imaginary permittivity components increase with the liquid water content, the real component is more sensitive to changes in moisture content over the range of standard SAR frequencies (Figures 2.2a and 2.2b). Increasing permittivity can (1) reduce the penetration depth δ_p of the radar signal ($\delta_p \approx \sqrt{\varepsilon'}/\left[k_0\varepsilon''\right]$, where k_0 is the radar wavenumber in free space; Figure 2.2c), (2) increase the wavenumber of the penetrating radar signal ($k = k_0\sqrt{\varepsilon}$), and (3) increase the power scattered by the free surface due to increased surface reflectivity, which scales with permittivity and local incidence angle. (Ulaby et al. (1986) offers a more thorough treatment of the electromagnetic properties of various media, as it pertains to radar remote sensing.)

An idealized, heuristic model of InSAR phase shows the effect of changing permittivity between two SAR scenes. This conceptual model is concerned only with changes in moisture that occur over short (hourly-to-daily) timescales because InSAR is generally ineffective at longer timescales, particularly in areas that experience surface melt. We adopt a basic two-layer model, one thin layer overlying a half-space, to describe moisture changes. Over the timescales of interest, we assume that ν_m is a function of only depth z and varies only in the uppermost layer extending to depth h; ν_m

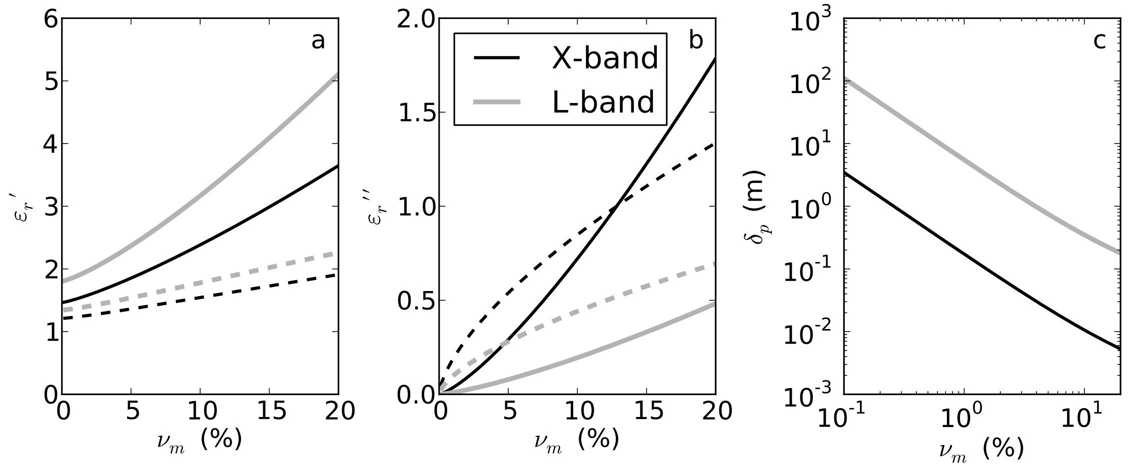

Figure 2.2: Real (a) and imaginary (b) components of the permittivity of snow as a function of liquid water content ν_m calculated from Eqs. 2.20–2.23 (solid lines) using $\rho_s = 500$ kg m^{-3} (Hallikainen et al., 1986), $f_0 = 1.25$ GHz for L-band, and $f_0 = 9.65$ GHz for X-band. Dashed lines show the square root of the like-colored solid line. (c) The penetration depth δ_p of a homogenous medium with a constant permittivity profile dictated by the liquid water content.

is constant for $z > h$. If $h \ll \delta_p$, δ_p will be approximately constant between SAR acquisitions. If we neglect the surface scattered component of the received radar signal, a reasonable approximation when ν_m is small (Mätzler, 1998; Oveisgharan and Zebker, 2007), we can write a simple model for the InSAR phase ϕ of a unit-amplitude incident electric field scattered from a stationary volume as:

$$\phi \approx 2k_0 \int_0^h \left\{ \mu_a \Re\left[\sqrt{\varepsilon_a(z)}\right] - \mu_b \Re\left[\sqrt{\varepsilon_b(z)}\right] \right\} dz \tag{2.24}$$

where subscripts a and b indicate the two SAR scenes used to generate the interferogram, $\Re[\cdot]$ indicates the real component of the complex argument, and $\mu_i = \sqrt{\left[\varepsilon_i'(0) / \left(\varepsilon_i'(0) - \sin^2\theta_i\right)\right]}$, where θ_i is the local radar incidence angle. By comparing Eqs. 2.20–2.23 and 2.24 and the permittivity values shown in Figure 2.2a, we see that even small changes in ν_m for $h > 0$ will influence the InSAR phase. Interested readers can find more in-depth descriptions of the salient physics in Ishimaru (1978) and Ulaby et al. (1986).

2.4 Data

In June 2012, we collected GPS and InSAR data over Langjökull and Hofsjökull ice caps. NASA's Uninhabited Aerial Vehicle Synthetic Aperture Radar (UAVSAR) system collected InSAR data for six days beginning June 3. Ten GPS stations deployed on Vestari-Hagafellsjökull collected 15-second dual-frequency data during the InSAR campaign. Two of these GPS stations, at elevations relative to mean sea level of approximately 490 m and 1100 m, were collocated with automatic weather stations that recorded air temperatures throughout the campaign.

2.4.1 UAVSAR acquisitions

The data used in this study were collected as part of a UAVSAR campaign in which we collected data for 6 noncontinuous days over the course of 12 days. At the time of data acquisition, UAVSAR was being flown aboard a NASA Gulfstream III aircraft that cruises at approximately 12.5 km altitude, providing an incidence angle range of $22°$– $65°$, which we trim to approximately $40°$– $65°$. Data were collected along 15 unique flight lines that were designed to image Langjökull and Hofsjökull (Figure 2.1) from at least three different LOS vectors during each data collection. The flights were scheduled such that the first three days of data were collected in the afternoon, a few hours after the expected maximum daily melt based on temperature, and the final three days of data were collected in the early morning, approximately 12 hours offset from the afternoon data collection. The viewing geometries of the flight lines provide good constraints on the ice flow over most areas (Figure 2.3).

UAVSAR is a fully polarimetric, L-band (1.25 GHz) SAR system whose integrated autopilot system, inertial navigation unit (INU), and real-time GPS system are capable of piloting the aircraft through a 10-m diameter tube that encases the proposed flight line. This aerial precision facilitates repeat-pass interferometric observations whose temporal baseline and LOS vectors can be programmed. High bandwidth (80 MHz) and a large along-track antenna length give UAVSAR a raw spatial resolution of 1.9 m in range (cross-track) and 0.8 m in azimuth (along-track) (Hensley et al., 2009b).

Random aircraft motions complicate the InSAR processing task for UAVSAR data relative to data acquired by satellite-based SAR systems. During processing, these random motions are largely accounted for using data from the INU and GPS system. Centimeter-scale motion between aircraft repeat passes (i.e., the residual interferometric baseline) that is not accounted for using the INU and GPS data is estimated by calculating the amplitude cross-correlation of the two scenes and consider-

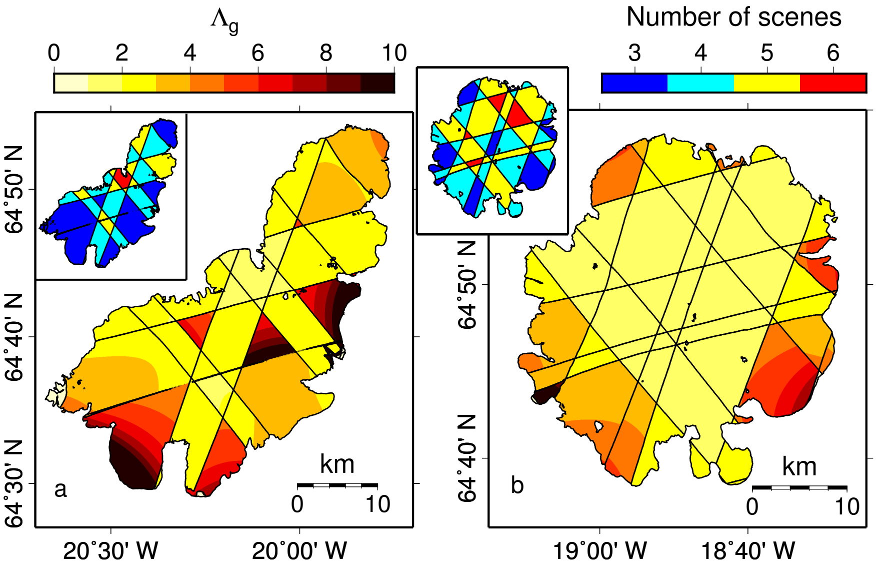

Figure 2.3: Λ_g and (inset) number of SAR scenes collected each day by UAVSAR in June 2012 for (a) Langjökull and (b) Hofsjökull ice caps. Black contour lines denote UAVSAR scene boundaries.

ing only the range-correlated signals to be artifacts of aircraft motion (Hensley et al., 2009a). Small residuals can remain after this process, but because UAVSAR maintains very small perpendicular baselines (typically less than 2 m), the baseline correlation component γ_b is approximately unity. Small perpendicular baselines and UAVSAR's high SNR help ensure that the majority of decorrelation in the repeat-pass interferograms is due to temporal variations in the scatterers and volumetric decorrelation.

2.4.2 InSAR Post-processing

After most of the random motion components were removed from the phase, along with estimates of Earth's curvature and local topography provided by a digital elevation model (DEM), we further processed the data to retrieve interferograms that are useful for inferring the velocity field. We employ a custom DEM that combines data from the Advanced Spaceborne Thermal Emission and Reflection Radiometer (ASTER; version 1) with DEMs for Langjökull, derived from a GPS survey conducted in 1997 (Palmer et al., 2009), and Hofsjökull, derived from LiDAR surveys conducted in 2008 and 2010 (Jóhannesson et al., 2013). Post-processing includes:

- Averaging and decimating each interferogram using a 3×12 (range $\times$ azimuth pixels) averaging window (a process commonly called "looking") which yields an 5×7.2 m pixels in radar coordinates

- Filtering the interferogram using a 10×10 pixel equi-weighted moving average, or lowpass, filter
- Unwrapping the filtered interferogram using the Statistical Cost, Network Flow Algorithm for Phase Unwrapping (SNAPHU) (Chen and Zebker, 2000, 2001, 2002). During unwrapping, we do not distinguish between pixels that image the glaciers from pixels that image the bare ground surrounding the glaciers so InSAR phase is continuous when transitioning between rock and ice
- Geolocating the unwrapped interferograms
- Flattening the geolocated interferograms by fitting and removing a phase surface from the bare ground surrounding the glaciers. We assume the ground around the glaciers was stationary during the 24-hour period between data acquisitions and that this flattening process removes the majority of tropospheric delay (Zebker et al., 1997)

Hereafter, we refer to the flattened, unwrapped, geolocated interferograms simply as interferograms.

We calculated the LOS unit vectors for each interferogram from the geometry of the flight track and the platform position. We reference the LOS vectors to a local east-north-up coordinate system whose origin is coincident with the pixel location in the geolocated image and referenced to the WGS-84 spheroid. The modeled velocity field is referenced to the same coordinate system.

2.4.3 GPS collection and processing

We deployed ten GPS stations on Vestari-Hagafellsjökull, an outlet glacier chosen for logistical simplicity and safety of the field crew. Data were continuously collected every 15 seconds for approximately two weeks. The GPS collection window began two days prior to the first UAVSAR acquisition. Eight of the GPS stations operated throughout the two week deployment period while the other two stations lost power and stopped collecting data after approximately one week. All GPS receivers were mounted on poles sunk several meters into the ice so that the GPS data captures the kinematics of the underlying ice, not the free surface.

We processed the raw GPS data using kinematic precise-point positioning (PPP) methods available as part of GNSS-Inferred Positioning System and Orbit Analysis Simulation Software (GIPSY-OASIS) (e.g., Bertiger et al., 2010). PPP eliminates the need for a ground reference station by using precise clocks along with predetermined satellite orbits (Zumberge et al., 1997) and kinematic processing allows for higher-frequency position updates during processing, which is most suitable for continuously deforming areas. We smoothed the processed positions over a 6-hour window and referenced all motions to the same reference frame as the InSAR-derived velocity fields.

2.5 Results

2.5.1 Inferred velocity field

We present examples of the inferred horizontal component of ice flow for Langjökull and Hofsjökull ice caps along with estimates of the viscous component of ice flow (Figure 2.4). Arrows in Figures 2.4a and 2.4c indicate the direction of horizontal flow and the colormap represents the horizontal speed, which we smoothed using a 200 m × 200 m lowpass filter. The InSAR data were collected in the early mornings of June 13 and June 14, 2012 ($\Delta t \approx 24$ hrs), approximately 14 hours after the maximum daily melt. Unusually warm weather over much of Iceland in early June 2012 caused the atmospheric temperature over central Iceland to peak above freezing in the late afternoon for several days prior to and during data collection.

Juxtaposed with the horizontal velocity fields are velocity fields estimated from a simple ice-flow model that accounts for only the internal viscous deformation in the ice, neglecting all sliding along the glacier bed (Figures 2.4b and 2.4d). Assuming surface-parallel flow and a linear depth-dependent driving stress profile, it can be shown that the viscous component of the ice flow has a power-law relation to ice thickness and surface slope and is given as (Cuffey and Paterson, 2010):

$$v_d = \frac{2A}{n+1}\tau_b^n H \tag{2.25}$$

where τ_b is basal shear stress and H is ice thickness. We assume $\tau_b = \rho_{ice} g H \alpha$, the gravitational driving stress, where α is the ice surface slope, and $\rho_{ice} = 900$ kg m^{-3} is the depth-averaged density of glacier ice. Over broad areas, basal stress cannot exceed gravitational driving stress, meaning that our results for Eq. 2.25 approximate the maximum viscous deformation rate. The variables n and A arise from Glen's flow law, the nonlinear constitutive relationship between the effective strain rate, $\dot{\varepsilon}_E$, and the effective stress, τ_E, within the ice ($\dot{\varepsilon}_E = A\tau_E^n$), and are taken to be 3 and 2.4×10^{-24} Pa^{-3}s^{-1}, respectively (Cuffey and Paterson, 2010). We averaged slope and thickness over a window that is approximately 10 times the average ice thickness in all directions. Arrows in Figures 2.4b

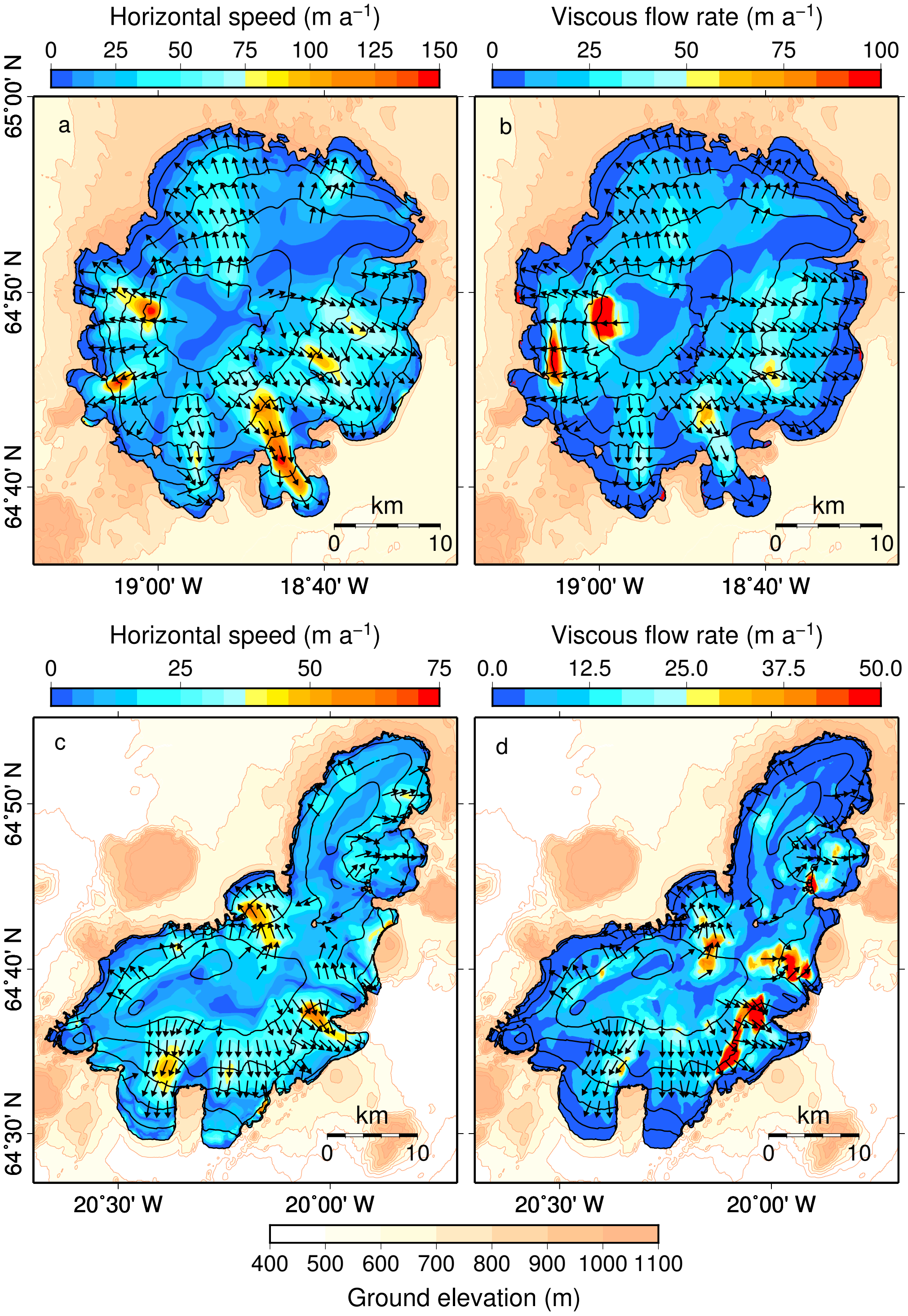

Figure 2.4: (a) Horizontal velocity field for Hofsjökull ice cap inferred from InSAR data collected on June 13 and 14, 2012 ($\Delta t \approx 24$ hrs). Arrows indicate the direction of the ice flow and the colormap indicates the horizontal speed. (b) Velocity estimated from a simple viscous flow model that does not account for basal slip (Eq. 2.25). The color map indicates the speed of viscous flow and arrows the ice surface gradient. The difference between the estimated viscous flow speed and the measured speed in the outlet glaciers is indicative of slip at the glacier bed. Black contour lines are the same as in Figure 2.1 and tan colored areas surrounding the glacier show ground elevation. (c) and (d) are the same as panels (a) and (b), respectively, but for Langjökull.

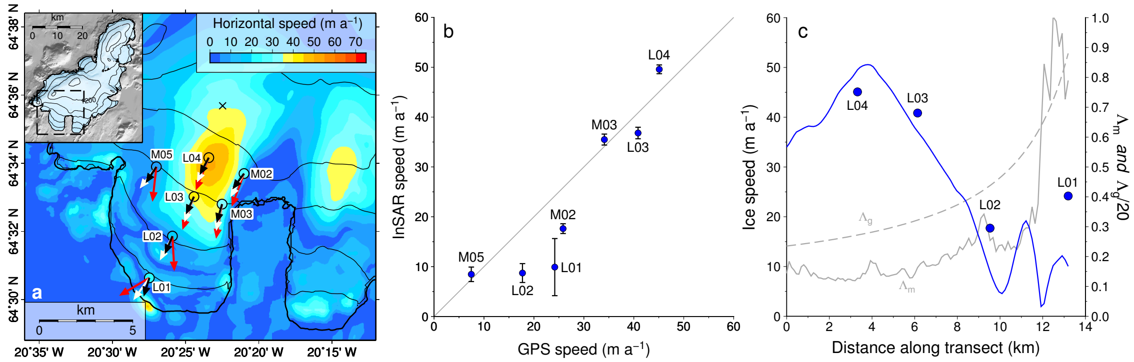

Figure 2.5: (a) GPS receiver locations, flow direction (black arrows), and horizontal speed (colored circles) overlaying the contemporaneous InSAR-derived horizontal speed (colored surface) and collocated flow direction (red arrows) calculated using $\kappa = 10^{-5}$ (Eq. 2.18)–the same velocity field as in Figure 2.4c. Circles are colored on the same color scale as the InSAR-derived field. White arrows indicate the horizontal component of the collocated mean ice surface gradient. Arrow lengths are not to scale. Inset map indicates the extent and location of the main map. Black contour lines are the same as in Figure 2.1. (b) InSAR versus GPS-derived horizontal speed. InSAR values are taken from the velocity field shown in a. Vertical error bars are derived from Λ_m. GPS errors are too small to represent on this scale. (c) InSAR (blue line) and GPS-derived horizontal speeds (blue circles), Λ_m (solid gray line), and Λ_g (dashed gray line) along the transect that begins at the black X in panel a and follows GPS stations L04–L01.

and 2.4d, which are co-located with arrows in Figures 2.4a and 2.4c, respectively, indicate the free surface gradient and the colormap represents the speed calculated from Eq. 2.25. Because the surface slopes are small ($< 20°$) and the viscous flow model is a simple model, we do not convert the surface-parallel values from Eq. 2.25 to true horizontal motion.

2.5.2 InSAR and GPS results

GPS data collected on Vestari-Hagafellsjökull provide an opportunity to validate a portion of the InSAR-derived velocity field (Figure 2.5). Horizontal speeds calculated from GPS data represent the mean velocity over the same time window as the UAVSAR data. Black, white, and red arrows in Figure 2.5a indicate the GPS measured flow vector, the mean surface gradient vector, and the InSAR-derived flow vector, respectively, and are not drawn to scale. Collocated GPS and InSAR-derived horizontal speeds are shown in Figure 2.5b, where the solid gray line is the one-to-one regression line and the vertical error bars are derived from Λ_m. Horizontal speeds along a transect that runs from the black X in Figure 2.5a through GPS stations L04–L01 are shown in Figure 2.5c along with Λ_m and Λ_g for the same transect.

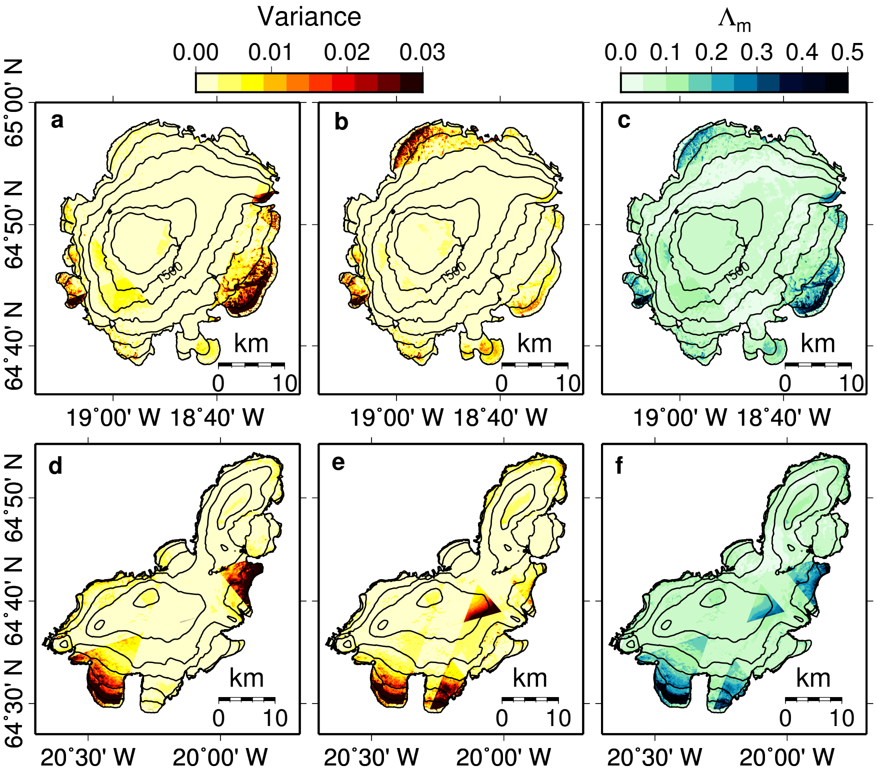

Figure 2.6: East (left column) and north (center column) variance and Λ_m (right column) for the InSAR-derived velocity fields in Figures 2.4a and 2.4c for Hofsjökull (a-c) and Langjökull (d-f) ice caps. Black contour lines are the same as in Figure 2.1.

2.5.3 Posterior Model Covariance

East and north variances from $\widetilde{\mathbf{C}}_m$ provide estimates of the reliability of the respective inferred velocity component (Figures 2.6a and 2.6b for Hofsjökull and Figures 2.6d and 2.6e for Langjökull) while Λ_m indicates the total error in the posterior model (Figures 2.6c and 2.6f). Hofsjökull and, to a lesser extent, Langjökull have low expected errors over most of their surface. High variance values occur in areas where the ice motion is poorly constrained by InSAR observations (Figure 2.3). High frequency features in Figure 2.6 are attributable to variations in interferometric correlation.

2.5.4 Moisture-induced error

The interferograms used to derive the velocity fields contain phase offsets that we attribute to differential volumetric moisture content in the glacier near-surface. Examples of these offsets are shown along with estimates of ambient air temperature in Figure 2.7. We present interferograms collected from two different flight lines that image Hofsjökull on different days (Figures 2.7b–e) along with double-differenced interferograms, i.e. the differences of the respective interferograms (Figures 2.7f–h). Because Hofsjökull is roughly dome-shaped and we designed the flightlines to look up the surface slope as much as possible, these lines are representative of all flightlines. Data used to derive the velocity field in Figure 2.4a are shown in Figure 2.7e. Interferograms (Figures 2.7b–c) and double-differenced interferograms (Figure 2.7f) corresponding to data collected in the afternoon, when surface moisture content should be highest, show a more distinct phase offset relative to data collected in the morning at higher elevations. The differential phase sign change in Figure 2.7f occurs at an elevation where temperatures are approximately 0° C on June 5.

Differential surface moisture content is the only plausible explanation for the residual phase offsets shown in Figure 2.7. All InSAR data used in this study have perpendicular baselines, $B_\perp$, smaller than 10 m, and most data have $B_\perp$ values less than 5 m. Because topographic sensitivity scales with $B_\perp$, the InSAR data shown here have virtually no sensitivity to DEM errors. Furthermore, the residual phase increases from near zero over the bare ground to more than one radian over approximately 10 m near at the edge of the ice. The troposphere is not capable of supporting moisture gradients steep enough to account for such steep phase gradients. Instead, atmospheric phase offsets should smoothly vary from the ice to bare ground over length scales that are at least an order of magnitude longer than the one observed in Figure 2.7.

2.6 Discussion

Our derived horizontal velocity fields on both ice caps qualitatively agree with previously published results that used ERS data collected in February 1994. Over Hofsjökull, Gourmelen et al. (2011) show the same outlet glaciers and general flow pattern, but flow velocities on Illviðrajökull, Þjórsárjökull, and Blautukvislarjökull are markedly higher in February 1994 relative to our results. Because the earlier data were collected in winter and show higher velocities, it is likely that these three glaciers were surging in February 1994. Þjórsárjökull is known to have surged in 1994 (Björnsson et al., 2003), but these observations mark the first recorded surges on Illviðrajökull and Blautukvislarjökull. Our results on Langjökull generally agree with Gourmelen et al. (2011) and Palmer et al. (2009). Slower flow velocities on Suðurjökull in our study relative to 1994 lends credence to the postulate by Palmer et al. (2009) that this glacier was surging in 1994. Unlike Palmer et al. (2009), we do not observe elevated velocities at the edges of the ice cap.

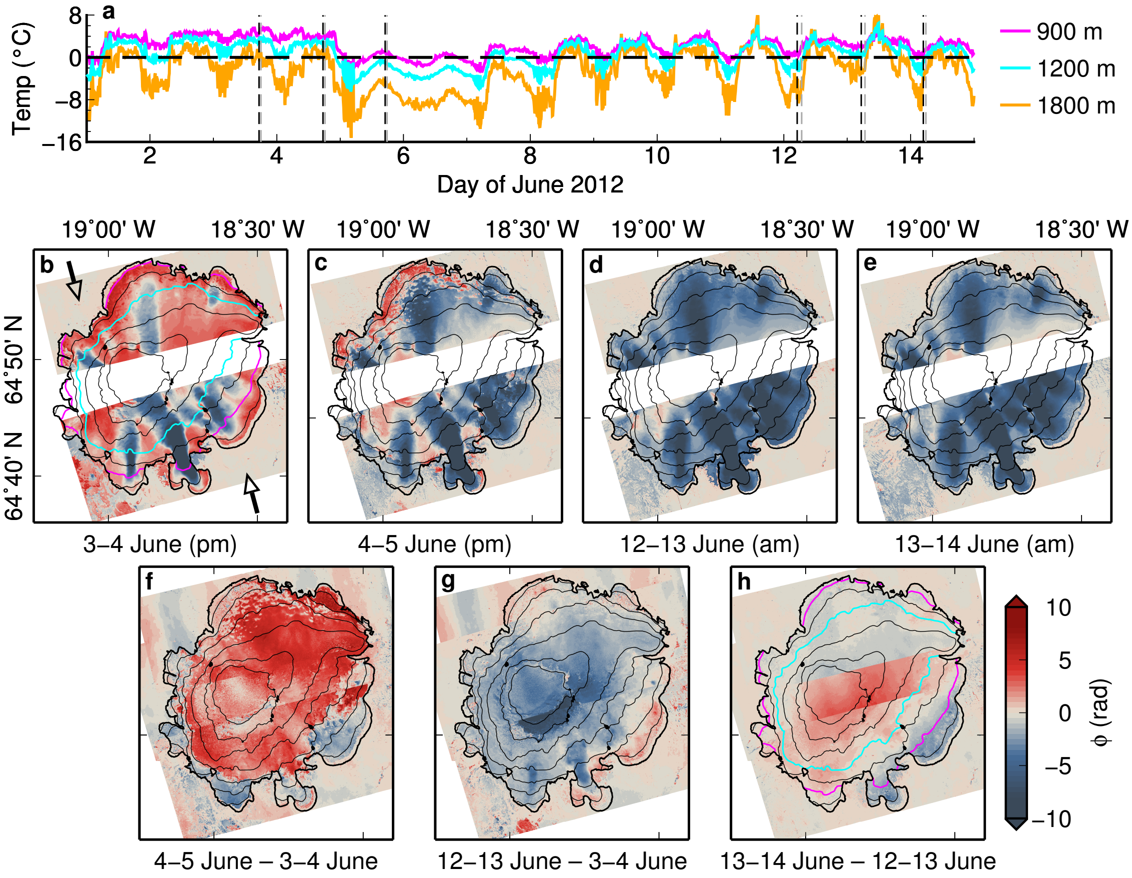

Figure 2.7: Evidence of moisture-induced phase offsets. (a) Estimates of air temperature at elevations indicated in the legend and by like-colored contour lines in panels b and h. Vertical black and gray dashed lines indicate the time of the first and last UAVSAR acquisitions, respectively. (b–e) Examples of flattened, unwrapped interferograms of Hofsjökull for various daily pairs. The respective line-of-sight directions are shown by arrows in panel b and the parenthetical “am” and “pm” indicate that the data were collected in the morning and afternoon, respectively. Note that colormaps are saturated to elucidate phase variations in regions of slow-moving ice. (f–h) Double-differenced interferograms for the two flightlines shown in panels b–e and an additional flightline covering the area in between. LOS direction in the central flightline is the same as the southern flightline. The striped pattern evident outside of the glacier boundary in the northern flightline in panels f and g is residual aircraft motion and the region southwest of Hofsjökull was covered with snow throughout the UAVSAR campaign. Contour line elevations are the same as in Figure 2.1.

Spatial patterns in the horizontal velocity fields of Hofsjökull and Langjökull are broadly consistent with the models of viscous ice flow and the directionality of the measured ice flow is generally along the ice surface slope on both ice caps. Areas of low velocity not located near the edge of the glacier indicate ice divides and areas of high velocity correspond to known outlet glaciers (Figure 2.1; Björnsson, 1988; Björnsson and Pálsson, 2008; Gourmelen et al., 2011). Significant differences between the magnitude of estimated viscous flow and measured velocity fields indicate that basal slip is likely to be an important component of the ice flow. Basal slip rates may be greater on Hofsjökull which typically has higher driving stresses than Langjökull and comparable mechanical properties at the bed (Björnsson, 1986, 1988; Jóhannesson and Sæmundsson, 1998). It remains an open question for future work to ascertain the extent to which surface meltwater flux may be influencing basal slip on each glacier.

On Vestari-Hagafellsjökull, southwest Langjökull, the InSAR-derived velocities agree with collocated GPS velocity measurements. Expected errors in the InSAR-derived velocity field near the upstream GPS stations, L04 and M02, are relatively low and the errors increase by more than a factor of 5 downstream. Stations L03, L04, and M03, whose locations have small Λ_m values, are in close agreement with the InSAR-derived horizontal velocities. High noise in the east component of the InSAR-derived velocity field causes a significant eastward shift in the inferred velocity vector at M05 but not the velocity magnitude, which matches the GPS-measured speed. GPS-derived horizontal speed is higher at station M02 than the InSAR derived velocity field. Because M02 is located in an area with a steep velocity gradient, spatial filtering of the InSAR data is likely to account for the discrepancy between GPS and InSAR speeds. The InSAR-derived velocity near station L01 should be considered unreliable due to high noise caused by suboptimal viewing geometries and low correlation. During field work, we observed significant surface lowering in the vicinity of L02 and postulate that surface dynamics are the source of the disparate InSAR and GPS velocities. We secured the GPS antenna poles several meters into the ice, making GPS measurements largely independent of changes in the local free surface height. By contrast, radar waves incident on the area around L02, where the surface was either wet snow or exposed ice throughout the data collection window, are likely to be influenced by free-surface dynamics because of high radar reflectivity at the surface. The generally good agreement between InSAR-derived and GPS velocities at most station locations suggests that the InSAR-derived velocity fields of both ice caps are reliable enough to allow for analysis of the ice flow.

A variety of characteristic features are evident in the outlet glaciers on both ice caps. Approximately one third of the outlet glaciers, Múlajökull (HM), Blautukvislarjökull (HT), Blágnípujökull (HB), Kvíslajökull (HK), Vestari-Hagafellsjökull (LV), Þrístapajökull (LÞ), and Suðurjökull (LS), form concentrated ice streams that have distinct regions of considerably higher velocity than the surrounding ice. Most of these glaciers occur in areas with high driving stress, though the viscous flow model is a poor indicator of the location and magnitude of the fastest moving ice, further supporting the idea that basal slip is an important contributor to the total ice flux. The remaining outlet glaciers tend to transport ice more diffusively across their widths, having lower shear rates at their margins relative to the more stream-like glaciers. The general characteristics of these sheet-like outlet glaciers are represented, for the most part, in the simple viscous flow models, though their inferred horizontal speeds can be more than a factor of two larger than the model predicts.

The fastest glaciers on Hofsjökull are Múlajökull, Blágnípujökull, and Kvíslajökull, with Múlajökull having the highest transport of the three. These three fast glaciers, along with Sátujökull (HS) in the north, Þjórsárjökull in the east, and Blöndujökull in the west, are known to surge (Björnsson et al., 2003). It is worth noting that only the high velocity area of Kvíslajökull correlates to an expected high in viscous ice flow, based on the simple viscous model, indicating that a large amount of basal slip may be present beneath these glaciers.

Fast glaciers on Langjökull include Þrístapajökull, Norðurjökull, and Vestari-Hagafellsjökull, the deployment site for the GPS stations used in this study. The highest-velocity areas in these fast glaciers generally correlates with areas that have higher predicted rates of viscous flow, though the measured velocity is between a factor 1.5–2 faster than the viscous deformation component, likely indicating significant basal slip in these areas. Vestari-Hagafellsjökull and its eastern neighbor Eystri-Hagafellsjökull, are known surge-type glaciers (Björnsson et al., 2003).

We omit results for the vertical component of the InSAR-derived velocity field from this study because moisture-induced phase offsets make the true vertical component of the ice velocity inaccessible. For example, inferred vertical velocity components corresponding to the horizontal velocity fields given in Figure 2.4 have a median value of approximately 20 m/yr in the up direction, with higher values manifested in the southeast quadrant which receives relatively high levels of solar radiation during the early melt season, and few areas that indicate down-slope flow. None of glaciers that are apparent in the horizontal field are manifested in the vertical velocity component. These results are not physically justifiable. We note that phase offsets occur along the radar LOS and are approximately constant on given days, meaning that the vertical component of the velocity field is particularly sensitive to moisture-induced phase offsets. Future work should focus on methods to decouple the moisture-induced phase offsets from ice motion to allow for accurate estimates of the surface-normal component of the velocity field, an important quantity for ice flow modeling and studies of basal slip.

Moisture-induced phase offsets in InSAR data have the potential to pose problems for high-precision InSAR applications in areas where liquid water is present at the glacier surface. These areas include southern Greenland, the Canadian Arctic Archipelago, the Antarctic Peninsula and peripheral zones, and many mountain glaciers. Here we have shown examples of moisture-induced phase offsets in repeat-pass interferograms, but we note that the dependence of phase on the radar incidence angle (Eq. 2.24) suggests that InSAR-derived DEMs, which utilize SAR data collected from different antenna positions at approximately the same time, may also contain biases that can be linked to volumetric surface moisture content. As a result, InSAR-based studies of glacial mass balance as well as kinematics will benefit from careful scrutiny of the data and consideration of the possible presence of moisture-induced phase offsets.

2.7 Conclusion

We present a new Bayesian approach for inferring 3D velocity fields from multiple InSAR acquisitions and use the new method to infer the horizontal velocity fields for two temperate ice caps, Langjökull and Hofsjökull, central Iceland, from airborne, L-band, repeat-pass InSAR scenes collected in June 2012. The flow directions of the horizontal fields on both ice caps closely agree with the free surface slope and patterns in the horizontal speed are broadly consistent with estimates of viscous flow calculated from surface and bedrock DEMs using a simple model. InSAR-derived horizontal velocities correspond to collocated GPS velocities for the same time period on Vestari-Hagafellsjökull except in areas where the ice motion is not well constrained by the InSAR data.

The InSAR-derived horizontal speeds differ markedly from the predicted viscous flow speeds, likely indicating the importance of basal slip to total ice flow on Langjökull and Hofsjökull. Both ice caps contain numerous outlet glaciers with various flow characteristics. These characteristics range from stream-like outlet glaciers which flow significantly faster than the surrounding ice to sheet-like glaciers which transport ice over broad regions with little internal strain and low strain rates at the margins. Due to the variety of outlet glaciers, similar bed properties, and consistent climate forcing, these ice caps offer a valuable natural laboratory with which to study the mechanics of basal slip.

Differential surface moisture content on the glaciers prevented reliable estimates of the vertical component of the velocity fields. Because moisture-induced phase offsets are approximately constant across all interferograms and are small relative to the phase offsets over the flowing ice, the error is manifested primarily in the vertical velocity field and have little influence on the horizontal velocities.

2.8 Acknowledgements

Funding for the UAVSAR campaign was provided by NASA's Cryospheric Sciences Program. B.M. was supported by a NASA Earth and Space Sciences fellowship and an ARCS Foundation fellowship. We thank the UAVSAR team and the NASA-Dryden flight crew who collected and helped process the InSAR data, T. Johannesson of the Icelandic Meteorological Office for providing the Hofsjökull surface DEM, S. Owen (JPL) for assistance with GIPSY-OASIS, and F. Ortega (Caltech) for reviewing the manuscript.

Bibliography

T. C. Bartholomaus, R. S. Anderson, and S. P. Anderson. Growth and collapse of the distributed subglacial hydrologic system of Kennicott Glacier, Alaska, USA, and its effects on basal motion. *Journal of Glaciology*, 57(206):985–1002, 2011.

I. Bartholomew, P. Nienow, D. Mair, A. Hubbard, M. A. King, and A. Sole. Seasonal evolution of subglacial drainage and acceleration in a Greenland outlet glacier. *Nature Geoscience*, 3(6): 408–411, 2010. doi: 10.1038/ngeo863.

W. Bertiger, S. D. Desai, B. Haines, N. Harvey, A. W. Moore, S. Owen, and J. P. Weiss. Single receiver phase ambiguity resolution with gps data. *Journal of Geodesy*, 84(5):327–337, 2010.

H. Björnsson. Surface and bedrock topography of ice caps in Iceland mapped by radio echo soundings. *Annals of Glaciology*, 8:11–18, 1986.

H. Björnsson. *Hydrology of Ice Caps in Volcanic Regions*. Societas Scientarium Islandica, University of Iceland, Reykjavik, Iceland, 1988.

H. Björnsson and F. Pálsson. Icelandic glaciers. *Jökull*, 58:365–386, 2008.

H. Björnsson, F. Pálsson, O. Sigurðsson, and G. Flowers. Surges of glaciers in Iceland. *Annals of Glaciology*, 36:82–90, 2003.

G. S. Boulton. Processes of glacier erosion on different substrata. *Journal of Glaciology*, 23(89): 15–37, 1979.

C. W. Chen and H. A. Zebker. Network approaches to two-dimensional phase unwrapping: intractability and two new algorithms. *Journal of the Optical Society of America A*, 17(3):401–414, 2000.

C. W. Chen and H. A. Zebker. Two-dimensional phase unwrapping with use of statistical models for cost functions in nonlinear optimization. *Journal of the Optical Society of America A*, 18(2): 338–351, 2001.

C. W. Chen and H. A. Zebker. Phase unwrapping for large SAR interferograms: Statistical segmentation and generalized network models. *IEEE Transactions on Geoscience and Remote Sensing*, 40(8):1709–1719, 2002.

K. M. Cuffey and W. S. B. Paterson. *The Physics of Glaciers*. Elsevier, 4th edition, 2010.

Z. Duputel, P. S. Agram, M. Simons, S. E. Minson, and J. L. Beck. Accounting for prediction uncertainty when inferring subsurface fault slip. *Geophysical Journal International*, 197(1):464–482, 2014.

T. R. Emardson, M. Simons, and F. H. Webb. Neutral atmospheric delay in interferometric synthetic aperture radar applications: Statistical description and mitigation. *Journal of Geophysical Research: Solid Earth*, 108(B5):2231, 2003.

H. Engelhardt and B. Kamb. Basal sliding of Ice Stream B, West Antarctica. *Journal of Glaciology*, 44(147):223–230, 1998.

J. W. Glen. The creep of polycrystalline ice. *Proceedings of the Royal Society of London A*, 228 (1175):519–538, 1955.

N. Gourmelen, S.W. Kim, A. Shepherd, J.W. Park, A.V. Sundal, H. Björnsson, and F. Pálsson. Ice velocity determined using conventional and multiple-aperture InSAR. *Earth and Planetary Science Letters*, 307(1–2):156–160, 2011.

B. Hallet. Glacial quarrying: a simple theoretical model. *Annals of Glaciology*, 22:1–8, 1996.

M. Hallikainen, F. T. Ulaby, and M. Abdelrazik. The dielectric properties of snow in the 3- to 37 GHz range. *IEEE Transactions on Antennas and Propogation*, 34(11):1329–1340, 1986.

R. F. Hanssen. *Radar Interferometry: Data Interpretation and Error Analysis*. Springer, 1st edition, 2001.

S. Hensley, T. Michel, M. Simard, C. Jones, R. Muellerschoen, C. Le, H. Zebker, and B. Chapman. Residual motion estimation for UAVSAR: Implications of an electronically steered array. In *Proceedings 2009 IEEE Radar Conference*, Pasadena, CA, 2009a.

S. Hensley, H. Zebker, C. Jones, T. Michel, R. Muellerschoen, and B. Chapman. First demonstration results using the NASA/JPL UAVSAR instrument. In *2nd Annual Asia Pacific SAR Conference*, Xian, China, 2009b.

E. A. Hetland, P. Musé, M. Simons, Y. N. Lin, P. S. Agram, and C. J. DiCaprio. Multiscale InSAR Time Series (MInTS) analysis of surface deformation. *Journal of Geophysical Research: Solid Earth*, 117(B2):n/a–n/a, 2012. doi: 10.1029/2011JB008731.

I. J. Hewitt. Seasonal changes in ice sheet motion due to melt water lubrication. *Earth and Planetary Science Letters*, 371–372:16–25, 2013. doi: http://dx.doi.org/10.1016/j.epsl.2013.04.022.

I. M. Howat, S. Tulaczyk, E. Waddington, and H. Björnsson. Dynamic controls on glacier basal motion inferred from surface ice motion. *Journal of Geophysical Research*, 113(F03015):1–15, 2008.

A. Iken and R. Bindschadler. Combined measurements of subglacial water pressure and surface velocity of Findelengletscher, Switzerland: conclusions about drainage systems and sliding mechanisms. *Journal of Glaciology*, 32(110):101–119, 1986.

A. Ishimaru. *Wave Propogation and Scattering in Random Media*. Academic Press, New York, NY, 1978.

N. R. Iverson. A theory of glacial quarrying for landscape evolution models. *Geology*, 40(8): 679–682, 2013.

H. Jóhannesson and K. Sæmundsson. Geological map of Iceland. 1: 500 000. *Tectonics. Icelandic Institute of Natural History, Reykjavik*, 1998.

T. Jóhannesson, H. Björnsson, E. Magnússon, S. Guðmundsson, F. Pálsson, O. Sigurðsson, T. Thorsteinsson, and E. Berthier. Ice-volume changes, bias estimation of mass-balance measurements and changes in subglacial lakes derived by lidar mapping of the surface of icelandic glaciers. *Annals of Glaciology*, 54(63):63–74, 2013. doi: doi:10.3189/2013AoG63A422.

I. Joughin, M. Fahnestock, D. MacAyeal, J. L. Bamber, and P. Gogineni. Observation and analysis of ice flow in the largest Greenland ice stream. *Journal of Geophysical Research: Atmospheres*, 106(D24):34021–34034, 2001.

I. Joughin, B. E. Smith, I. M. Howat, D. Floricioiu, R. B. Alley, and M. Truffer, M. Fahnestock. Seasonal to decadal scale variations in the surface velocity of Jakobshavn Isbrae, Greenland: Observation and model-based analysis. *Journal of Geophysical Research*, 117(F02030):1–20, 2012.

B. Kamb. Glacier surge mechanisms based on linked cavity configuration of the basal water conduit system. *Journal of Geophysical Research*, 92(B9):9083–9100, 1987.

B. Kamb. Basal zone of the West Antarctic Ice Streams and its role in lubrication of their rapid motion. In *The West Antarctic Ice Sheet: Behavior and Environment, Antarctic Research Series*, volume 77, pages 157–199. AGU, 2001.

U. K. Khankhoje, J. J. van Zyl, and T. A. Cwik. Computation of radar scattering from heterogeneous rough soil using the finite-element method. *IEEE Transactions on Geoscience and Remote Sensing*, pp(99), 2012.

R. Lohman and M. Simons. Some thoughts on the use of InSAR data to constrain models of surface deformation: Noise structure and data downsampling. *Geochemistry, Geophysics, Geosystems*, 6 (1):1–12, 2005.

D. MacAyeal. Large-scale ice flow over a viscous basal sediment - Theory and application to ice stream-B, Antarctica. *Journal of Geophysical Research*, 94(B4):4071–4087, 1989.

E. Magnússon, H. Rott, H. Björnsson, and F. Pálsson. The impacts of jökulhlaups on basal sliding observed by SAR interferometry on Vatnajökull, Iceland. *Journal of Glaciology*, 53(181):232–240, 2007.

E. Magnússon, H. Björnsson, H. Rott, and F. Pálsson. Reduced glacier sliding caused by persistent drainage from a subglacial lake. *The Cryosphere*, 4:13–20, 2010.

E. Magnússon, H. Björnsson, H. Rott, M. J. Roberts, F. Pálsson, S. Guðmundsson, R. A. Bennett, H. Geirsson, and E. Sturkell. Localozed uplift of Vatnajökull ice cap, Iceland: subglacial water accumulation deduced from InSAR and GPS observations. *Journal of Glaciology*, 57(203):475–484, 2011.

C. Mätzler. Improved Born approximation for scattering of radiation in a granular medium. *Journal of Applied Physics*, 83(11):6111–6117, 1998.

P. Misra and P. Enge. *Global Positioning System: Signals, Measurements, and Performance*. Ganga-Jamuna Press, Lincoln, Massachusetts, 2nd edition, 2006.

M. Nolan and D. R. Fatland. Penetration depth as a DInSAR observable and proxy for soil moisture. *IEEE Transactions on Geoscience and Remote Sensing*, 41(3):532–537, 2003.

M. Nolan, D. R. Fatland, and L. Hinzman. DInSAR measurement of soil moisture. *IEEE Transactions on Geoscience and Remote Sensing*, 41(12):2802–2813, 2003.

J. F. Nye. The distribution of stress and velocity in glaciers and ice-sheets. *Proceedings of the Royal Society of London A*, 239(1216):113–133, 1957.

F. Ortega. *Aseismic deformation in subduction megathrusts : central Andes and north-east Japan*. PhD dissertation, California Institute of Technology, 2013.

S. Oveisgharan and H. A. Zebker. Estimating snow accumulation from InSAR correlation observations. *IEEE Transactions on Geoscience and Remote Sensing*, 45(1):10–20, 2007.

S. Palmer, A. Shepherd, H. Björnsson, and F. Pálsson. Ice velocity measurements of Langjökull, Iceland, from interferometric synthetic aperture radar (InSAR). *Journal of Glaciology*, 55(193): 834–838, 2009.

B. Riel, M. Simons, P. Agram, and Z. Zhan. Detecting transient signals in geodetic time series using sparse estimation techniques. *Journal of Geophysical Research: Solid Earth*, 2014.

E. Rignot and P. Kanagaratnam. Changes in the velocity structure of the Greenland Ice Sheet. *Science*, 311:986–990, 2006.

E. Rignot, J. Mouginot, and B. Scheuchl. Ice Flow of the Antarctic Ice Sheet. *Science*, 333(6048): 1427–1430, 2011. doi: 10.1126/science.1208336.

E. Rodriguez and J.M. Martin. Theory and design of interferometric synthetic aperture radars. *Radar and Signal Processing, IEE Proceedings F*, 139(2):147 –159, 1992.

P. A. Rosen, S. Hensley, I. R. Joughin, F. K. Li, S. N. Madsen, E. Rodriguez, and R. M. Goldstein. Synthetic aperture radar interferometry. *Proceedings of the IEEE*, 88(3):333 –382, 2000.

C. Schoof. Ice-sheet acceleration driven by melt supply variability. *Nature*, 468:803–806, 2010.

A. Shepherd, A. Hubbard, P. Nienow, M. King, M. McMillan, and I. Joughin. Greenland ice sheet motion coupled with daily melting in late summer. *Geophysical Research Letters*, 36(1), 2009. doi: 10.1029/2008GL035758.

A. M. Stuart. Inverse problems: A Bayesian perspective. *Acta Numerica*, 19:451–559, 2010.

A. Tarantola. *Inverse problem theory and methods for model parameter estimation*. Society for Industrial and Applied Mathematics, 2005.

S. Tulaczyk, W. B. Kamb, and H. F. Engelhardt. Basal mechanics of Ice Stream B, west Antarctica: 2. Undrained plastic bed model. *Journal of Geophysical Research: Solid Earth*, 105(B1):483–494, 2000.

F. T. Ulaby, R. K. Moore, and A. K. Fung. *Microwave Remote Sensing: Active and Passive*. Artech House, Dedham, Massachusetts, 1986.

M. A. Werder, I. J. Hewitt, C. G. Schoof, and G. E. Flowers. Modeling channelized and distributed subglacial drainage in two dimensions. *Journal of Geophysical Research: Earth Surface*, 118: 1–19, 2013.

H. A. Zebker and J. Villasenor. Decorrelation in interferometric radar echoes. *IEEE Transactions on Geoscience and Remote Sensing*, 30(5):950–959, 1992.

H. A. Zebker, P. A. Rosen, and S. Hensley. Atmospheric effects in interferometric synthetic aperture radar surface deformation and topographic maps. *Journal of Geophysical Research*, 102(B4): 7547–7563, 1997.

J. F. Zumberge, M. B. Heflin, D. C. Jefferson, M. M. Watkins, and F. H. Webb. Precise point positioning for efficient and robust analysis of gps data from large networks. *Journal of Geophysical Research*, 102(B3):5005–5071, 1997.

H. J. Zwally, W. Abdalati, T. Herring, K. Larson, J. Saba, and K. Steffen. Surface melt-induced acceleration of Greenland Ice-Sheet flow. *Science*, 297(5579):218–222, 2002. doi: 10.1126/science.1072708.

Chapter 3

Plastic bed beneath Hofsjökull Ice Cap, central Iceland, and the sensitivity of ice flow to surface meltwater flux

This chapter is in press as:

B. M. Minchew, M. Simons, H. Björnsson, F. Pálsson, M. Morlighem, H. Seroussi, E. Larour, and S. Hensley. Plastic bed beneath Hofsjökull Ice Cap, central Iceland, and the sensitivity of ice flow to surface meltwater flux. *Journal of Glaciology*, 2016.

3.1 Abstract

Mechanical properties of glacier beds play a fundamental role in regulating the sensitivity of glaciers to environmental forcing across a wide range of timescales. Glaciers are commonly underlain by deformable till whose mechanical properties and influence on ice flow are not well understood but are critical for reliable projections of future glacier states. Using synoptic-scale observations of glacier motion in different seasons to constrain numerical ice flow models, we study the mechanics of the bed beneath Hofsjökull, a land-terminating ice cap in central Iceland. Our results indicate that the bed deforms plastically and weakens following incipient summertime surface melt. Combining the inferred basal shear traction fields with a Coulomb-plastic bed model, we estimate the spatially distributed effective basal water pressure and show that changes in basal water pressure and glacier accelerations are nonlocal and nonlinear. These results motivate an idealized physical model relating mean basal water pressure and basal slip rate wherein the sensitivity of glacier flow to changes in basal water pressure is inversely related to the ice surface slope.

3.2 Introduction

The mechanical properties of glacier beds, hereafter called basal mechanics, are a fundamental components of glacier dynamics. The importance of basal mechanics is most pronounced in areas of fast-flowing ice, where much of the ice flow is likely to be accommodated by slip along or deformation within the bed and where resistive basal shear traction can be appreciably less than gravitational driving stress (e.g., Raymond, 1996; Tulaczyk et al., 2000b; Morlighem et al., 2013). The mechanical properties of glacier beds are not fully understood, which has clear implications for the veracity of models of future glacier states (Schoof, 2007a; Favier et al., 2014; Joughin et al., 2014; Tsai et al., 2015). We can improve upon our understanding of basal mechanics by studying temporal variabilities in basal slip, leveraging the response of glaciers to changes in environmental forcing to constrain the set of admissible models of basal mechanics. Here we focus on the special case of the response of land-terminating glaciers with deformable beds to surface meltwater flux.

Glaciers accelerate and decelerate on hourly-to-seasonal timescales in response to surface meltwater flux, changes in terminus position, and thinning at the margins (e.g., Iken and Bindschadler, 1986; Sugiyama and Gudmundsson, 2004; Rignot and Kanagaratnam, 2006; Joughin et al., 2008; Bartholomew et al., 2010). The latter two perturbations primarily affect marine- and lacustrine-terminating glaciers and are not given further consideration in this study. Because viscous deformation rates are controlled by the geometry and mechanical properties of ice, which remain approximately constant on sub-annual timescales, changes in basal mechanical properties are the only plausible sources of observed hourly-to-seasonal timescale flow variability in land-terminating glaciers. These short-timescale ice flow variations have been shown to correlate with surface meltwater flux in the early melt season, sometimes becoming increasingly muted as the melt season progresses and the basal hydrological system evolves (Sugiyama and Gudmundsson, 2004; Bartholomew et al., 2010; Pimentel and Flowers, 2011; Moon et al., 2014).

The states of basal hydrological systems are thought to be bounded by two configurations: cavities that open downstream of bumps and channels that are melted into the base of the ice by flowing water (Röthlisberger, 1972; Nye, 1976; Kamb, 1987; Schoof, 2010). Beginning in spring, water that drains to a glacier's bed likely inundates an inefficient distributed hydrological system, effectively lubricating the bed and accelerating glacier flow (Lliboutry, 1968; Kamb, 1987; Raymond et al., 1995). As the melt season progresses, cavities become linked and will eventually form efficient, arterial channel networks if sufficient water flux is available (Schoof, 2010; Sundal et al., 2011).

Under steady state conditions, channel networks feature lower water pressure than distributed systems and, consequently, lower glacier speeds (Pimentel and Flowers, 2011; Hewitt, 2013; Werder et al., 2013). Throughout the melt season and regardless of the hydrological state, enhanced water flux from rainfall or elevated melt rates can temporarily overwhelm and pressurize basal hydrological systems leading to evanescent increases in glacier flow (Shepherd et al., 2009; Schoof, 2010; Bartholomew et al., 2010). Increasing the frequency and duration of these accelerations results in dynamic glacier thinning (Parizek and Alley, 2004).

Evolution of the basal hydrological system complicates the response of glacier flow to surface meltwater flux, leading some authors to suggest that increased meltwater flux can enhance dynamic mass loss in a warming climate (e.g., Zwally et al., 2002; Parizek and Alley, 2004; Bougamont et al., 2014) while others postulate a limited response (e.g., Joughin et al., 2008; Tedstone et al., 2013, 2015). Understanding the dynamic response of glaciers to surface meltwater flux and the potential for dynamically enhanced mass loss in warming climates requires understanding two separate questions: How does basal water pressure respond to surface meltwater flux and how does glacier flow respond to changes in basal water pressure? In this study, we address only the latter question while considering surface meltwater flux to be the driver of basal water pressure variations.

To better understand the fundamental mechanics of glacier beds and the response of glacier flow to surface meltwater flux, we consider Hofsjökull, a relatively small ice cap in central Iceland (Fig. 3.1). Hofsjökull experiences seasonal melt and contains multiple land-terminating outlet glaciers. Land termination isolates the influence of basal water pressure on glacier flow by eliminating ocean tidal forcing and seasonal accelerations attributable to displacement of calving fronts (Joughin et al., 2008). Hofsjökull's small size (diameter ≈ 40 km), gentle surface slopes, and dome-like shape (Fig. 3.1b) allow all outlet glaciers to experience roughly the same climate, thereby helping to elucidate the spatially heterogenous response of individual outlet glaciers to comparable environmental forcing. Hofsjökull, which blankets a dormant volcanic caldera, is known to be underlain by till (Björnsson et al., 2003; Björnsson and Pálsson, 2008), which we show deforms plastically. While observations indicate that plastically deforming beds are well-represented in nature (Boulton, 1979; Iverson et al., 1998; Tulaczyk et al., 2000a), most models of basal mechanics and the influence of basal water pressure on ice flow dynamics focus on rigid-bedded glaciers. Therefore, while our observations focus solely on Hofsjökull, our physical model and conclusions have implications for understanding glacier systems worldwide.

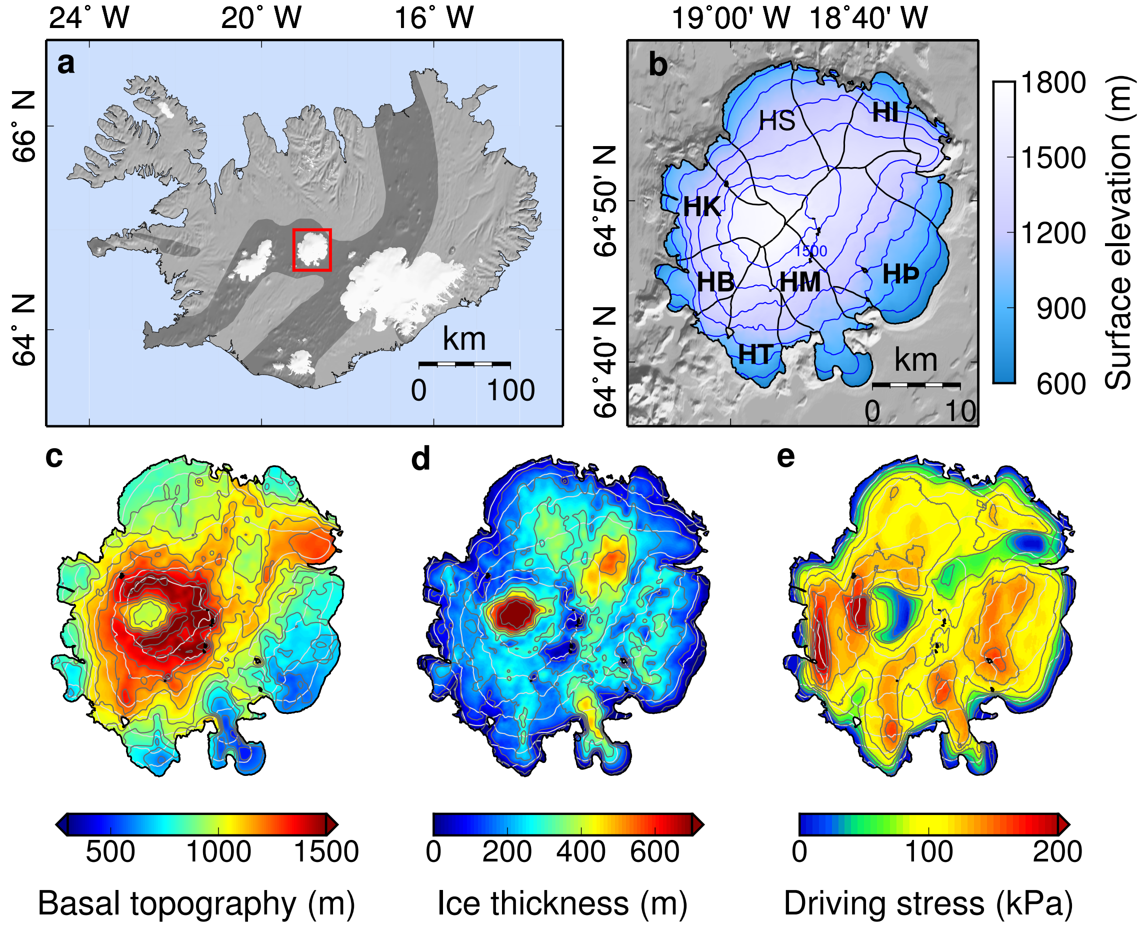

Figure 3.1: **a** Shaded relief map of Iceland. Glaciers are white, Hofsjökull is enclosed by the red box, and darkened regions delineate volcanic zones. The red triangle shows the location where meteorological data shown in Fig. 3.3 were collected and the blue triangle indicates the study area of Boulton (1979). **b** Surface topography (Jóhannesson et al., 2013) (colormap and blue contours)), ice divides (black lines; modified from Björnsson (1986)), and major outlet glaciers of Hofsjökull (Björnsson, 1988). Contour lines indicate ice surface elevation in 150-m increments with the maximum contour at 1650 m. Glacier labels stand for: Illviðrajökull (HI), Þjórsárjökull (HÞ), Múlajökull (HM), Blautukvislarjökull (HT), Blágnípujökull (HB), Kvíslajökull (HK), and Sátujökull (HS). Bolded labels indicate known surge-type glaciers (Björnsson et al., 2003; Minchew et al., 2015). **c** Basal topography relative to mean sea level (Björnsson, 1986) (colormap and dark contours); dark contours are at 100-m increments. **d** Ice thickness (colormap and dark contours); dark contours are at 100-m increments. **e** Gravitational driving stress $\tau_d = \rho g h \alpha$ (colormap and dark contours) with $\rho = 900$ kg m^{-3}; dark contours are at 25-kPa increments. In **c** to **e**, light contour lines are the same as in **b**.

3.3 Data and Methods

3.3.1 Surface velocity observations

We capture temporal flow variability in multiple outlet glaciers during the early melt season by inferring complete velocity fields over Hofsjökull using repeat-pass interferometric synthetic aperture radar (InSAR) data (Fig. 3.2). Airborne InSAR data were collected with NASA's Uninhabited Aerial Vehicle Synthetic Aperture Radar (UAVSAR) (Hensley et al., 2009) in June 2012, beginning approximately two weeks after the onset of seasonal melt on Hofsjökull (Fig. 3.3), and in February 2014, the middle of winter (Minchew et al., 2015). We expect basal water pressure during winter to be at or near annual minimum pressure due to the lack of surface melt, so we take the February data as the reference velocity field (Fig. 3.2a). Because InSAR measures the component of displacement occurring in the time between two radar acquisitions along the (oblique) radar line-of-sight (LOS) vector (Rosen et al., 2000), we designed the UAVSAR data collection to observe all of Hofsjökull from at least three unique LOS directions with approximately equal azimuthal spacing. For each azimuth heading, three flight tracks were needed to cover all of the ice cap, yielding a total of nine different flight tracks (Minchew et al., 2015). UAVSAR was flown aboard a NASA Gulfstream III aircraft that cruises at approximately 12.5 km altitude, providing an incidence angle range of 22°–65°. We incorporated all InSAR data collected on given dates to estimate the horizontal velocity fields using a Bayesian approach (Minchew et al., 2015). The resulting velocity fields have approximately 200-m resolution with typical errors less than 1 cm d^{-1} (Figs. 3.2g–i).

3.3.2 Basal mechanics

To infer the basal shear traction and slip rate, we use the observed velocity fields to constrain finite-element ice flow models. Employing the Ice Sheet Systems Model (ISSM) (Morlighem et al., 2010), we constructed the geometry of Hofsjökull using basal topography derived from ice-penetrating radar surveys (Björnsson, 1986) and lidar-derived surface topography (Jóhannesson et al., 2013) (Figs. 3.1b–e). In ISSM the basal boundary condition uses a Weertman-type sliding law whose scalar form is defined as:

$$\tau_b = C u_b^{1/m} \tag{3.1}$$

where τ_b is the basal shear traction, u_b is the basal slip rate, $m \geq 1$, and coupling between ice and the bed is indicated by the nonnegative scalar C (e.g., Weertman, 1957; Gudmundsson and Raymond,

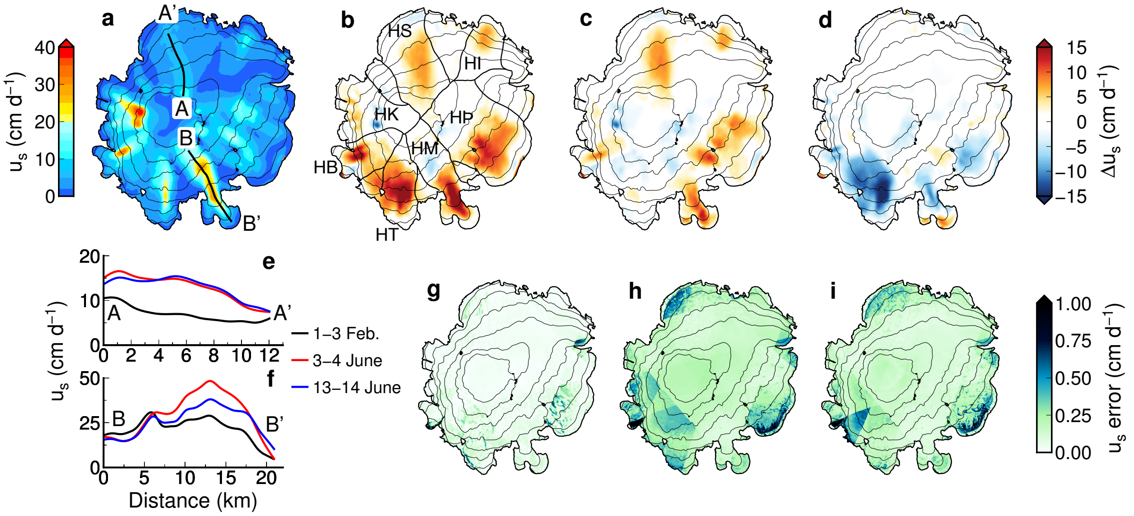

Figure 3.2: Seasonal ice flow variability. **a** Horizontal surface speeds on Hofsjökull recorded 1–3 February 2014. Black contour lines indicate ice surface elevation in 150-m increments (maximum contour at 1650 m). **b** and **c** Horizontal surface speed relative to **a** recorded 3–4 June 2012 and 13–14 June 2012, respectively. **d** Horizontal surface speed on 13–14 June 2012 relative to 3–4 June 2012. **e** and **f** Transects of horizontal surface speed along A–A' and B–B', respectively. **g–i** Formal errors in InSAR-derived estimates of the horizontal velocity fields, derived from the method in Minchew et al. (2015), for data collected **g** 1–3 February 2014, **h** 3–4 June 2012, and **i** 13–14 June 2012. Ice divides and labels in **b** are the same as in Fig. 3.1b.

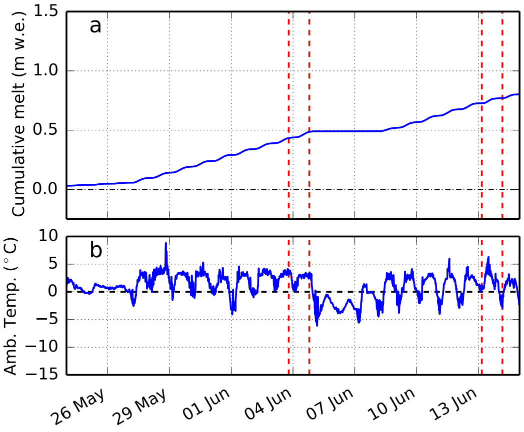

Figure 3.3: **a** Cumulative seasonal melt inferred from meteorological data collected at approximately 1100 m elevation on nearby Langjökull glacier (red triangle in Fig. 3.1). Data include incoming and outgoing solar and thermal radiation, relative humidity, and windspeed and temperature at approximately 3 m above the ice surface. **b** Ambient temperature from the same meteorological data. Red dashed lines indicate the times when UAVSAR data were collected.

2008). Using a higher-order ice-flow model to estimate viscous deformation in the ice (Blatter, 1995; Pattyn, 2003; Morlighem et al., 2013), we solved for the optimal values of C at each mesh node such that τ_b satisfies global stress balance and u_b minimizes the residual between modeled and observed surface velocities. Ice is treated as an incompressible viscous fluid whose constitutive relation is $\tau_{ij} = 2\eta\,\dot{\varepsilon}_{ij}$, where $\dot{\varepsilon}_{ij}$ and τ_{ij} are components of the strain rate and deviatoric stress tensors, respectively, $\eta = A^{-1/n}\dot{\varepsilon}_e^{(1-n)/n}/2$ is the effective dynamic viscosity, and $\dot{\varepsilon}_e$ is effective strain rate (calculated from the second invariant of the strain rate tensor). Hofsjökull is temperate and damage in the ice is predominantly restricted to areas that are not of interest in this study (Björnsson et al., 2003), so we take A and n to be spatially and temporally constant, assigning $n = 3$ and $A = 2.4 \times 10^{-24}$ Pa^{-3} s^{-1} (Cuffey and Paterson, 2010). Results given in this study were obtained using $m = 5$. Further details of the inversion and ice flow model are given in Morlighem et al. (2013).

A Weertman-type sliding law (Eq. 3.1) with small values of m may not be physically applicable to Hofsjökull because of its till-covered bed (Iverson et al., 1998; Björnsson et al., 2003; Björnsson and Pálsson, 2008). The exponent $1/m$ is a prescribed value in ISSM so it is important that we test the sensitivity of inferred basal shear traction and basal slip rate to m. We expect inferred basal shear traction to be insensitive to prescribed values of m because basal shear traction must satisfy global stress balance (Joughin et al., 2004). To confirm this postulate, we infer C using multiple values of m, such that $1 \leq m \leq 50$. The higher-order ice flow model is computationally expensive to implement so we only inferred basal conditions with the higher-order model for $m = 1$, 3, and 5. For $m = 1$, 3, 5, 10, 20, and 50 we applied the 2D shallow shelf model (e.g., MacAyeal, 1989) to infer basal conditions using ISSM and the same mesh grids. The higher-order and shallow-shelf models yield the same basal shear traction for $m = 1$, 3, and 5, so we expect results from the shallow-shelf model and large m values to represent the sensitivity of inferred τ_b to large m. For all tested m values, we retrieve basal shear traction fields that are within a few percent of one another because $C \propto u_b^{-1/m}$ for any m in all observed data (Fig. 3.4). We will exploit this behavior to interpret inferred basal shear tractions in the context of sliding laws that differ from Eq. 3.1.

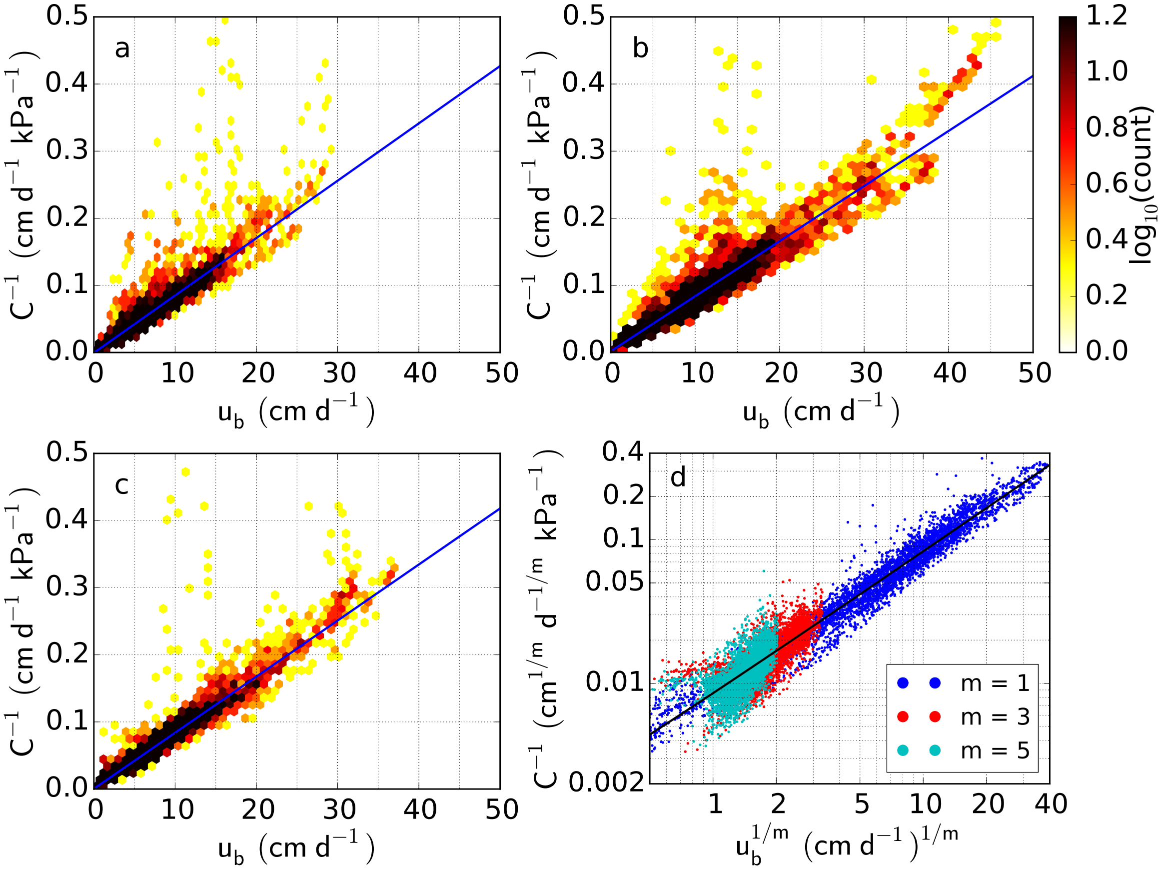

Figure 3.4: **a–c** Basal slipperiness versus basal slip rate inferred using a linear viscous sliding law ($m = 1$ in Eq. 3.1) for horizontal surface speeds recorded **a** 1–3 February 2014, **b** 3–4 June 2012, and **c** 13–14 June 2012. Blue lines are the best-fit linear trends. **d** Basal slipperiness versus basal slip rate for 13–14 June inferred with $m = 1$, 3, and 5 (Eq. 3.1). The solid black line is the best linear fit and indicates that, in general, $C \propto u_b^{-1/m}$ for any m, implying that τ_b is independent of u_b and the bed deforms plastically.

3.4 Results

3.4.1 Surface velocity observations

Comparing winter and summer surface speeds, we find that early summer acceleration is evident in most outlet glaciers (Figs. 3.2a–f). The only named glacier that does not appear to accelerate in our data is Kvíslajökull (Fig. 3.1b), which partially drains ice collected in the central caldera through a notch in the caldera rim, causing the observed surface speeds to be dominated by viscous deformation (Minchew et al., 2015). In other glaciers, typical increases in velocity are approximately double wintertime velocities, meaning that faster flowing areas tend to experience higher acceleration than slower moving areas. Highest accelerations are more evident at intermediate elevations (Figs. 3.2e–f), with ice flow in higher and lower elevations indicating lower rates of acceleration, likely due to limited surface meltwater supply and the existence of a relatively efficient basal hydrological system, respectively. These observations are consistent with an influx of surface meltwater to, and subsequent pressurization of, a distributed hydrological system along much of the length of the outlet glaciers during the early melt season.

Between 3–4 June and 13–14 June the meteorological data indicate 4 days of little-to-no melt followed by 6 days of higher melt rates (Fig. 3.3) and UAVSAR data show notable changes in the relative surface velocities of the outlet glaciers. Glaciers that previously accelerated slowed except Sátujökull (transect A–A’ in Fig. 3.2a) and Illviðrajökull, suggesting that during the 10-day interim the capacity of the hydrological system beneath the other glaciers increased through a combination of enhanced efficiency, connectivity, and the opening of cavities leeward of bumps in the bed (Fig. 3.2b–c) (e.g., Schoof, 2010; Hoffman and Price, 2014; Andrews et al., 2014). While they likely have similar bed properties to the rest of Hofsjökull (Björnsson et al., 2003), Sátujökull and Illviðrajökull have relatively small water catchment areas feeding their hydrological systems (Björnsson, 1988), which can delay evolution of the subglacial hydrological system (Schoof, 2010). Glaciers in the southwest quadrant slowed to near wintertime velocities while other outlet glaciers only partially slowed, consistent with differential evolution of the basal hydrological systems (Iken and Bindschadler, 1986; Sugiyama and Gudmundsson, 2004; Bartholomew et al., 2010). Múlajökull (transect B–B’ in Fig. 3.2a) slowed considerably, losing approximately half of its early melt season acceleration, but maintained elevated flow speeds. Þjórsárjökull generally experienced slowdown between 3–4 June and 13–14 June, though its southern-most portion accelerated slightly over the same time. There are no indications that any outlet glaciers slowed to below wintertime flow rates except in upstream areas with slightly reduced flow rates located at elevations that experienced little or no surface melt (Fig. 3.3). Given their overall minor changes and general association with relatively strong beds (see next section), we do not consider areas that experience higher wintertime ice speeds to be germane to this study.

3.4.2 Basal mechanics

Modeled surface speeds match observed surface speeds to within 10% (20%) over more than 50% (70%) of areas where observed flow speeds exceed 4 cm d^{-1} (Fig 3.5). Notable misfits include the midstream region of Múlajökull, lower extent of Blöndujökull, and high-velocity region of Kvíslajökull (all circled in green dashed lines and respectively labeled A, B, and C in Fig 3.5a). In all three cases the modeled viscous flow component of surface speed exceeds the observed surface flow speed. Three likely causes for the misfits in these areas are: (1) ice thickness overestimation, (2) excessive surface slope estimates, and (3) failure of the underlying assumptions in the higher-order ice flow model. Viscous flow in areas with low basal slip rates approximately scales as $\alpha^n h^{n+1}$, where α is the surface slope (in radians) and h is ice thickness, so small errors in ice thickness and surface slope are amplified in the viscous flow estimates. In all three glaciers in question, surface crevassing led to gaps in the bedrock topography observations which were filled by interpolation (Björnsson, 1986). Modeling errors on Kvíslajökull could be exacerbated by a large increase in local surface slope that is not properly accounted for in the surface elevation measurements, which were collected at a different time than the InSAR data. The upper extent of Kvíslajökull is coincident with a significant slope break at the lip of the underlying caldera and therefore may be especially prone to errors in surface slope. Where high horizontal normal stresses are present, the assumption of hydrostatic normal pressure at the bed breaks down and the use of the higher-order model incurs larger errors (Schoof and Hindmarsh, 2010). However, for this study, our interest is in areas with relatively high and seasonally variable basal slip rates, all of which are well fit by the modeled ice flow and have flow characteristics that support the underlying assumptions in the higher-order model (Blatter, 1995; Pattyn, 2003; Schoof and Hindmarsh, 2010). Therefore, we disregard the aforementioned and other areas containing high misfits between modeled and observed ice flow (magenta and cyan colored regions in Fig. 3.5a) and analyze basal shear traction and basal slip rates in the remaining areas.

Inferred basal shear traction and basal slip rate fields indicate that the bed beneath Hofsjökull

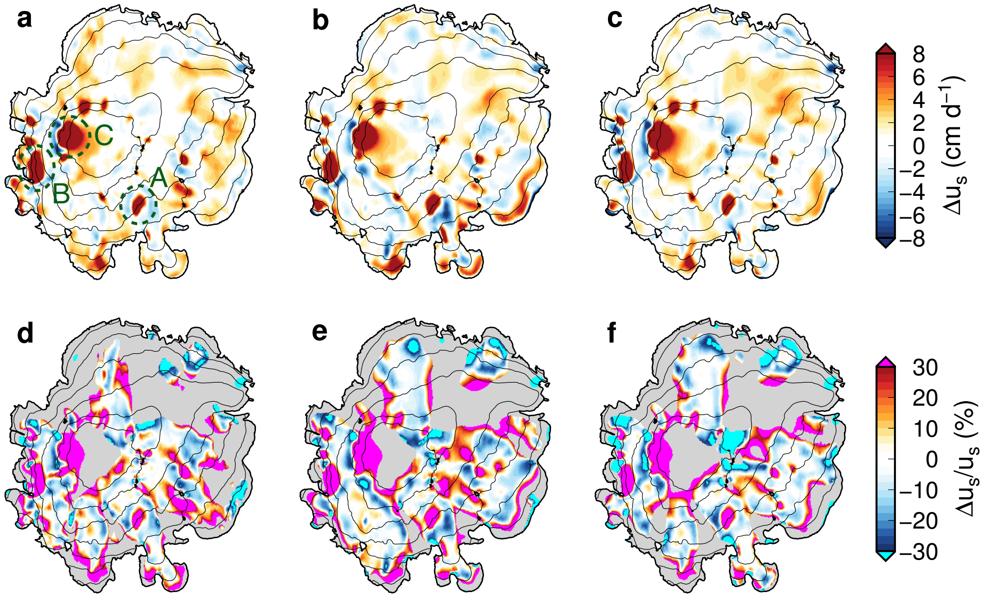

Figure 3.5: **a–c** Residual surface velocities between modeled and observed surface speeds ($\Delta u_s = u_s^{mod} - u_s^{obs}$) for **a** 1–3 February 2014, **b** 3–4 June 2012, and **c** 13–14 June 2012. **d–f** Same as **a–c** but normalized by observed surface speeds. Gray regions indicate areas where observed surface speeds are less than 4 cm d^{-1}.

deforms plastically. Inferred basal shear tractions typically are between 100 kPa and 150 kPa in areas where basal slip rate is nonzero (Figs. 3.6a–h and 3.7a–f) and are within a factor of two of the gravitational driving stress, $\tau_d = \rho g h \alpha$, where ρ is the mean density of ice, g is gravitational acceleration, and α is taken to be small such that $\sin(\alpha) \approx \alpha$ (Fig. 3.7g–i). Basal shear tractions generally increase linearly with basal slip rate for slow basal slip ($u_b \lesssim 5$ cm d^{-1}) and are independent of basal slip rate and observed surface speed in areas of faster slip, behavior that is consistent with a plastically deforming bed. This conclusion is supported by laboratory tests of plastically deforming subglacial till (Kamb, 1991; Tulaczyk et al., 2000a). The existence of plastically deforming till beneath Hofsjökull is bolstered by direct observations of the bed of nearby Breiðamerkurjökull (blue triangle in Fig. 3.1a) (Boulton, 1979), the known bed composition of Hofsjökull (Björnsson et al., 2003; Björnsson and Pálsson, 2008), and the presence of an active drumlin field at the Mulajökull (transect B–B' in Fig. 3.2a) terminus (Johnson et al., 2010). The existence of an active drumlin field is particularly salient given that drumlins are thought to be primarily depositional, rather than erosional, features that arise due to the behavior of plastically deforming till (Fowler, 2000, 2001; Schoof, 2007b). This suite of observations diminishes the applicability of rigid-bed sliding laws to our study site (e.g. Lliboutry, 1968; Fowler, 1987; Schoof, 2005) and supports limiting our focus to models that account for deformation within a finite till layer. Though the thickness of the till remains unknown, as do the mechanisms for maintaining a till layer (Iverson, 2010), we note that till layers only need to be centimeters thick to facilitate plastic deformation. The mechanical properties of till layers depend on pore water pressure (Tulaczyk et al., 2000a), represented herein by mean basal water pressure.

Given a plastic bed, it is straightforward to estimate mean basal water pressure using inferred basal shear tractions. We assume that basal slip is facilitated solely by plastic bed deformation (Tulaczyk et al., 2000b), thereby ignoring any linear relationship between basal shear traction and basal slip rate at low basal slip rates (Fig. 3.7a–c). We define the bed yield stress using the Mohr-Coulomb criteria (Iverson et al., 1998; Kamb, 1991; Tulaczyk et al., 2000a):

$$\tau_y = (\rho g h - p_w) f_c \tag{3.2}$$

where p_w is the mean basal water pressure, f_c is the internal friction parameter for till, and we have assumed negligible till cohesion (Iverson, 2010). For a plastic bed, $\tau_b = \tau_y$ wherever basal slip occurs ($u_b > 0$) and $\tau_b < \tau_y$ where there is no basal slip ($u_b = 0$). By setting $\tau_b = \tau_y$ and taking the unknown f_c to be the median of published values ($f_c = 0.4$; Iverson, 2010), we can solve for estimates of water pressure (Fig. 3.6i–p). In areas with little or no basal slip (Fig. 3.6a), the estimated water pressure is the upper bound (indicated by subdued colors in Figs. 3.6i and 3.6m).

The accuracy of estimated water pressure is relatively insensitive to the chosen value of f_c. The error in estimated water pressure arising from incorrect values of f_c is given as:

$$\begin{aligned} \delta p_w &= \frac{\partial p_w}{\partial f_c}\delta f_c \\ &= \frac{\tau_y}{f_c^2}\delta f_c \end{aligned} \tag{3.3}$$

Taking $f_c = 0.4$ and $\delta f_c = 0.2$ (Iverson, 2010), Eq. 3.3 gives $\delta p_w = 1.25\tau_y$. Given that p_w is generally more than an order of magnitude larger than τ_y (*cf.* Fig. 3.6e and 3.6i), δp_w is less than 10 percent of typical inferred p_w values in the areas of interest. This relatively small uncertainty provides some confidence in absolute estimates of basal water pressure. We note that because seasonal variations in inferred τ_b are relatively small, errors in f_c have negligible influence on estimated seasonal changes in p_w (Figs. 3.6j–l and 3.6n–p).

We infer higher basal water pressure in areas where observed glacier flow is faster during the

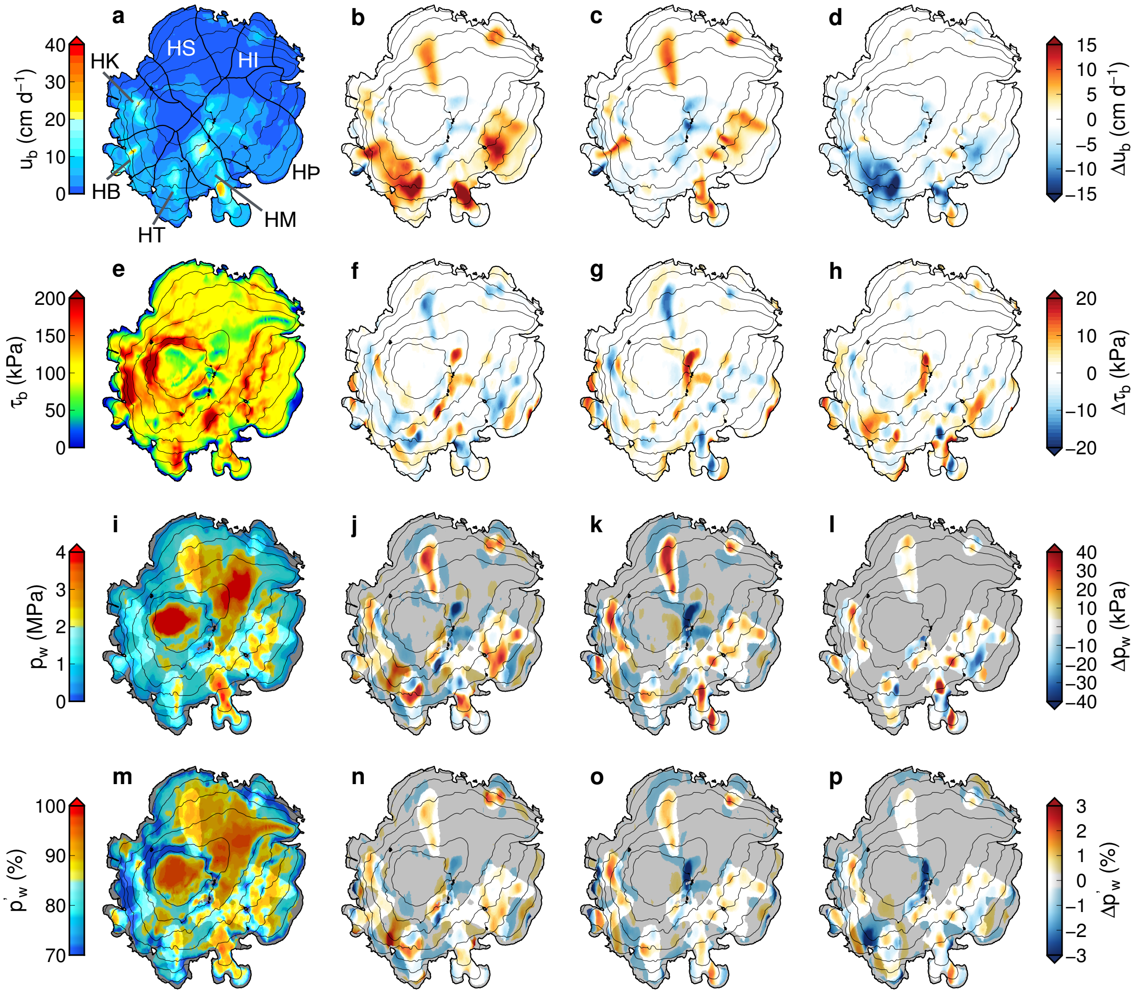

Figure 3.6: Inferred **a–d** basal slip rates, **e–h** basal shear tractions, **i–l** basal water pressures, and **m–p** normalized basal water pressure $p'_w = p_w/(\rho g h)$ for $\rho = 900$ kg m^{-3}. The left column contains properties inferred from data collected 1–3 February 2014 while the two center columns contain inferred properties for 3–4 June 2012 and 13–14 June 2012, respectively, relative to the left column. The right column shows 13–14 June 2012 relative to 3–4 June 2012. Bright areas in **i–p** indicate regions where $\tau_b = \tau_y$, allowing for direct estimates of basal water pressure, while water pressures in subdued regions (*i.e.* areas of lower color intensity that tend to appear grey) are an upper bound on the absolute estimates in **i** and **m** or at least one estimate in the differences in **j–l** and **n–p**. Ice divides and labels in **a** are the same as in Fig. 3.1b.

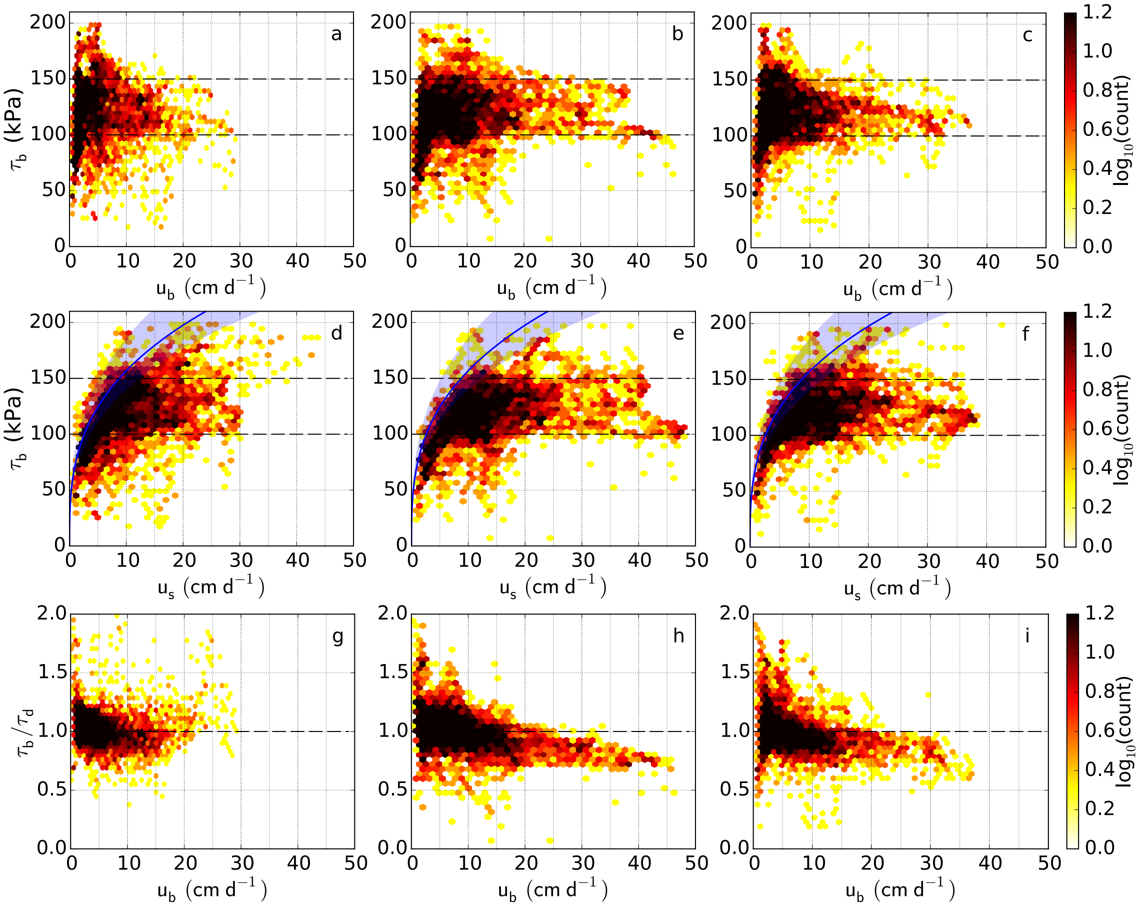

Figure 3.7: Mechanical properties of the bed. **a–c** Inferred basal shear traction versus inferred basal slip rate. **d–f** Inferred basal shear traction versus observed horizontal surface speed. Blue lines (and shaded regions) represent the viscous deformation rate for 250 m (±100 m) thick ice approximated as $u_v = 2A\tau_b^n h/(n+1)$. The range of ice thicknesses corresponds to the mean and standard deviation in rapid-flowing areas. **g–i** Ratio of inferred basal shear traction to gravitational driving stress versus inferred basal slip rate. In all figures dot colors represent number of data points within each hexagonal bin. Columns contain properties inferred from data collected 1–3 February 2014 (**a**, **d**, and **g**) 3–4 June 2012 (**b**, **e**, and **h**), and 13–14 June 2012 (**c**, **f**, and **i**).

early melt season (Fig. 3.6i–p). The relationship between temporal changes in surface speed and the corresponding inferred changes in basal water pressure is nonlocal (Figs. 3.2a–d and 3.6) because perturbations in basal shear traction can affect ice flow over larger spatial scales (Raymond, 1996). On Sátujökull and Illviðrajökull, we note that elevated basal water pressure is present under much of the outlet glaciers whereas basal water pressure variations are less spatially extensive beneath other outlet glaciers. Sustained elevated water pressure beneath Sátujökull and Illviðrajökull supports our previous postulate that the respective basal hydrological systems did not channelize during the timespan of our data collection. Overall, estimates of basal water pressure show that water pressure and flow speed are nonlinearly related, with small changes in water pressure ($\lesssim 2$ %) producing more substantial ($\gtrsim 100$ %) changes in surface speed (Figs. 3.6i–p and 3.2a–d, respectively). This nonlinearity, which has been previously noted on an Alaskan glacier (Jay-Allemand et al., 2011), combined with the plasticity of the bed motivates an idealized physical model for the influence of basal hydrology on ice flow.

3.5 Discussion

When the bed is perfectly plastic, the Weertman-type sliding law (Eq. 3.1), which is predicated on the assumption of a rough, rigid bed (Weertman, 1957; Nye, 1970; Kamb, 1970), does not provide insight into the coupling between basal shear traction and ice flow because the exponent $1/m \approx 0$ (Iverson et al., 1998). In deriving an alternative basal slip model, we consider an idealized case in which basal slip along a smooth, horizontal bed arises solely from an imbalance between basal shear traction and gravitational driving stress (Fig. 3.7g–i). In areas where basal slip is a significant fraction of the total surface velocity, slip along or within the glacier margins is negligible, and speed varies gradually along flowlines, we can consider ice flow to be controlled primarily by basal shear traction and lateral shearing in the glacier side walls. Sidewall shearing tends to concentrate near glacier margins, because ice is a non-Newtonian viscous fluid, so we further simplify the model by considering only the central trunk of a symmetric glacier, of width $2w$, where lateral shearing is locally negligible (e.g., Joughin et al., 2004). Under these assumptions, the normalized basal slip rate $u_b' = u_b/u_{b_{max}} = [1 - \tau_b/\tau_d]^n$, where n is the stress exponent in the constitutive relation for ice and the maximum basal slip rate, $u_{b_{max}} = 2A\tau_d^n(w/h)^n w/(n+1)$, corresponds to $\tau_b = 0$ (Raymond, 1996). Maximum basal slip rate is a function of glacier geometry and ice viscosity, parameters that vary over annual or longer timescales, meaning that u_b' captures all of the sub-annual-timescale variability in the idealized model. The dependence of basal slip rate on the stress ratio τ_b/τ_d is consistent with the inferred basal properties discussed above where the stress ratio decreases with increasing basal slip rate, reaching a minimum in the early melt season of $\tau_b/\tau_d \approx 0.75$ (Fig. 3.7g–i). After applying the Mohr-Coulomb criteria (Eq. 3.2) by imposing $\tau_b = \tau_y$, we can write a single equation for normalized basal slip rate as a function of normalized basal water pressure, $p'_w = p_w/(\rho g h)$, (Fig. 3.8a):

$$u'_b = [H(\Theta)\Theta]^n \ ; \qquad \Theta = 1 - \mu(1 - p'_w) \tag{3.4}$$

where $\mu = f_c/\alpha$ is the stress factor that represents the ratio of dry ($p_w = 0$) basal shear traction to gravitational driving stress. Over the timescales of interest, it is reasonable to think of μ as the static stress component and $(1 - p'_w)$ as the dynamic component. That basal slip arises from unbalanced basal shear traction and driving stress requires the basal slip parameter, Θ, to be positive for basal slip to occur. Because basal shear traction can be less than the bed yield stress, we apply $H(\Theta)$, the Heavyside step function ($H(\Theta) = 1$ for $\Theta > 0$ and $H(\Theta) = 0$ otherwise), in Eq. 3.4 to ensure u'_b is everywhere nonnegative and real for any n. This condition provides some insight as to when certain glaciers accelerate in response to variations in basal water pressure. Setting $\Theta = 0$ (*i.e.* $\tau_d = \tau_y$) yields the critical water pressure:

$$p^*_w = \rho g h(1 - \mu^{-1}) \tag{3.5}$$

above which basal slip is nonzero. Only basal water pressure variations above the critical water pressure will lead to glacier flow variability.

Basal water pressure is equal to critical water pressure whenever gravitational driving stress is equal to the yield stress of the bed. During winter on Hofsjökull, inferred basal shear traction and driving stress are roughly balanced in areas with high basal slip rates (Fig. 3.7g). Consequently, inferred wintertime basal water pressure (Fig. 3.6i) and critical water pressure (Eq. 3.5) should be approximately equal as well. Indeed we find good agreement between p^*_w and wintertime p_w in areas with basal slip rates above 4 cm d^{-1} (Fig. 3.8b). This agreement suggests that estimates of annually averaged, effective water pressures for broad spatial areas (several ice thicknesses) can be gleaned from surface slope and thickness measurements on glaciers that are at or near steady state.

For sub-annual water pressure variations, our basal slip model (Eq. 3.4) shows that the sensitiv-

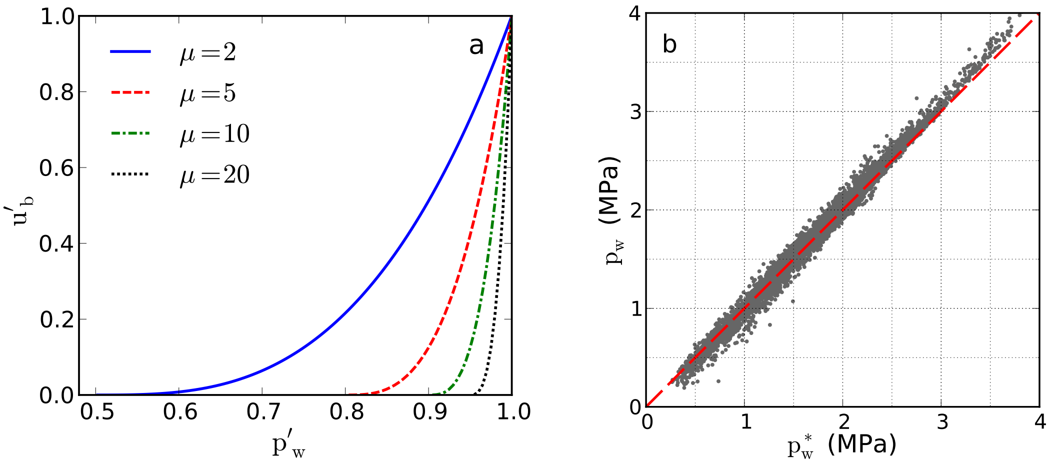

Figure 3.8: **a** Modeled normalized slip rate as a function of normalized basal water pressure (Eq. 3.4) for different values of μ. **b** Inferred wintertime basal water pressure from Fig. 3.6i versus critical water pressure in areas where $u_b \geq 4$ cm d^{-1}.

ity of basal slip rate to changes in mean basal water pressure is given as:

$$\psi = \frac{\partial u'_b}{\partial p'_w} = \mu n \left[H(\Theta)\Theta\right]^{n-1} \tag{3.6}$$

and scales as the inverse of the ice surface slope. Published values give $0.3 \leq f_c \leq 0.5$, with f_c being approximately constant in time (Iverson, 2010), while observed surface slopes vary by up to two orders of magnitude, with minimum values $\sim 10^{-3}$, and may change on multi-annual timescales. Therefore, ice surface slope is the dominant factor in μ at seasonal and shorter timescales. Consequently, for a given f_c, glaciers with gentler surface slopes require higher mean basal water pressures to initiate slip, but once slip has commenced these glaciers are highly sensitive to subsequent changes in water pressure. This behavior is due to the dependence of basal slip rate on the ratio τ_b/τ_d: for a given ice thickness, glaciers with gentle surface slopes have relatively low gravitational driving stress, τ_d, requiring basal water pressure to approach ice overburden pressure (*i.e.* for the glacier to approach floatation) for basal slip to commence. Once basal slip is underway, basal slip rates become increasingly sensitive to changes in water pressure as basal slip rates increase (Fig. 3.8a) because shearing in the glacier sidewalls is a fundamental control on ice flow in our model. A consequence of nonlinearity in ψ is that for a given change in the absolute value of mean basal water pressure ($|\delta p_w|$) the amplitude of increases in basal slip rate ($|\delta u_b(\delta p_w > 0)|$) will exceed the amplitude of decreases in basal slip rate (*i.e.* $|\delta u_b(\delta p_w < 0)| < |\delta u_b(\delta p_w > 0)|$). Furthermore, that

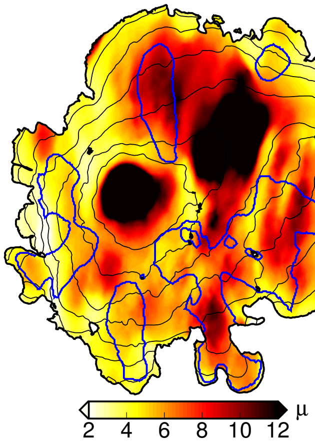

Figure 3.9: Stress factor μ for Hofsjökull calculated assuming $f_c = 0.4$ and with surface slopes averaged over approximately 10 ice thicknesses. Blue contour lines delineate the bright regions in Figs. 3.6i–p, indicating that basal slip occurs in these areas.

ψ scales as the inverse of ice surface slope helps explain some of the variable response to meltwater flux on Hofsjökull, where typical surface slopes are less than 0.2, with a median of 0.06, making $2 \leq \mu \leq 12$ for $f_c = 0.4$ (Fig. 3.9).

The sensitivity of basal slip rate to changes in basal water pressure can be understood in a Mohr's circle framework (Fig. 3.10), which considers the relationship between shear stress and effective normal stress (Malvern, 1969). In the idealized model, effective normal stress is equal to effective pressure N, where $N = p_i - p_w$ and $p_i = \rho g h$. For basal slip, we consider the gravitational driving stress and the basal shear tractions, which form the radii of the concentric half-circles labeled D, for driving stress (green), and B, for basal shear traction (red). We delineate the Mohr-Coulomb criteria (Eq. 3.2) using the line labeled "yield criteria" which slopes at an angle $\phi = \tan^{-1}(f_c)$. The value of τ_d dictates the maximum size of the half-circles because the Mohr-Coulomb criteria, along with the existence of nonzero stresses within the ice, requires B to be smaller than D at all times. Over the timescales of interest, τ_d is constant and τ_b is bounded by the bed yield stress. Thus half-circle D can enter the gray-shaded region but half-circle B cannot and B intersects the yield line at $p_w = p_w^*$.

The disparity between driving stress and basal shear traction in their response to yielding informs the sensitivity of basal slip rate to changes in basal water pressure. When $\tau_b < \tau_y$, both circles have approximately the same radius. Decreasing α reduces τ_d, shrinking half-circle D. If we hold f_c constant, then glaciers with smaller α will have greater freedom to traverse along the

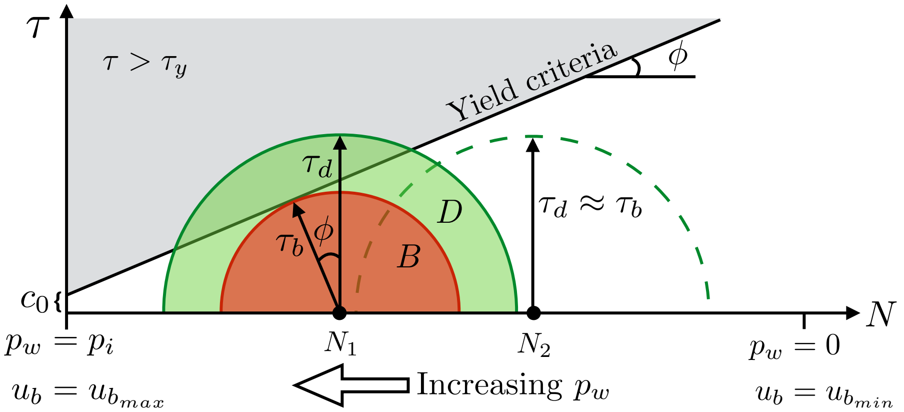

Figure 3.10: Mohr's circle representation of basal shear traction and driving stress, where $\phi = \tan^{-1}(f_c)$ is the internal friction angle, $N = p_i - p_w$ is the effective pressure at the bed, assumed equal to the effective normal stress; $p_i = \rho g h$, the ice overburden pressure; and c_0 is the till cohesion, assumed negligible in Eq. 3.2.

x-axis (effective normal stress) without their stress circles intersecting the yield line, meaning that p_w^* is large, as expected from Eq. 3.5. Once the bed beneath a shallow-sloping glacier begins to yield, there is less space between N at yielding and the origin where $u_b = u_{b_{max}}$, meaning that ψ must be large. Conversely, increasing α enlarges half-circle D causing the Mohr circles to intersect the yielding criteria at higher values of N (lower p_w^*) than for shallower-sloping glaciers, requiring relatively large subsequent increases in p_w to achieve $u_b = u_{b_{max}}$ (*i.e.* ψ is small). We can achieve the same effect by increasing (decreasing) f_c instead of decreasing (increasing) α. Thus the sensitivity of basal slip rate to changes in basal water pressure scales as μ.

Together, spatial variability in μ (Fig. 3.9) and inferred basal water pressure (Fig. 3.6i–p) more closely represent patterns in seasonal velocity (Fig. 3.2a–c) than either individually. Outlet glaciers on Hofsjökull that show the greatest decrease in speed during the early melt season have the lowest μ values due to steep ice surface slopes. Outlet glaciers that experience nearly complete cessation of the observed acceleration within 10 days have $\mu < 5$ (Fig. 3.9) and show sharp reductions in basal water pressure (Figs. 3.6j–k and 3.6n–o). Conversely, outlet glaciers that maintained elevated ice flow between early and mid-June 2012 have relatively high μ values due to gradual surface slopes, except for Illviðrajökull, whose basal hydrological system likely did not become channelized. Glaciers in the southeast quadrant, which have relatively high μ values, sustain increased speeds during the period of observation despite modestly elevated basal water pressures.

These observations indicate that the stress factor, μ, is a useful parameter in establishing a glacier's dynamic response to basal water flux. Glaciers accelerate in response to rapid changes in melting or precipitation so long as basal water pressure exceeds the critical water pressure (Eq. 3.5), a function of ice overburden pressure and μ. Initial melt-season accelerations may be ephemeral owing to evolving hydrological systems but diurnal melt cycles and periodic rain events can continue to episodically overwhelm and pressurize the system throughout the melt season. Ice flow responds readily to these continual, short-term water pressure fluctuations (Shepherd et al., 2009; Schoof, 2010) and this response will be amplified on glaciers with gentle surface slopes. Longer melt seasons, increasing diurnal temperature variations, and more frequent rain events (e.g., Schuenemann and Cassano, 2010) brought on by a warming climate will potentially bolster total melt-season mass flux in gently sloping glaciers while glaciers with steep surface slopes will be less susceptible to these prolonged cyclical basal water pressure variations. Given the prevalence of till-covered glacier beds, these findings should help reconcile observations of the influence of basal hydrology and surface meltwater flux on glacier flow (Zwally et al., 2002; Joughin et al., 2008; Shepherd et al., 2009; Bartholomew et al., 2010; Moon et al., 2014; Tedstone et al., 2013, 2015). In particular, it may be useful to classify glaciers by μ to facilitate mechanistically consistent comparisons of the response of different glaciers to surface meltwater flux and enhance our understanding of basal processes.

Our model has some limitations in its immediate applicability to understanding the response of soft-bedded glaciers to surface meltwater flux. The primary limitation is that not all glaciers closely adhere to the idealized assumptions employed in the model derivation. More robust testing with numerical models and further observations on other glacier systems are needed to support the model and lend credence to μ as a viable mechanistic parameter. Another limitation is the need to decouple the dependence of ψ and the evolution of the basal hydrological system on the ice surface slope in observations (e.g., Schoof, 2010). These mechanical and hydrological dependencies work together, with gentler surface slopes potentially resisting channelization of the hydrological system by increasing the critical meltwater flux needed to facilitate the switch from an inefficient distributed system to an efficient channelized system. This resistance to channelization increases the likelihood that an inefficient distributed hydrological system will persist later in the melt season on shallower sloping glaciers, resulting in higher basal water pressure variability (Schoof, 2010) in a system with higher dynamical sensitivity to such variability (Eq. 3.6). Because it may not be possible to know the state of the basal hydrological system during the early melt season, collecting observations aimed at understanding ψ is challenging. In this work, we avoid the complexities of evolving basal hydrological systems by estimating the effective basal water pressure directly from observations of surface velocity and the inferred basal shear traction fields. Our approach isolates the mechanical basal properties from the hydrological properties, providing insight into the mechanics of deformable glacier beds.

Improved understanding of basal mechanics is a key component of the physical foundation on which we can build predictive models to explore a range of plausible future glacier states in a warming climate. One outstanding problem currently prohibiting reliable predictive models is an incomplete understanding of how changes in water flux at the bed of glaciers, arising from surface meltwater flux, transmission of tidal loads (e.g., Thompson et al., 2014), or subglacial lake drainage (e.g., Magnússon et al., 2007, 2010; Fricker and Scambos, 2009), influences multi-annual-timescale ice flow. Solving this problem requires defining the sensitivity of basal slip rate to changes in q_w, the water flux through the basal hydrological system, given as:

$$\frac{\partial u_b}{\partial q_w} = \frac{\partial u_b}{\partial p_w}\frac{\partial p_w}{\partial q_w} \tag{3.7}$$

The second term on the righthand side of Eq. 3.7 ($\partial p_w/\partial q_w$) is a function of the time-varying state of the basal hydrological system and is the subject of numerous studies (e.g., Lliboutry, 1968; Röthlisberger, 1972; Nye, 1976; Kamb, 1987; Schoof, 2010). With this study, we define the first term on the righthand side of Eq. 3.7—simply the dimensional form of Eq. 3.6 in which both sides are multiplied by $u_{b_{max}}/(\rho g h)$—in an idealized framework for glaciers with deformable beds.

3.6 Conclusion

We use InSAR-derived measurements of ice surface velocity combined with a numerical ice-flow model to study the response of several outlet glaciers on Hofsjökull ice cap to surface melt during the early melt season. Observations indicate that the outlet glaciers respond differently to similar environmental forcing with some glaciers maintaining fast ice flow relative to winter while other glaciers appear to accelerate then slow to wintertime speeds over the same time period. This spatial heterogeneity in the response of ice flow to surface melt is at least partially explained by differential evolution of the basal hydrological systems of the outlet glaciers, which influences how surface meltwater flux can alter basal shear traction and consequently ice flow. We infer basal shear tractions using the observed velocities and note that the bed beneath Hofsjökull deforms plastically, allowing for a straightforward means of estimating absolute and seasonally variable basal water pressures.

The resulting water pressure estimates indicate that changes in basal water pressure and surface velocity are non-local and nonlinearly related. These findings motivate an idealized model of basal slip rate wherein the response of glaciers with plastically deforming beds is largely determined by the relationship between the intrinsic mechanical properties of the deforming bed and glacier geometry. This relationship is quantified by the stress factor, μ, defined as the ratio of the internal friction parameter for the bed to the ice surface slope.

In plastic-bedded glaciers, μ helps determine the critical basal water pressure, p_w^*, at which basal slip commences and the sensitivity of basal slip rate to changes in basal water pressure. Given the ranges of plausible values for internal friction in till and ice surface slopes, both the critical water pressure and sensitivity of basal slip rate to changes in basal water pressure are driven primarily by the ice surface slope. Glaciers with shallower ice surface slopes require higher basal water pressure (relative to overburden pressure) for incipient basal slip, but basal slip rate is then more sensitive to basal water pressure variations than in steeper sloping glaciers. Our observations support this conclusion by showing that outlet glaciers that maintained elevated ice flow between early and mid-June, despite evidence that the respective hydrological systems evolved toward being channelized, have relatively high μ values, arising from gentle surface slopes. Conversely, outlet glaciers that experienced the greatest slowdowns over the same time period have relatively low μ values, or steep surface slopes.

3.7 Acknowledgements

The authors benefited from discussions with R. Arthern, H. Gudmundsson, I. Hewitt, J.-P. Ampuero, T. Johannesson, and T. van Boeckel. Thanks to Y. Lou, B. Hawkins, Y. Zheng, and the UAVSAR crew for assistance with InSAR data collection and processing. T. Johannesson, on behalf of the Icelandic Meteorological Office, provided the Hofsjökull digital elevation model. This research was conducted at the California Institute of Technology and the University of Iceland with funding provided by the NASA Crysopherice Sciences Program (Award NNX14AH80G). B. M. was partially funded by a NASA Earth and Space Sciences Fellowship and an Achievement Rewards for College Students (ARCS) fellowship. InSAR data are freely available from the Alaska Satellite Facility via the UAVSAR website (http://uavsar.jpl.nasa.gov).

Bibliography

L. C. Andrews, G. A. Catania, M. J. Hoffman, J. D. Gulley, M. P. Lüthi, C. Ryser, R. L. Hawley, and T. A. Neumann. Direct observations of evolving subglacial drainage beneath the Greenland Ice Sheet. *Nature*, 514:80–83, 2014. doi: 10.1038/nature13796.

I. Bartholomew, P. Nienow, D. Mair, A. Hubbard, M. A. King, and A. Sole. Seasonal evolution of subglacial drainage and acceleration in a Greenland outlet glacier. *Nature Geoscience*, 3(6): 408–411, 2010. doi: 10.1038/ngeo863.

H. Björnsson. Surface and bedrock topography of ice caps in Iceland mapped by radio echo soundings. *Annals of Glaciology*, 8:11–18, 1986.

H. Björnsson. *Hydrology of Ice Caps in Volcanic Regions*. Societas Scientarium Islandica, University of Iceland, Reykjavik, Iceland, 1988.

H. Björnsson and F. Pálsson. Icelandic glaciers. *Jökull*, 58:365–386, 2008.

H. Björnsson, F. Pálsson, O. Sigurðsson, and G. Flowers. Surges of glaciers in Iceland. *Annals of Glaciology*, 36:82–90, 2003. doi: 10.3189/172756403781816365.

H. Blatter. Velocity and stress-fields in grounded glaciers: A simple algorithm for including deviatoric stress gradients. *Journal of Glaciology*, 41(138):333–344, 1995.

M. Bougamont, P. Christoffersen, A. L Hubbard, A. A. Fitzpatrick, S. H. Doyle, and S. P. Carter. Sensitive response of the Greenland Ice Sheet to surface melt drainage over a soft bed. *Nature Communications*, 5(5052):1–9, 2014. doi: 10.1038/ncomms6052.

G. S. Boulton. Processes of glacier erosion on different substrata. *Journal of Glaciology*, 23(89): 15–37, 1979.

K. M. Cuffey and W. S. B. Paterson. *The Physics of Glaciers*. Elsevier, 4th edition, 2010.

L. Favier, G. Durand, S. L. Cornford, G. H. Gudmundsson, O. Gagliardini, F. Gillet-Chaulet, T. Zwinger, A. J. Payne, and A. M. Le Brocq. Retreat of Pine Island Glacier controlled by marine ice-sheet instability. *Nature Climate Change*, 4:117–121, 2014. doi: 10.1038/nclimate2094.

A. C. Fowler. Sliding with cavity formation. *Journal of Glaciology*, 33:255–267, 1987.

A. C. Fowler. An instability mechanism for drumlin formation. *Geological Society, London, Special Publications*, 176(1):307–319, 2000. doi: 10.1144/GSL.SP.2000.176.01.23.

A.C. Fowler. Dunes and drumlins. In N.J. Balmforth and A. Provenzale, editors, *Geomorphological Fluid Mechanics*, volume 582 of *Lecture Notes in Physics*, pages 430–454. Springer Berlin Heidelberg, 2001. doi: 10.1007/3-540-45670-8_18. URL `http://dx.doi.org/10.1007/3-540-45670-8_18`.

H. A. Fricker and T. Scambos. Connected subglacial lake activity on lower mercer and whillans ice streams, west antarctica, 2003–2008. *Journal of Glaciology*, 55(190):303–315, 2009. doi: doi:10.3189/002214309788608813.

G. H. Gudmundsson and M. Raymond. On the limit to resolution and information on basal properties obtainable from surface data on ice streams. *The Cryosphere*, 2(2):167–178, 2008. doi: 10.5194/tc-2-167-2008.

S. Hensley, H. Zebker, C. Jones, T. Michel, R. Muellerschoen, and B. Chapman. First demonstration results using the NASA/JPL UAVSAR instrument. In *2nd Annual Asia Pacific SAR Conference*, Xian, China, 2009. doi: 10.1109/APSAR.2009.5374246.

I. J. Hewitt. Seasonal changes in ice sheet motion due to melt water lubrication. *Earth and Planetary Science Letters*, 371–372:16–25, 2013. doi: 10.1016/j.epsl.2013.04.022.

M. Hoffman and S. Price. Feedbacks between coupled subglacial hydrology and glacier dynamics. *J. Geophys. Res.*, 119:414–436, 2014. doi: 10.1002/2013JF002943.

A. Iken and R. Bindschadler. Combined measurements of subglacial water pressure and surface velocity of Findelengletscher, Switzerland: conclusions about drainage systems and sliding mechanisms. *Journal of Glaciology*, 32(110):101–119, 1986.

N. R. Iverson. Shear resistance and continuity of subglacial till: hydrology rules. *Jounal of Glaciology*, 56(200):1104–1114, 2010. doi: 10.3189/002214311796406220.

N. R. Iverson, T. S. Hooyer, and R. W. Baker. Ring-shear studies of till deformation: Coulomb plastic behavior and distributed strain in glacier beds. *Jounal of Glaciology*, 44:634–642, 1998.

M. Jay-Allemand, F. Gillet-Chaulet, O. Gagliardini, and M. Nodet. Investigating changes in basal conditions of variegated glacier prior to and during its 1982–1983 surge. *The Cryosphere*, 5(3): 659–672, 2011. doi: 10.5194/tc-5-659-2011.

T. Jóhannesson, H. Björnsson, E. Magnússon, S. Guðmundsson, F. Pálsson, O. Sigurðsson, T. Thorsteinsson, and E. Berthier. Ice-volume changes, bias estimation of mass-balance measurements and changes in subglacial lakes derived by lidar mapping of the surface of icelandic glaciers. *Annals of Glaciology*, 54(63):63–74, 2013. doi: doi:10.3189/2013AoG63A422.

M. D. Johnson, A. Schomacker, Í. Ö. Benediktsson, A. J. Geiger, A. Ferguson, and Ó. Ingólfsson. Active drumlin field revealed at the margin of Múlajökull, Iceland: A surge-type glacier. *Geology*, 38(10):943–946, 2010. doi: 10.1130/G31371.1.

I. Joughin, D. MacAyeal, and S. Tulaczyk. Basal shear stress of the Ross ice stream from control method inversions. *Journal of Geophysical Research*, 109(B09405):1–20, 2004. doi: 10.1029/2003JB002960.

I. Joughin, S. B. Das, M. A. King, B. E. Smith, I. M. Howat, and T. Moon. Seasonal speedup along the western flank of the Greenland Ice Sheet. *Science*, 320(5877):781–783, 2008. doi: 10.1126/science.1153288.

I. Joughin, B. E. Smith, and B. Medley. Marine ice sheet collapse potentially under way for the Thwaites Glacier Basin, West Antarctica. *Science*, 344(6185):735–738, 2014. doi: 10.1126/science.1249055.

B. Kamb. Sliding motion of glaciers: theory and observations. *Reviews of Geophysics*, 8(4):673–728, 1970.

B. Kamb. Glacier surge mechanisms based on linked cavity configuration of the basal water conduit system. *Journal of Geophysical Research*, 92(B9):9083–9100, 1987.

B. Kamb. Rheological nonlinearity and flow instability in the deforming-bed mechanism of ice stream motion. *Journal of Geophysical Research: Solid Earth*, 96(B10):16585–16595, 1991. doi: 10.1029/91JB00946.

L. Lliboutry. General theory of subglacial cavitation and sliding of temperate glaciers. *Journal of Glaciology*, 7(49):21–58, 1968.

D. MacAyeal. Large-scale ice flow over a viscous basal sediment - Theory and application to ice stream-B, Antarctica. *Journal of Geophysical Research*, 94(B4):4071–4087, 1989.

E. Magnússon, H. Rott, H. Björnsson, and F. Pálsson. The impacts of jökulhlaups on basal sliding observed by SAR interferometry on Vatnajökull, Iceland. *Journal of Glaciology*, 53(181):232–240, 2007. doi: 10.3189/172756507782202810.

E. Magnússon, H. Björnsson, H. Rott, and F. Pálsson. Reduced glacier sliding caused by persistent drainage from a subglacial lake. *The Cryosphere*, 4, 2010. doi: 10.5194/tc-4-13-2010.

L. E. Malvern. *Introduction to the Mechanics of a Continuous Medium*. Prentice-Hall, Englewood Cliffs, NJ, 1969.

B. M. Minchew, M. Simons, S. Hensley, H. Björnsson, and F. Pálsson. Early melt-season velocity fields of Langjökull and Hofsjökull ice caps, central Iceland. *Journal of Glaciology*, 61(226): 253–266, 2015. doi: 10.3189/2015JoG14J023.

T. Moon, I. Joughin, B. Smith, M. R. van den Broeke, Willem J. van de Berg, B. Noël, and M. Usher. Distinct patterns of seasonal Greenland glacier velocity. *Geophysical Research Letters*, 41(20): 7209–7216, 2014. doi: 10.1002/2014GL061836.

M. Morlighem, E. Rignot, H. Seroussi, E. Larour, H. Ben Dhia, and D. Aubry. Spatial patterns of basal drag inferred using control methods from a full-Stokes and simpler models for Pine Island Glacier, West Antarctica. *Geophysical Research Letters*, 37(14):1–6, 2010. doi: 10.1029/2010GL043853. L14502.

M. Morlighem, H. Seroussi, E. Larour, and E. Rignot. Inversion of basal friction in Antarctica using exact and incomplete adjoints of a higher-order model. *Journal of Geophysical Research: Earth Surface*, 118(3):1746–1753, 2013. doi: 10.1002/jgrf.20125.

J. F. Nye. Glacier sliding without cavitation in a linear viscous approximation. *Proceeding of the Royal Society of London. Series A, Mathematical and Physical Sciences*, 315(1522):381–403, 1970.

J. F. Nye. Water flow in glaciers: jökulhlaups, tunnels and veins. *Journal of Glaciology*, 17:181–207, 1976.

B. R. Parizek and R. B. Alley. Implications of increased greenland surface melt under global-warming scenarios: ice-sheet simulations. *Quaternary Science Reviews*, 23(9–10):1013 – 1027, 2004. doi: 10.1016/j.quascirev.2003.12.024.

F. Pattyn. A new three-dimensional higher-order thermomechanical ice sheet model: Basic sensitivity, ice stream development, and ice flow across subglacial lakes. *Journal of Geophysical Research: Solid Earth*, 108(B8):1–15, 2003. doi: 10.1029/2002JB002329.

S. Pimentel and G. E. Flowers. A numerical study of hydrologically driven glacier dynamics and subglacial flooding. *Proceedings of the Royal Society A: Mathematical, Physical and Engineering Science*, 67(2121):537–558, 2011. doi: 10.1098/rspa.2010.0211.

C. Raymond. Shear margins in glaciers and ice sheets. *Journal of Glaciology*, 42(140):90–102, 1996.

C. F. Raymond, R. J. Benedict, W. D. Harrison, K. A. Echelmeyer, and M. Sturm. Hydrological discharges and motion of Fels and Black Rapids Glaciers, Alaska, U.S.A.: implications for the structure of their drainage systems. *Journal of Glaciology*, 41(138):290–304, 1995.

E. Rignot and P. Kanagaratnam. Changes in the velocity structure of the Greenland Ice Sheet. *Science*, 311:986–990, 2006. doi: 10.1126/science.1121381.

P. A. Rosen, S. Hensley, I. R. Joughin, F. K. Li, S. N. Madsen, E. Rodriguez, and R. M. Goldstein. Synthetic aperture radar interferometry. *Proceedings of the IEEE*, 88(3):333 –382, 2000. doi: 10.1109/5.838084.

H. Röthlisberger. Water pressure in intra- and subglacial channels. *Journal of Glaciology*, 11: 177–203, 1972.

C. Schoof. The effect of cavitation on glacier sliding. *Proceeding of the Royal Society of London. Series A, Mathematical and Physical Sciences*, 461:609–627, 2005. doi: 10.1098/rspa.2004.1350.

C. Schoof. Ice sheet grounding line dynamics: Steady states, stability, and hysterisis. *Journal of Geophysical Research*, 112(F3):1–19, 2007a. doi: 10.1029/2006JF000664. F03S28.

C. Schoof. Pressure-dependent viscosity and interfacial instability in coupled ice-sediment flow. *Journal of Fluid Mechanics*, 570:227–252, 2007b. doi: 10.1017/S0022112006002874.

C. Schoof. Ice-sheet accerleration driven by melt supply variability. *Nature*, 468(7325):803–806, 2010. doi: 10.1038/nature09618.

C. Schoof and R. C. A. Hindmarsh. Thin-film flows with wall slip: an asymptotic analysis of higher order glacier flow models. *The Quarterly Journal of Mechanics and Applied Mathematics*, 63(1): 73–114, 2010. doi: 10.1093/qjmam/hbp025.

K. C. Schuenemann and J. J. Cassano. Changes in synoptic weather patterns and Greenland precipitation in the 20th and 21st centuries: 2. Analysis of 21st century atmospheric changes using self-organizing maps. *Journal of Geophysical Research: Atmospheres*, 115(D5):n/a–n/a, 2010. doi: 10.1029/2009JD011706.

A. Shepherd, A. Hubbard, P. Nienow, M. King, M. McMillan, and I. Joughin. Greenland ice sheet motion coupled with daily melting in late summer. *Geophysical Research Letters*, 36(1), 2009. doi: 10.1029/2008GL035758. L01501.

S. Sugiyama and G. H. Gudmundsson. Short-term variations in glacial flow controlled by subglacial water pressure at Lauteraargletscher, Bernese Alps, Switzerland. *Journal of Glaciology*, 50(170): 353–362, 2004. doi: 10.3189/172756504781829846.

A. V. Sundal, A. Shepherd, P. Nienow, E. Hanna, S. Palmer, and P. Huybrechts. Melt-induced speed-up of greenland ice sheet offset by efficient subglacial drainage. *Nature*, 469(7331):521–524, 2011. doi: 10.1038/nature09740.

A. J. Tedstone, P. W. Nienow, A. J. Sole, D. W. F. Mair, T. R. Cowton, I. D. Bartholomew, and M. A. King. Greenland ice sheet motion insensitive to exceptional meltwater forcing. *Proceedings of the National Academy of Sciences*, 110(49):19719–19724, 2013. doi: 10.1073/pnas.1315843110.

A. J. Tedstone, P. W. Nienow, N. Gourmelen, A. Dehecq, D. Goldberg, and E. Hanna. Decadal slowdown of a land-terminating sector of the Greenland Ice Sheet despite warming. *Nature*, 526 (7575):692–695, 2015. doi: 10.1038/nature15722.

J. Thompson, M. Simons, and V. C. Tsai. Modeling the elastic transmission of tidal stresses to great distances inland in channelized ice streams. *The Cryosphere*, 8(6):2007–2029, 2014. doi: 10.5194/tc-8-2007-2014.

V. C. Tsai, A. L. Stewart, and A. F. Thompson. Marine ice-sheet profiles and stability under coulomb basal conditions. *Journal of Glaciology*, 61(226):205–215, 2015. doi: 10.3189/2015JoG14J221.

S. Tulaczyk, W. B. Kamb, and H. F. Engelhardt. Basal mechanics of Ice Stream B, west Antarctica: 1. Till mechanics. *Journal of Geophysical Research: Solid Earth*, 105(B1):463–481, 2000a. doi: 10.1029/1999JB900329.

S. Tulaczyk, W. B. Kamb, and H. F. Engelhardt. Basal mechanics of Ice Stream B, west Antarctica: 2. Undrained plastic bed model. *Journal of Geophysical Research: Solid Earth*, 105(B1):483–494, 2000b. doi: 10.1029/1999JB900328.

J. Weertman. On the sliding of glaciers. *Journal of Glaciology*, 3(21):33–38, 1957.

M. A. Werder, I. J. Hewitt, C. G. Schoof, and G. E. Flowers. Modeling channelized and distributed subglacial drainage in two dimensions. *Journal of Geophysical Research: Earth Surface*, 118(4): 2140–2158, 2013. doi: 10.1002/jgrf.20146.

H. J. Zwally, W. Abdalati, T. Herring, K. Larson, J. Saba, and K. Steffen. Surface melt-induced acceleration of Greenland Ice-Sheet flow. *Science*, 297(5579):218–222, 2002. doi: 10.1126/science.1072708.

Chapter 4

Incipient surge motion in glaciers with till-covered beds

4.1 Abstract

Surges are quasi-periodic episodes of rapid flow caused by increases in slip rate at the ice-bed interface. Because surge motion arises from enhanced basal slip, the underlying surge mechanisms offer a unique window into the mechanics of glacier beds. Here we develop a mechanistic model of incipient surge motion for the special case of glaciers with till-covered beds. Our model is informed by soil mechanics and current research on earthquake nucleation and slow-slip events on gouge-filled tectonic faults. Among the strengths of our model is that it does not depend on changes in water pressure in the subglacial hydrological system or freeze-thaw cycles in the till to produce surges, which makes our model viable for temperate and polythermal glaciers and consistent with observations of wintertime onset of surge motion. We propose four necessary conditions for glaciers to surge. Condition 1 links bed shear strength and local climate by requiring that till shear strength be less than the gravitational driving stress necessary for the glacier to achieve balance velocity. The caveat is that till must have sufficiently high shear strength to allow the glacier to build enough driving stress to facilitate order-of-magnitude speedups relative to quiescent phase velocities. Condition 2: Slip-rate-dependent weakening in the till must override dilatant hardening such that till shear strength decreases with the onset of surge motion. Condition 3: Surge-phase velocities must exceed balance velocity during the nascent surge phase. Condition 4: Till must have a finite hydraulic diffusivity, meaning that the bed can not be perfectly drained. Through derived theory and linear stability analysis, we show how these conditions arise from the fundamental principles of ice flow and a mechanical model of till that accounts for changes in till shear strength caused by

changes in effective pressure, basal slip rate, and basal slip history.

4.2 Introduction

Surges are among the most enigmatic characteristics of glacier flow. Broadly speaking, glacier surges are quasi-periodic, sub-annual to multi-annual periods of relatively rapid flow interspersed within decadal-to-centennial timescale quiescent periods (e.g., Meier and Post, 1969; Raymond, 1987). Surface velocities during a surge can reach 5–100 times typical quiescent phase velocities because of radical increases in slip rate at the ice-bed interface, hereafter called basal slip rate. Accelerated basal slip rates are facilitated by changes in the bed's mechanical, thermal, and hydrological properties, which may work independently or in concert to initiate and sustain glacier surges (e.g., Raymond, 1987; Kamb, 1987; Murray et al., 2000; Fowler et al., 2001; Murray et al., 2003; Flowers et al., 2011). Understanding these mechanisms will help address broader questions relating to how basal properties influence ice flow.

Surges are known to occur in only about 1% of glaciers worldwide (Jiskooot et al., 1998). Known surge-type glaciers are clustered in a handful of globally dispersed geographic regions, share comparable geological factors, but inhabit a variety of climates (Meier and Post, 1969; Jiskoot et al., 2000). The most common feature identified in surge-type glaciers is the presence of mechanically weak beds consisting of thick layers of deformable sediment and highly erodible sedimentary or volcanic rock. This commonality suggests that the mechanics of deformable glacier beds play an outsized role in initiating and sustaining glacier surges, but the fact that many glaciers are underlain by deformable glacier beds while few glaciers surge indicates that the existence of a deformable bed may be a necessary, but certainly not a sufficient, condition for surging (Harrison and Post, 2003).

Here we consider the special case of surges arising from increases in basal slip rate facilitated entirely by deformation of subglacial till. We focus on illuminating the basal properties and slip mechanisms that allow for surge initiation and sustainment in order to gain broader insight into the mechanics of deformable glacier beds. By better understanding the underlying mechanisms of surges in soft-bedded glaciers, we can constrain the set of admissible models of the mechanics of glacial till. Because basal slip can be the dominant component in ice flow and offers the shortest timescale coupling between glacier flow and environmental forcing, accurate representations of basal mechanics are critical for the development of plausible models of future glacier states and the response of glaciers to changing climate. The prevalence of subglacial till places high value on understanding the mechanics of soft-bedded glaciers in order to understand the evolution of glaciers worldwide. Surging glaciers afford opportunities to study the mechanical properties of till because many surge-type glaciers are known to be underlain by till and transient behaviors, such as surges, offer unique insight into the physical properties of the respective system (e.g., Truffer et al., 2000; Björnsson et al., 2003; Harrison and Post, 2003; Woodward et al., 2003). Here we develop a new physical model of incipient surge motion with the ultimate goal of contributing to a deeper understanding of the mechanics of deformable glacier beds and shedding light on the longstanding questions concerning the mechanisms responsible for the onset of glacier surges (Meier and Post, 1969; Raymond, 1987; Harrison and Post, 2003).

One prevailing theory of glacier surges holds that incipient surge motion arises from a switch in the subglacial hydrological system from a relatively efficient channelized system to an inefficient distributed, or linked-cavity, system (Kamb et al., 1985; Kamb, 1987). Throughout the surge phase, the basal hydrological system likely remains relatively inefficient, facilitating rapid ice flow, until reestablishment of an efficient channelized system terminates the surge (Kamb et al., 1985; Bjornsson, 1998). Given a supply of water to the bed of the glacier, this theory could potentially explain rapid surge motion and coincident increases in basal water pressure (Kamb et al., 1985). Indeed observations of a subglacial flood that fortuitously occurred during, but did not initiate, a surge indicate that the basal hydrological system was likely inefficient during the surge and became channelized just prior to surge termination (Bjornsson, 1998). However, surges are often observed to begin in late fall or winter, when surface meltwater supplies are limited (Kamb et al., 1985; Echelmeyer et al., 1987; Roush et al., 2003; Bevington and Copland, 2014; Dunse et al., 2015) and observations of numerous surge-type glaciers in Iceland show that jökulhaups, or subglacial floods, do not cause surges in spite of massive, rapid increases in basal water flux (Björnsson et al., 2003). As noted by Kamb (1987), often credited with introducing hydrological switching as an incipient surge mechanism, surge onset in the absence of surface meltwater flux requires an incipient surge mechanism beyond a switch from an efficient to an inefficient basal hydrological system. So the causal link between the efficiency of the basal hydrological system and surge motion remains unclear: Does a switch from an efficient to an inefficient system cause surges or does surge motion destroy efficient hydrological systems, leaving behind an inefficient, nascent basal hydrological system? Our model, combined with the fact that surges are observed to begin when there is little or no surface melt, supports the latter case but does not rule out the former case.

An alternative theory of glacier surges, first advocated by Robin (1955), contends that sediment underlying a polythermal glacier may freeze during the quiescent phase, strengthening the bed. As ice collects in an upstream reservoir, reductions in melting temperature caused by thickening ice (increasing overburden pressure) will cause the bed to thaw and, subsequently, weaken. Warm weakened beds facilitate basal slip, resulting in frictional heating that melts basal ice. Melted ice further lubricates the bed leading to enhanced basal slip and more heating, thereby closing the positive thermal feedback loop (e.g., Clarke, 1976; Clarke et al., 1977; Fowler et al., 2001). Because thermal control of glacier sliding requires ice to freeze to the bed, it cannot explain surging in temperate glaciers, whose ice is at the melting temperature and unable to freeze to the bed. This limitation led Clarke (1976) and others to propose that thermal instability, if it is a viable mechanism, is only one of several possible surge mechanisms. Recent observational work shows that at least some surges in polythermal glaciers initiate in temperate zones, suggesting further limitations on the applicability of thermal instability to incipient surge motion (Sund et al., 2014).

The prevalence of till layers beneath surge-type glaciers suggests that changes in the mechanical properties of till caused by varying porosity and pore water pressure are a promising alternative to the previous models of incipient surge mechanisms. Such models have been proposed by other authors, notably Truffer et al. (2000), who intuited till mobilization as a surge mechanism from direct observations of till deformation beneath a surge-type in Alaska, and Woodward et al. (2003), who proposed their model based on ice penetrating radar surveys of a surge-type glacier in Svalbard. These models are conceptual and lack a rigorous mathematical treatment of the salient physical processes. Motivated in part by these models, we present a physical model that leverages the mechanical properties of granular material to help explain incipient surge motion and observed increases in basal water pressure in the absence of additional surface meltwater flux and frozen beds. Our model is informed by studies of soil mechanics and earthquake nucleation and slow-slip events on tectonic faults containing water-saturated gouge. Gouge and glacial till are mechanistically analogous materials in that both are fine-grained and, in the cases of fault breccia and till, may feature coarse clasts (Moore and Iverson, 2002). Regardless of the presence of coarse clasts, the load is carried by the fine-grained matrix. Laboratory experiments on fault gouge and till indicate that these materials have elastic-plastic rheologies with yield stresses defined by the normal effective stress and the tendency of the till to undergo internal frictional slip (Dieterich, 1979; Ruina, 1983; Kamb, 1991; Kilgore et al., 1993; Iverson et al., 1998; Tulaczyk et al., 2000a; Hooke, 2005; Iverson, 2010). Shear strength is a function of shear rate within the till, hereafter called basal slip rate for glacier applications, and the shear history of the till. Accounting for shear history is important because shearing

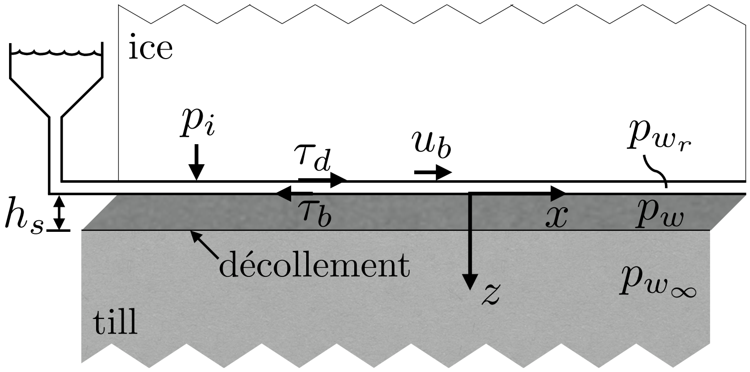

Figure 4.1: Model setup. The diagram shows a zoomed in view of the base of the idealized glacier with important parameters labeled. Parameters are defined in the notation section.

can cause granular materials to dilate or compress depending on the state of consolidation in the material (Lambe and Whitman, 1969). Dilation has been identified through theory and observation as an important component controlling basal slip rates for glaciers in Svalbard, ice caps in Iceland, and ice streams in Antarctica and here we seek to better understand the role of till compaction and dilation in incipient surge motion (e.g. Kamb, 1991; Tulaczyk et al., 2000a,b; Fuller and Murray, 2002; Woodward et al., 2003).

4.3 Model derivation

Consider an idealized glacier with length ℓ, thickness h, and constant width $2w$ where $h \ll w \ll \ell$. Let us define a coordinate system oriented such that x is along-flow, y is across-flow in a right-handed configuration, and z is downward (Fig. 4.1). Assume that ice thickness varies along-flow and is constant across-flow such that $h = h(x)$.

Water-saturated till underlies the glacier. We divide the till into two layers, a deformable layer with thickness h_s and pore water pressure p_w, and a stationary, non-deforming half-space with pore water pressure p_{w_∞}. Aside from strain rate, pore water pressure, and otherwise stated properties, all physical properties of the till are assumed to be the same above and below the décollement.

Our idealized glacier has a subglacial hydrological system that, like any glacier, evolves in time due to changes in meltwater flux (e.g., Schoof, 2010; Werder et al., 2013). The details of this evolution are not germane to this study and both the state of the hydrological system and the basal water flux are accounted for in p_{w_r}, the water pressure within the hydrological system, depicted as a reservoir in the system diagram (Fig. 4.1). Here we assume that basal slip is due entirely to deformation of the upper till layer, meaning that p_{w_r} only influences ice flow through its influence on p_w. We make this simplifying assumption in spite of the fact that p_{w_r} may cause sliding of the ice relative to the bed (Lliboutry, 1968; Kamb, 1970; Fowler, 1987; Schoof, 2005; Hewitt, 2013) because our focus is on how the mechanical properties of till might induce surging in the absence of externally sourced meltwater flux. Unless there is a significant flux of meltwater into the subglacial hydrological system, an unlikely scenario during winter, p_{w_r} should remain approximately constant in time when averaged over a spatial scale on the order of ice thickness. This assumption of nearly constant wintertime p_{w_r} is merely conceptual and is not a necessary condition in the subsequent derivation because time-varying p_{w_r} is accounted for in our model. For simplicity, we ignore potential changes in pore water pressure caused by plowing particles (e.g. Thomason and Iverson, 2008; Zoet et al., 2013).

4.3.1 Pre-surge behavior

Our most basic premise is that surge motion is the result of significant increases in basal slip rate, u_b, and not changes in the rheology of ice (Raymond, 1987). Large increases in basal slip rate mean that basal shear traction, τ_b, is a controlling factor in surge onset and sustainability (Kamb et al., 1985; Raymond, 1987; Jay-Allemand et al., 2011; Gladstone et al., 2014). Because gravity is the sole driver of glacier motion, surges require an abundance of gravitational driving stress relative to resistive basal shear traction. Our idealized glacier rests on a horizontal bed and as a result the gravitational driving stress is the product of ice overburden pressure and the ice surface slope α given as:

$$\tau_d = \rho_i g h \alpha \tag{4.1}$$

where ρ_i is the mass density of ice and g is the gravitational acceleration. We assume α is small such that $\sin(\alpha) \approx \alpha$ and varies smoothly across spatial scales of order several ice thicknesses. During quiescence, gravitational driving stress increases as ice fills a reservoir in the upper accumulation zone where basal slip rates are likely to be small (Kamb et al., 1985; Raymond and Harrison, 1988; Jay-Allemand et al., 2011). Low basal slip rates indicate that $\tau_b \approx \tau_d$ is a reasonable assumption. Therefore, while basal slip rates are low, increasing driving stress requires the bed to resist ever greater shear traction as the reservoir fills, ice thickens, and the slope steepens (Raymond, 1987; Raymond and Harrison, 1988).

It is natural, then, to begin the model derivation by considering the loading on the bed induced by changes in gravitational driving stress. Taking ρ_i to be constant, the rate of change in driving stress is:

$$\begin{aligned} \dot{\tau}_d &= \rho_i g \left(\dot{h}\alpha + h\dot{\alpha}\right) \\ &= \frac{\rho_i g \dot{h}}{\alpha}\left(\alpha^2 + h\frac{\partial^2 h}{\partial x^2}\right) \\ &= \rho_i g \dot{h}\alpha\Theta \end{aligned} \tag{4.2}$$

where $\Theta = 1 + \frac{h}{\alpha^2}\frac{\partial^2 h}{\partial x^2}$ is a dimensionless geometric parameter defined such that $0 < \Theta < 1$ (Appendix A) and overhead dots indicate time derivatives of the respective variables. Eq. 4.2 shows that the rate of change in driving stress is proportional to the product of the rate of change in ice thickness and the instantaneous glacial geometry described by the product $\alpha\Theta$. This expression indicates that the rate of change in gravitational driving stress at a given time is proportional to the rate of ice thickening but that the constant of proportionality will evolve as α steepens due to thickening in the accumulation zone and thinning in the ablation zone and the curvature of the surface increases (Raymond, 1987).

Conservation of ice mass accounts for the evolution of ice thickness as the balance between ice flux and the rate of net mass change, such that:

$$\dot{h} = \dot{M} - \nabla \cdot (h\bar{\mathbf{u}}) \tag{4.3}$$

where $\bar{\mathbf{u}}$ is the depth-averaged velocity vector and $\dot{M}$ is the total mass balance, which includes surface and basal mass balance and is positive for mass accumulation. By adopting the idealized glacier geometry discussed previously, where h varies only in the along-flow (x) direction, and focusing only on the central trunk of the glacier where across-flow variations in $\bar{\mathbf{u}}$ can be neglected (see §4.3.4), Eq. 4.3 becomes:

$$\dot{h} = \dot{M} - \eta\alpha u_s \tag{4.4}$$

$$= \eta\alpha\left(u_{s*} - u_s\right) \tag{4.5}$$

where $\eta = \bar{u}/u_s$, u_s is the glacier surface velocity, $u_{s*} = \dot{M}/(\eta\alpha)$ is the surface balance velocity at which ice thickness is in steady state ($\dot{h} = 0$), and we have assumed negligible along-flow strain rate (i.e. $|\partial u_s/\partial x| \ll u_s/(\ell - x)$). Taking ice to be a viscous fluid, we have $(n+1)/(n+2) \leq \eta \leq 1$, where n is the stress exponent in the flow law for ice (Glen, 1955). Here we adopt the most common value in glaciology, $n = 3$, such that $0.8 \leq \eta \leq 1$. Note that hereafter balance values are indicated by subscript $_*$ while superscript * indicates critical values, discussed later.

Plugging Eq. 4.5 into Eq. 4.2 yields:

$$\dot{\tau}_d = \rho_i g \eta \alpha^2 \Theta \left(u_{s*} - u_s \right) \tag{4.6}$$

This expression describes the conditions necessary for changing the shear loading on the glacier bed over time in areas where basal slip rate is small and gives the intuitive result that gravitational driving stress increases when the surface speed is less than the balance velocity ($\dot{\tau}_d > 0$ for $u_s < u_{s*}$). In other words, glaciers thicken and their slopes steepen when mass accumulation exceeds mass evacuation from ice flow. The rate of change in driving stress increases with steepening surface slope, increasing ice thickness, and reduced curvature of the ice surface but is largely controlled by the difference between flow speed and balance velocity. Because flow speed, whether contributed by viscous deformation within the ice column or basal slip, increases with steepening surface slopes and ice thickness, the last term in Eq. 4.6 is likely to set the rate of change in driving stress.

According to Eq. 4.6, reduction in driving stress occurs when the flow rate exceeds the balance velocity. However, because we neglected longitudinal, or along-flow, strain rate, a potentially poor assumption during the early surge phase, Eq. 4.6 may not accurately represent local $\dot{\tau}_d$ during transit of the surge wave, which is communicated through longitudinal stress (Kamb et al., 1985; Raymond, 1987). Because our interest is in the mechanics of incipient surge motion, this potential limitation in Eq. 4.6 has minimal adverse impact on our model.

In the accumulation zones of surging glaciers, flow speeds must be slower than the balance velocity to build a reservoir over time (Björnsson et al., 2003). This condition must be persistent throughout the quiescent phase because once the flow speed reaches the balance velocity, there is no mechanism that would further load the bed—a consequence of the fact that basal shear traction must be less than gravitational driving stress. In other words, mass balance along with the geometric and rheological properties of surge-type glaciers allow them to build a reservoir that exerts a driving stress equal to bed failure strength before flow rates reach the balance velocity. To illustrate this point, consider that the maximum load a glacier can apply to its bed is given by the gravitational driving stress when $u_s = u_{s*}$ and basal slip rate is negligible ($\tau_b \approx \tau_d$). Surface velocity due solely to viscous deformation within the ice column is given by assuming that stress increases linearly with depth, that ice rheology is constant with depth, and that ice flow is parallel to the ice surface, yielding:

$$u_v = \frac{2A}{n+1}\tau_d^n h \tag{4.7}$$

where A is the constant of proportionality and n is the stress exponent in the constitutive relation for ice, often called Glen's flow law (Eq. 4.85). Setting $u_s = u_v$ in Eq. 4.6 gives the maximum balance driving stress:

$$\begin{aligned} \tau_{d*} &= \left(\rho_i g \dot{M} \frac{n+2}{2A}\right)^{1/(n+1)} \\ &= \tilde{\tau}_d \left(\frac{n+2}{2}\right)^{1/(n+1)} \\ &\approx 1.25\tilde{\tau}_d \end{aligned} \tag{4.8}$$

where the approximation $(1+n/2)^{1/(n+1)} \approx 1.25$ holds for all values of n within the range for viscous ice flow ($1 \lesssim n \lesssim 5$) and asymptotically approaches unity as ice rheology approaches perfect plasticity ($n \to \infty$). We define the potential shear traction on the bed as:

$$\tilde{\tau}_d = \left(\frac{\rho_i g \dot{M}}{A}\right)^{1/(n+1)} \tag{4.9}$$

where the variables $\dot{M}$, A, and to a lesser extent ρ_i are determined by climate (Van der Veen, 2013) and $\tilde{\tau}_d$ for an idealized glacier is determined almost exclusively by $\dot{M}/A$, the ratio of mass balance, $\dot{M}$, to ice rheology. In more realistic glacier models, $\tilde{\tau}_d$ would be a function of glacier geometry as well. Eqs. 4.8 and 4.9 underpin necessary condition 1 for surging (§4.5): At a minimum, surging glaciers must have a climate, and geometry, that allows for sufficiently large $\tilde{\tau}_d$ values—a combination of high mass balance and stiff ice (i.e. small A)—to overcome the strength of their beds. As a result, the geographic distribution of surge-type glaciers will reflect areas that combine large amounts of snow, relatively low summertime melt and cold, stiff ice with beds that have yield stresses below the respective $\tilde{\tau}_d$ but that are sufficiently strong to allow the glacier to build enough driving stress to cause order-of-magnitude increases in ice flow. These beds must be rate-weakening, meaning that they are weaker during periods of rapid basal slip than during quiescent periods with little basal slip. Any model of incipient surge motion needs to account for all of these bed properties and we now turn our attention to a mechanical model of subglacial till.

4.3.2 Mechanical properties of till

We adopt a model for the mechanical strength of the till-covered bed that depends on basal slip rate, u_b, and the state of the subglacial till, θ. This rate-and-state model provides a formal framework that accounts for instantaneous basal slip rate and, importantly, basal slip history. The model, which is based on numerous laboratory measurements involving fault gouge and is widely used in studies of earthquake nucleation and slow-slip events on tectonic faults, is given as (Dieterich, 1979; Ruina, 1983; Kilgore et al., 1993):

$$\tau_t = N\left[f_n + a\ln\left(\frac{u_b}{u_{b_c}}\right) + b\ln\left(\frac{\theta u_{b_c}}{d_c}\right)\right] \tag{4.10}$$

where f_n is the nominal internal friction of the subglacial till, d_c is the characteristic slip displacement, u_{b_c} is an arbitrary normalizing constant, and constants a and b are material parameters. In our idealized glacier geometry, the bed is horizontal and effective normal stress is equal to effective pressure, defined as:

$$N = p_i - p_w \tag{4.11}$$

$$p_i = \rho_i g h \tag{4.12}$$

where p_i is the ice overburden pressure and p_w is the pore water pressure within the till.

Rate-and-state models have been applied to glacier till and have been widely studied on faults containing gouge, a material mechanistically similar to till (Rathbun et al., 2008; Zoet et al., 2013). Distinct in many respects, earthquakes and glacier surges are nonetheless analogous in the sense that both involve long quiescent periods and relatively short activation timescales. Slow-slip on tectonic faults are particularly relevant to studying glacier surges because of their comparable slip durations and slow slip rates compared with major earthquakes (Segall and Rice, 2006; Segall et al., 2010). Incipient motion in both earthquakes and glacier surges is brought on by excess applied stress relative to frictional resistance. While stresses and displacement rates are orders of magnitude higher in earthquakes than in glaciers, rate-and-state is applicable to the glacier surges because there is no known lower bound on velocity for the model to be valid (Dieterich, 2007).

Rate-and-state friction (Eq. 4.10) is similar to the more commonly used Mohr-Coulomb yield criteria, which is defined as:

$$\tau_y = N f_c + c_o \tag{4.13}$$

where f_c is the constant internal friction parameter and c_o is the cohesion, often assumed constant and negligible. There are some advantages to adopting rate-and-state friction over the more common Mohr-Coulomb criteria with constant f_c and negligible c_o. The first advantage is that the rate-and-state model accounts for rate-weakening of the till with incipient motion (τ_b decreases with increasing u_b), whereas the Mohr-Coulomb yield criteria with constant cohesion is independent of basal slip rate for constant f_c. Because τ_t scales as $\log(u_b)$, increasing u_b in fast-slipping glaciers has little influence on τ_t, supporting the use of simpler Mohr-Coulomb friction in studies of fast-flowing glaciers and ice streams (Kamb, 1991; Tulaczyk et al., 2000a,b; Minchew et al., 2016; Tsai et al., 2015). Minimal rate weakening at high basal slip rates is consistent with laboratory measurements and the common assumptions of constant f_c and c_o (Iverson et al., 1998; Moore and Iverson, 2002; Iverson, 2010). Our interest is in areas with low quiescent-phase basal slip rates, so these laboratory observations and the possibility of rate-weakening till are consistent.

The second advantage to using rate-and-state friction is that it provides a means to account for compaction and dilation of the till, which influence bed strength. Till compaction and dilation provides a mechanism by which the bed can strengthen under an approximately stagnant load and increasing gravitational driving stress. When basal slip rates are small, the overburden pressure of ice will compact the till until it reaches a minimum porosity. As the till is sheared, porosity increases, causing water pressure to decrease in the absence of a sufficient water supply (*i.e.* undrained or pseudo-undrained conditions) and the till to strengthen. This "dilatant strengthening" has been proposed as the mechanism behind stagnation and excitation of ice streams (Tulaczyk et al., 2000a,b). Dilatant strengthening under shear stress at near-zero basal slip rates affords a glacier the opportunity to build up gravitational driving stresses that exceed the ultimate, or steady-state, till strength. Because porosity cannot increase indefinitely, it must tend toward steady state under shear, which helps set the peak till strength. Once driving stress exceeds the peak strength of the till, basal slip rates will increase because of the imbalance between driving stress and basal shear traction. Increases in u_b will be immediately followed by a transient, compaction-driven decrease in bed strength, leading to further increases in u_b. Till strength will approach steady-state under further strain and in time, reducing and eventually arresting glacier acceleration as ice thins and surface slopes shallow, both of which cause driving stress to decrease. Steady state till shear strength occurs when state evolution ceases ($\dot{\theta} = 0$) and is defined as:

$$\hat{\tau}_t = N\left[f_n + (a-b)\ln\left(\frac{\hat{u}_b}{u_{b_c}}\right)\right] \tag{4.14}$$

where $\hat{u}_b = d_c/\hat{\theta}$ is the steady state basal slip rate and till is steady state rate-weakening when $b > a$. Hereafter, hatted values indicate steady state for the respective variable.

State, θ, which has dimensions of time, represents the product of the contact area and intrinsic strength of contacts between asperities (Ampuero and Rubin, 2008) but also has been interpreted as the average time that load-supporting asperities are in contact (Dieterich and Kilgore, 1994). Under either interpretation, state is expected to evolve as a function of time, slip, and effective normal stress (Dieterich, 1979, 1981; Dieterich and Kilgore, 1994). An analytical expression for the evolution of θ that accounts for all three dependencies does not currently exist, but two common models of state evolution are given as (Ruina, 1983):

$$\dot{\theta} = 1 - \frac{\theta u_b}{d_c} \tag{4.15}$$

$$\dot{\theta} = -\frac{\theta u_b}{d_c} \ln\left(\frac{\theta u_b}{d_c}\right) \tag{4.16}$$

Eq. 4.15, known as the “aging law”, facilitates healing when the load-bearing asperities are in stationary contact ($u_b = 0$) while Eq. 4.16, known as the “slip law”, dictates that state evolves only in the presence of slip ($\dot{\theta} = 0$ when $u_b = 0$). In both laws, steady state occurs when $\theta = \hat{\theta} = d_c/u_b$. Under constant (and nonzero, in the case of the slip law) u_b, θ always tends toward steady state. Increasing u_b beyond d_c/θ, through enhanced surface meltwater flux, calving, or other external forcing, will reduce θ over time in both the aging and slip laws. Similarly, when $u_b < d_c/\theta$, θ will increase toward steady state. In the next section we show that changes in θ are brought about through till compaction and dilation. As such, θ accounts for the basal slip history and plays a key role in determining bed strength and the response of bed strength to shear and external forcing. The influence of θ on bed strength underscores the importance of the state evolution laws.

Uncertainty remains as to which state evolution law best represents a dynamic system (e.g. Ampuero and Rubin, 2008; Segall et al., 2010). Aging and slip laws are asymptotically equivalent when the till is near steady state but the laws differ markedly in behavior at large departures from steady state (Fig. 4.2a; Ampuero and Rubin, 2008). Qualitatively, the aging law likely better represents the evolution of state when two surfaces are in stationary contact because it is plausible that some state evolution (healing) will occur in the absence of slip due to deformation caused by nonzero effective normal stress (Dieterich and Kilgore, 1994). Slip-rate stepping experiments, on the other hand, indicate a symmetry in the magnitude of slip-rate-induced stress changes in response to faster and slower slip rates. Such symmetric behavior is consistent with the slip law (Fig. 4.2b) and not

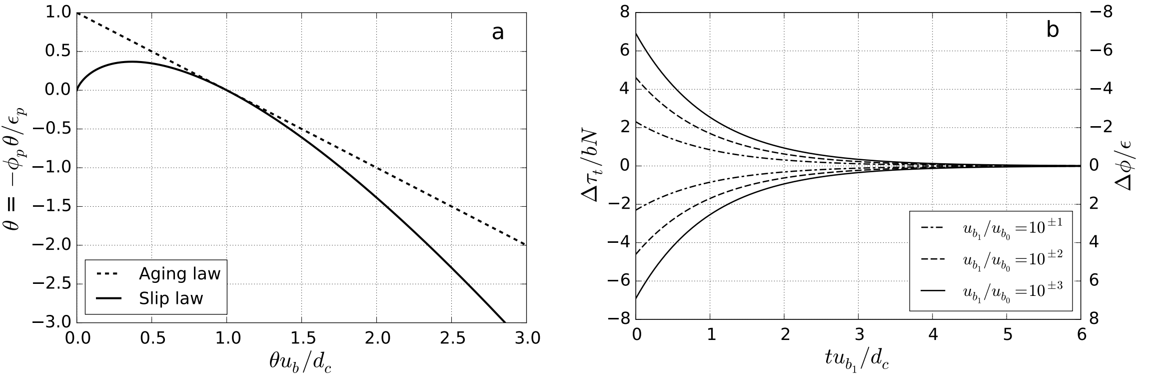

Figure 4.2: (a) Rate of change in state in the vicinity of steady state ($\dot{\theta} = 0$). Note that both the aging and slip laws are equivalent at steady state, when $\theta = \hat{\theta} = d_c/u_b$, but exhibit markedly different behavior well above and below steady state. (b) Normalized till shear strength (left y-axis) and till porosity relative to future steady state values for a step increase in basal slip rate from u_{b_0} to u_{b_1} using the slip law for state evolution (see Eq. 4.18).

the aging law (Blanpied et al., 1998; Ampuero and Rubin, 2008). The same experiments show that stress evolves to steady state over a distance scale that is independent of the magnitude of change in slip rate, a feature that is also consistent only with the slip law (Fig. 4.2b) (Ruina, 1983). Furthermore, the magnitude of changes in basal slip rate during nascent surges indicate that incipient surge motion is influenced by the behavior of till near or well above steady-state basal slip rates. Under these conditions, the slip law is more appropriate (Ampuero and Rubin, 2008). Based on this rational and studies of slow slip events on tectonic faults (e.g., Segall et al., 2010), we adopt the slip law (Eq. 4.16) for the remainder of the model derivation.

It is important to understand some characteristics of till rheology under the chosen state evolution law. Integrating Eq. 4.16 over time for a step change in u_b from u_{b_0} to u_{b_1} gives:

$$\theta\left(t\right) = \hat{\theta}_1 \left(\frac{\hat{\theta}_0}{\hat{\theta}_1}\right)^{\exp\left\{-u_{b_1}t/d_c\right\}} \tag{4.17}$$

where $\hat{\theta}_0$ and $\hat{\theta}_1$ are the steady state values associated with basal slip rates u_{b_0} and u_{b_1}, respectively. Plugging Eq. 4.17 into Eq. 4.10, assuming constant N, we find (Ampuero and Rubin, 2008):

$$\begin{aligned} \frac{\Delta\tau_t}{bN} &= \ln\left(\frac{\hat{\theta}_0}{\hat{\theta}_1}\right)\exp\left\{-\frac{t}{\hat{\theta}_1}\right\} \qquad (4.18) \\ &= \ln\left(\frac{u_{b_1}}{u_{b_0}}\right)\exp\left\{-\frac{u_{b_1}t}{d_c}\right\} \end{aligned}$$

where $\Delta\tau_t = \tau_t - \hat{\tau}_{t_1}$ and $\hat{\tau}_{t_1}$ is the steady state shear stress associated with $\hat{\theta}_1$ (Fig. 4.2b). As expected, $\Delta\tau_t$ is symmetric about $u_{b_1} = u_{b_0}$, such that the magnitude of decreases in $\Delta\tau_t$ following an order-of-magnitude reduction in slip rate are equivalent to increases in $\Delta\tau_t$ brought on by positive order-of-magnitude increases in slip rate. Eq. 4.18 also reveals that immediately after a step change in basal slip rate ($t = 0^+$), $\Delta\tau_t = bN\ln(u_{b_1}/u_{b_0})$ and that τ_t tends toward its new steady state value, $\hat{\tau}_{t_1}$, with characteristic time $\hat{\theta}_1 = d_c/u_{b_1}$. In general, $d_c < 1$ m and $u_b^{surge} \sim$ 100–1000 m/yr in many known surge-type glaciers (Cuffey and Paterson, 2010), meaning that the shear strength of subglacial till will reach approximate steady state over timescales of days to weeks if u_b^{surge} remains approximately constant during that time. Similarly, time to steady state can be of order weeks to months with $u_b^{quies} \lesssim 10$ m/yr.

During both surge and quiescent phases, glaciers experience seasonal and diurnal ice flow variations, often attributed to surface meltwater flux and displacement of the calving front (e.g., Raymond, 1987; Björnsson et al., 2003). These flow variations are facilitated by basal slip, which contributes to the state of the subglacial till. In the interest of simplicity, let us suppose that these changes in basal slip rate begin at $t = 0$ and vary sinusoidally in time such that:

$$u_b(t) = \begin{cases} u_{b_0} & \text{for } t < 0 \\ u_{b_0} + \breve{u}_b \sin(\omega_b t) & \text{for } t \geq 0 \end{cases} \tag{4.19}$$

where $\breve{u}_b \leq u_{b_0}$ is the amplitude and ω_b is the angular frequency. At $t = 0$, the system is at steady state such that $\hat{\theta}_0 = d_c/u_{b_0}$. At this point, we are not concerned with what causes u_b to vary in time, and we assume N is constant. With this assumption, which is reasonable given the small seasonal changes in mean pore water pressure (Minchew et al., 2016), we define the normalized till shear strength relative to its initial steady state, $\hat{\tau}_{t_0}$, as:

$$\frac{\tau_t - \hat{\tau}_{t_0}}{bN} = a_b \ln\left(1 + \frac{\breve{u}_b}{u_{b_0}}\sin(\omega_b t)\right) + \ln\left(\frac{\theta}{\hat{\theta}_0}\right) \qquad \text{for } t \geq 0 \tag{4.20}$$

where $a_b = a/b$, whose value is often taken to be $0.6 \leq a_b < 1$ for rate-weakening materials (Segall et al., 2010). Given this narrow range, the value of a_b has little qualitative impact on the response of changes in bed shear strength to sinusoidal u_b, serving primarily to increase (decrease) the amplitude of normalized relative bed shear strength with higher (lower) a_b values. Therefore the response of till shear strength to sinusoidal u_b is defined primarily by the nature of the sinusoidal basal slip rate relative to the initial steady state condition, *i.e.* by $\breve{u}_b/u_{b_0}$ and ω. Numerically integrating θ over several u_b cycles and solving Eq. 4.20 for different values of $\breve{u}_b/u_{b_0}$ and ω reveals several characteristics of the response of till strength to changes in shear strain rate (Fig. 4.3). The most prominent characteristic is the nonlinearity of till shear strength with respect to the sinusoidal properties. When the period is very long relative to $\hat{\theta}_0$ and $\breve{u}_b/u_{b_0} \gtrsim 0.5$, maximum normalized till shear strength exceeds the amplitude of the associated minima by approximately a factor of 4 and till shear strength is symmetric about the extrema (Fig. 4.3a). Maximum (minimum) till shear strength is coincident with minimum (maximum) u_b because the long period allows for till compaction and dilation (recall that N is constant, so dilation should weaken the till) and dynamic equilibration. As the sinusoidal period is reduced, the amplitudes of maximum and minimum till shear strength converge while till shear strength becomes asymmetric about the extrema at higher amplitudes. At sufficiently large sinusoidal amplitudes, non-extrema inflections in till shear strength occur as u_b decreases. Extrema in τ_t no longer correspond to the extrema in u_b (Fig. 4.3b). The inflections diminish with further reductions in sinusoidal period, eventually becoming jogs, where slope changes but not the curvature. Extrema in τ_t move toward alignment with extrema in u_b and the amplitude of the minimum till shear strength exceeds the maximum value, a trend that continues with further increases in ω_b (Fig. 4.3c). When the sinusoidal period is shorter than $\hat{\theta}_0$, τ_t is approximately symmetric about the extrema, whose values asymptotically approach constants with the number of cycles. The number of cycles required for the system to stabilize scales as $\omega_b\hat{\theta}_0$ (not shown). As $\omega_b\hat{\theta}_0$ becomes large, maximum and minimum τ_t align in phase with maximum and minimum u_b (Fig. 4.3d). The point of this analysis is to illustrate the nonlinearity of state and to underscore that because the response of glacier flow to surface meltwater flux increases with time during the quiescent phase, quiescent-phase till state is not constant and may undergo important changes in the months and years leading up to a surge (e.g. Kamb et al., 1985; Raymond and Harrison, 1988).

4.3.3 Pore water pressure

In steady state, till shear strength is proportional to the effective normal stress, here assumed equal to effective pressure (Eq. 4.11). Meaningful ice thickness changes occur over timescales that are much longer (months to years) than timescales of incipient surge motion (days to weeks), making pore water pressure the primary driver of changes in bed strength during nascent surges. Pore water pressure is linked to till compaction and dilation through changes in till porosity. If the bed is effectively undrained (approximately constant pore water volume), shear-induced changes in

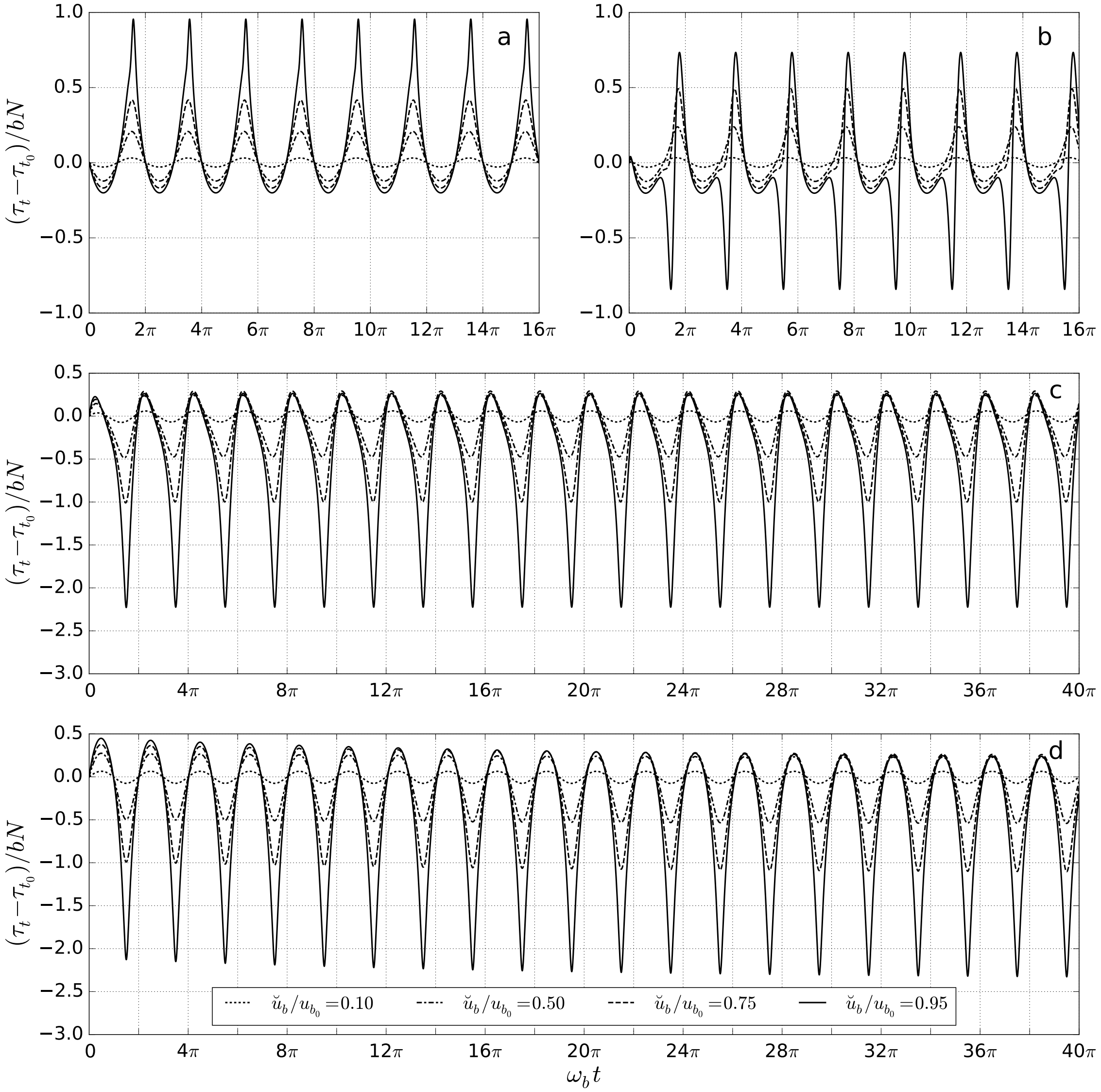

Figure 4.3: Change in normalized till shear strength for $u_b(t) = u_{b_0} + \breve{u}_b \sin(\omega_b t)$ relative to steady-state till shear shear strength for $u_b = u_{b_0}$ (see Eq. 4.20). Line dashes represent different values of $\breve{u}_b/u_{b_0}$ and subplots represent different values of ω: (a) $\omega_b = 2\pi \times 10^{-3}/\hat{\theta}_0$ (period $\sim$ 1 year), (b) $\omega_b = 0.05\pi/\hat{\theta}_0$ (period $\sim$ 14 days), (c) $\omega_b = 0.67\pi/\hat{\theta}_0$ (period $\sim$ 1 day), and (d) $\omega_b = 20\pi/\hat{\theta}_0$. In all cases, $a_b = 0.7$.

porosity will alter pore water pressure and, consequently, bed strength. Conversely, if the bed is effectively drained, pore water pressure remains approximately constant. In this section we derive the rate of change in pore water pressure as a function of basal slip rate under the basic assumptions that water is incompressible over the range of reasonable subglacial pressures and that temperature changes due to straining in till are negligible.

Suppose that the till is initially saturated such that all of the pore spaces are filled with water. Then the rate of change of water mass per unit volume within the till is given as:

$$\dot{m}_w = \rho_w \dot{\phi} \tag{4.21}$$

where ϕ is the (dimensionless) till porosity, defined as the ratio of pore volume to total volume, and ρ_w is the density of water. We separate porosity changes into a plastic component, ϕ_p, and an elastic component such that (Walder and Nur, 1984; Segall and Rice, 1995):

$$\dot{\phi} = \dot{p}_w \beta + \dot{\phi}_p \tag{4.22}$$

where:

$$\begin{aligned} \beta &= \frac{\partial \phi}{\partial p_w} \\ &= \frac{\epsilon_e \left(1 - \phi\right)^2}{N} \end{aligned} \tag{4.23}$$

is the till compressibility and $\epsilon_e \sim 10^{-3}$–10^{-1} is the elastic compressibility coefficient (Appendix B). Following Segall and Rice (1995) and Segall et al. (2010) we assume that the plastic component of porosity is defined as:

$$\phi_p = \phi_c - \epsilon_p \ln\left(\frac{\theta u_{b_c}}{d_c}\right) \tag{4.24}$$

where ϕ_c is the characteristic porosity and ϵ_p is the plastic dilatancy coefficient, a dimensionless, empirically derived parameter. Hereafter we take ϵ_p to be constant, though, in reality, ϵ_p may scale inversely with normal effective pressure. Laboratory experiments on fault gouge indicate that $\epsilon_p \sim 10^{-4}$ for normal effective pressures $\sim$ 10–100 MPa (Segall et al., 2010). Given that these experiments were conducted at effective pressures that are one to two orders of magnitude higher than expected in the subglacial environment, laboratory measurements are needed to estimate ϵ_p in till at realistic subglacial pressures. This lack of emperical data is not a limiting factor for our study and later we will show that plausible values for ϵ_p for subglacial till are $\sim 10^{-4}$.

The time dependence of till porosity is a function of only the log of state, θ, because all other parameters in Eq. 4.24 are constant. As a consequence of using the slip law for state evolution, ϕ_p is constant when $u_b = 0$ or $u_b = d_c/\theta$. The first condition of zero basal slip rate is reasonable in that a static normal load on a granular media would need to induce some component of shear in order to change porosity. The second condition is steady-state for both evolution laws discussed before and we should expect porosity to remain constant when till is at steady state. When the till is not at steady state and basal slip rates are nonzero, plastic porosity evolves over a distance d_c, reaching steady state ($\dot{\theta} = 0$ with $\hat{\theta} = d_c/u_b$) at:

$$\hat{\phi}_p = \phi_c + \epsilon_p \ln\left(\frac{u_b}{u_{b_c}}\right) \tag{4.25}$$

The fact that $\hat{\phi}_p$ is a function of u_b allows steady state till porosity to evolve as basal slip rates change. The sensitivity of $\hat{\phi}_p$ to changes in u_b is $\partial\hat{\phi}_p/\partial u_b = \epsilon_p/u_b$, so faster basal slip rates produce smaller changes in steady-state porosity with acceleration than do slower basal slip rates. This is consequential for incipient surge motion because late quiescent phase basal slip rates at the incipient surge position are likely to be small (Kamb et al., 1985; Raymond and Harrison, 1988; Björnsson et al., 2003; Jay-Allemand et al., 2011). As an aside, it is worth noting that ice streams are likely to experience relatively small changes in till porosity for changes in basal slip rate (Tulaczyk et al., 2000a,b).

Differentiating Eq. 4.24 in time yields the rate of change in plastic porosity:

$$\begin{aligned} \dot{\phi}_p &= -\epsilon_p \frac{\dot{\theta}}{\theta} \\ &= \epsilon_p \frac{u_b}{d_c} \ln\left(\frac{\theta u_b}{d_c}\right) \\ &= \frac{u_b}{d_c}\left(\hat{\phi}_p - \phi_p\right) \end{aligned} \tag{4.26}$$

(Fig. 4.2a). This expression indicates that till compacts ($\dot{\phi}_p < 0$) under shear strain when θ is below steady-state ($\theta < d_c/u_b$) and dilates when θ is above steady-state. Such behavior is consistent with observations of the response of over- and under-consolidated soils to shear (Lambe and Whitman, 1969). True to the definition of θ, porosity remains constant at steady state.

Integrating the rate of porosity change over time for a step in basal slip rate yields:

$$\begin{aligned}\Delta\phi_p &= -(\hat{\phi}_{p_1} - \hat{\phi}_{p_0})\exp\{-u_{b_1}t/d_c\} \\ &= -\epsilon_p \ln\left(\frac{u_{b_1}}{u_{b_0}}\right)\exp\left\{-\frac{u_{b_1}t}{d_c}\right\} \\ &= -\epsilon_p\frac{\Delta\tau_t}{bN}\end{aligned} \tag{4.27}$$

where $\Delta\phi_p = \phi_p - \hat{\phi}_{p_1}$. Note that the response of porosity to step changes in u_b is proportional to the response of normalized till shear strength, where the constant of proportionality is negative (Fig 4.2b). In other words, porosity, relative to its future steady state value, is linearly mapped to normalized till shear strength, relative to its future steady state value. For effectively drained till, where N is constant, Eq. 4.27 is consistent with our expectation that till compaction ($\hat{\phi}_{p_0} > \hat{\phi}_{p_1}$) increases till shear strength while dilation weakens the bed for step changes in u_b. Because the constant of proportionality is $-\epsilon_p$, the value of ϵ_p plays an important role in determining the surge characteristics of a soft-bedded glacier, as we discuss in §4.5.

We now turn our attention to till water flux in response to changes in porosity and sources outside the till shear layer. The rate of change of water mass is given by plugging the expressions for the total rate of change in porosity (Eq. 4.22) and the rate of change in plastic porosity (Eq. 4.26) into the expression for the rate of change in mass per unit volume (Eq. 4.21) yielding:

$$\dot{m}_w = \rho_w \dot{p}_w \beta + \epsilon_p \rho_w \frac{u_b}{d_c}\ln\left(\frac{\theta u_b}{d_c}\right) \tag{4.28}$$

Conservation of water mass gives:

$$\nabla \cdot q_w + \dot{m}_w = 0 \tag{4.29}$$

where q_w is the water mass flux. Fluid flux through a granular material is a diffusive process and we assume that the diffusion length scale is long relative to the slip region. Relatively long diffusion length means water flux parallel to the bed is negligible. Taking basal ice to be impermeable means that water flux is entirely into and out of the bed. Under these conditions, Darcy's law is:

$$q_w = -\frac{\rho_w \gamma_h}{\nu_w}\frac{\partial p_w}{\partial z} \tag{4.30}$$

where γ_h is the till permeability and ν_w is the dynamic viscosity of water. Combining Eqs. 4.28, 4.29, and 4.30 under the assumption that till permeability is spatially constant gives:

$$\begin{aligned} \dot{p}_w &= \frac{1}{\beta}\left[\frac{\gamma_h}{\nu_w}\frac{\partial^2 p_w}{\partial z^2} - \epsilon_p \frac{u_b}{d_c}\ln\left(\frac{\theta u_b}{d_c}\right)\right] \\ &= \kappa_h \frac{\partial^2 p_w}{\partial z^2} - \frac{u_b N}{d_c \Lambda}\ln\left(\frac{\theta u_b}{d_c}\right) \end{aligned} \tag{4.31}$$

where:

$$\kappa_h = \frac{\gamma_h}{\nu_w \beta} \tag{4.32}$$

$$\Lambda = \frac{\epsilon_e}{\epsilon_p}(1-\phi)^2 \tag{4.33}$$

are the hydraulic diffusivity of the till and the (dimensionless) porosity number, respectively.

Shearing in till concentrates in a thin zone, consisting of numerous layers (e.g., Iverson and Iverson, 2001), that is typically of order several centimeters thick (Boulton and Hindmarsh, 1987; Boulton et al., 2001; Tulaczyk et al., 2000a). Therefore, we approximate the second derivative of p_w with depth as:

$$\frac{\partial^2 p_w}{\partial z^2} \approx \frac{p_{w_\infty} + p_{w_r} - 2p_w}{h_s^2} \tag{4.34}$$

where h_s is the thickness of the shear zone in the till, p_{w_∞} is the water pressure in the underlying permeable half space, and p_{w_r} is the water pressure in the basal hydrological system (Fig. 4.1). With this approximation, Eq. 4.31 becomes:

$$\dot{p}_w = \dot{p}_{w_{st}} + \dot{p}_{w_{dy}} \tag{4.35}$$

where, for convenience, we have written the total rate of change in pore water pressure as the sum of static and dynamic components, defined respectively as:

$$\dot{p}_{w_{st}} = c_h\left(p_{w_\infty} + p_{w_r} - 2p_w\right) \tag{4.36}$$

$$\dot{p}_{w_{dy}} = -\frac{u_b N}{d_c \Lambda}\ln\left(\frac{\theta u_b}{d_c}\right) \tag{4.37}$$

The static component of pore water pressure evolution is proportional to the characteristic diffusivity of the till layer (units of time^{-1}) defined as:

$$c_h = \kappa_h / h_s^2 \tag{4.38}$$

Both κ_h (Eq. 4.32) and h_s scale as N (Cuffey and Paterson, 2010), making $c_h \sim N^{-1}$. The inverse dependence of $\dot{p}_{w_{st}}$ and $\dot{p}_{w_{dy}}$ on N indicates that dynamically induced changes in p_w diminish as p_w approaches overburden pressure ($N \to 0$) and that $\dot{p}_w$ is large when $2p_i \approx 2p_w \neq p_{w_\infty} + p_{w_r}$. In glaciers with till-covered beds, $p_{w_\infty} < p_i$ and $p_{w_r} \leq p_i$, particularly during winter when most surges are observed to start, which means that pore water pressure must remain below overburden pressure over finite time periods. Based on this line of reasoning and owing to the relatively small expected changes in N during a surge (Jay-Allemand et al., 2011), we hereafter assume c_h is constant for simplicity.

The coefficient in $\dot{p}_{w_{dy}}$ is always negative, so the sign of $\dot{p}_{w_{dy}}$ is determined by the state of the till relative to steady state. When θ is below (above) steady state and c_h is finite, pore water pressure will increase (decrease) until steady state is achieved. These changes in pore water pressure are due entirely to changes in till porosity: compaction ($\dot{\phi}_p < 0$) results in increases in $\dot{p}_{w_{dy}}$ and vice versa because $\dot{p}_{w_{dy}} = -\dot{\phi}_p/\beta$. Whether p_w increases or decreases following step changes in basal slip rate depends on the whether the ratio $\theta u_b/d_c$ is greater or less than unity. Because state evolution lags basal slip rate evolution (Eq. 4.17), large $|\dot{u}_b|$ cause nonzero $\dot{p}_{w_{dy}}$ over timescales longer than the acceleration timescale.

With an expression for $\dot{p}_w$ we can define the rate of change in effective pressure, the key component in bed strength. Assuming the mass density of ice remains constant in time we have:

$$\begin{aligned}
\dot{N} &= \rho_i g \dot{h} - \dot{p}_w && (4.39)\\
&= \frac{\dot{\tau}_d}{\alpha\Theta} - \dot{p}_{w_{st}} - \dot{p}_{w_{dy}} && (4.40)\\
&= \rho_i g \eta \alpha (u_{s*} - u_s) - c_h \left(p_{w_\infty} + p_{w_r} - 2p_w\right) + \frac{u_b N}{d_c \Lambda} \ln\left(\frac{\theta u_b}{d_c}\right) && (4.41)
\end{aligned}$$

To glean further intuition from Eq. 4.39, we separate surface velocity into viscous, u_v and u_{v*}, and basal slip components such that $u_{s*} = u_{v*} + u_{b*}$ and $u_s = u_v + u_b$. Just prior to and during the nascent surge phase we expect, and will later show, that $u_{v*} \approx u_v$, allowing us to rewrite Eq. 4.39 as:

$$\dot{N} = \rho_i g \eta \alpha u_{b*} - \dot{p}_{w_{st}} - u_b \left[\rho_i g \eta \alpha - \frac{N}{d_c \Lambda} \ln\left(\frac{\theta u_b}{d_c}\right)\right] \quad (4.42)$$

In the form of Eq. 4.42, the mechanisms driving evolution of effective normal stress are more evident. The first term represents the rate of increase in normal stress due to mass balance (Eq. 4.4). The second term, $\dot{p}_{w_{st}}$, is the pore water pressure evolution caused by water pressure gradients between the deforming till, the stationary underlying till, and the subglacial hydrological system. The final term, which is proportional to basal slip rate, represents the balance between modulations in normal stress evolution caused by basal slip and dynamically induced pore water pressure evolution that arises from till dilation and compaction.

4.3.4 Basal slip acceleration

Surges occur when basal slip rate increases significantly due to reductions in basal shear traction and ice in our idealized glacier behaves as an incompressible, highly viscous fluid with a spatially and temporally constant shear-thinning, power-law rheology (Appendix C). During a surge, $u_s \approx u_b$ (Kamb et al., 1985). Assuming the areal extent of incipient surge motion is at least several ice thicknesses—so that along-flow strain rates are negligible—and considering only the central trunk of the symmetric idealized glacier where lateral shearing is negligible, we can show that basal slip rate is given as (Appendix C) (Raymond, 1996):

$$u_b = v_o \left(\tau_d - \tau_b\right)^n \tag{4.43}$$

where:

$$v_o = \frac{2A}{n+1} \left(\frac{w}{h}\right)^n w \tag{4.44}$$

is a scalar relating glacier geometry,through half-width w and thickness h, and ice rheology, via A and n, to basal slip rate.

Basal shear traction cannot exceed the lesser of applied stress and bed yield stress, giving rise to the relation:

$$\tau_b = \min(\tau_d^-, \tau_t) \tag{4.45}$$

where $\tau_t = Nf$ is the till shear strength (Eq. 4.10) and $\tau_d^- < \tau_d$. We use τ_d^- to account for the fact that ice supports stress, requiring basal shear traction to be less than driving stress in order to maintain stress balance. In our idealized model, $\tau_d^- \approx \tau_d$ because normal and lateral shear stresses in the ice are negligible in the areas of interest. Setting $\tau_d^- = \tau_d$, assuming v_o is temporally constant, and differentiating Eq. 4.43 with respect to time yields:

$$\dot{u}_b = n v_o \left(\tau_d - \tau_b\right)^{n-1} \left(\dot{\tau}_d - \dot{\tau}_b\right) \tag{4.46}$$

When the shear strength of till is sufficient to balance gravitational driving stress, $\dot{\tau}_d = \dot{\tau}_b$ and $\dot{u}_b = 0$ for any ice rheology and geometry. When gravitational driving stress exceeds till shear strength ($\tau_b = \tau_t$), acceleration in basal slip rate is nonzero and is given as:

$$\dot{u}_b = nu_b \left(\frac{\dot{\tau}_d - \dot{N}f - Nb\dot{\theta}/\theta}{\tau_d - \tau_t + naN} \right) \tag{4.47}$$

wherein the evolution of driving stress, effective pressure, state all contribute to the basal slip acceleration along with instantaneous basal slip rate, driving stress, basal shear strength, effective pressure, and state. Recalling the equations of evolution for gravitational driving stress (Eq. 4.2), effective pressure (Eqs. 4.39–4.42), and pore water pressure (Eqs. 4.36–4.37), Eq. 4.47 becomes:

$$\dot{u}_b = nu_b \left(\frac{\dot{\tau}_d \left(1 - \mu/\Theta\right) + f \left[\dot{p}_{w_{st}} + \left(1 - \lambda\right) \dot{p}_{w_{dy}}\right]}{\tau_d \left[1 - \mu \left(1 - p_w/p_i\right)\right] + naN} \right) \tag{4.48}$$

where:

$$\mu = f/\alpha \tag{4.49}$$

$$\lambda = b\Lambda/f \tag{4.50}$$

are the stress number and friction-dilatancy parameter, respectively.

When the mechanical properties of till change with basal slip rate and state, both the stress number and the friction-dilatancy parameter are important parameters in establishing the evolution of basal slip rate for a given glacier. We will explore the role of both parameters in more detail below, but it is worth considering these parameters on their own first. The stress number is derived from the ratio τ_t/τ_d and is a key component in determining the sensitivity of ice flow to changes in pore water pressure and setting the critical pore water pressure, $p_w^* = p_i(1 - \mu^{-1})$, at which till begins to deform (Minchew et al., 2016). Nonzero basal slip acceleration requires $p_w > p_w^*$. Once basal slip is underway, μ plays a leading role in determining how $\dot{u}_b$ responds to u_b. The friction-dilatancy parameter gives the relative importance of frictional weakening and dilatancy to the till strength (Segall et al., 2010). When $\lambda \ll 1$, dilatant hardening suppresses basal slip acceleration. When $\lambda \gg 1$, frictional weakening, brought on by compaction, creates a positive feedback between basal slip rate and acceleration. Note that the influence of dilatancy on till strength increases with increasing porosity and that both dilatancy and frictional weakening are similarly dependent on effective normal stress such that λ is independent of N.

Eqs. 4.46–4.48 illuminate a number of characteristics of basal slip acceleration. One of the most basic features is that the coefficient and, importantly, the denominator are always positive. As a result, $\dot{u}_b$ avoids singularity at $N = 0$ in all glaciers of interest in this study because $\tau_d > 0$ is a necessary condition for surging to occur. Because the given $\dot{u}_b$ model is only valid when $\tau_d \geq \tau_t$, there are no admissible stress conditions that will drive the denominator to zero. This condition is intuitive because if $\tau_d < \tau_t$, $\tau_d \approx \tau_b$ and basal slip rate is minimal (Eqs. 4.43–4.45). With a positive coefficient and denominator, the numerator alone determines whether basal slip rate increases or decreases in time.

The first term in the numerator in Eq. 4.48 is the difference in the rates of change in gravitational driving stress and normal stress, or overburden pressure. The evolution of driving stress, $\dot{\tau}_d$, is approximately equal to the evolution of overburden pressure, $\dot{p}_i$, multiplied by $\alpha\Theta$ (Eqs. 4.2 and 4.40). Consequently, for physical values of surface slope and f, we have $\mu > 1$ leading to $1-2\mu < 0$ in all cases (Minchew et al., 2016). In other words, the magnitude of the rate of reduction in overburden pressure outpaces the rate of change in driving stress such that thinning ($u_b > u_{b*}$) leads to further acceleration. When $u_b < u_{b*}$, acceleration is suppressed at constant pore water pressure due to insufficient excess stress to drive increases in ice flow. Because $\mu > 1$ in all cases and surges must occur while $u_b < u_{b*}$, the onus is on pore water pressure to facilitate enough positive acceleration over long enough timescales that u_b surpasses u_{b*}, at which point acceleration becomes self-sustaining in the absence of further changes in water pressure.

Sudden increases in pore water pressure will immediately begin to decrease due to diffusion into the lower till layer and basal hydrological system and through evolution of till state. These factors impose a lower bound on the ratio u_b^-/u_{b*} for sustained surge acceleration, where u_b^- is the basal slip rate just prior to initial acceleration. The details of the evolution of the basal hydrological system and how water pressure within the hydrological system may change in response to basal slip acceleration render intractable an analytical solution that captures all of the various complexities. To estimate the absolute lower bound on u_b^-/u_{b*}, let us consider the special case of an undrained bed, where $\dot{p}_{w_{st}} = 0$. At initial acceleration, we have $\tau_d = \tau_t$ and we are solving for the case where

$\dot{\tau}_d \rightarrow 0$. Under these conditions, we can rearrange Eq. 4.48 to yield the relation:

$$\begin{aligned} u_{b*}\left(1-\frac{u_b^-}{u_{b*}}\right) &= \int_0^t \dot{u}_b \mathrm{d}t \\ &\approx \int_0^t u_b \frac{f\left(1-\lambda\right)}{Na}\dot{p}_{w_{dy}}\mathrm{d}t \end{aligned} \tag{4.51}$$

Recall that $\dot{p}_{w_{dy}} = -\dot{\phi}_p/\beta$. Furthermore, let us assume $\dot{\beta} \approx 0$ and that changes in u_b are well approximated as step functions. With these simplifications, we find that u_b^-/u_{b*} must satisfy the condition:

$$\frac{1-u_b^-/u_{b*}}{\ln\left(u_b^-/u_{b*}\right)} > \frac{f\left(1-\lambda\right)}{\Lambda a} \tag{4.52}$$

for basal slip to exceed the balance slip rate, allowing thinning of the ice to sustain surge motion. As u_b^-/u_{b*} approaches unity, the left hand side of the inequality approaches -1.

Glaciers cannot accelerate indefinitely and will eventually reach a maximum flow rate as set by glacier geometry, ice rheology, and surge-phase basal shear traction. Absolute maximum glacier flow speed, $u_b^{max} = v_0\tau_d^n$, occurs when $N = 0$. Observations and numerical models of surge-phase basal water pressure show that it is not significantly higher than quiescent-phase pressures and typically remains below overburden pressure such that $u_{b*} < u_b^{surge} < u_b^{max}$ (Kamb et al., 1985; Jay-Allemand et al., 2011). Because surge-phase basal slip rates exceed balance velocities, strengthening of the bed due to decreases in pore water pressure and reduction in gravitational driving stress due to thinning and flattening of the ice surface are the only potential mechanisms for initial negative acceleration. The more pronounced thinning and flattening become, the less strength the bed would need to acquire to slow the glacier. Once $u_b < u_{b*}$, abrupt slowdowns can occur as $\dot{\tau}_d$ becomes positive, making the first term in the numerator of Eq. 4.48 negative.

When basal slip rate changes, state evolves toward steady state over time. The time required for till to reach a new steady state is a function of the magnitude of change in basal slip rate. For step changes in u_b from u_{b_0} to u_{b_1}, this latency scales as d_c/u_{b_1} (Eqs. 4.17 and 4.18). Time dependence in state evolution means that incipient surge motion results in $\ln\left(\theta u_b/d_c\right) > 0$ when till is near steady state just prior to incipient surge motion. This leads to further acceleration so long as $\lambda > 1$. Conversely, once the surge is underway, rapid basal slip rates cause state to evolve toward steady state over short timescales, of order days to weeks. Once steady state is achieved, slowdowns lead to further slowdowns because $\ln\left(\theta u_b/d_c\right) < 0$.

4.4 Linear stability analysis

As we have discussed, basal slip acceleration is driven by reductions in basal shear strength that occur more rapidly than reductions in gravitational driving stress. In this section we consider the conditions under which a glacier can experience unstable acceleration caused by changes in till shear strength through a linear stability analysis that closely follows the analysis presented by Segall and Rice (1995). We begin by considering a glacier at equilibrium, such that $\tau_d = \tau_t$, and then evaluating small departures from equilibrium. To simplify our analysis and focus on changes in basal slip rate, we again separate surface velocity into viscous and basal slip components—such that $u_{s*} = u_{v*} + u_{b*}$ and $u_s = u_v + u_b$, where subscript v indicates the surface expression of viscous deformation within the ice column—and assume $u_{v*} \approx u_v$. Taking u_{b*}, η, and α to constant over the time intervals of incipient surge motion, the basal stress balance is given as:

$$Nf = \rho_i g \eta \alpha^2 \Theta \left(u_{b*} t_f - d_f \right) \tag{4.53}$$

where f is defined in Eq. 4.10 and d_f is the total basal slip occurring in time t_f. Equilibrium values for the relevant variables are:

$$\begin{gathered} \check{u}_b = u_{b*}\ ; \qquad \check{\theta} = d_c/\check{u}_b\ ; \qquad \check{p}_w = p_{w_r} = p_{w_\infty}\ ; \\ \check{\tau}_b = \check{\tau}_t = \check{N}\check{f} = (\check{p}_i - \check{p}_w)\check{f}\ ; \qquad \check{\phi} = \epsilon_p \ln\left(\check{u}_b/u_{b_c}\right) \end{gathered} \tag{4.54}$$

Note that because $\check{u}_b = u_{b*}$, we have $\check{\theta} = \theta_*$, $\check{f} = f_*$, and $\check{\phi} = \phi_*$.

Linearizing about equilibrium and denoting small departures from equilibrium with δ operator yields:

$$N \left. \frac{\partial f}{\partial u_b} \right|_{eq} \delta u_b + N \left. \frac{\partial f}{\partial \theta} \right|_{eq} \delta\theta - \check{f} \delta p_w = -k_\tau \delta d_f \tag{4.55}$$

where the system psuedo-stiffness is:

$$k_\tau = \rho_i g \eta \alpha^2 \left(\Theta - \check{\mu} \right) \tag{4.56}$$

and $\check{\mu} = \mu_*$, the stress number at equilibrium. For the remainder of the stability analysis, we assume that the partial derivatives are constant. Evaluating the partial derivatives at equilibrium and considering state evolution (Eq. 4.16), porosity evolution (Eq. 4.26), and pore water pressure evolution (Eq. 4.35) yields a system of coupled differential equations given as:

$$N\frac{a}{\check{u}_b}\delta\dot{u}_b = -N\frac{b}{\check{\theta}}\delta\dot{\theta} + \check{f}\delta\dot{p}_w - k_\tau\delta u_b \tag{4.57}$$

$$\delta\dot{\theta} = -\frac{\check{u}_b}{d_c}\delta\theta - \frac{1}{\check{u}_b}\delta u_b \tag{4.58}$$

$$\delta\dot{\phi} = -\frac{\check{u}_b}{d_c}\delta\phi + \frac{\epsilon_p}{d_c}\delta u_b \tag{4.59}$$

$$\delta\dot{p}_w = -c_h\delta p_w - \frac{1}{\beta}\delta\dot{\phi} \tag{4.60}$$

$$\delta\dot{d}_m = \delta u_b \tag{4.61}$$

Our interest is in the stability of the system, so we seek solutions of the form:

$$\delta u_b = \widehat{u}_b\, e^{st}\,; \qquad \delta p_w = \widehat{p}_w\, e^{st}\,; \qquad \delta\theta = \widehat{\theta}\, e^{st}\,; \qquad \delta\phi = \widehat{\phi}\, e^{st} \tag{4.62}$$

The system of equation in Eqs. 4.57–4.61 is formulaically identical to the elastic model in Segall and Rice (1995, Eq. 23) because we can describe gravitational driving stress evolution as a linear function of basal slip rate (Eq. 4.2). These authors show that plugging the forms in Eq. 4.62 into Eqs. 4.57–4.61 results in a cubic equation in s and that the critical system stiffness, k_τ^*, is determined by the largest value of k_τ for which the real component of the j^{th} root, s_j, is positive. This condition arises because $s > 0$ causes system instability in time. We leave the remainder of the derivation for k_τ^* to Segall and Rice (1995, Appendix B) and adopt their solution for the critical system stiffness, given as:

$$k_\tau^* = \frac{bN}{d_c}\left(1 - a_b - \Omega\right) \tag{4.63}$$

where $a_b = a/b$ and:

$$\Omega = \frac{1}{2}\left(\xi_1 - \sqrt{\xi_1^2 - \xi_2}\right) \tag{4.64}$$

$$\xi_1 = \frac{1}{\lambda_*} + \frac{1 + a_b\left(\psi_*^2 - 1\right)}{\psi_* + 1} \tag{4.65}$$

$$\xi_2 = \frac{4\left(1 - a_b\right)}{\lambda_*\left(\psi_* + 1\right)} \tag{4.66}$$

where $\lambda_* = b\Lambda_*/f_*$ (Eq. 4.33). The quantity beneath the radical in Eq. 4.64 is always positive, ensuring that Ω and k_τ^* are real-valued (Segall and Rice, 1995). Eqs. 4.63–4.66 provide insights into incipient surge motion and the rest of this section focuses on some of the salient points from Segall and Rice (1995, 2006) and Segall et al. (2010).

Fluid transport through till scales with the (dimensionless) diffusivity parameter:

$$\psi_* = \frac{c_h d_c}{u_{b*}} \tag{4.67}$$

which is the ratio of the characteristic state evolution time (d_c/u_{b*}) to the characteristic fluid transport time ($1/c_h$) (Segall and Rice, 1995; Segall et al., 2010). Undrained conditions prevail at $\psi_* \ll 1$ because of insufficient diffusivity relative to the state evolution demands. Conversely, drained conditions prevail at $\psi_* \gg 1$. Dynamically driven transitions between drained and undrained conditions occur when $u_b \sim c_h d_c$, *i.e.* at a critical value $\psi^* \sim u_b/u_{b*} \sim 1$.

The two dimensionless parameters, ψ_* and λ_*, are the primary factors in the dilatancy parameter Ω, which captures the influence of till dilatancy on k^*_τ. In the absence of dilatancy, $\Omega = 0$ and k^*_τ is independent of till diffusivity, behavior that is equivalent to having drained conditions at the bed ($\Omega \to 0$ as $c_h \to \infty$). Alternatively, strongly dilatant tills ($\Omega \approx \lambda_*^{-1}$) will exhibit undrained behavior ($\Omega \to \lambda_*^{-1}$ as $c_h \to 0$), so long as $\lambda_* > 0$. When $\lambda_* = 0$, $\Omega = 0$ for all ψ and the system is effectively drained; this condition requires $\phi \to 1$, a nonphysical configuration that is not given further consideration. Motivated by the tradeoff between dilatancy strength and diffusivity dependence, we define the drained and undrained critical stiffnesses, $k^*_{\tau_{dr}}$ and $k^*_{\tau_{un}}$, respectively, such that:

$$k^*_{\tau_{dr}} = \frac{bN}{d_c}\left(1 - a_b\right) \tag{4.68}$$

$$k^*_{\tau_{un}} = \frac{bN}{d_c}\left(1 - a_b - \lambda^{-1}\right) \tag{4.69}$$

$$\frac{k^*_\tau}{k^*_{\tau_{dr}}} = 1 - \frac{\Omega}{1 - a_b} \tag{4.70}$$

Because λ is always nonnegative, the drained and undrained conditions define the end member cases such that $k^*_{\tau_{un}} \leq k^*_\tau \leq k^*_{\tau_{dr}}$ (Fig. 4.4).

Instability requires $k_\tau < k^*_\tau$. From the definition of the system psuedo-stiffness—so named because $k_\tau < 0$ but its influence on the system calls to mind stiffness in Hooke's Law for an elastic media—we can immediately anticipate that glaciers resting on till-covered beds are inherently unstable. Closer examination of Eqs. 4.68–4.69 indicates that in the case of rate-weakening till ($a_b < 1$), all glaciers with drained beds are potentially susceptible to unstable slip, though few surge for reasons discussed above and outlined in the next section. In a perfectly drained bed where $c_h \to \infty$, pore water pressure remains constant in time because p_{w_∞} is assumed constant. Because

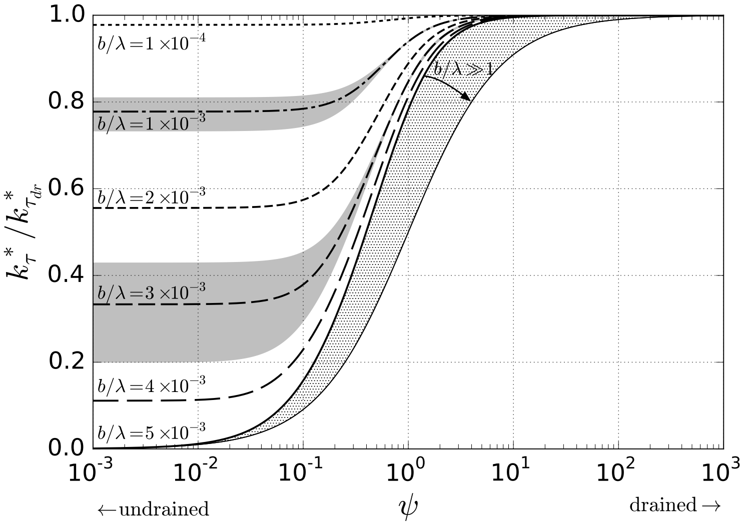

Figure 4.4: Normalized critical stiffness versus normalized diffusivity parameter for a range of b/λ values with $b = 0.015$ and $a_b = 0.7$ (solid and dashed lines) adapted from Segall and Rice (1995). The system approaches drained behavior, independent of ψ, as $\lambda \to \infty$. Gray shaded regions around $b/\lambda = 1 \times 10^{-3}$ and $b/\lambda = 3 \times 10^{-3}$ lines indicate $0.65 \leq a_b \leq 0.75$. Dot-shaded region labeled $b/\lambda \gg 1$ shows the response of $k_\tau^*/k_{\tau_{dr}}^*$ as $b\lambda$ becomes large; in the limit $b/\lambda \to \infty$, dilatancy is suppressed and the system is effectively drained at all values of ψ.

increases in pore water pressure are necessary to drive surge motion and borehole observations indicate pore water pressure variations over finite time, we discard the case of perfectly drained beds. In the previous section, we established that $\lambda > 1$ is necessary to facilitate slip acceleration through frictional weakening, a finding that is supported by the linear stability analysis. Assuming reasonable values for the parameters in Eq. 4.56, $\rho_i = 900$ kg/m^3, $\alpha > 10^{-2}$, and $f \approx 0.5$, we have $k_\tau < -40$ Pa/m, meaning that all values of $\lambda > 1$ can facilitate unstable slip.

4.5 Discussion

4.5.1 Surge conditions

We have laid out four conditions for a glacier to surge. Two of these conditions are exclusively related to the mechanical properties of the bed while the other conditions link local climate and basal mechanics.

4.5.1.1 Condition 1: Till shear strength is less than balance driving stress

Till shear strength, τ_t (Eq. 4.10), just prior to a surge must be less than the gravitational driving stress at balance (Eq. 4.8) but large enough to allow gravitational driving stress to build to a point that will allow order of magnitude increases in surface velocity. Assuming that the pre-surge surface velocity, $u_{s_{pre}}$, in the region where a surge begins is primarily due to viscous deformation in the ice column (i.e. $\tau_{b_{pre}} \approx \tau_{d_{pre}}$) and considering that surface velocity at peak surge speeds, $u_{s_{surge}}$, is due primarily to basal slip, the gravitational driving stress necessary to produce a given speedup can be approximated as:

$$\tau_{d_{pre}} \approx \tau_{t_{surge}} \left[1 - \frac{u_{s_{surge}}}{u_{s_{pre}}} \frac{h_{surge}^n h_{pre}}{w^{n+1}}\right]^{-1/n} \tag{4.71}$$

Combining Eq. 4.71 with the balance velocity explicitly gives condition 1 as:

$$\tilde{\tau}_d > \tau_{d_{pre}} \tag{4.72}$$

or:

$$\frac{\rho_i g \dot{M}}{A} > 2\frac{\left(\tau_{t_{surge}}\right)^{n+1}}{n+2} \left[1 - \frac{u_{s_{surge}}}{u_{s_{pre}}} \frac{h_{surge}^n h_{pre}}{w^{n+1}}\right]^{-(n+1)/n} \tag{4.73}$$

The range of reasonable values on $\rho_i g$ is small, so to a good approximation, whether a glacier meets condition 1 is determined primarily by mass balance, ice rheology, bed strength and cross-sectional geometry. The dependence on mass balance is consistent with observations that have shown cumulative quiescent-phase mass balance to be a reliable predictor of surging on Variegated Glacier, Alaska (Eisen et al., 2001, 2005).

Some glaciers are observed to undergo intensifying seasonal variations in ice flow in years leading up to a surge (Kamb et al., 1985; Raymond and Harrison, 1988). This characteristic likely indicates that the driving stress is nearing the till shear strength for mean wintertime pore water pressures and enhanced summertime velocities are the result of surface meltwater increasing water pressure in the basal hydrological system, which increases the pore water pressure through diffusion as long as $c_h > 0$. As we discussed with regard to changes in till strength due to sinusoidal variations in u_b, seasonal speedups are unlikely to play an important role in setting the ultimate shear strength of the till but may somewhat delay the onset of surge through small reductions in the rate of ice thickening and steepening.

4.5.1.2 Condition 2: Frictional weakening exceeds dilatant hardening

When frictional weakening exceeds dilatant strengthening the friction-dilatancy parameter $\lambda > 1$. When met, this condition ensures that increases in basal slip rate when the till is near steady state result in increases in pore water pressure, which further weakens the bed allowing for enhanced basal slip. The friction-dilatancy parameter varies with basal slip and till state and is strongly dependent on till porosity. Frictional weakening is favored for low porosity and the lack of basal slip during quiescent phase is expected to compact the till.

A necessary extension of this condition is the need for the till to be steady-state rate-weakening ($a < b$). We can derive this condition from the critical pseudo-stiffness parameters defined in the linear stability analysis. In that analysis, we showed that the glacier pseudo-stiffness (Eq. 4.56) must be less than a critical stiffness defined in Eq. 4.63. For the values of glacier geometry discussed previously, we have $k_\tau < -40 Pa/m$. Values for N are typically of order 10^6 Pa and values for $b/d_c \gtrsim 10^{-3}$ m. Considering that λ is finite, the critical stiffness parameter requires $a_b < 1$.

4.5.1.3 Condition 3: Surge-phase basal slip rate exceeds balance velocity

Given the evolving nature of basal hydrological systems, the permeability of realistic glacier beds and, the fact that till always tends toward steady state, thereby diminishing initial dynamic changes in water pressure, thinning caused by velocities in excess of the balance velocity is necessary to facilitate rapid surge motion over timescales of months to years. Observations showing that surging glaciers continue to experience seasonal variations in ice flow caused by surface meltwater runoff supports this notion in that it indicates that high pore water pressures alone are not sufficient to carry rapid incipient motion through to a developed surge (Björnsson et al., 2003).

4.5.1.4 Condition 4: Finite hydraulic diffusivity in till

Under natural conditions and assuming the underlying deformable till layer has a sufficiently high capacity to maintain constant p_{w_∞}, perfectly drained beds would have constant pore water pressure. Any dynamically induced pore water pressure changes would be instantly offset through diffusion to the basal hydrological system and the underlying till layer. Rapid bed weakening through dynamically induced increases in water pressure are necessary for incipient surge motion, requiring that surge-type glaciers have finite hydraulic diffusivity in till. This condition supports the original idea by Post (1969) that bed permeability may be among the characteristics controlling whether glaciers surge.

Regardless of initial till diffusivity, dynamic influences on diffusivity will cause glacier beds to tend toward undrained conditions during the surge phase (Eq. 4.67). This effect is characterized by the diffusivity parameter, ψ, which is the ratio of state evolution time to diffusion time. As basal slip rate increases, ψ decreases. Drainage conditions at the bed switch from drained ($\psi > 1$) to undrained as u_b exceeds u_{b*}. Condition 3 ensures then that the beds of glaciers during a surge are largely, though not fully, undrained. The opposite is true at termination, when a bed that is typically drained during the quiescent phase will revert back to drained conditions at a rate proportional to the slowdown in ice flow, releasing pressurized water stored in the till. Dramatic discharges during surge termination have been observed (e.g. Kamb et al., 1985; Bjornsson, 1998), though it remains unclear if these observed discharges are from water stored in the hydrological system, the till itself, or both. Because dynamic influences can not drive the bed to be perfectly undrained, comminuted debris can be transported during a surge and thereby increase observed surge-phase turbidity in glacier runoff (e.g. Kamb et al., 1985; Echelmeyer et al., 1987; Björnsson et al., 2003).

4.5.2 Model limitations and future work

Our goal with this work is to better understand basal mechanics by developing a model for incipient surge motion in glaciers with till-covered beds. We do not attempt to capture all of the processes that my be important in initiating and sustaining glacier surges. As a result, our model has some limitations that provide avenues for future work.

A notable limitation is the lack of explicit treatment for evolution of the subglacial hydrological system during any stage of the surge or the quiescent phase. The influence of basal hydrological characteristics is manifest in the model through the system water pressure p_{w_r}, but we implicitly treat this water pressure as passive in the model develop. A fully passive basal hydrological system is unlikely given the rapid, extreme changes in glacier dynamics that define a surge. During surges, significant volumes of till are displaced, filling most existing cavities, basal crevasses, or channels that constitute the contemporaneous hydrological system (Woodward et al., 2003). This lack of explicit treatment for changes in p_{w_r} due to till displacement leaves open the question posed earlier as to whether increases in basal water pressure caused by changes in the basal hydrological system cause surges, or if surges cause cause changes in the basal hydrological system. What we have provided in this study is a potential mechanism of incipient surge motion that is not dependent on, but may be aided by, changes in the basal hydrological system. The existence of such a mechanism, which works equally well for temperate and polythermal glaciers, and observations of surges beginning in times of the year when there is little or no additional surface meltwater available to pressurize a basal hydrological system, supports the hypothesis that it is the incipient surge motion that diminishes the efficiency of any extant hydrological system rather than changes in the hydrological system that lead to surges.

We do not explicitly consider enhanced melting of basal ice caused by increased flow speeds. The reason for this exclusion is twofold. First, melt rate scales linearly with the product of basal slip rate and till shear strength. While this product likely increases during the early surge phase, the tradeoff between diminished till shear strength, basal slip rate, and the characteristics of subglacial hydrological systems is nontrivial and leads to melt rates that are orders of magnitude below surface meltwater fluxes in many areas (Tulaczyk et al., 2000b). The second reason we exclude slip-induced melting is that melting only influences ice dynamics through changes in basal and pore water pressure. Without a reliable model for subglacial hydrology, there is no way to effectively link basal melt rate and water pressure.

Our model for incipient surge motion should hold for a developed surge, but not during the time and in areas where the surge wave is propagating down glacier (Kamb et al., 1985). This limitation arises from our assumption that normal along-flow stresses and strain rates are negligible (Eqs. 4.4 and 4.46–4.48). During the quiescent phase, the assumption of negligible normal stress is likely valid anywhere in the upper accumulation zone where surges are prone to begin. Here surface velocities tend to be slow and relatively consistent over large spatial scales, meaning that along-flow strain rates are low. From the flow law for ice, low strain rates mean low stresses. During the surge, the surface velocities are high but with the exception of the period when surge waves are present, velocity is expected to have small spatial gradients, satisfying the condition for negligible along-flow strain rates: $|\partial u_s/\partial x| \ll u_s/(\ell - x)$ (e.g. Murray et al., 2003; Dunse et al., 2015).

Future work involves addressing these limitations, developing numerical models of surge motion, and conducting an observational campaign to verify the model. A simple 1D numerical model should adequately capture the general characteristics of surge by demonstrating the inherent instability of some glaciers with till covered beds. With this model, we will explore the parameter space to define the range of values for each of the salient parameters. Coupling the model for till shear strength and a flowline for ice flow is the next logical step beyond the 1D model. A coupled flowline model will enhance our understanding of the feedback of realistic glacier geometries with surge characteristics, informing possible extensions to 3D models capable of accounting for till strength as defined here. Such models do not currently exist, but will prove valuable in further developing our understanding of basal mechanics.

4.6 Conclusions

We develop a model of incipient surge motion in glaciers with till covered beds that occurs in the absence of enhanced water flux to the bed, changes to the basal hydrological system, and freeze-thaw cycles in till. Incipient surge motion in our model arises from dynamic weakening in till shear strength caused by transient increases in pore water pressure brought on by shear-induced compaction. In the case when these dynamic increases in pore water pressure are large enough and occur for long enough, thinning of ice caused by flow velocities that exceed the balance velocity act to sustain incipient surge acceleration by reducing normal stress on the bed at a faster rate than thinning and shallowing of the surface slope reduce gravitational driving stress. Over timescales that depend on basal slip rate, ice thins and the surface slope shallows while till tends toward steady state. These changes in bed strength and glacier geometry act together to arrest surge motion. Abrupt slowdowns are possible as the surface velocity slows below steady-state velocity for the given till state and, later, the surface balance velocity.

Many till drainage conditions facilitate surges, but surges can not occur unless diffusivity is finite. During surge, all glaciers will tend toward undrained conditions because the state evolution time is inversely proportional to basal slip rate. In glaciers with relatively low quiescent phase hydraulic diffusivity, diffusion time of water through the till greatly exceeds till evolution timescales, leading to effectively undrained conditions.

We propose four conditions for glaciers to be capable of surging. The first condition links bed strength and local climate by requiring that till shear strength must be less than the gravitational driving stress needed to achieve balance velocities through viscous deformation in the ice column. If balance velocities are achieved before a surge begins, there is no way for the glacier to continue to increase the load on the bed and glacier will not surge. Conversely, the bed needs to be strong enough to allow sufficiently high gravitational driving stresses to produce order-of-magnitude increases in ice flow rate, which are necessary for a surge. If the bed is too weak, basal slip will occur at relatively low gravitational driving stresses and the glacier will eventually achieve balance velocity if mass balance remains constant in time. The second condition is that frictional weakening must exceed dilatant hardening, a condition that we parameterize through the friction-dilation parameter λ. Satisfying this condition requires that material parameters $a < b$, ensuring that till shear strength during a surge is less than till shear strength just prior to the surge, allowing for excess gravitational driving stress that leads to enhanced surge-phase ice flow rates. The third condition is that surge-phase velocities must exceed balance velocity. This condition needs to be met early in the surge phase so that weakening of till shear strength caused by thinning of the ice can sustain acceleration over timescales sufficient to constitute a surge. Considering the evolutionary nature of basal hydrological systems, it is unlikely that surges can be caused by changes in pore water pressure alone. In order to accelerate beyond surface balance velocity, the till must have a finite diffusivity, the fourth condition. In other words, the till can not be perfectly drained. Undrained conditions are permissible so long as $\lambda > 1$.

4.7 Appendix A

When in balance ($\dot{h} = 0$), our idealized glacier will have a parabolic profile such that $h(x) = c_1\sqrt{\ell - x}$ and c_1 is a constant related to basal shear traction (Van der Veen, 2013). Ice surface slope and curvature are then:

$$\begin{aligned} \frac{\partial h}{\partial x} &= -\frac{c_1}{2\left(\ell - x\right)^{1/2}} && (4.74)\\ &= -\alpha && (4.75)\\ \frac{\partial^2 h}{\partial x^2} &= -\frac{c_1}{4\left(\ell - x\right)^{3/2}} && (4.76)\\ &= -\alpha^2/h && (4.77) \end{aligned}$$

Then from Eq. 4.2 we have:

$$\begin{aligned} \Theta_* &= 1 + \frac{h}{\alpha^2}\frac{\partial^2 h}{\partial x^2} && (4.78)\\ &= 0 \end{aligned}$$

when the glacier is in balance. As discussed in §4.3.4, if a surge is going to occur, it must occur before the glacier reaches balance, so Eq. 4.78 requires that $\Theta > 0$. Furthermore, curvature over spatial scales of several ice thicknesses will be nonnegative (Van der Veen, 2013), so the opposite extreme is zero curvature, or constant surface slope. Taking into account Eq 4.78 and the zero-curvature condition, we have $0 < \Theta < 1$.

4.8 Appendix B

Here we carry out a dimensional analysis of $\partial\phi/\partial p_w$ based on laboratory measurements of subglacial till collected from Willans Ice Stream, West Antarctica (Tulaczyk et al., 2000a). We start by defining the void ratio ($e = \phi/[1-\phi]$) as:

$$e = e_0 - c_\zeta \log_{10}(N/N_0) \tag{4.79}$$

where e_0 is a constant, N_0 is an arbitrary normalizing stress, and c_ζ is the (dimensionless) coefficient of compressibility, assumed equal for both compression and dilation. From laboratory measurements, Tulaczyk et al. (2000b) give $c_\zeta = \ln(10)/21.7$. Taking the derivative of porosity with respect to water pressure yields:

$$\beta = \frac{\partial\phi}{\partial p_w} = \frac{\partial\phi}{\partial e}\frac{\partial e}{\partial p_w} = \frac{(1-\phi)^2}{21.7N} \tag{4.80}$$

The value 21.7 is a fit to laboratory data collected using till extracted from a specific area, so we simply consider:

$$\beta = \frac{\epsilon_e (1-\phi)^2}{N} \tag{4.81}$$

where $\epsilon_e \sim 0.05$. Because data in Tulaczyk et al. (2000b) are from a single study sight on a marine ice sheet, which may not be representative of glaciers worldwide, we generalize ϵ_e to be of order 10^{-3}–10^{-1}.

4.9 Appendix C

Ice in our idealized glacier behaves as an incompressible, highly viscous fluid with a spatially and temporally constant, shear-thinning, power-law rheology. As previously stated, the mass density of ice is assumed constant in space and time and ice thickness is constant across the flow. With a time-invariant ice rheology, we can describe ice flow by conservation of mass, linear momentum, and angular momentum, and by adopting a constitutive relation for ice (commonly known as Glen's flow law (Glen, 1955)). Taking $\boldsymbol{\tau}$ to be the deviatoric stress tensor, p_c to be the pressure at depth in the ice column—equal to the mean of the diagonal elements in the Cauchy stress tensor—and $\mathbf{g}$ to the be the gravitational acceleration vector—equal to g in the z direction and zero elsewhere—the three conservation laws and the flow law are respectively given as:

$$\nabla \cdot u = 0 \tag{4.82}$$

$$\nabla \cdot \boldsymbol{\tau} - \nabla p_c - \rho_i \mathbf{g} = 0 \tag{4.83}$$

$$\tau_{ij} - \tau_{ji} = 0 \qquad i, j \in x, y, z \tag{4.84}$$

$$\dot{\varepsilon}_e = A \tau_e^n \tag{4.85}$$

where A is the rate factor, which depends on ice rheology, n is a constant here assumed to be 3, $\dot{\varepsilon}_e$ is the effective strain rate—the square root of the negative second strain-rate tensor invariant—and τ_e is the effective deviatoric stress within the ice column (Cuffey and Paterson, 2010). Due to the orientation of the model domain and the simplifying assumptions that went into defining the idealized glacier, $\tau_{yy} = \tau_{yz} = 0$. Eq. 4.83 is subject to boundary conditions:

$$\tau_{zz} = 0 \qquad \text{on } \Gamma_s \tag{4.86}$$

$$\tau_{xz} - \tau_b = 0 \qquad \text{on } \Gamma_b \tag{4.87}$$

where Γ_s is the free surface and Γ_b is the base of the model domain.

Surges occur when basal slip rate increases significantly due to reductions in basal shear traction. Under these conditions, $u_s \approx u_b$ (Kamb et al., 1985) and the horizontal gradient of shearing within the ice column, $\partial \tau_{xz}/\partial x$, sometimes called the bridging stress, is negligible (Blatter, 1995; Pattyn, 2003). We further simplify the model by assuming that the areal extent of incipient motion is at least several ice thicknesses in length, as measured along-flow. Under this assumption, along-flow normal stress, τ_{xx}, is negligible and Eq. 4.83 reduces to (MacAyeal, 1989; Raymond, 1996):

$$h \frac{\partial \tau_{xy}}{\partial y} = \tau_b - \tau_d \tag{4.88}$$

Integrating from $y = 0$, at the glacier boundary, to $y = w$, the plane of symmetry where $\tau_{xy} = 0$, gives:

$$\tau_{xy} = \frac{w - y}{h} \left(\tau_d - \tau_b \right) \tag{4.89}$$

Applying the ice flow law (Eq. 4.85) yields:

$$\frac{\partial u_b}{\partial y} = 2A\left[\frac{w-y}{h}\left(\tau_d - \tau_b\right)\right]^n \tag{4.90}$$

Taking u_b at the glacier boundary ($y = 0$) to be zero, integrating across the flow from $y = 0$ to $y = w$, and then considering only the central trunk of the glacier where lateral shearing is negligible yields (Raymond, 1996; Cuffey and Paterson, 2010):

$$u_b = v_o\left(\tau_d - \tau_b\right)^n \tag{4.91}$$

where:

$$v_o = \frac{2A}{n+1}\left(\frac{w}{h}\right)^n w \tag{4.92}$$

4.10 Notation

a, b	rate-state friction coefficients [-].
a_b	a/b [-].
A	rate factor in Glen's Flow Law [Pa^{-n} s^{-1}].
c_h	characteristic diffusivity of deformable till layer [s^{-1}].
d_c	characteristic slip displacement [m].
d_f	basal slip over time interval t_f [m].
f_n	nominal internal friction of subglacial till [-].
f_c	internal friction of subglacial till [-].
f_*	steady state internal friction of subglacial till at balance velocity [-].
$\mathbf{g}$	gravitational acceleration vector [m s^{-2}].
g	vertical gravitational acceleration [m s^{-2}].
h	ice thickness [m].
h_s	thickness of deformable till layer [m].
k_τ	effective stiffness [Pa m^{-1}].
k_τ^*	critical stiffness [Pa m^{-1}].
ℓ	glacier length [m].
m_w	water mass per unit volume of till [kg m^{-3}].

$\dot{M}$	total mass balance [m s^{-1}].
N	effective pressure [Pa].
n	exponent in Glen's Flow Law [-].
p_c	pressure at depth in ice column [Pa].
p_i	ice overburden pressure [Pa].
p_w	pore water pressure in layer of deforming till [Pa].
p_{w_∞}	pore water pressure in non-deforming substrate [Pa].
p_{w_r}	water pressure in subglacial hydrological system [Pa].
q_w	water flux in the deformable till layer [kg m^{-2} s^{-1}].
$\bar{u}$	depth-averaged speed [m s^{-1}].
u_b	basal slip rate [m s^{-1}].
u_{b_c}	nominal basal slip rate [m s^{-1}].
u_{b*}	balance basal slip rate [m s^{-1}].
u_s	surface speed [m s^{-1}].
u_{s*}	balance surface speed [m s^{-1}].
w	glacier half-width [m].
x, y, z	system coordinates [m].
α	ice surface slope [-].
β	till compressibility [Pa^{-1}].
γ_h	till permeability [m^2].
ϵ_e	elastic compressibility parameter [-].
ϵ_p	plastic dilatancy parameter [-].
$\dot{\varepsilon}_e$	effective strain rate [s^{-1}].
η	ratio of depth-averaged velocity to surface velocity [-].
κ_h	diffusivity of till [m^2 s^{-1}].
Λ	porosity number [-].
λ	friction-dilatancy parameter [-].
μ	stress number [-].
θ	state [s].
ν_w	dynamic viscosity of water [Pa s].
ρ_i	density of ice [kg m^{-3}].

ρ_w	density of water [kg m^{-3}].
$\boldsymbol{\tau}$	deviatoric stress tensor [Pa].
τ_b	basal shear traction [Pa].
τ_d	gravitational driving stress [Pa].
τ_{d*}	balance driving stress [Pa].
$\tilde{\tau}_d$	potential shear traction on the bed [Pa].
τ_e	effective deviatoric stress [Pa].
τ_t	till shear strength [Pa].
τ_y	Mohr-Coulomb yield strength [Pa].
ϕ	till porosity [-].
ϕ_c	nominal till porosity [-].
ϕ_p	plastic component of till porosity [-].
$\hat{\phi}_p$	steady-state plastic till porosity [-].
ψ	fluid transport number [-].
ψ^*	critical fluid transport number [-].
Ω	dilatancy parameter [-].

4.11 Acknowledgments

B.M. was partially funded by a NASA Cyospheric Sciences Award NNX14AH80G and generous donations from the Albert Parvin and ARCS LA Chapter foundations.

Bibliography

J.-P. Ampuero and A. M. Rubin. Earthquake nucleation on rate and state faults – aging and slip laws. *Journal of Geophysical Research: Solid Earth*, 113(B1):n/a–n/a, 2008. ISSN 2156-2202. doi: 10.1029/2007JB005082. B01302.

A. Bevington and L. Copland. Characteristics of the last five surges of Lowell Glacier, Yukon, Canada, since 1948. *Journal of Glaciology*, 60(219):113–123, 2014. doi: 10.3189/2014JoG13J134.

H. Bjornsson. Hydrological characteristics of the drainage system beneath a surging glacier. *Nature*, 395(6704):771–774, 1998. doi: 10.1038/27384.

H. Björnsson, F. Pálsson, O. Sigurðsson, and G. Flowers. Surges of glaciers in Iceland. *Annals of Glaciology*, 36:82–90, 2003. doi: 10.3189/172756403781816365.

M. L. Blanpied, C. J. Marone, D. A. Lockner, J. D. Byerlee, and D. P. King. Quantitative measure of the variation in fault rheology due to fluid-rock interactions. *Journal of Geophysical Research: Solid Earth*, 103(B5):9691–9712, 1998. doi: 10.1029/98JB00162.

H. Blatter. Velocity and stress-fields in grounded glaciers: A simple algorithm for including deviatoric stress gradients. *Journal of Glaciology*, 41(138):333–344, 1995.

G. S. Boulton and R. C. A. Hindmarsh. Sediment deformation beneath glaciers: Rheology and geological consequences. *Journal of Geophysical Research: Solid Earth*, 92(B9):9059–9082, 1987. doi: 10.1029/JB092iB09p09059.

G.S. Boulton, K.E. Dobbie, and S. Zatsepin. Sediment deformation beneath glaciers and its coupling to the subglacial hydraulic system. *Quaternary International*, 86(1):3–28, 2001. doi: doi:10.1016/S1040-6182(01)00048-9.

G. K. C. Clarke. Thermal regulation of glacier surging. *Journal of Glaciology*, 16(74):231–250, 1976.

G. K. C. Clarke, U. Nitsan, and W. S. B. Paterson. Strain heating and creep instability in glaciers and ice sheets. *Reviews of Geophysics and Space Physics*, 15(2):235–247, 1977.

K. M. Cuffey and W. S. B. Paterson. *The Physics of Glaciers*. Elsevier, 4th edition, 2010.

J. H. Dieterich. Modeling of rock friction. Part 1: Experimental results and constitutive equations. *Journal of Geophysical Research*, 84(B5):2161–2168, 1979. doi: 10.1029/JB084iB05p02161.

J. H. Dieterich. Constitutive properties of faults with simulated gouge. In N. L. Carter, M. Friedman, J. M. Logan, and D. W. Stearns, editors, *Mechanical Behavior of Crustal Rocks: The Handin Volume*, pages 103–120. American Geophysical Union, 1981. doi: 10.1029/GM024p0103.

J. H. Dieterich. Applications of rate- and state-dependent friction to models of fault slip and earthquake occurence. In G. Schubert, editor, *Treatise on Geophysics*, pages 107–129. Elsvier, Amsterdam, 2007. doi: 10.1016/B978-044452748-6.00059-6.

J. H. Dieterich and B. D. Kilgore. Direct observations of frictional contacts: New insights for sliding memory effects. *Pure and Applied Geophysics*, 143:283–302, 1994.

T. Dunse, T. Schellenberger, J. O. Hagen, A. Kääb, T. V. Schuler, and C. H. Reijmer. Glacier-surge mechanisms promoted by a hydro-thermodynamic feedback to summer melt. *The Cryosphere*, 9: 197–215, 2015. doi: 10.5194/tc-9-197-2015.

K. Echelmeyer, R. Butterfield, and D. Cuillard. Some observations on a recent surge of Peters Glacier, Alaska, U.S.A. *Journal of Glaciology*, 33(115):341–345, 1987.

O. Eisen, W. D. Harrison, and C. F. Raymond. The surges of Variegated Glacier, Alaska, USA, and their connection of climate and mass balance. *Journal of Glaciology*, 47(158):351–358, 2001.

O. Eisen, W. D. Harrison, C. F. Raymond, K. A. Echelmeyer, G. A. Bender, and J. L. D. Gorda. Variegated Glacier, Alaska, USA: a century of surges. *Journal of Glaciology*, 51(174):399–406, 2005.

G. E. Flowers, N. Roux, S. Pimentel, and C. G. Schoof. Present dynamics and future prognosis of a slowly surging glacier. *The Cryosphere*, 5:299–313, 2011. doi: 10.5194/tc-5-299-2011.

A. C. Fowler. Sliding with cavity formation. *Journal of Glaciology*, 33:255–267, 1987.

A. C. Fowler, T. Murray, and F. S. L. Ng. Thermally controlled glacier surging. *Journal of Glaciology*, 47(159):527–538, 2001.

S. Fuller and T. Murray. Sedimentological investigations in the forefield of an Icelandic surge-type glacier: implications for the surge mechanism. *Quaternary Science Reviews*, 21:1503–1520, 2002.

R. Gladstone, M. Schäfer, T. Zwinger, Y. Gong, T. Strozzi, R. Mottram, F. Boberg, and J. C. Moore. Importance of basal processes in simulations of a surging svalbard outlet glacier. *The Cryosphere*, 8(4):1393–1405, 2014. doi: 10.5194/tc-8-1393-2014.

J. W. Glen. The creep of polycrystalline ice. *Proceedings of the Royal Society of London A*, 228 (1175):519–538, 1955.

W. D. Harrison and A. S. Post. How much do we really know about glacier surging? *Annals of Glaciology*, 36:1–6, 2003.

I. J. Hewitt. Seasonal changes in ice sheet motion due to melt water lubrication. *Earth and Planetary Science Letters*, 371–372:16–25, 2013. doi: 10.1016/j.epsl.2013.04.022.

R. LeB. Hooke. *Principles of Glacier Mechanics*. Cambridge University Press, New York, NY, second edition, 2005.

N. R. Iverson. Shear resistance and continuity of subglacial till: hydrology rules. *Jounal of Glaciology*, 56(200):1104–1114, 2010. doi: 10.3189/002214311796406220.

N. R. Iverson and R. M. Iverson. Distributed shear of subglacial till due to Coulomb slip. *Journal of Glaciology*, 47(158):481–488, 2001.

N. R. Iverson, T. S. Hooyer, and R. W. Baker. Ring-shear studies of till deformation: Coulomb plastic behavior and distributed strain in glacier beds. *Jounal of Glaciology*, 44:634–642, 1998.

M. Jay-Allemand, F. Gillet-Chaulet, O. Gagliardini, and M. Nodet. Investigating changes in basal conditions of variegated glacier prior to and during its 1982–1983 surge. *The Cryosphere*, 5(3): 659–672, 2011. doi: 10.5194/tc-5-659-2011.

H. Jiskooot, P. Boyle, and T. Murray. The incidence of glacier surging in Svalbard: evidence from multivariate statistics. *Computational Geoscience*, 24(4):387–399, 1998.

H. Jiskoot, T. Murray, and P. Boyle. Controls on the distribution of surge-type glaciers in Svalbard. *Journal of Glaciology*, 46(154):412–422, 2000.

B. Kamb. Sliding motion of glaciers: theory and observations. *Reviews of Geophysics*, 8(4):673–728, 1970.

B. Kamb. Glacier surge mechanisms based on linked cavity configuration of the basal water conduit system. *Journal of Geophysical Research*, 92(B9):9083–9100, 1987.

B. Kamb. Rheological nonlinearity and flow instability in the deforming-bed mechanism of ice stream motion. *Journal of Geophysical Research: Solid Earth*, 96(B10):16585–16595, 1991. doi: 10.1029/91JB00946.

B. Kamb, C. F. Raymond, W. D. Harrison, H. Engelhardt, K. A. Echelmeyer, N. Humphrey, M. M. Brugman, and T. Pfeffer. Glacier surge mechanism: 1982-1983 surge of variegated glacier, alaska. *Science*, 227(4686):469–479, 1985. doi: 10.1126/science.227.4686.469.

B. D. Kilgore, J. H. Dieterich, and M. L. Blanpied. Velocity dependent friction of granite over a wide range of conditions. *Geophysical Research Letters*, 20(10):903–906, 1993. doi: 10.1029/93GL00368.

T. W. Lambe and R. V. Whitman. *Soil Mechanics*. Wiley, New York, NY, 1969.

L. Lliboutry. General theory of subglacial cavitation and sliding of temperate glaciers. *Journal of Glaciology*, 7(49):21–58, 1968.

D. MacAyeal. Large-scale ice flow over a viscous basal sediment - Theory and application to ice stream-B, Antarctica. *Journal of Geophysical Research*, 94(B4):4071–4087, 1989.

M. F. Meier and A. Post. What are glacier surges? *Canadian Journal of Earth Sciences*, 6(4): 807–817, 1969.

B. M. Minchew, M. Simons, M. Morlighem, H. Björnsson, F. Pálsson, S. Hensley, and E. Larour. Plastic bed beneath Hofsjökull Ice Cap, central Iceland, and the sensitivity of ice flow to surface meltwater flux. *Journal of Glaciology*, in press, 2016.

P. L. Moore and N. R. Iverson. Slow episodic shear of granular materials regulated by dilatant strengthening. *Geology*, 30(9):843–846, 2002. doi: 10.1130/0091-7613(2002)030<0843:SESOGM>2.0.CO;2.

T. Murray, G. W. Stuart, P. J. Miller, J. Woodward, A. M. Smith, P. R. Porter, and H. Jiskoot. Glacier surge propagation by thermal evolution at the bed. *Journal of Geophysical Research: Solid Earth*, 105(B6):13491–13507, 2000. doi: 10.1029/2000JB900066.

T. Murray, T. Strozzi, A. Luckman, H. Jiskoot, and P. Christakos. Is there a single surge mechanism? Contrasts in dynamics between glacier surges in Svalbard and other regions. *Journal of Geophysical Research*, 108(B5):1–15, 2003. doi: 10.1029/2002JB001906. 2237.

F. Pattyn. A new three-dimensional higher-order thermomechanical ice sheet model: Basic sensitivity, ice stream development, and ice flow across subglacial lakes. *Journal of Geophysical Research: Solid Earth*, 108(B8):1–15, 2003. doi: 10.1029/2002JB002329.

A. Post. Distribution of surging glaciers in western North America. *Journal of Glaciology*, 8(53): 229–240, 1969.

A. P. Rathbun, C. Marone, R. B. Alley, and S. Anandakrishnan. Laboratory study of the frictional rheology of sheared till. *Journal of Geophysical Research*, 113(F2):1–14, 2008. doi: 10.1029/2007JF000815. F02020.

C. Raymond. How do glaciers surge? A review. *Journal of Geophysical Research*, 92(B9):9121–9134, 1987. doi: 10.1029/JB092iB09p09121.

C. Raymond. Shear margins in glaciers and ice sheets. *Journal of Glaciology*, 42(140):90–102, 1996.

C. F. Raymond and W. D. Harrison. Evolution of Varigated Glacier, Alaska, U.S.A., prior to its surge. *Journal of Glaciology*, 34(117):154–169, 1988.

G. de Q. Robin. Ice movement and temperature distribution in glaciers and ice sheets. *Journal of Glaciology*, 2(18):523–532, 1955.

J. J. Roush, C. G. Lingle, R. M. Guritz, D. R. Fatland, and V. A. Voronina. Surge-front propagation and velocities during the early 1993–1995 surge of Bering Glacier, Alaska, U.S.A., from sequential SAR imagery. *Annals of Glaciology*, 36:37–44, 2003.

A. Ruina. Slip instability and state variable friction laws. *Journal of Geophysical Research*, 88 (B12):10359–10370, 1983. doi: 10.1029/JB088iB12p10359.

C. Schoof. The effect of cavitation on glacier sliding. *Proceeding of the Royal Society of London. Series A, Mathematical and Physical Sciences*, 461:609–627, 2005. doi: 10.1098/rspa.2004.1350.

C. Schoof. Ice-sheet accerleration driven by melt supply variability. *Nature*, 468(7325):803–806, 2010. doi: 10.1038/nature09618.

P. Segall and J. R. Rice. Dilatancy, compaction, and slip instability of a fluid-infiltrated fault. *Journal of Geophysical Research*, 100(B11):22155–22171, 1995. doi: 10.1029/95JB02403.

P. Segall and J. R. Rice. Does shear heating of pore fluid contribute to earthquake nucleation? *Journal of Geophysical Research*, 111(B09316):1–17, 2006. doi: 10.1029/2005JB004129.

P. Segall, A. M. Rubin, A. M. Bradley, and J. R. Rice. Dilatant strengthening as a mechanism for slow slip events. *Journal of Geophysical Research*, 115(B12305):1–37, 2010. doi: 10.1029/2010JB007449.

M. Sund, T. R. Lauknes, and T. Eiken. Surge dynamics in the Nathorstbreen glacier system, Svalbard. *The Cryosphere*, 8:623–638, 2014.

J. F. Thomason and N. R. Iverson. A laboratory study of particle ploughing and pore-pressure feedback: a velocity-weakening mechanism for soft glacier beds. *Journal of Glaciology*, 54 (184):169–181, 2008. doi: 10.3189/002214308784409008.

M. Truffer, W. D. Harrison, and K. A. Echelmeyer. Glacier motion dominated by processes deep in underlying till. *Journal of Glaciology*, 46(153):213–221, 2000. doi: 10.3189/172756500781832909.

V. C. Tsai, A. L. Stewart, and A. F. Thompson. Marine ice-sheet profiles and stability under coulomb basal conditions. *Journal of Glaciology*, 61(226):205–215, 2015. doi: 10.3189/2015JoG14J221.

S. Tulaczyk, W. B. Kamb, and H. F. Engelhardt. Basal mechanics of Ice Stream B, west Antarctica: 1. Till mechanics. *Journal of Geophysical Research: Solid Earth*, 105(B1):463–481, 2000a. doi: 10.1029/1999JB900329.

S. Tulaczyk, W. B. Kamb, and H. F. Engelhardt. Basal mechanics of Ice Stream B, west Antarctica: 2. Undrained plastic bed model. *Journal of Geophysical Research: Solid Earth*, 105(B1):483–494, 2000b. doi: 10.1029/1999JB900328.

C. J. Van der Veen. *Fundamentals of glacier dynamics*. CRC Press, 2013.

Joseph Walder and Amos Nur. Porosity reduction and crustal pore pressure development. *Journal of Geophysical Research: Solid Earth*, 89(B13):11539–11548, 1984. doi: 10.1029/JB089iB13p11539.

M. A. Werder, I. J. Hewitt, C. G. Schoof, and G. E. Flowers. Modeling channelized and distributed subglacial drainage in two dimensions. *Journal of Geophysical Research: Earth Surface*, 118(4): 2140–2158, 2013. doi: 10.1002/jgrf.20146.

J. Woodward, T. Murray, R. A. Clark, and G. W. Stuart. Glacier surge mechanisms inferred from ground-penetrating radar: Kongsvegen, Svalbard. *Journal of Glaciology*, 49(167):473–480, 2003. doi: 10.3189/172756503781830458.

L. K. Zoet, B. Carpenter, M. Scuderi, R. B. Alley, S. Anandakrishnan, C. Marone, and M. Jackson. The effects of entrained debris on the basal sliding stability of a glacier. *Journal of Geophysical Research: Earth Surface*, 118(2):656–666, 2013. doi: 10.1002/jgrf.20052.

Chapter 5

Tidally induced flow variations in Rutford Ice Stream, West Antarctica, inferred from continuous synthetic aperture radar observations

5.1 Abstract

We develop a method for inferring 3D surface velocity field time series, hereafter called 4D velocity fields, from continuous synthetic aperture radar (SAR) and, optionally, optical remotely sensed observations of glaciers. We focus on the special case where ice flow at a given point can be described as the sum of a 3D secular velocity and a family of 3D sinusoidal functions, including in the methodological development the capability to estimate corrections to the digital elevation model (DEM) used during processing of SAR data. Through synthetic tests designed to resemble our study area as closely as possible, we show that our method for inferring 4D velocity fields produces results accurate to within 10% for the two primary observable vertical tidal constituents, and the longer period of horizontal flow variability. We examine 4D velocity fields inferred from SAR data collected from the COSMO-SkyMed SAR satellite constellation over a 9-month period beginning in August 2013. The results indicate that the response of horizontal ice flow to ocean tidal forcing is most pronounced over the ice shelf and subsequently propagates through the grounded ice stream at an approximate mean rate of 29 km/day, decaying quasi-linearly with distance over ~ 85 km upstream of the grounding zone. We observe multiple regions over the ice shelf whose motion is consistent with subglacial pinning points, which provide a potential explanation for observed variations in horizontal ice flow. Cross-flow profiles of horizontal ice flow taken upstream of the

grounding zone indicate that ice in the shear margins is weak relative to the central ice stream trunk, allowing for the possibility that buttressing stresses from the ice shelf are transmitted upstream through the ice column and are damped from a combination of basal shear traction and shearing in the margins.

5.2 Introduction

The mechanics of ice flow and of glacier beds, hereafter called basal mechanics, impose fundamental constraints on glacier flow and help set the timescales of ice sheet collapse (Echelmeyer et al., 1994; Schoof, 2007; Tsai et al., 2015). Despite their importance, neither the mechanics of ice flow nor basal mechanics are well understood, hindering the development of plausible models of future glacier states. We can improve our understanding of basal mechanics through a variety of observational and modeling approaches, among them using synoptic-scale observations of surface velocities as constraints on numerical ice flow models (e.g., MacAyeal, 1992, 1993; Joughin et al., 2003, 2004, 2009; Morlighem et al., 2010, 2013; Minchew et al., 2016). This approach has been developed and employed over the past decades using available surface velocity data attained from synthetic aperture radar (SAR) and optical data (e.g. MacAyeal, 1992; Goldstein et al., 1993; Rignot, 1998; Rignot et al., 2004, 2011a; Rott et al., 2002; Joughin et al., 2003, 2004, 2009). These velocity fields are typically either available for only one or a few points in time (e.g., Minchew et al., 2015) or aggregate data collected at multiple times (e.g., Rignot et al., 2011a), limiting our ability to study the spatial dimensions and mechanisms of known temporal variations in glacier flow (e.g., Anandakrishnan et al., 2003; Gudmundsson, 2006). Observing and understanding how ice flow changes over a variety of timescales in response to internal instabilities and environmental forcing is crucial for constraining the set of viable mechanical models for the bed and ascertaining physically justifiable, observationally tested constitutive relations for ice flow and deformable beds. An important goal in the ongoing development of geodetic techniques is then to capture synoptic-scale, time-dependent glacier flow characteristics.

Glacier flow responds to hourly timescale forcings, such as changes in basal water pressure caused by surface meltwater flux; seasonal timescale forcings, such as retreat and advance of calving front positions; and multi-annual timescale changes in glacier geometry (e.g., Weertman, 1957; Fowler, 1987; Kamb, 1987; Sugiyama and Gudmundsson, 2004). Basal mechanics can play a leading role in altering glacier flow at all timescales, but short-timescale variations provide opportunities for extensive observations. Remotely sensed radar and optical observations have proven among the most useful for spatially extensive studies of glacier dynamics but satellite orbits and limitations on range and flight duration of airborne platforms restrict the frequencies of phenomena that can be observed.

Tidal-timescales are optimal for existing and planned remote sensing platforms because tidally induced ice flow variations are primarily of order two weeks in some observed Antarctic ice streams (e.g. Murray et al., 2007; Gudmundsson, 2011). Two weeks is an advantageous timescale for synoptic-scale studies because it is long enough to be adequately sampled by some remote-sensing platforms and short enough to allow for observations of multiple cycles within a reasonable study period. On the West Antarctic Ice Sheet, horizontal flow in some ice streams responds to tidal forcing, with ice velocities varying by as much as 20% over the dominant spring-neap (14.77-day) tidal cycle (e.g., Gudmundsson, 2006; Murray et al., 2007; Aðalgeirsdóttir et al., 2008; Gudmundsson, 2011). Here we use spatially and temporally dense synthetic aperture radar (SAR) observations of Rutford Ice Stream, West Antarctica, to study the upstream extent and spatial properties of tidally induced ice flow variability.

SAR data can be used to calculate ice motion along a path parallel to the instrument velocity vector (azimuth direction) and along the radar line-of-sight (LOS), the latter being oblique relative to vertical and typically orthogonal to the instrument velocity vector. In both cases, estimates of displacement are attainable using absolute or relative positions. Absolute displacement observations are often calculated by applying 2D cross correlation to processed radar scenes, a method widely known as speckle tracking when applied to complex SAR data and feature tracking when applied to SAR amplitude or optical images (Joughin, 2002; Bamler and Eineder, 2005). Relative displacements can be calculated using interferometric methods, namely repeat-pass interferometric SAR (InSAR) for LOS displacements (Rosen et al., 2000) and multi-aperture interferometry (MAI) for azimuth displacements (Bechor and Zebker, 2006). Absolute and relative methods each have unique advantages with the primary tradeoffs being between precision, spatial resolution, and robustness: relative position methods, such as InSAR, are more precise and generally offer higher spatial resolution (Rosen et al., 2000; Simons and Rosen, 2015) while absolute methods, like feature- or speckle-tracing, are more robust to large displacements, minor changes in target scattering properties, and in certain terrain types where InSAR methods yield low signal-to-noise ratios (SNR) (Gray et al., 2001; Joughin, 2002). For many applications, judicious use of both absolute and relative methods for inferring motion from SAR data maximizes the amount of spatiotemporal information that can be gleaned from a set of observations.

Here we develop a method for inferring 3D, time-dependent velocity fields (hereafter called 4D velocity fields) and apply it to SAR data collected over Rutford in order to elucidate the spatially heterogenous response of the ice stream to tidal forcing. Our method for inferring 4D velocity fields is independent of the approach used to calculate displacements and relies only on having three or more unique observation vectors and an appropriate time sampling given the desired form of the output model. In developing the method, we assume the data are appropriately sampled in all three spatial dimensions and have sufficient sampling rates and durations to avoid aliasing the specified temporal basis functions. We demonstrate and validate our method on a synthetic ice stream designed to resemble Rutford, including all known temporal variabilities in vertical and horizontal ice flow. We also use this example to explore the model components and error metrics. We then apply our method to data collected over Rutford with the Constellation of Small Satellites for Mediterranean basin Observation (CSK, a.k.a. COSMO-SkyMed). Data were collected continuously for approximately 9 months along 32 unique satellite tracks. We calculated 2D displacements using speckle-tracking methods for all scene pairs collected within 10 days of one another. This approach yielded more than 3000 displacement fields, of which 1486 have acceptable SNR. All 1486 usable displacement fields are included in the Rutford velocity fields presented here.

5.3 Methodology

5.3.1 Time-dependent displacement

In the most general case, observed displacements can be described as a sum of a secular velocity and numerous periodic and transient terms (e.g. Hetland et al., 2012). Here, we are primarily interested in the influence of ocean tides on ice stream flow, so we consider the special case where the instantaneous displacement, f, along an observational unit vector $\hat{\boldsymbol{\ell}}$ of a point on the surface at time t and location $\mathbf{r}$, relative to the observer, is a function of a mean, time-invariant velocity $\mathbf{v}$ and a family of sinusoidal functions such that:

$$f(\hat{\boldsymbol{\ell}}, \mathbf{r}, t) = \hat{\boldsymbol{\ell}} \cdot \left(\mathbf{v}t + \sum_{i=1}^{k} \mathbf{p}_i \right) \tag{5.1}$$

where $\hat{\boldsymbol{\ell}}$ is equal to the LOS or the ground-track velocity unit vector, as appropriate, and the vector of periodic functions is defined as:

$$\mathbf{p}_i(\mathbf{r}, t) = \begin{bmatrix} a_i^e \sin\left(\omega_i t + \phi_i^e\right) \\ a_i^n \sin\left(\omega_i t + \phi_i^n\right) \\ a_i^u \sin\left(\omega_i t + \phi_i^u\right) \end{bmatrix} \tag{5.2}$$

Each periodic function i has angular frequency ω_i, amplitude $a_i^\zeta = a_i^\zeta(\mathbf{r})$, and phase $\phi_i^\zeta = \phi_i^\zeta(\mathbf{r})$ for $\zeta = e, n, u$, representing three mutually orthogonal coordinate directions, hereafter taken to be east, north, and up, respectively. In formulating Eq. 5.1, we have assumed that all data are referenced to areas with zero displacement. Note that we designate all vectors with bold font and unit vectors with hats.

Using SAR or optical images, we can estimate the displacement of a target over some time interval. Measurements of displacement contain noise that we separate into baseline errors for LOS displacements (see Rosen et al., 2000) and other noise. Accounting for noise, the measured displacement of the target relative to the observer over the time interval [t_a, t_b] is then:

$$d_{ab}(\hat{\boldsymbol{\ell}}, \mathbf{r}, t_a, t_b) = f_a - f_b + b_{ab} + \epsilon_{ab} \tag{5.3}$$

where b_{ab} represents baseline errors, ϵ_{ab} accounts for all other noise factors, and $f_\xi = f(\mathbf{r}, t_\xi)$ for $\xi = a, b$. For repeat observations where the platform follows or is processed to lie along approximately the same path, we take $\hat{\boldsymbol{\ell}}$ to be constant for two SAR acquisitions yielding:

$$f_a - f_b = \hat{\boldsymbol{\ell}} \cdot \left\{ \mathbf{v}(t_b - t_a) + \sum_{i=1}^{k} \left[\mathbf{p}_i(t_b) - \mathbf{p}_i(t_a) \right] \right\} \tag{5.4}$$

Later we employ matrix-based inverse methods to infer the 4D velocity field, so we apply a basic trigonometric identity to rewrite Eq. 5.4 as:

$$f_a - f_b = \hat{\boldsymbol{\ell}} \cdot \left[\mathbf{v} \Delta^t_{ab} + \sum_{i=1}^{k} \left(\mathbf{c}_i \Delta^c_{i_{ab}} + \mathbf{s}_i \Delta^s_{i_{ab}} \right) \right] \tag{5.5}$$

$$\Delta^t_{ab} = t_b - t_a \tag{5.6}$$

$$\Delta^c_{i_{ab}} = \cos(\omega_i t_b) - \cos(\omega_i t_a) \tag{5.7}$$

$$\Delta^s_{i_{ab}} = \sin(\omega_i t_b) - \sin(\omega_i t_a) \tag{5.8}$$

$$\mathbf{c}_i = \begin{bmatrix} a^e_i \sin(\phi^e_i) & a^n_i \sin(\phi^n_i) & a^u_i \sin(\phi^u_i) \end{bmatrix}^T \tag{5.9}$$

$$\mathbf{s}_i = \begin{bmatrix} a^e_i \cos(\phi^e_i) & a^n_i \cos(\phi^n_i) & a^u_i \cos(\phi^u_i) \end{bmatrix}^T \tag{5.10}$$

After inferring the components of $\mathbf{c}_i$ and $\mathbf{s}_i$ using the approach described later, it is desirable to recover the physically intuitive amplitude and phase for each periodic function by recognizing:

$$a^\zeta_i = \sqrt{(c^\zeta_i)^2 + (s^\zeta_i)^2} \tag{5.11}$$

$$\phi^\zeta_i = \tan^{-1}\left(c^\zeta_i / s^\zeta_i \right) \tag{5.12}$$

If displacement data were collected with a SAR instrument, it may be possible to glean additional information about the local time-invariant topographic residuals because observations collected along the radar LOS are sensitive to topography. The topographic signal component is commonly accounted for during processing using an independently derived digital elevation model (DEM) (e.g., Rosen et al., 2000). When the DEM is known but is expected to have errors or is lower resolution than the SAR data, it may be desirable to estimate residual topographic signals along with the velocity fields. Residual topography, z_d, contributes to the SAR deformation measurements as:

$$b_{ab} = \psi_{ab} z_d \tag{5.13}$$

$$\psi_{ab} = \begin{cases} B_{\perp_{ab}} / (r_0 \sin\theta_0) & \text{along LOS} \\ 0 & \text{otherwise} \end{cases} \tag{5.14}$$

where $B_{\perp_{ab}}$ is the perpendicular baseline, and r_0 and θ_0 are the range and incidence angle—measured relative to local up—to a smooth reference surface, respectively (Rosen et al., 2000; Simons and Rosen, 2015).

When considering whether to attempt to estimate residual topographic signals, it is important to consider the total error and error components in z_d. From Eq. 5.13, the error in residual topographic signals is given as:

$$\sigma_{z_d}^2 = \left(\frac{\partial z_d}{\partial b_{ab}}\right)^2 \sigma_{b_{ab}}^2 + \left(\frac{\partial z_d}{\partial B_{\perp_{ab}}}\right)^2 \sigma_{B_{\perp_{ab}}}^2 + \left(\frac{\partial z_d}{\partial r_0}\right)^2 \sigma_{r_0}^2 + \left(\frac{\partial z_d}{\partial \theta_0}\right)^2 \sigma_{\theta_0}^2 \tag{5.15}$$

To illustrate the sensitivity of z_d to measurement noise, let us assume accurate orbital positions such that $\sigma_{B_{\perp_{ab}}}^2 \approx \sigma_{r_0}^2 \approx \sigma_{\theta_0}^2 \approx 0$. This assumptions simplifies Eq. 5.15 such that:

$$\sigma_{z_d} \approx \frac{r_0 \sin \theta_0}{B_{\perp_{ab}}} \sigma_{b_{ab}} \tag{5.16}$$

where, from Eq. 5.3, we have:

$$\begin{aligned} \sigma_{b_{ab}}^2 &= \left(\frac{\partial b_{ab}}{\partial d_{ab}}\right)^2 \sigma_{d_{ab}}^2 + \left(\frac{\partial b_{ab}}{\partial \Delta_{ab}^f}\right)^2 \sigma_{\Delta_{ab}^f}^2 + \left(\frac{\partial b_{ab}}{\partial \epsilon_{ab}}\right)^2 \sigma_{\epsilon_{ab}}^2 \\ &= \left(\Delta_{ab}^f + \epsilon_{ab}\right)^2 \sigma_d^2 + (d_{ab} - \epsilon_{ab})^2 \sigma_{\Delta_{ab}^f}^2 + \left(d_{ab} - \Delta_{ab}^f\right)^2 \sigma_{\epsilon_{ab}}^2 \end{aligned} \tag{5.17}$$

where $\Delta_{ab}^f = f_a - f_b$ (Eq. 5.4). SAR systems always have oblique LOS geometries such that $20° < \theta_0 < 65°$ and their flight paths are constrained to minimize $B_{\perp_{ab}}/r_0$ so that InSAR measurements are more sensitive to target motion than to topography. Therefore, for spaceborne and airborne SAR platforms, $r_0 \sin \theta_0 / B_{\perp_{ab}} \sim 10^3$–$10^4$ (Rosen et al., 2000; Hensley et al., 2009a,b). To ensure meter-scale precision in estimates of residual topographic signals, it is necessary that $\sigma_{b_{ab}} \lesssim 10^{-3}$ m. This condition is likely to be met only when the signal-to-noise ratio (SNR) is high ($\epsilon_{ab} \ll \Delta_{ab}^f + b_{ab}$; Eq. 5.3), where the form of Δ_{ab}^f is well constrained, and where the data allow for accurate estimates of Δ_{ab}^f. For the foreseeable future, the SNR condition necessitates coherent InSAR data for fine resolution estimates of topographic residuals, excluding many LOS displacement measurements taken from speckle or feature tracking methods, especially for large Δ_{ab}^t in areas with rapid displacement rates (Bamler and Eineder, 2005). If relatively coarse resolution estimates of topographic residuals are acceptable, we can filter inferred z_d values to reduce ϵ_{ab} by a factor $\sqrt{N_f}$, where N_f is the number of pixels in the filter window. This will give accurate estimates of long-wavelength residual topography from LOS displacements when the instrument resolution is sufficiently fine and the displacements are calculated on a sufficiently tight grid to allow for large N_f while maintaining acceptable spatial resolution.

5.3.2 4D displacement model

To infer solutions at each grid point in the 4D velocity field, we cast the problem in a general matrix form:

$$\mathbf{G}\mathbf{m} = \mathbf{d} \tag{5.18}$$

where $\mathbf{d}$ is the vector of observed displacements, $\mathbf{m}$ is the model vector, and $\mathbf{G}$ is the design matrix. For any given grid location, the model vector has the form:

$$\mathbf{m} = \begin{bmatrix} \mathbf{v} & \mathbf{c}_1 & \mathbf{s}_1 & \cdots & \mathbf{c}_k & \mathbf{s}_k & \{z_d\} \end{bmatrix}^T \tag{5.19}$$

for k periodic functions, and a corresponding design matrix for q pairs given as:

$$\mathbf{G} = \begin{bmatrix} \hat{\boldsymbol{\ell}}_1 \Delta_1^t & \hat{\boldsymbol{\ell}}_1 \Delta_{1_1}^c & \hat{\boldsymbol{\ell}}_1 \Delta_{1_1}^s & \cdots & \hat{\boldsymbol{\ell}}_1 \Delta_{k_1}^c & \hat{\boldsymbol{\ell}}_1 \Delta_{k_1}^s & \{\psi_1\} \\ \vdots & & & \ddots & & & \vdots \\ \hat{\boldsymbol{\ell}}_q \Delta_q^t & \hat{\boldsymbol{\ell}}_q \Delta_{1_q}^c & \hat{\boldsymbol{\ell}}_q \Delta_{1_q}^s & \cdots & \hat{\boldsymbol{\ell}}_q \Delta_{k_q}^c & \hat{\boldsymbol{\ell}}_q \Delta_{k_q}^s & \{\psi_q\} \end{bmatrix} \tag{5.20}$$

where $\{\cdot\}$ represents the optional elements needed for topographic residual estimation. Note that we number ab pairs from 1 to q in Eq. 5.20 and omit the transpose sign on the interior vectors in Eqs. 5.19 and 5.20 for clarity.

Following Minchew et al. (2015), who applied Bayesian methods described by Tarantola (2005) to the problem of inferring 3D velocity fields using InSAR data collected from multiple LOS vectors, we can write the posterior model vector $\widetilde{\mathbf{m}}$, *i.e.* the best-fit solution to Eq. 5.18, in its most general form as:

$$\widetilde{\mathbf{m}} = \left(\mathbf{G}^T \mathbf{C}_d^{-1} \mathbf{G} + \mathbf{C}_m^{-1}\right)^{-1} \left(\mathbf{G}^T \mathbf{C}_d^{-1} \mathbf{d} + \mathbf{C}_m^{-1} \mathbf{m}_0\right) \tag{5.21}$$

where $\mathbf{m}_0$ is the prior model vector and $\mathbf{C}_d$ and $\mathbf{C}_m$ are the data and prior model covariance matrices, respectively (Tarantola, 2005). The data covariance matrix, $\mathbf{C}_d$, accounts for errors and interdependencies of the displacement measurements while the prior model covariance matrix, $\mathbf{C}_m$, accounts for *a priori* assumptions of the model parameters, their inter-dependencies and, possibly, the spatial characteristics of the model. The form of $\mathbf{C}_d$ is based on the characteristics of the data (as discussed in §5.3.3), whereas the form of $\mathbf{C}_m$ should be chosen based on the physical processes under consideration.

There are a number of valid options for the form of $\mathbf{C}_m$. One option is to impose spatial smoothness in the velocity field, an approach that can incur high computational costs because all model parameters within areas of interest must be inferred simultaneously (Minchew et al., 2015). Our experience with the data presented here indicated that spatial smoothing is unnecessary. Instead, we found that there can be tradeoffs between the sinusoidal amplitudes and phases when multiple periodic functions are included in the posterior. GPS data collected in our study area (e.g. Murray et al., 2007) and physical intuition of ice flow tell us that variations in horizontal ice flow occur over fortnightly and longer periods while vertical motion occurs primarily at semi-diurnal and diurnal periods. Therefore, we adopt a form for $\mathbf{C}_m$ that penalizes nonzero amplitudes for sinusoids with periods shorter than a reference period in the horizontal components of $\widetilde{\mathbf{m}}$ and sinusoids with periods longer than a reference in the vertical components of $\widetilde{\mathbf{m}}$. This form of $\mathbf{C}_m$ is diagonal and defined as:

$$\begin{aligned}
\mathbf{C}_m^{-1} &= \operatorname{diag}\Big[\ 0 \quad 0 \quad 0 \quad \Omega_1^h \quad \Omega_1^h \quad \Omega_1^v \quad \cdots \quad \Omega_k^h \quad \Omega_k^h \quad \Omega_k^v \quad \{0\}\ \Big] && (5.22)\\
\Omega_i^h &= \kappa_p\left(\frac{\omega_i}{\omega_{ref}^h} - 1\right)^2 && (5.23)\\
\Omega_i^v &= \kappa_p\left(\frac{\omega_{ref}^v}{\omega_i} - 1\right)^2 && (5.24)
\end{aligned}$$

where κ_p is a scalar weighting parameter whose units are assigned so that the units of $\mathbf{C}_m^{-1}$ match those of $\mathbf{G}^T\mathbf{C}_d^{-1}\mathbf{G}$ and ω_{ref}^h and ω_{ref}^u are the reference angular frequencies for horizontal and vertical periodic functions, respectively. Nonzero elements of $\mathbf{C}_m^{-1}$ correspond to elements of $\widetilde{\mathbf{m}}$ that we expect to be small, so it follows that $\mathbf{C}_m^{-1}\mathbf{m}_0 \ll \mathbf{G}^T\mathbf{C}_d^{-1}\mathbf{d}$, reducing Eq. 5.21 to a form similar to Tikhonov regularized least squares.

5.3.3 Formal error estimation

The first term in Eq. 5.21 is the posterior model covariance matrix:

$$\widetilde{\mathbf{C}}_m = \left(\mathbf{G}^T\mathbf{C}_d^{-1}\mathbf{G} + \mathbf{C}_m^{-1}\right)^{-1} \tag{5.25}$$

which provides estimates of the formal errors in $\widetilde{\mathbf{m}}$ (Tarantola, 2005). Elements along the diagonal are the variances for each component of $\widetilde{\mathbf{m}}$, while off-diagonal elements provide the covariances between model parameters. As a result, higher amplitudes in the components of $\widetilde{\mathbf{C}}_m$ indicate higher uncertainty in $\widetilde{\mathbf{m}}$. One way to encapsulate the error of the posterior model is to consider:

$$\Lambda_m = \sqrt{\mathrm{tr}[\widetilde{\mathbf{C}}_m]} \tag{5.26}$$

where tr is the trace operator. Note that the tradeoff inherent in the summation is that the lumped variance parameter Λ_m represents the total error, thereby providing a convenient error metric that yields no information about each component's individual error contribution.

In some cases, particularly for the purposes of observational planning, it is advantageous to estimate only the contribution of non-ideal viewing geometries to uncertainty in the posterior model. A set of ideal viewing geometries has consistent, oblique incidence angles, full azimuthal coverage, and constant azimuthal spacing between platform velocity vectors (Minchew et al., 2015). These conditions are rarely achievable in practice because of orbital or funding constraints. Estimates of the uncertainty attributable to non-ideal viewing geometries are contained in the noise-sensitivity matrix:

$$\mathbf{S} = \left(\mathbf{G}^T\mathbf{G}\right)^{-1} \tag{5.27}$$

The diagonal terms of $\mathbf{S}^{-1}$ are the sums of the squares of the displacement components contained in the design matrix and the off-diagonal terms are the sums of the cross products of the components. The off-diagonal components of $\mathbf{S}^{-1}$ indicate coupling between respective posterior model constituents that results from a non-ideal set of viewing geometries while the diagonal components quantify how measurement errors propagate into the components of $\widetilde{\mathbf{m}}$. When the viewing geometry is ideal, each diagonal component in $\mathbf{S}$ is simply the inverse of the respective diagonal component in $\mathbf{G}^T\mathbf{G}$. When the viewing geometry is non-ideal, off-diagonal components in $\mathbf{S}^{-1}$ contribute to the diagonal components through the adjugate and determinant of $\mathbf{S}^{-1}$. Differential incidence angles, inconsistent azimuthal spacing, or incomplete azimuthal coverage in the viewing geometries all lead to non-zero off-diagonal components in $\mathbf{S}^{-1}$ and increased sensitivity to measurement noise. We can characterize the contribution of the LOS geometry to the model uncertainty with the lumped geometric deviation parameter:

$$\Lambda_g = \sqrt{\mathrm{tr}[\mathbf{S}]} \tag{5.28}$$

which provides a single metric for multiplicative propagation of measurement noise into the posterior model (Minchew et al., 2015). Readers familiar with GPS analysis will recognize Λ_g as the position dilution of precision (PDOP), the spatial component of the geometric dilution of precision

(GDOP) (e.g., Misra and Enge, 2006). The fundamental difference between Λ_g and Λ_m is the lack of accounting for $\mathbf{C}_d$ and $\mathbf{C}_m$ in the former.

In general, the data covariance matrix, $\mathbf{C}_d$, can have contributions from atmospheric phase delay (e.g., Hanssen, 2001; Emardson et al., 2003; Lohman and Simons, 2005), interferometric decorrelation (e.g., Rodriguez and Martin, 1992; Hanssen, 2001; Zebker and Villasenor, 1992), and spatial dependences within the displacement data. In practice, it is often difficult to estimate atmospheric phase delay and spatial dependencies in the data in the geographic regions of interest in this study. For this reason and for simplicity and computational tractability, we assume that the data covariance matrix is diagonal such that:

$$C_{d_{ij}} = \begin{cases} \sigma^2_{d_i} & i = j \\ 0 & i \neq j \end{cases} \tag{5.29}$$

where $\sigma^2_{d_i}$ is the variance of displacement field i. For InSAR data, the variance can be estimated from the standard InSAR correlation γ using the Cramer-Rao bound (Rodriguez and Martin, 1992):

$$\sigma^2_{d_i} = \frac{\lambda}{4\pi N_{f_i}} \frac{1 - \gamma_i^2}{\gamma_i^2} \tag{5.30}$$

where λ is the radar wavelength and N_{f_i} is the number of pixels in the filtering window applied to displacement field i. The interferometric correlation γ_i is defined as (e.g., Rosen et al., 2000):

$$\gamma_i = \frac{|\langle s_a s_b^* \rangle|_i}{\sqrt{\langle s_a s_a^* \rangle_i \langle s_b s_b^* \rangle_i}} \tag{5.31}$$

where $0 \leq \gamma_i \leq 1$, s_ξ is the complex scattered signal in SAR image ξ, s_ξ^* is the corresponding complex conjugate, and $\langle \cdot \rangle$ indicates averaging over N_{f_i} realizations of the argument. Variances for displacements calculated using feature or speckle tracking can be estimated from the curvature of the correlation surface (Joughin, 2002).

Given the form of the design matrix $\mathbf{G}$, phase and amplitude errors are implicit in the posterior model covariance matrix $\widetilde{\mathbf{C}}_m$ while errors for the components of $\mathbf{c}_i$ and $\mathbf{s}_i$ are explicit. We need phase and amplitude errors to go with phase and amplitude outputs. To derive errors for amplitude and phase, let us first write the errors for the components of $\mathbf{c}_i$ and $\mathbf{s}_i$ as functions of amplitude and phase errors:

$$\begin{aligned} \sigma^2_{c_i^\zeta} &= \left(\frac{\partial c_i^\zeta}{\partial a_i^\zeta}\right)^2 \sigma^2_{a_i^\zeta} + \left(\frac{\partial c_i^\zeta}{\partial \phi_i^\zeta}\right)^2 \sigma^2_{\phi_i^\zeta} \\ &= \sin^2(\phi_i^\zeta)\sigma^2_{a_i^\zeta} + \left(a_i^\zeta \cos(\phi_i^\zeta)\right)^2 \sigma^2_{\phi_i^\zeta} \end{aligned} \tag{5.32}$$

$$\begin{aligned} \sigma^2_{s_i^\zeta} &= \left(\frac{\partial s_i^\zeta}{\partial a_i^\zeta}\right)^2 \sigma^2_{a_i^\zeta} + \left(\frac{\partial s_i^\zeta}{\partial \phi_i^\zeta}\right)^2 \sigma^2_{\phi_i^\zeta} \\ &= \cos^2(\phi_i^\zeta)\sigma^2_{a_i^\zeta} + \left(a_i^\zeta \sin(\phi_i^\zeta)\right)^2 \sigma^2_{\phi_i^\zeta} \end{aligned} \tag{5.33}$$

for coordinate ζ and periodic function i. Eqs. 5.32 and 5.33 are a system of two equations with two unknowns so long as $a_i^\zeta > 0$ and $\phi_i^\zeta \neq \xi\pi/4$ for $\xi = 1$, 3, 5, or 7. Solving the system of equations for amplitude and phase errors yields:

$$\sigma^2_{a_i^\zeta} = \frac{\sigma^2_{c_i^\zeta}\sin^2(\phi_i^\zeta) - \sigma^2_{s_i^\zeta}\cos^2(\phi_i^\zeta)}{\sin^4(\phi_i^\zeta) - \cos^4(\phi_i^\zeta)} \tag{5.34}$$

$$\sigma^2_{\phi_i^\zeta} = \frac{-\sigma^2_{c_i^\zeta}\cos^2(\phi_i^\zeta) + \sigma^2_{s_i^\zeta}\sin^2(\phi_i^\zeta)}{\left(a_i^\zeta\right)^2\left(\sin^4(\phi_i^\zeta) - \cos^4(\phi_i^\zeta)\right)} \tag{5.35}$$

Both amplitude and phase errors are functions of the inferred phase value and the respective c_i^ζ and s_i^ζ errors. Phase errors also scale as the inverse of amplitude squared, meaning phase values in areas with small sinusoidal amplitudes are likely to be erroneous. In the extreme case, phase errors approach infinity as amplitude approaches zero, which does not pose a challenge to interpreting the data because the phase of a zero-amplitude periodic function contains no information. The other singularity in Eqs. 5.34 and 5.35 arises from the fact that when phase is an odd-integer multiple of $\pi/4$, Eqs. 5.32 and 5.33 are equivalent, leaving one equation and two unknowns. In that case, it is not possible to uniquely solve for amplitude and phase errors from $\sigma_{c_i^\zeta}$ and $\sigma_{s_i^\zeta}$. This latter singularity is unlikely to pose a problem in practice because measurement noise, the accuracy of efficient numerical solvers, and floating point precision in modern computers diminish the probability that phase values will be exact integer multiples of $\pi/4$ over meaningful spatial scales.

5.3.4 Synthetic ice stream tests

5.3.4.1 Synthetic data

To explore the methods developed in the previous section, we generated a synthetic ice stream covering the geographic region of Rutford (Fig. 5.1). The synthetic ice stream is symmetric about the central flowline with half-width w and length L. We compute the velocity profile using an idealized ice stream model (Raymond, 1996; Cuffey and Paterson, 2010) and place grounded ice in the north and an ice shelf in the south with a smooth transition in vertical tidal influence between grounding and floating ice. The synthetic ice stream can be summarized as:

$$\mathbf{v}_{syn}(x,y,t) = \begin{bmatrix} v_{syn}^{e} & v_{syn}^{n} & v_{syn}^{u} \end{bmatrix}^{T} \tag{5.36}$$

$$v_{syn}^{e}(x,y,t) = 0 \tag{5.37}$$

$$v_{syn}^{n}(x,y,t) = s_v \frac{x}{L}\left[-v_{ideal} + P^{n}\right] \tag{5.38}$$

$$v_{syn}^{u}(x,y,t) = s_v \frac{x-L}{10L} v_{ideal} + P^{u} \tag{5.39}$$

$$P^{\zeta}(x,y,t) = \sum_{i=1}^{k} \Gamma_i^{\zeta}\left[\sin\left(\omega_i t_a + \phi_i^{\zeta}\right) - \sin\left(\omega_i t_b + \phi_i^{\zeta}\right)\right] \tag{5.40}$$

$$\Gamma_i(x,y) = \frac{v_{ideal}}{v_{ideal}^{center}} \begin{bmatrix} 0 & \tilde{a}_i^{n} & \tilde{a}_i^{u}\Upsilon \end{bmatrix}^{T} \tag{5.41}$$

$$\Upsilon(x,y) = \left\{1 + \tanh\left[k_h\left(x - 0.6L\right)\right]\right\}/2 \tag{5.42}$$

$$v_{ideal}(y) = v_{ideal}^{center}\left[1 - \left(1 - \frac{y}{w}\right)^{n_g+1}\right] \tag{5.43}$$

$$v_{ideal}^{center} = \frac{2Aw}{n_g+1}\left[\tau_d \frac{w}{h}\left(1 - \frac{\tau_b}{\tau_d}\right)\right]^{n_g} \tag{5.44}$$

where Υ defines the ice shelf such that ice in the northern 60% of the ice stream is grounded, $k_h = 10^{-|\log_{10}(L) - 0.8|}$ dictates the sharpness of the grounding zone transition, $\tau_d = \rho g h \alpha$ is the gravitational driving stress and x and y are spatial coordinates defined such that $0 \leq x/L < 1$ and $0 \leq y/w \leq 2$. Parameter definitions and values, given in Table 5.1, are constant in space and time. Note that the synthetic ice stream is flowing due south and its maximum vertical speed is 10% of the maximum horizontal speed (Figs. 5.2Sa–Sf and 5.4Sa–Sf).

Horizontal and vertical components of the simulated ice stream contain 11 tidal constituents. In order to make our synthetic ice stream flow as much like Rutford as possible, we assigned the amplitude and phase values using results from more than 2 years of GPS measurements collected on Rutford and reported by Murray et al. (2007, Table 1). For convenience, we summarize these

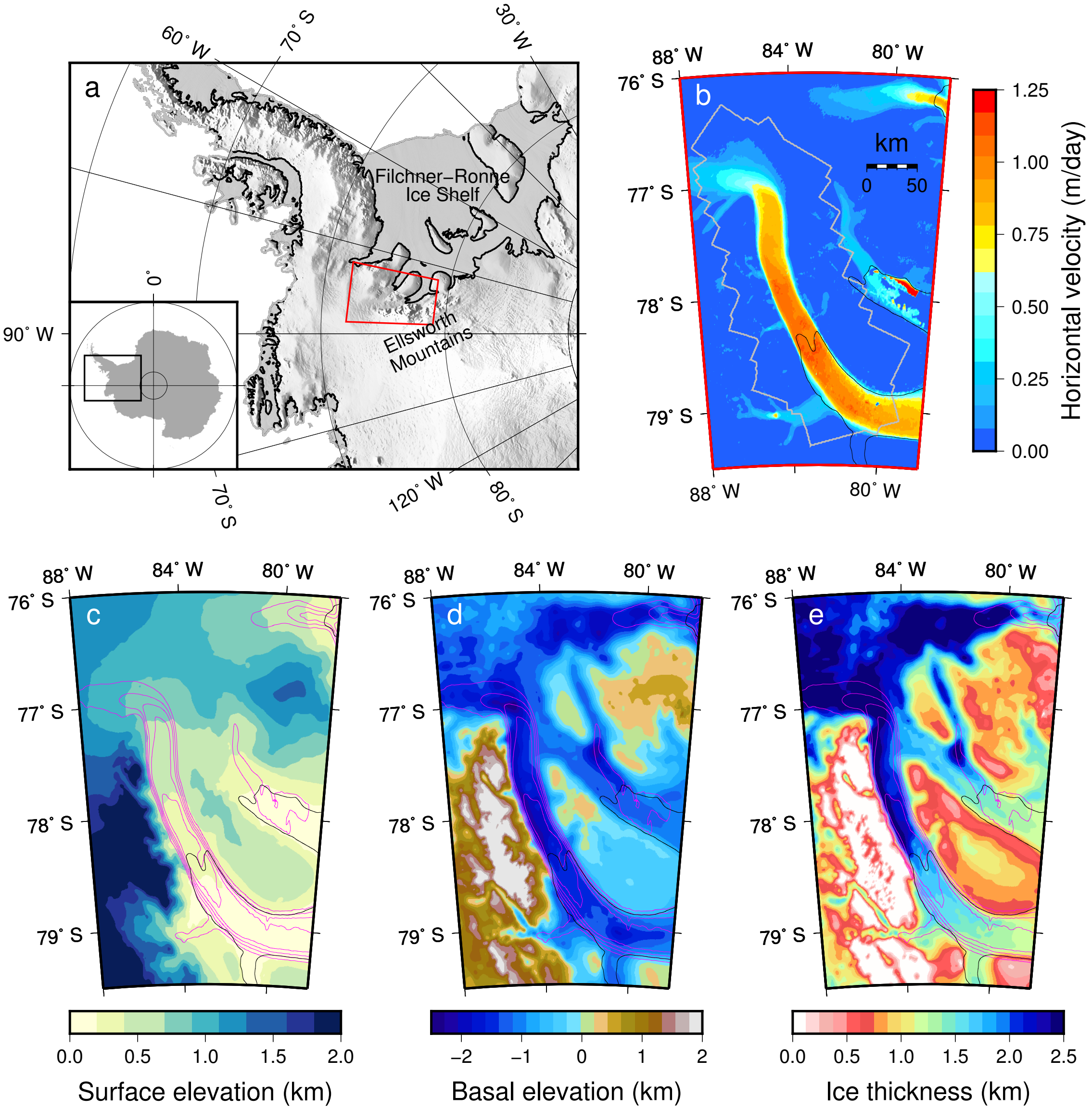

Figure 5.1: (a) Shaded relief map of Rutford Ice Stream and surrounding area. Red box indicates the region shown in b–e. (b) Horizontal speed from Rignot et al. (2011a). Gray outline indicates the extent of the CSK observations used in this study. (c) and (d) Surface and basal elevation in km relative to mean sea level, respectively. (e) Ice thickness in km. Magenta contour lines in c–e indicate smoothed horizontal surface velocity from (b) in 0.2 m/day increments. In all panels, irregular black lines indicate grounding zones. All geometric and grounding line data are from Bedmap2 (Fretwell et al., 2013).

Table 5.1: Synthetic ice stream parameters

Parameter	Definition	Value	Unit
A	rate factor in ice flow law[a]	2.4×10^{-24}	$\mathrm{Pa}^{-3}\ \mathrm{s}^{-1}$
α	ice surface slope	0.04	rad.
g	gravitational acceleration	9.81	$\mathrm{m\ s}^{-2}$
h	ice thickness	1000	m
n_g	exponent in ice flow law[a]	3	-
ρ	ice density	900	$\mathrm{kg\ m}^{-3}$
s_v	constant	0.6	-
τ_b	basal shear traction	$0.8\tau_d$	Pa

[a] $\dot{\varepsilon}_e = A\tau_e^n$ where $\dot{\varepsilon}_e$ and τ_e are effective strain rate and stress in the ice, respectively

Table 5.2: Tidally induced velocity variations included in simulated ice stream flow. Amplitude and phase values are reproduced from Murray et al. (2007, Table 1)

Tide	Period (days)	Horizontal amplitude (cm)	Horizontal phase (deg)	Vertical amplitude (cm)	Vertical phase (deg)
K_2	0.498	0.31	163.0	29.1	99
S_2	0.5	0.363	184.0	101.6	115
M_2	0.52	0.259	177.0	156.3	70
K_1	1.00	0.19	79.0	49.0	73
P_1	1.003	0.24	77.0	16.6	64
O_1	1.08	0.264	81.0	43.0	54
M_f	13.66	2.54	250.0	2.9	163
M_{sf}	14.77	13.28	18.8	0.3	164
M_m	27.55	5.04	253.0	1.6	63
S_{sa}	182.62	26.74	256.0	1.5	179
S_a	365.27	19.18	273.0	0.2	179

values in Table 5.2. Amplitudes vary over the grounded ice in the same manner as the velocities and are constant over the central ice shelf. Because there is only slight latency in tidal response as a function of distance upstream of the grounding line, we made phase values spatially constant (Gudmundsson, 2006).

We observed the simulated ice stream with the same set of viewing geometries as we use for Rutford (see §5.4). We added zero-mean Gaussian white noise with a 2-cm standard deviation, approximately twice the typical noise level in our data, to each offset field. Importantly, we do not weight the simulated data by the additive noise as we do the actual data. This means our simulated observations have levels of unaccounted noise that are roughly double the formally estimated noise levels in the data. We do this to provide a cushion in validating our inversion method.

5.3.4.2 Results from synthetic tests

Results from multiple simulated tests provide 3D secular velocity values and a suite of amplitude and phase values corresponding to the user-defined set of sinusoids. Formal error estimates are also included. In this section, we detail only the components of the noise-sensitivity matrix, $\mathbf{S}$ (Eq. 5.27) and reserve discussion of $\widetilde{\mathbf{C}}_m$ for the observed data. The components of $\mathbf{S}$ are functions of only the set viewing geometries at a given point and so are identical to the observational data discussed in the next section.

We conducted numerous tests using different families of periodic functions. We limit the potential members to only those periods that are short enough to be adequately sampled by our observations and that are not obviously aliased by the repeat time between CSK observations. Data presented here were collected over 9 months, so the first condition eliminates the solar semi-annual, S_{sa}, and annual, S_a, constituents. Times between CSK observations are always within seconds of being integer days, thus aliasing the solar semidiurnal constituent, S_2, and the lunar semidiurnal constituent, K_2, along with the diurnal solar—S_1 and P_1—and lunar, K_1, constituents. Valid members are then the lunar semidiurnal, M_2, and diurnal, O_1, constituents; the lunisolar fortnightly M_f and the lunisolar synodic fortnightly M_{sf} constituents; and the lunar monthly M_m constituent.

We inferred 4D velocity fields for every combination of valid tidal constituents using the synthetic ice stream described in Eqs. 5.36–5.44 and Table 5.2, with $\kappa_p = 10$ m^{-2} (Eq. 5.22), a value derived through trial and error. Here, we present a representative set of 5 tests. Results from each test occupy unique rows in Figs. 5.2–5.9 with the tidal constituents used in the inversion labeled on the left side. Left columns in Figs. 5.2–5.4 contain the secular velocities along the respective spatial dimension and other column positions correspond to the tidal constituent designated in the top rows. Results from the 4D inversion tests are given as differences between the inferred value and the corresponding synthetic value.

Our synthetic ice stream flows due south with maximum southerly speeds of approximately 1 m/day (Fig. 5.2), and zero easterly speeds (Fig. 5.3). Southerly flow is captured within 2% of the simulated flow speed and easterly velocities are near zero in all well-observed areas in all 4D inversion tests, as well as 3D tests (not shown) that output only the three-component secular velocity fields. When M_2 tides are included in the inverse model, estimated north velocities are well within 1% of the actual velocity, and easterly velocities remain near zero. These results suggest that the horizontal velocity fields in the observational data will have errors that are within 5% of the expected

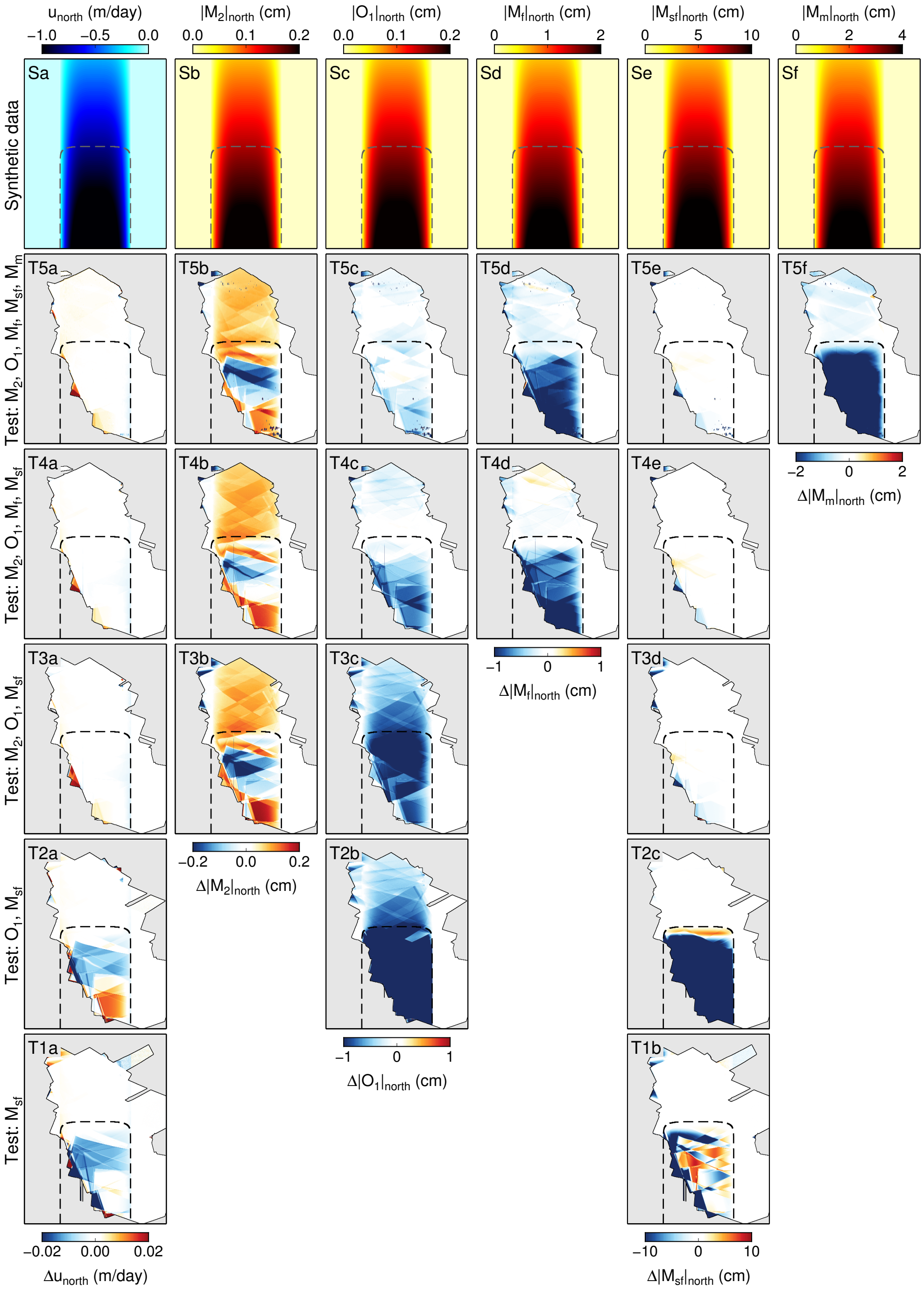

Figure 5.2: North component of synthetic ice stream flow and tidally induced flow variation amplitudes (Sa–Sf) along with inferred values of ice flow and amplitudes of tidally induced flow variations (T5a–T1b). Rows represent different inversion tests. Tidal constituents considered in each test are given on the left side of the row. Panels within each row are labelled with 'T', the number of tidal constituents in the respective test, and letters in alphabetical order. Columns contain consistent data types. Inferred values for each test are given as the difference between the synthetic ice stream value and the inferred value. All differenced plots in a particular column use the same colormap bounds. Colormaps are scaled to best represent the respective data. Dashed lines in all plots indicate the grounding zone, which bounds the ice shelf.

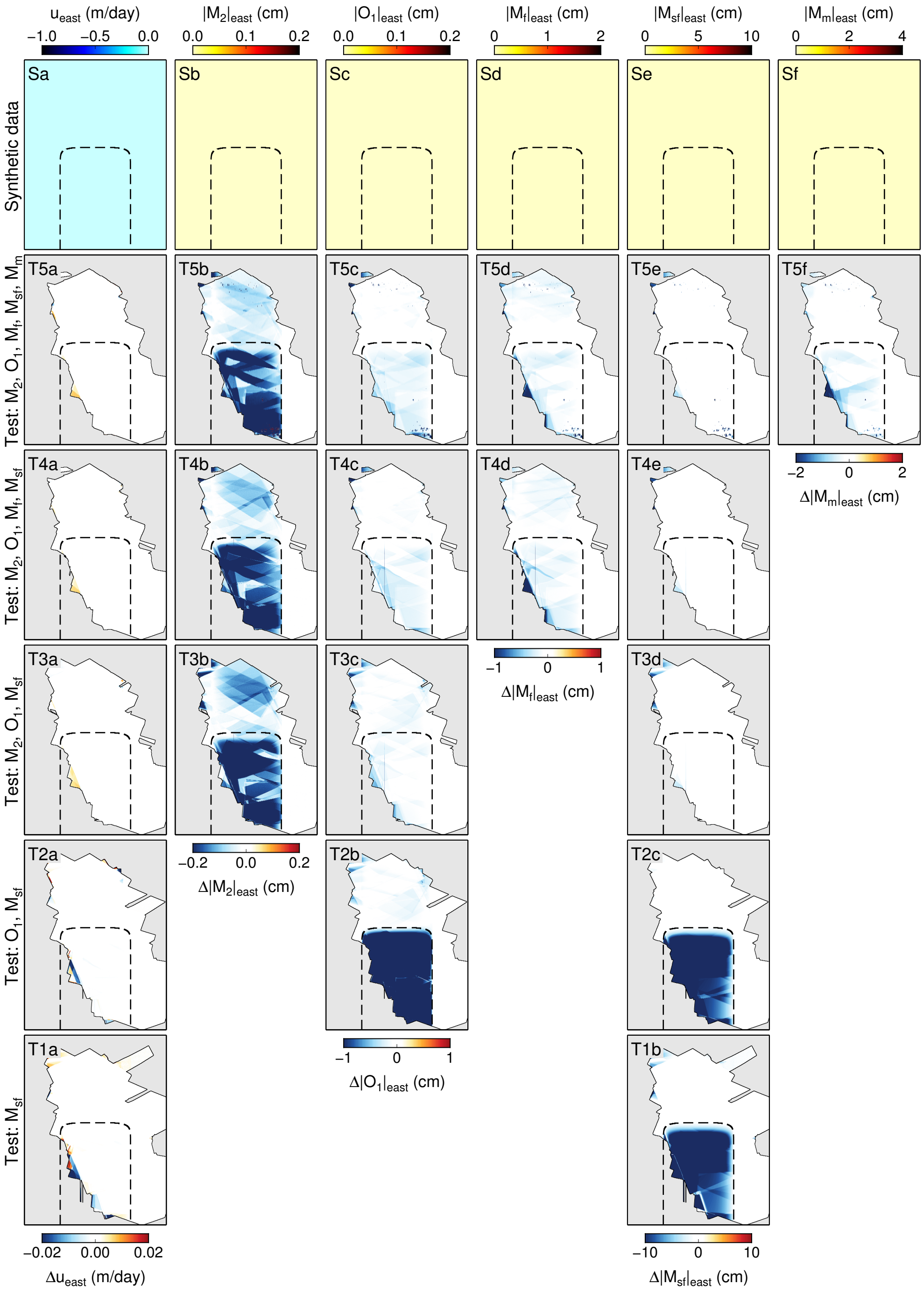

Figure 5.3: East component of synthetic ice stream flow and tidally induced flow variation amplitudes along with inferred values of ice flow and amplitudes of tidally induced flow variations. Figure layout and labelling follows Fig. 5.2.

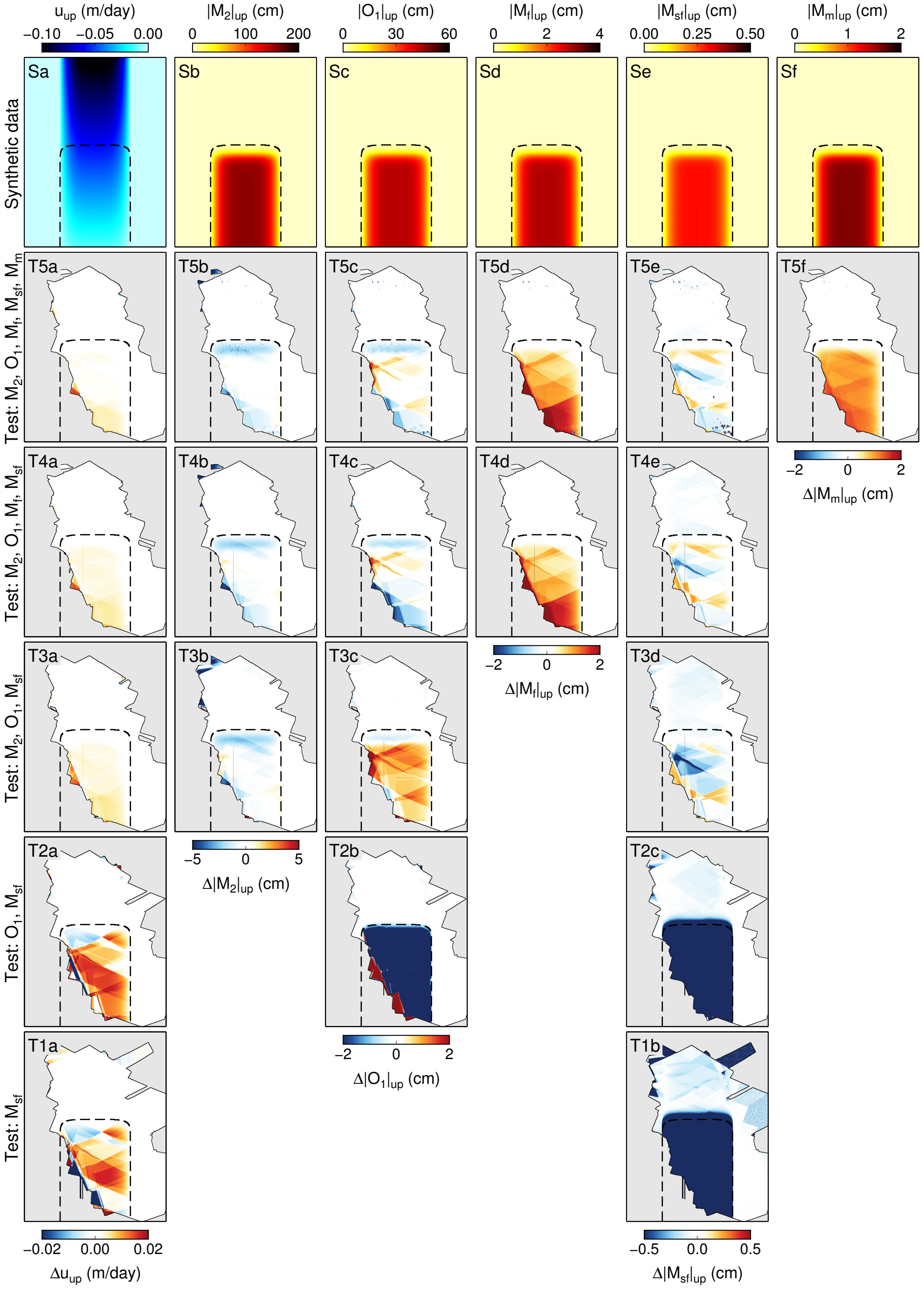

Figure 5.4: Synthetic data and inferred values of vertical ice motion and tidally induced variations. Figure layout and labelling follows Fig. 5.2. Positive values in Sa–Sf are upward.

values.

In practice, the up component of the velocity field can be difficult to obtain for a variety of reasons that are related to limited data, minimal viewing geometry diversity, and varying environmental conditions (e.g. Joughin, 2002; Rignot et al., 2011a; Minchew et al., 2015). Owing to the quantity of data and diversity in viewing geometries afforded by the CSK observations, we are able to fit the vertical velocity component to within 2% over grounded ice and within 5% or 20% over the ice shelf, depending on which tidal constituents are included in the inverse model (Fig. 5.4). The largest absolute errors in vertical speed occur over the ice shelf when M_2 is not included in the inverse model (Figs. 5.4T2a and 5.4T1a) because M_2 is the largest contributor to vertical motion by at least a factor of 3. Given the sampling frequency and repeat time between CSK observations, not including M_2 in the inverse model causes some of the high-frequency vertical motion to bleed into the secular velocity term.

The horizontal tidal displacements give generally better results over grounded ice relative to floating ice (Figs. 5.2 and 5.3). As with the secular velocity results, we see a marked improvement in the inferred horizontal periodic amplitudes when M_2 is included in the inverse model. We attribute this improvement in overall accuracy to the fact that SAR provides measurements along either the oblique radar LOS or along the purely horizontal azimuth direction. Due to the satellite headings, north velocity components are constrained primarily by LOS observations, which contain both horizontal and vertical components. Excluding M_2, the largest vertical tidal constituent, causes some of the unaccounted vertical motion to manifest in the horizontal fields. When M_2 is included, errors in M_{sf}, the period with the largest influence in horizontal ice flow, are typically less than 5%. The O_1, and to a lesser degree M_2, horizontal components have large errors relative to their true amplitudes, but small absolute errors. Errors in O_1 diminish as long-period constituents, M_f and M_m, are added to the inverse model while misfits in M_2 and M_{sf} are largely unaffected by the presence of M_f and M_m. Given the sizable misfits in M_f and M_m, it is likely that improvements in O_1 occur because misfits are shifted to the longer period components as a consequence of including $\mathbf{C}_m$. In terms of fitting time varying horizontal velocity, these results suggest that the optimal family of periodic functions is M_2, O_1, and M_{sf}. Accounting for all misfits with this family of periodic functions, we should conservatively expect to observe the horizontal ice flow variability on Rutford to within 10% of the true signal.

Vertical tidal displacements have the largest amplitudes, by more than an order of magnitude compared with the largest horizontal amplitudes, and the inferred sinusoidal amplitudes are correspondingly well fit when M_2 is included in the inverse model (Fig. 5.4). When M_2 is excluded from the inversion, misfits in the vertical components are an order of magnitude or more larger than the true value because the inversion is compensating for much of the high-frequency vertical motion using the available low-frequency functions and the secular vertical velocity. When M_2 and O_1 occupy the inverse model, errors in the respective inferred amplitudes rarely exceed 2% in M_2 and 3% in O_1 within well observed areas. Errors at fortnightly and monthly periods approach 50% in some areas over the ice shelf, but because the amplitudes of the true low-frequency signals are small, the absolute values of these errors are negligible relative to the amplitude of the M_2 displacement. Over grounded ice, where vertical amplitudes at all tidal periods are zero, there are virtually no erroneous inferred values except on the edges of the observational domain where we have limited viewing geometry diversity. Based solely on misfits in vertical displacement, we contend that the M_2, O_1, and M_{sf} family of tidal frequencies affords the best solution for the given observational dataset.

Inferred phase values for the periodic functions match the respective synthetic components to well within 10° in all velocity components in regions where the amplitude is large and the amplitude misfit is small (Figs. 5.5–5.6). Here we exclude phase values for the east component because true and inferred amplitudes are near zero. We retain the complete observational domain in both the north an up components to illustrate the pseudo-random behavior of inferred phase in areas with small or zero amplitude. The phase results in areas with sufficiently large amplitudes are consistent with the secular velocity and periodic amplitudes in that the smallest misfits in all nonzero-amplitude components are achievable only when M_2 is included in the inversion. Of particular note is that large and spatially random errors occur in the inferred north component of M_{sf} when M_2 is not included in the inversion, a finding that has consequences for future mission planning with satellite platforms that offer less frequent data acquisitions than CSK. It is unclear as to why M_f phase values are consistently shifted by approximately -90° and M_m phase by approximately 180° in both the north and up components. The most likely explanation involves a combination of having complementary periods to the period with the strongest horizontal signal (M_{sf}), relatively little sampling given the $\lesssim$ 9-month duration of the CSK acquisitions, and viewing-geometry-induced covariance between the north and up components, which is discussed in the next paragraph and would account for the two periods having similar errors in both spatial dimensions. Given the large misfits in M_f and M_m phases, we conclude that the phase misfits support our previous assertions that the overall best results are attainable using the M_2, O_1, and M_{sf} family of tidal frequencies, though it is instructive to consider how the noise sensitivity changes as a function of which tidal periods are included in the

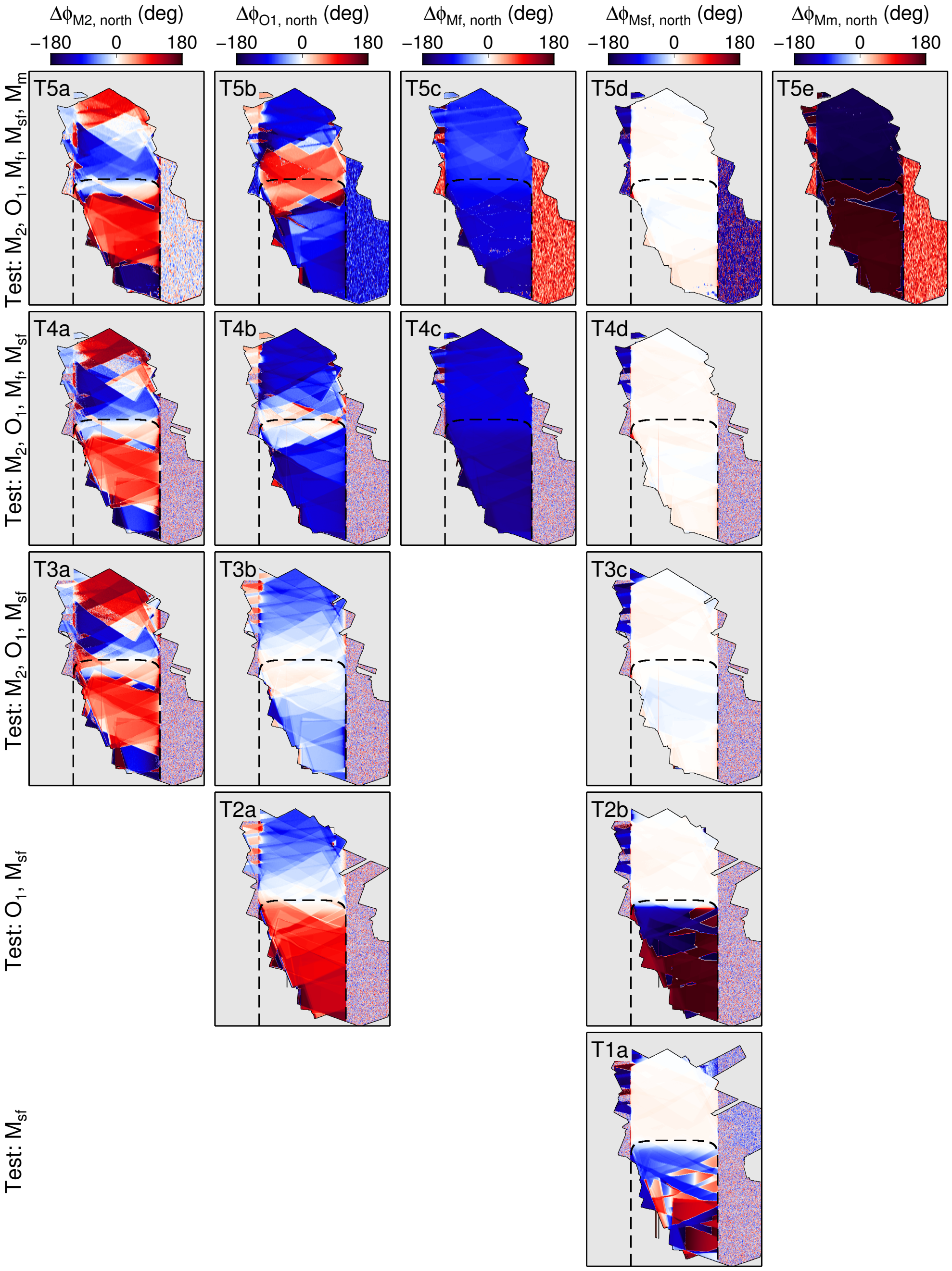

Figure 5.5: Inferred phase values relative to the respective, spatially constant, synthetic values for the north components. Figure layout and labelling follows Fig. 5.2.

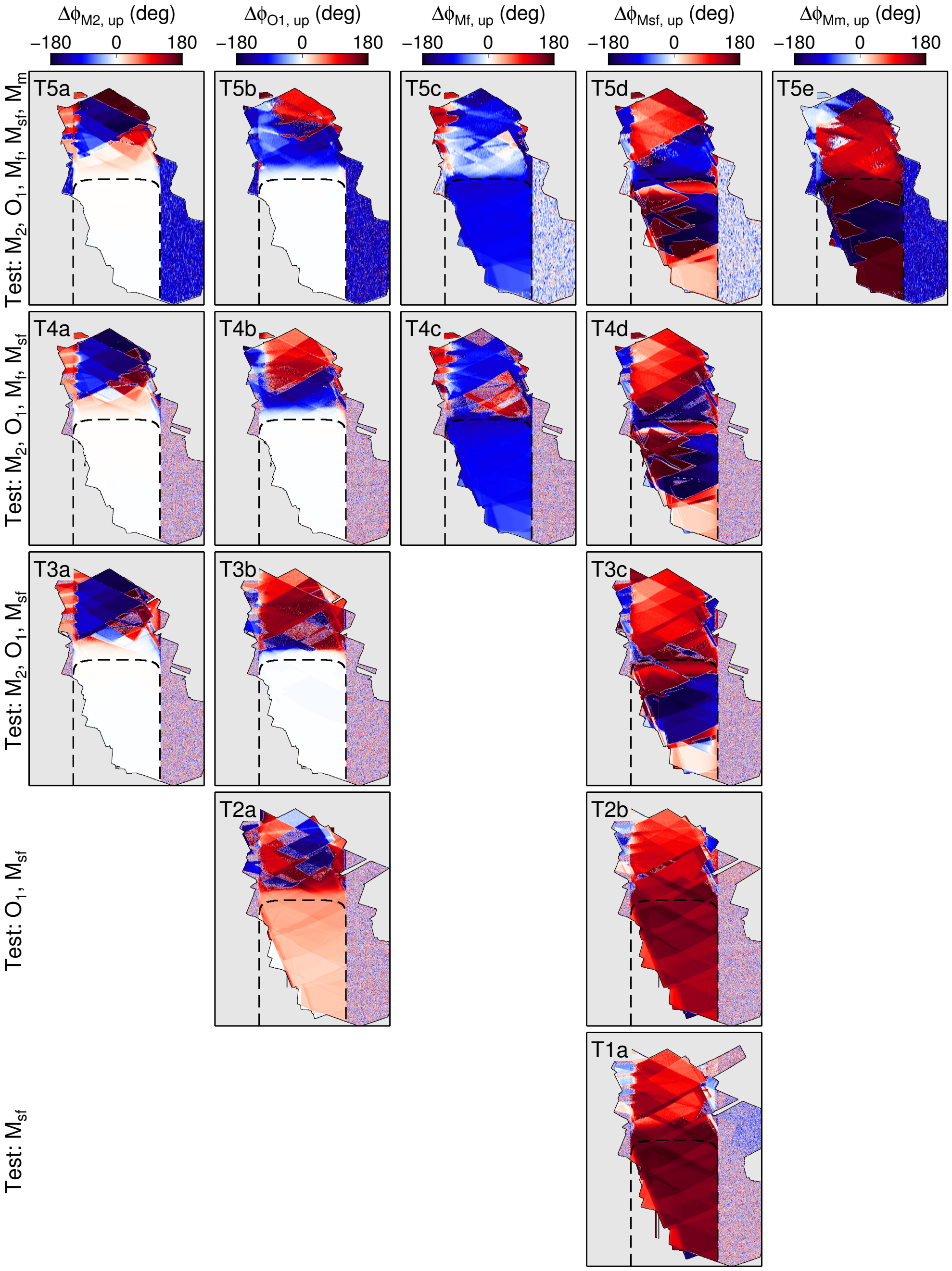

Figure 5.6: Inferred phase values relative to the respective, spatially constant, synthetic values for the up components. Figure layout and labelling follows Fig. 5.2.

inverse model.

Noise-sensitivity matrix, $\mathbf{S}$, elements provide information about the conditioning of the design matrix, which is directly related to how well the observations constrain ice motion (Figs. 5.7–5.9). Higher values in the $\mathbf{S}$ elements indicate poorer constraints on motion. In our observations, all three secular velocity components are tightly constrained with values $\sim 10^{-3}$. The poorest constraints on secular velocity are in the north component because the satellite headings in all 32 flight tracks are within 45° of west and are rarely less than 20° from west, meaning that the majority of LOS displacement measurements, which are sensitive to vertical and horizontal motion, are primarily oriented north while all measurements of displacement in the purely horizontal azimuth direction are primarily oriented east. A notable consequence of this viewing geometry is that there is strong positive (> 0.5) correlation between errors in the north and up components everywhere in the observational domain while errors in the east component, which are constrained primarily by purely horizontal displacement fields, are uncorrelated with the north and up components (not shown).

Tidal components are not as well constrained as the secular velocity components, but still have relatively low sensitivity to measurement noise. This low noise sensitivity is indicated by the fact that all tidal component amplitudes have corresponding $\mathbf{S}$ elements that are less than unity. The highest sensitivities in the tidal amplitudes occur in the M_2 and M_{sf} components, with the addition of M_2 imbuing M_{sf} with greater noise sensitivity in all components. This causal relationship arises from the complementary periods for M_2 and M_{sf} tides.

The tidal constituent with the greatest impact on the accuracy of the inferred 4D velocity fields is M_2. M_2 tides have the largest amplitudes and are not aliased by the satellite observational frequency, which means M_2 contributes significantly to the observed temporal variations in ice flow. The importance of M_2 is exacerbated by the satellite viewing geometries. Half of our observations are along the westerly azimuth vectors that have no sensitivity to vertical motion. The other half of our observations are collected along the radar LOS and are sensitive to horizontal, primarily northerly, and vertical motion. None of our observations are purely vertical, which means that the strong vertical motions caused by M_2 manifest in both vertical and horizontal velocity components unless they are properly captured by the inverse model. Synthetic results described here for all inferred values show that it is essential to include M_2 in the inverse model in order to properly constrain both vertical and horizontal motion over the ice shelf an in the vicinity of the grounding line. Because we based the synthetic ice stream on GPS observations collected on Rutford, we expect the results from the synthetic data to inform our observational results.

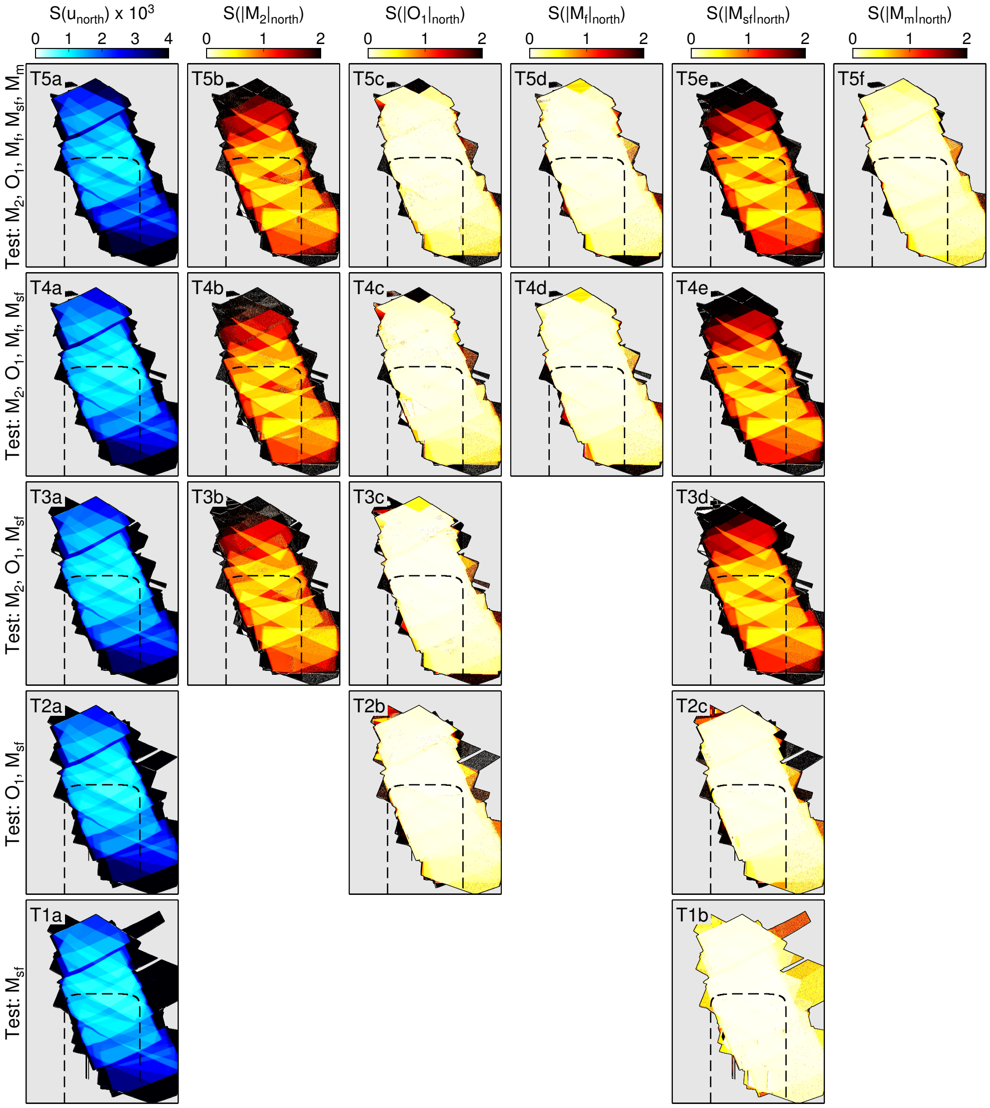

Figure 5.7: North components of the diagonal elements of the noise-sensitivity matrices, **S**, corresponding to velocity and sinusoidal amplitude for each test case. Figure layout and labelling follows Fig. 5.2.

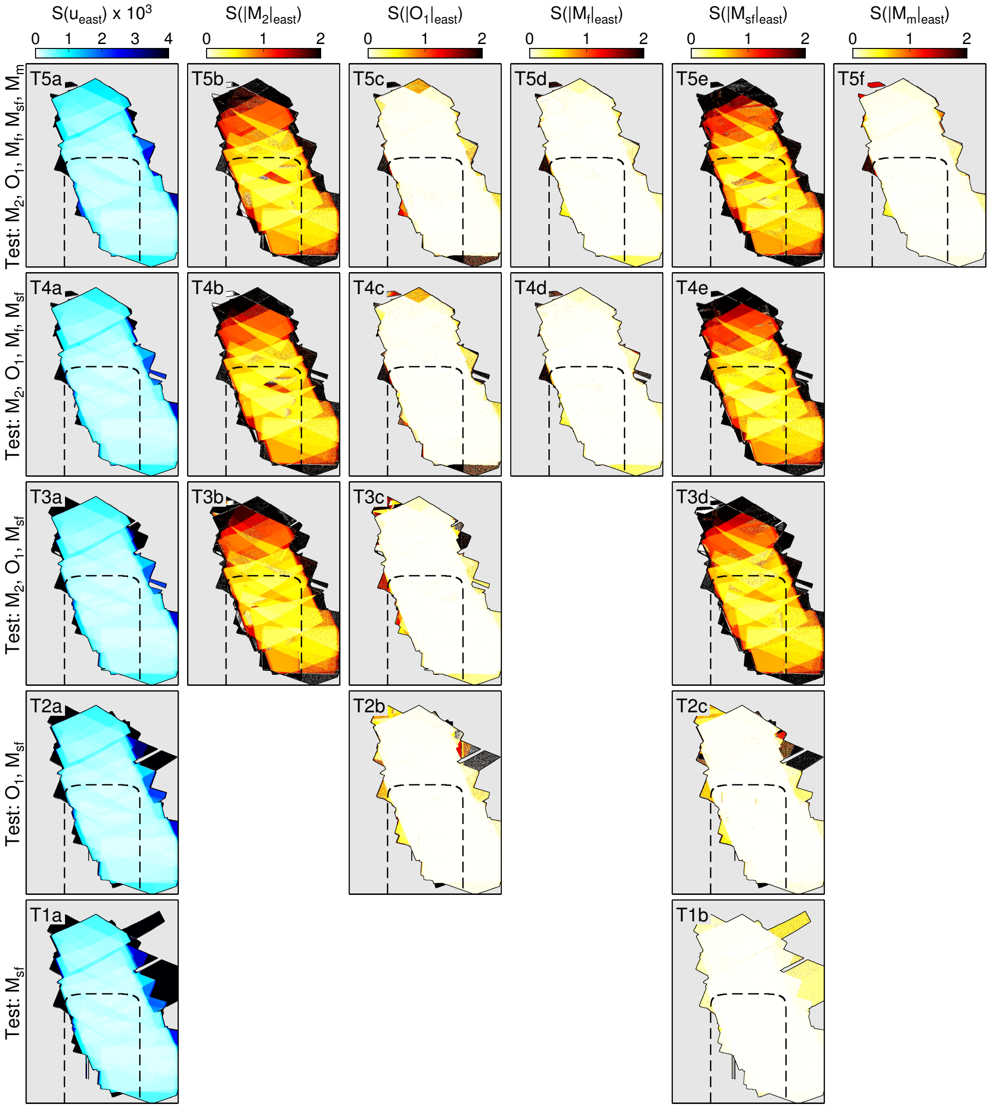

Figure 5.8: East components of the diagonal elements of the noise-sensitivity matrices, **S**, corresponding to velocity and sinusoidal amplitude for each test case. Figure layout and labelling follows Fig. 5.2.

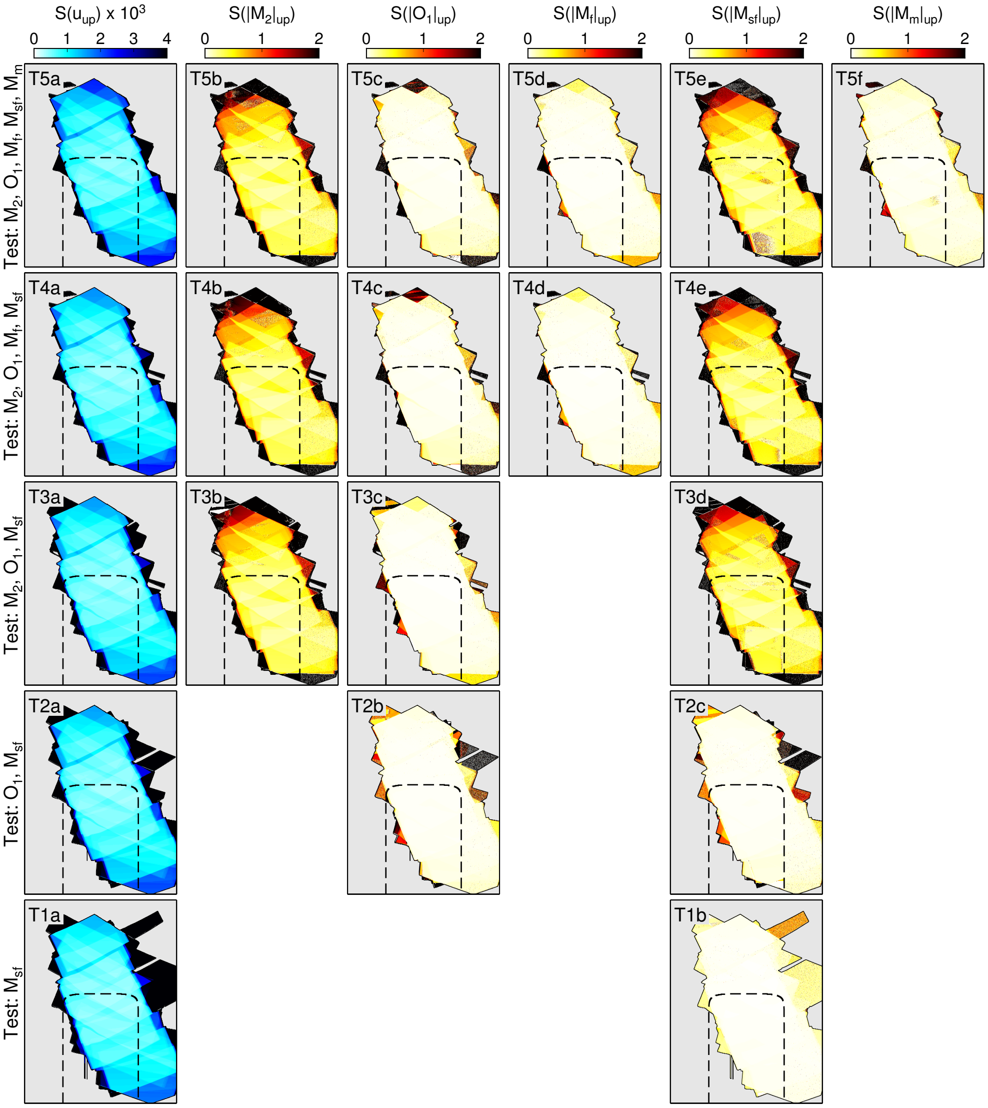

Figure 5.9: Up components of the diagonal elements of the noise-sensitivity matrices, **S**, corresponding to velocity and sinusoidal amplitude for each test case. Figure layout and labelling follows Fig. 5.2.

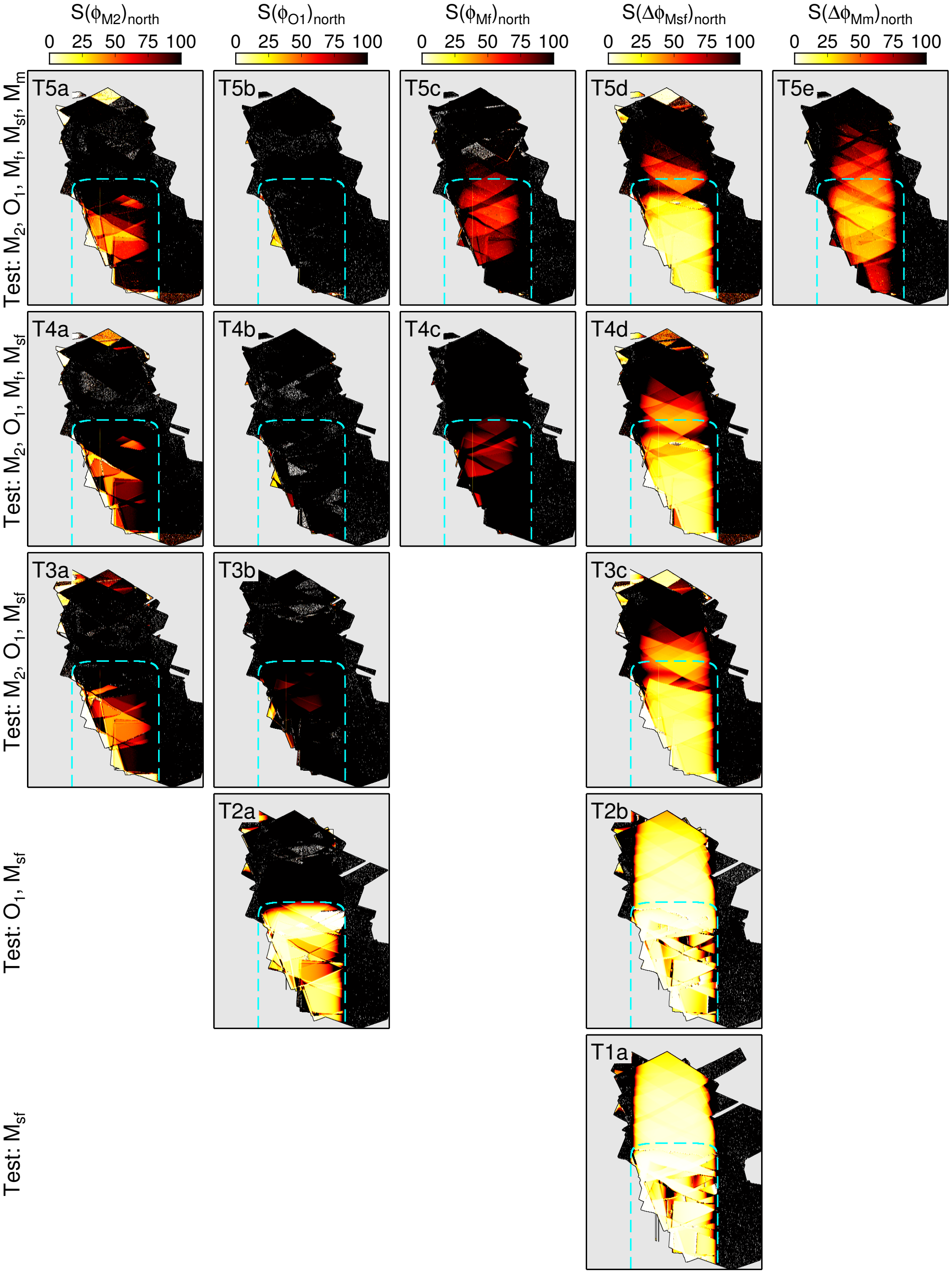

Figure 5.10: North components of the diagonal elements of the noise-sensitivity matrices, **S**, corresponding to sinusoidal phase for each test case. Figure layout and labelling follows Fig. 5.2.

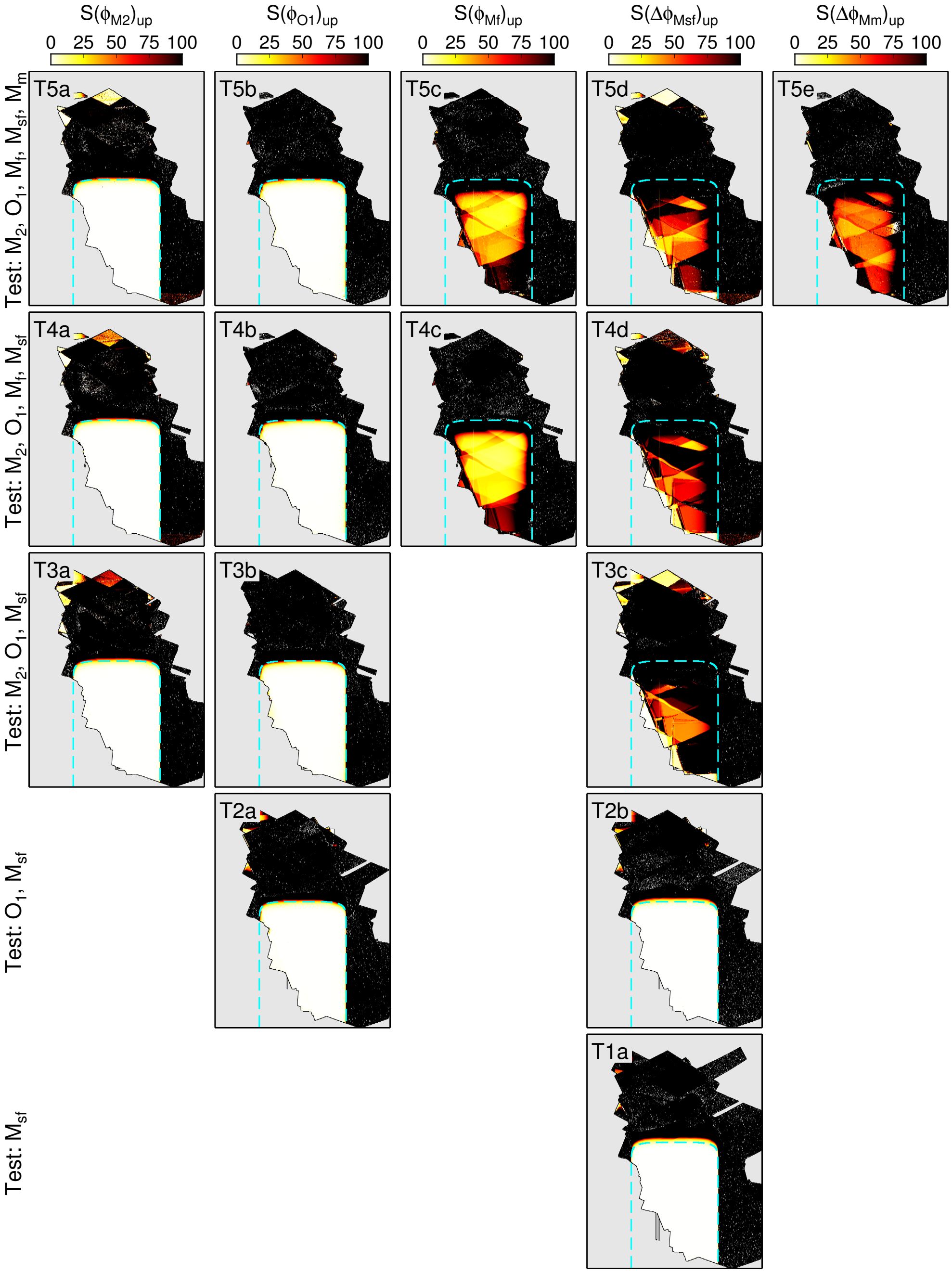

Figure 5.11: Up components of the diagonal elements of the noise-sensitivity matrices, **S**, corresponding to sinusoidal phase for each test case. Figure layout and labelling follows Fig. 5.2.

5.4 Observations of Rutford Ice Stream

5.4.1 Study site

Situated immediately east of the Ellsworth Mountain Range, Rutford is a major ice stream of the West Antarctic Ice Sheet that flows at a rate of approximately one meter per day (Rignot et al., 2011a) into the California-sized Filchner-Ronne Ice Shelf (FRIS; Fig. 5.1). FRIS is a cold-cavity ice shelf, meaning that ocean water contacting the ice shelf base is at or near the freezing temperature (Nicholls et al., 2009). Recent studies suggest that FRIS is gaining almost as much mass from accumulation as it is losing from melt (e.g., Pritchard et al., 2012; Rignot et al., 2013), meaning that the influence of FRIS on the flow of Rutford is approximately constant over multi-annual timescales. Relatively long-term observations of ice flow on Rutford show that there is currently little or no secular acceleration of ice stream flow and all flow variability is periodic (Scheuchl et al., 2012).

The geometry in and around Rutford is relatively well known (Fig. 5.1), which is advantageous for follow-on studies of basal mechanics using data presented here (e.g., King et al., 2009; Smith and Murray, 2009; Fretwell et al., 2013; Smith et al., 2015). Rutford is approximately 200 km long and 30 km wide with a typical ice thickness of approximately 2 km over its grounded portion. Rutford's bed sits entirely below sea level and features several prominent topographic highs, areas of deforming subglacial till, active drumlin formation, and an evolving basal hydrological system (Smith et al., 2007; King et al., 2009; Smith and Murray, 2009; Fretwell et al., 2013). A high in the basal topography is responsible for the sinuosity of the grounding line (Rignot et al., 2011b).

The feature of greatest interest in this study is the approximately 20% variation in flow velocity on tidal timescales observed on Rutford (e.g., Gudmundsson, 2006; Murray et al., 2007). Tides beneath FRIS have large amplitudes ($\sim$ 3 m; Figs. 5.12–5.13) that are dominated by the lunar semi-diurnal (M_2) and solar semi-diurnal (S_2) tidal constituents (Han et al., 2005; Padman et al., 2008). Over most of its areal extent, FRIS is afloat and follows the vertical motion of the tides, providing a convenient means for estimating grounding line positions, the approximate boundary between floating and grounded ice, using LOS displacements (e.g., Rignot et al., 2000, 2011b). Horizontal ice flow responds to vertical tidal motion tens of kilometers upstream of the grounding line at approximately 10 m s^{-1} with an upstream-distance-dependent phase shift of approximately 3.625 deg km^{-1} (Gudmundsson, 2006; Murray et al., 2007; Aðalgeirsdóttir et al., 2008; Gudmundsson, 2011). A testament to the nonlinearity of ice stream motion, the dominant period of horizontal ice

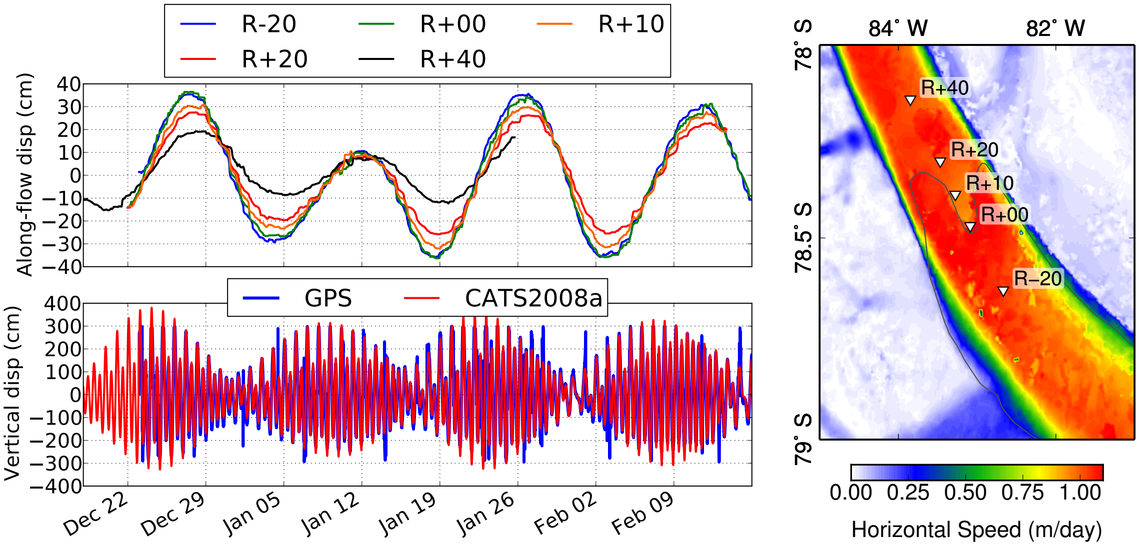

Figure 5.12: Tidally induced flow variation on Rutford beginning in December 2003. Top left panel shows along-flow displacements measured with GPS stations. Locations of stations are indicated in the map on the right. Numbers in the GPS designations indicate approximate distance upstream of the grounding line (e.g. R-20 is ≈ 20 downstream of grounding line and R+20 is ≈ 20 upstream). Lower panel shows vertical motion at R-20 in blue overlain by modeled tidal displacement calculated using CATS2008a_opt (Padman et al., 2002; Padman and Fricker, 2005). GPS data are from Gudmundsson (2006, 2011) and are low-pass filtered over a 24-hour window. Colormap on the right indicates horizontal speed in m/day from Rignot et al. (2011a)

flow variability is 14.77 days, corresponding to the spring-neap (lunisolar synodic fortnightly, or M_{sf}) tidal cycle (e.g., Gudmundsson, 2006; Murray et al., 2007; Aðalgeirsdóttir et al., 2008; King et al., 2010; Gudmundsson, 2011). Because ice behaves as a viscous fluid on the relevant timescales and Rutford is much longer than it is wide, upstream propagation of tidal loading may be difficult to transmit through the ice itself and could be facilitated by basal slip, which encompasses deformation within and sliding along the bed (Gudmundsson, 2007, 2011; Thompson et al., 2014; Rosier et al., 2014).

Spring-neap tides are synodic, arising from differential solar and lunar positions. Spring tides are larger than neap tides and occur when the Sun, Moon, and Earth are collinear and the Sun's gravitational attraction complements the Moon's gravity. Neap tides occur when the solar and lunar positions are offset by ±90°. This definition highlights the most important concept in understanding the mechanisms underlying tidally induced ice stream flow variability: The dominant period of ice stream flow arises from the beating between the two dominant constituents in the tidal (forcing) spectrum and, therefore, is negligibly small in the forcing spectrum itself (Murray et al., 2007;

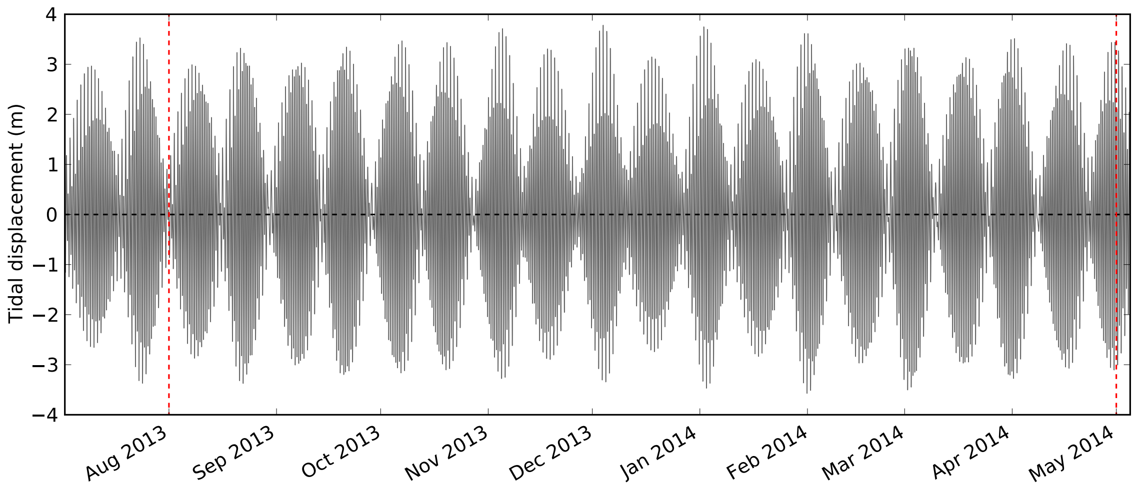

Figure 5.13: Modeled tidal displacement at location R-20 for the CSK observational period calculated using CATS2008a_opt (Padman et al., 2002; Padman and Fricker, 2005). Vertical red dashed lines indicate the approximate start and stop time of the CSK data collection, though we note that not all 32 tracks were acquired for the entire duration.

Gudmundsson, 2011). Any proposed mechanism for tidally induced ice stream variability must then account for the frequency shift in the power spectrum of the horizontal velocity in the grounded ice relative to the vertical motion of floating ice, the upstream phase shift of the horizontal velocity response to tides and the vertical tidal signal, the damping in ice flow variability, and the velocity of upstream propagation of the tidal signal. Proposed mechanisms include yielding of a pseudo-plastic bed (e.g., Gudmundsson, 2011) or variations in basal water pressure transmitted through a highly conductive basal hydrological system (e.g., Murray et al., 2007; Thompson et al., 2014; Rosier et al., 2015). Our results suggest that tidal variations arise from changes in ice shelf buttressing that are transmitted upstream through the ice column. Rutford is not unique in experiencing tidal timescale flow variability and insights into the underlying mechanisms on Rutford can inform our general understanding of basal mechanics (e.g., Anandakrishnan et al., 2003; Bindschadler et al., 2003a,b; Winberry et al., 2009).

5.4.2 Data and processing methodology

CSK, which is operated by the Italian Space Agency (ASI), collected SAR data over Rutford for approximately 9 months beginning in August 2013. We designed a data acquisition strategy to cover all of the grounded ice, extending approximately 75 km downstream of the grounding line (Rignot et al., 2011b; Fretwell et al., 2013), from ascending and descending orbits (Fig. 5.1b).

All four CSK satellites collected data, yielding SAR pairs with interim times between subsequent SAR acquisitions of 1, 3, 4, and 8 days. Each satellite features nearly identical X-band (3.1-cm wavelength; 9.6 GHz) SAR systems that have a usable spatial resolution as fine as 10 m.

We processed the raw CSK data using the InSAR Scientific Computing Environment (ISCE), a radar-processing software package developed primarily at NASA's Jet Propulsion Laboratory (Zebker et al., 2010; Rosen et al., 2012). We developed the top-level software used to calculate the LOS and azimuth offset fields, adopting basic functionality from both ISCE and the Repeat Orbit Interferometry Package (ROI_PAC) (Rosen et al., 2004). To calculate offset fields, we prescribed the 2D cross correlation windows to be 64 $\times$ 64 pixels, defined in the single-look complex (SLC) image grid, with a step size of 32 SLC-pixels in each direction. Using tools available in ISCE, we accounted for topography in the LOS offsets using the Bedmap2 DEM (Fretwell et al., 2013), resampled to a 25-m grid using bi-cubic interpolation implemented in Generic Mapping Tools (GMT) (Wessel et al., 2013), and geocoded all results to the resampled DEM. Following topographic correction and prior to geocoding, we filtered the resulting LOS and azimuth offset fields using a moving-window median filter with an 8 $\times$ 8 pixel window, where pixel size is now defined by the offset-field grid given in radar, or range-doppler, coordinates. To account for any small planar trends in the offset fields, we estimated and removed linear or quadratic trends from areas with relatively stagnant ice. This latter step helps ensure greater accuracy and reasonable transitions in the final velocity field at the edges of individual satellite tracks but does not significantly alter any of the inferred offset field values.

5.5 Results

We report inferences of secular velocity and the M_2, O_1, and M_{sf} family of sinusoidal periods. Based on tests with the synthetic ice stream, we set $\kappa_p = 10$ m^{-2} in the prior model covariance matrix. To organize the large amount of information that makes up the 4D velocity fields, we begin our description of the results with the time-invariant, or secular, velocity components (Figs. 5.14–5.15) and associated rotation and strain rates (Fig. 5.16). Time-dependent velocity fields and their associated rotation and strain rates follow (Figs. 5.17–5.22). Movies of temporally varying ice flow can be found in online supplementary materials.

5.5.1 Time-invariant fields

5.5.1.1 3D velocity fields

5.5.1.1.1 Horizontal velocity fields

The inferred horizontal velocity field has characteristics consistent with expected ice stream flow in Antarctica and qualitatively agrees with previously published velocity fields over Rutford (e.g. grayscale image in Fig. 5.14a, which comes from Rignot et al. (2011a)). Horizontal speeds over the CSK data collection, indicated by the colormap in Fig. 5.14a, range from ≈ 0.6 m/day in the northern extent of our observational domain to ≈ 1.1 m/day in the vicinity of the grounding line. The direction of ice flow, given by the vector field in Fig. 5.14a, curves eastward by approximately 45° within our observational domain from almost pure southerly flow in the upstream region to southeasterly flow in the downstream region. (Note that for clarity, the length of the vectors in Fig. 5.14a is constant.) Multiple tributary glaciers are present on both the east and west sides of Rutford. Mountain glaciers to the west have higher velocities than the tributary glaciers to the east, likely due to steeper surface slopes and higher topographically influenced accumulation rates.

A relatively low horizontal velocity zone is evident along the eastern wall of the ice shelf, defined at the landward extent by a patch projecting approximately a quarter of the local ice stream width into the main trunk (78.5° S, 82° W). The patch is located on the upstream side of a prominent high in the basal topography (Fig. 5.1d). The relatively low velocity region extends to the eastern boundary of the data domain and, as we later show, plays an important role in the response of the ice stream flow to tidal forcing. The relatively shallow basal topography and thick ice (Fig 5.1e) suggest that the shelf grounds in this region during low tide.

5.5.1.1.2 Vertical velocity fields

The up velocity field is broadly consistent with amplitudes expected for along-slope flow but reveals some high-frequency features of interest (Fig. 5.16b). Beginning upstream and moving in the flow direction, we see small-amplitude downward (values < 0 in Fig. 5.16b) motion that suggests thinning. In the same area, the ice stream flow direction is beginning to turn toward the east and the apparent thinning occurs on the outboard side of the turn where horizontal flow speeds are fast relative to the inboard (eastern) side of the ice stream. Immediately downstream of the area with slight thinning are three regions along the western ice stream margin that indicate uplift localized within the shear margin. These areas lie along the eastern extent of the Ellsworth Mountains. Uplift

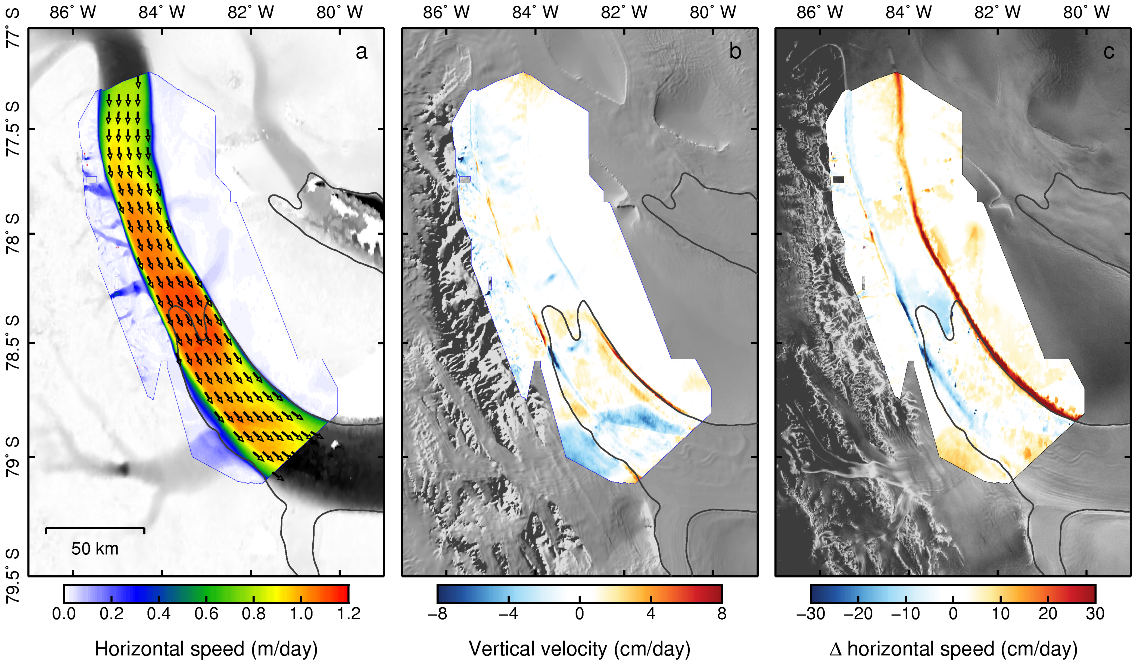

Figure 5.14: Secular velocity components. (a) Mean horizontal velocity: Colors indicate speed and vectors show flow direction. Vectors lengths are constant and are chosen only for clarity. (b) Mean vertical velocity, where positive values are moving upward. (c) Horizontal speed in (a) relative to horizontal speed from Rignot et al. (2011a); positive values indicate shower moving ice in (a). Spatial patterns in (b) and (c) are similar, suggesting that (b) indicates mean thickening over the timespan of CSK observations. Grayscale background images are: (a) horizontal speed from Rignot et al. (2011a), (b) MODIS mosaic of Antarctica 2009 (Haran et al., 2005; Scambos et al., 2007; Haran et al., 2014), and (c) RADARSAT-1 AMM-1 mosaic (Jezek et al., 2013). Grounding lines, traced by sinuous, dark gray lines, are the same as in Fig. 5.1.

is diminished where tributary glaciers flowing from the mountains intersect Rutford, suggesting that higher, steeper relief in the areas without tributary glaciers is partially responsible for the uplift. Later we show that the main areas of uplift are coincident with areas of high transverse normal strain rates and steep bathymetry. Further downstream, and approximately 40 km upstream of the grounding line, within the main trunk of the ice stream is an isolated patch of downward flow. This patch is within 10 km ($\sim$ 5 ice thicknesses) downstream of an area known to contain localized stiff basal sediments and a prominent bathymetric ridge bordered on the east and west by troughs filled with saturated, deforming sediments (King et al., 2009; Smith and Murray, 2009; Smith et al., 2015). To the east of this patch is a 30-km-long segment of downwelling coincident with a section of the shear margin that lies between two slow-flowing tributary glaciers.

In the vicinity of the grounding zone, we observe upstream thickening and downstream thinning. Thickening occurs landward of the bathymetric high located within the central trunk of the ice stream that causes the grounding line to take on a u-shape. We observe upward velocity in the western margin at the grounding zone in an area where the thickest ice within the grounding zone is being forced through the relatively narrow opening between the mountains and the bathymetric high in the center of the ice stream. Seaward of the grounding line is a section of relatively strong thinning localized in the shear margin and coincident with a tributary glacier whose flow is too slow to appear in the horizontal velocity field but that is evident from morphological features in optical imagery. The ice surface slope is steep in this area with the section of strong downward motion demarcating the higher elevation ice to the west of Rutford from the lower elevation ice within the ice stream (Fig 5.1c), which could account for the observed of downward flow of order 10 cm/day. Minnesota Glacier (MG), the large tributary glacier to the southwest in the extreme downstream area of the observational domain, indicates thinning at a rate of approximately 4 cm/day. As we discuss in the next paragraph, this apparent thinning is coincident with slower ice flow in our CSK velocity field relative to velocities reported by Rignot et al. (2011a). Therefore, MG must have slowed more than difference observed between our velocity field and Rignot et al. (2011a) and was speeding up during the CSK data acquisition. The potential cause for thinning and slowdown in this tributary glacier is unknown and is beyond the scope of this study.

The accuracy of vertical motion on the rest of the ice shelf is unclear. Synthetic tests discussed earlier indicate that we should expect small misfits in the vertical velocity component over the ice shelf because of unaccounted tidal motion and non-ideal viewing geometries. The standard deviation for the vertical component, which we discuss later in this section, is approximately equal to the values observed over the ice shelf. The large triangular-shaped patch of downward vertical motion in the center of the ice stream near the downstream extent of the observational domain is error caused by improperly fitting the quadratic plane to the stagnant ice during post-processing of the some of the displacement fields used to infer the velocity field.

5.5.1.1.3 Comparison with previous results

Comparison of our inferred horizontal velocity fields with results from Rignot et al. (2011a) shows consistency over the extent of the CSK observational domain (Fig. 5.14c). Positive values indicate slower speeds in our estimates and occur predominately along the eastern ice stream margin both inland and seaward of the grounding line. Ice within the central trunk of Rutford and within the central bend of the grounding line is moving approximately 10–15% faster in our data relative to Rignot et al. (2011a). But the most significant differences in terms of amplitude and width in the transverse-flow direction occur along the two ice stream margins and particularly the inboard (northeast) curve on the ice shelf. Large differences are also present in the eastern margin for approximately 75 km upstream of the grounding zone. Differences in horizontal speed taper off beyond 100 km inland of the grounding zone in the eastern margin, becoming slightly more pronounced in the northern extent of our observational domain. Differences in horizontal speed are less pronounced in the western margin and have the opposite sign as the relative speeds in the eastern margin. There is notably faster ice flow in our data, approximately 25 cm/day faster, within 30 km upstream of the grounding zone and markedly faster ice in our data along the western margin for approximately 50 km immediately downstream of the grounding zone. The most likely explanation for the disparity in shear margin speeds between the two datasets is the significant difference in spatial resolution. The CSK-derived velocity fields have an order of magnitude (≈ 45 m) finer resolution than the Rignot et al. (2011a) data (450-m grid spacing). Finer spatial resolution combined with the relatively high SNR ratio in the CSK data compared with the older satellite data used by Rignot et al. (2011a) allows sharper definition of the shear margins.

5.5.1.2 Velocity field error estimates

Formal errors in the secular velocity fields are typically less than 5% of the flow speed (Fig. 5.15a–c). Owing to the CSK viewing geometries, the north component generally has the highest absolute errors while the up component has the highest errors relative to its speed. The east component has the lowest errors because displacement fields that constrain the east component are azimuth offsets, which lie entirely in the horizontal plane, and are oriented within 45° of west. In other words, the east component is largely independent from the other two components and essentially has its own set of displacement fields to constrain the east motion. The north and up components, on the other hand, share the LOS displacement fields, resulting in strongly correlated errors (Fig. 5.15e–f). In general, formal errors are minimized at mid-latitudes within the observational domain because those areas have the highest number of scenes available for the inversion. As with any data stacking method, the uncertainly in inferred velocity fields decreases approximately as the square root of the number of scenes (Minchew et al., 2015; Simons and Rosen, 2015).

5.5.1.3 Strain and rotation rate tensors

Surface velocity fields provide direct estimates of areal strain rates, which can be related to stress through a constitutive relation. Our posterior model includes only secular and periodic components of displacement (Eq. 5.4), so we define the total velocity at a given position and time as:

$$\mathbf{u}\left(x,y,t\right) = \mathbf{v}(x,y) + \sum_{i=1}^{k} \dot{\mathbf{p}}_i(x,y,t) \tag{5.45}$$

where:

$$\dot{\mathbf{p}}_i = \omega_i \begin{bmatrix} \cos\left(\omega_i t + \phi_i^e\right) \\ \cos\left(\omega_i t + \phi_i^n\right) \\ \cos\left(\omega_i t + \phi_i^u\right) \end{bmatrix} \tag{5.46}$$

and overhead dots indicate time derivatives. The Jacobian of the velocity field can be decomposed in to a symmetric strain-rate tensor and an antisymmetric rotation rate tensor whose components are defined respectively as:

$$\dot{\varepsilon}_{\hat{x}\hat{y}} = \frac{1}{2}\left(\frac{\partial u_{\hat{x}}}{\partial \hat{y}} + \frac{\partial u_{\hat{y}}}{\partial \hat{x}}\right) \tag{5.47}$$

$$\dot{\mathrm{w}}_{\hat{x}\hat{y}} = \frac{1}{2}\left(\frac{\partial u_{\hat{x}}}{\partial \hat{y}} - \frac{\partial u_{\hat{y}}}{\partial \hat{x}}\right) \tag{5.48}$$

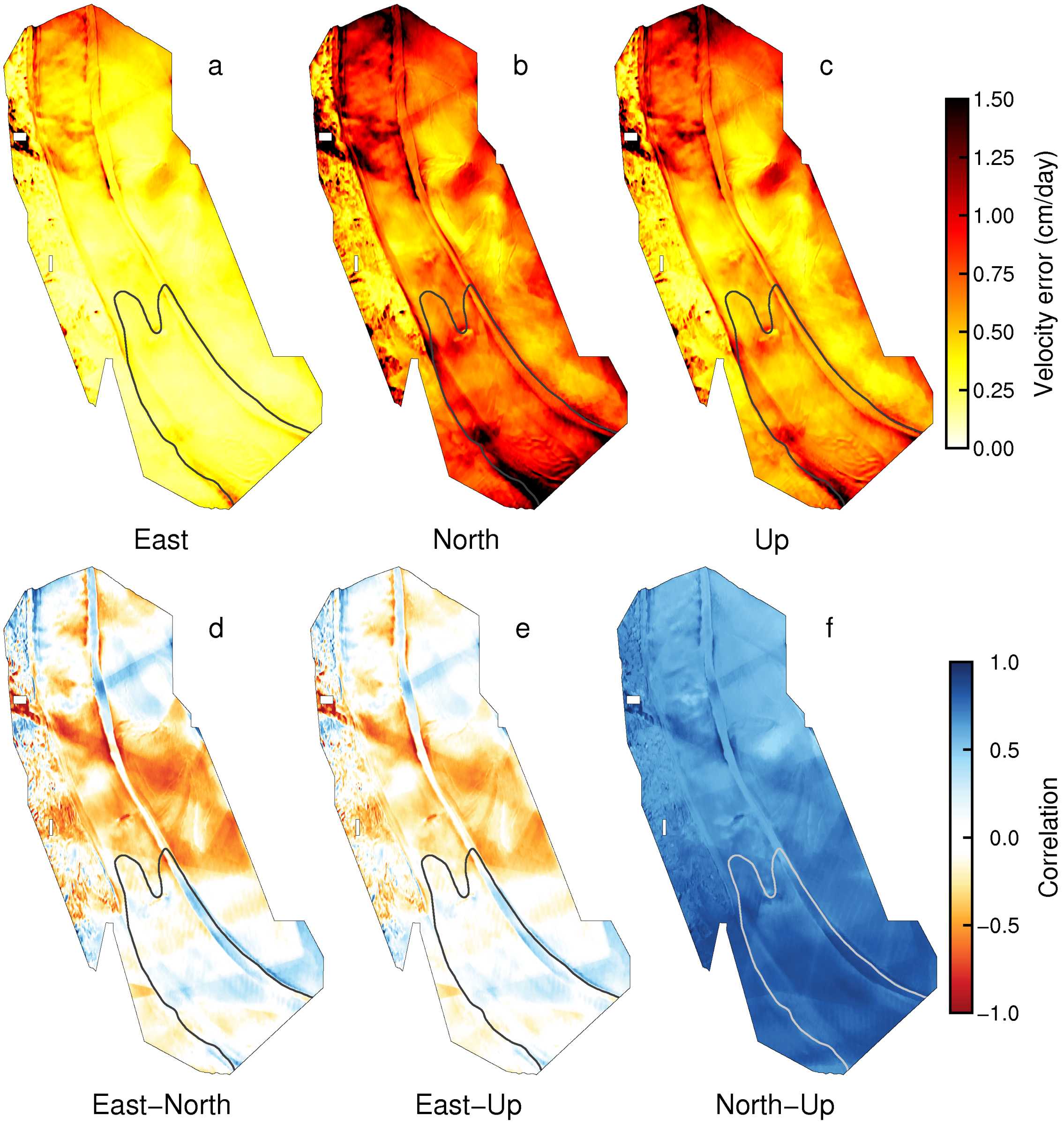

Figure 5.15: Formal errors and correlation in secular velocity components calculated from the posterior model covariance matrix, $\widetilde{\mathbf{C}}_m$. (a–c) Formal errors for (a) east, (b) north, and (c) up velocity components. Note that the error scale is cm/day, meaning that errors within the ice stream rarely exceed 5% of the observed velocity. (d–f) Correlation between (d) east and north, (e) east and up, and (f) north and up secular velocity components. Grounding lines are the same as in Fig. 5.1.

where $\hat{x}$ and $\hat{y}$ are orthogonal coordinate dimensions. From Eqs. 5.45–5.47 we can derive the total time-dependent strain-rate tensor components as:

$$\dot{\varepsilon}_{\hat{x}\hat{y}} = \dot{\varepsilon}'_{\hat{x}\hat{y}} + \dot{\varepsilon}''_{\hat{x}\hat{y}} \tag{5.49}$$

$$\dot{\varepsilon}'_{\hat{x}\hat{y}} = \frac{1}{2}\left(\frac{\partial \mathrm{v}_{\hat{x}}}{\partial \hat{y}} + \frac{\partial \mathrm{v}_{\hat{y}}}{\partial \hat{x}}\right) \tag{5.50}$$

$$\begin{aligned} \dot{\varepsilon}''_{\hat{x}\hat{y}} = \frac{1}{2}\sum_{i=1}^{k}\omega_i\Big[&\cos\left(\omega_i t + \phi_i^{\hat{x}}\right)\frac{\partial a_i^{\hat{x}}}{\partial \hat{y}} + \cos\left(\omega_i t + \phi_i^{\hat{y}}\right)\frac{\partial a_i^{\hat{y}}}{\partial \hat{x}} - \\ & a_i^{\hat{x}}\sin\left(\omega_i t + \phi_i^{\hat{x}}\right)\frac{\partial \phi_i^{\hat{x}}}{\partial \hat{y}} - a_i^{\hat{y}}\sin\left(\omega_i t + \phi_i^{\hat{y}}\right)\frac{\partial \phi_i^{\hat{y}}}{\partial \hat{x}}\Big] \end{aligned} \tag{5.51}$$

where $\dot{\varepsilon}'_{\hat{x}\hat{y}}$ and $\dot{\varepsilon}''_{\hat{x}\hat{y}}$ are the secular and periodic strain rates, respectively. Similarly, we can decompose the rotation rate tensor into secular and periodic tensors: $\dot{\mathrm{w}}_{\hat{x}\hat{y}} = \dot{\mathrm{w}}'_{\hat{x}\hat{y}} + \dot{\mathrm{w}}''_{\hat{x}\hat{y}}$. The areal divergence of velocity is equal to the trace, or first tensor invariant, of the strain rate tensor, which is nonzero in areas where the apparent volume of ice is changing, due to damage, or in areas which vertical motion, which may be balanced by mass accumulation or ablation. Effective strain rate, $\dot{\varepsilon}_e$, is calculated from the second invariant of the strain rate tensor, $\dot{\boldsymbol{\varepsilon}}$, and is defined as:

$$\dot{\varepsilon}_e = \sqrt{\left[\mathrm{tr}\left(\dot{\boldsymbol{\varepsilon}}\dot{\boldsymbol{\varepsilon}}\right) - \mathrm{tr}\left(\dot{\boldsymbol{\varepsilon}}\right)^2\right]/2} \tag{5.52}$$

Assuming $\dot{\varepsilon}'_{\hat{x}\hat{y}}$ and $\dot{\varepsilon}''_{\hat{x}\hat{y}}$ are uncorrelated, we can decompose effective strain rate into secular and period terms as:

$$\dot{\varepsilon}_e = \dot{\varepsilon}'_e\sqrt{1 + \left(\dot{\varepsilon}''_e/\dot{\varepsilon}'_e\right)^2} \tag{5.53}$$

Ice flow over the grounded ice in our observational domain is primarily due to slip at the ice-bed. Velocity is constant with depth when ice is afloat. Consequently, $\dot{\varepsilon}_{\hat{z}\hat{z}} = 0$ at the surface—which is the commonly applied stress boundary condition at the free surface in numerical models. Furthermore, $2\dot{\varepsilon}_{\hat{x}\hat{z}} \approx 2\dot{\varepsilon}_{\hat{z}\hat{x}} \approx \partial u_{\hat{z}}/\partial\hat{x}$, where $\hat{x}$ is a horizontal dimension and $\hat{z}$ is vertical (e.g. Morlighem et al., 2013). The vertical rotational tensor components are proportional to the respective vertical strain rate components such that $\dot{\mathrm{w}}_{\hat{x}\hat{z}} = -\dot{\mathrm{w}}_{\hat{z}\hat{x}} = -\dot{\varepsilon}_{\hat{x}\hat{z}}$. These relationships and the assumption of a stress-free ice surface result in six unique, nonzero strain and rotation rate tensor components, plus the two strain rate tensor invariants (Fig. 5.16). We filtered each of these eight strain fields using a Gaussian filter with a 6-standard-deviation width of 4 km, or approximately 2 ice thicknesses.

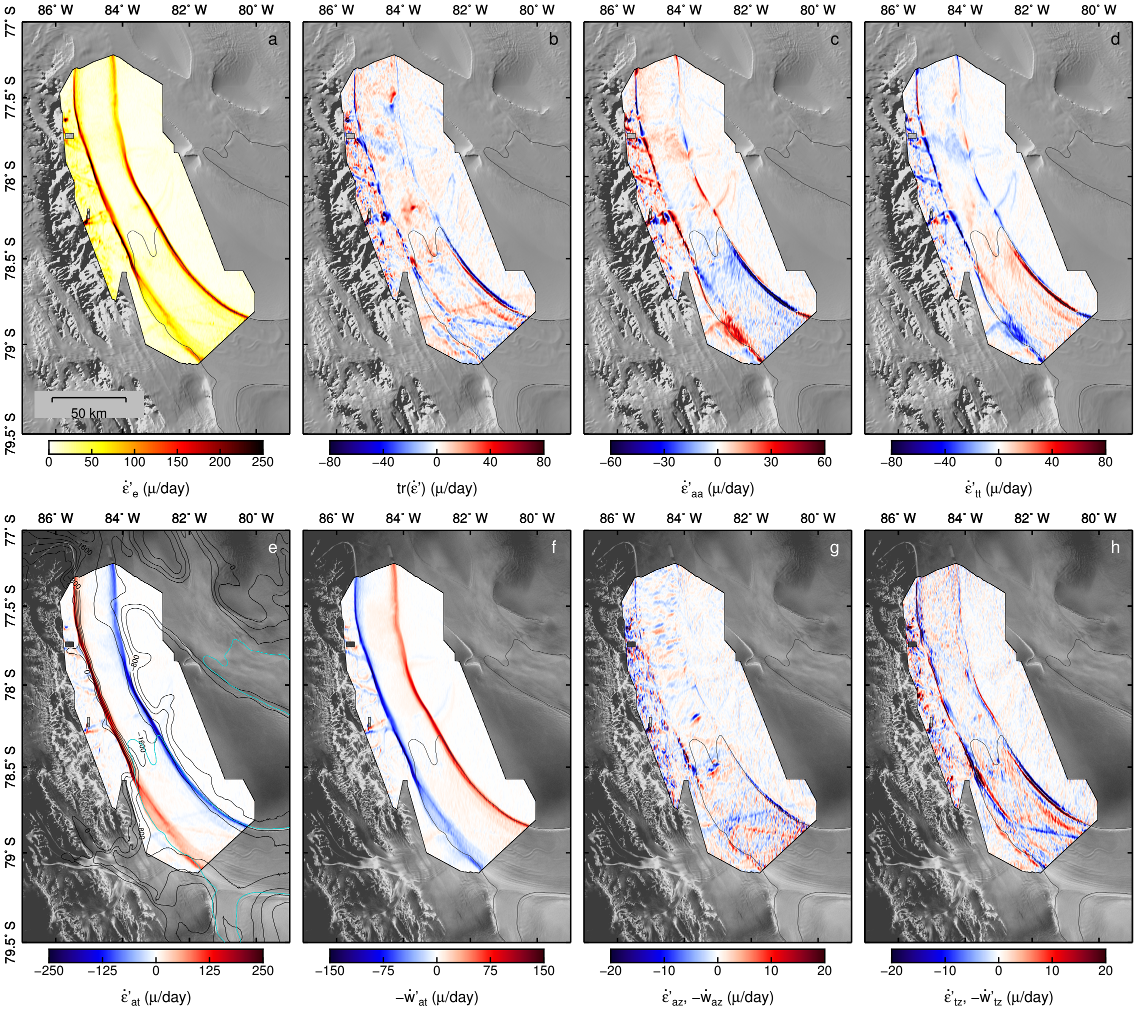

Figure 5.16: Unique, nonzero components of the micro (μ) secular strain rate and rotational tensors. All values are given in a local along-flow (subscript a), transverse- or across-flow (subscript t), up (subscript z) coordinate system. (a–b) Strain rate tensor invariants: (a) effective strain rate (Eq. 5.53) and (b) velocity divergence. (c) Along-flow and (d) across-flow deviatoric normal strain rates. (e) Lateral shear strain rate and (f) lateral rotation rate. Contour lines in (e) are bathymetry from Bedmap2. (g–h) Vertical shearing and rotation (g) along flow and (h) across flow. Background grayscale images are (a–d) MODIS mosaic of Antarctica and (e–h) RADARSAT-1 AMM-1 mosaic. Grounding lines are the same as in Fig. 5.1.

5.5.1.3.1 Effective strain rate

Rutford's lateral margins are delineated by high effective and shear strain rates. These strain rates are well resolved everywhere in the observational domain (Fig. 5.16). Secular effective strain rates are highest in the margins of the ice stream in most of the observational domain. The highest effective strain rates generally occur in areas overlying steep bathymetry, where the ice stream narrows, and where there are no incoming tributary glaciers. Effective strain rates are low in the margin within an approximately 60-km long region in the western margin of the ice shelf that aligns with MG, which is flowing from the southwest (Fig. 5.16a). In this area, ice from MG merges with the main ice stream flow, reducing effective strain rates.

5.5.1.3.2 Horizontal velocity field divergence

Divergence in the secular velocity field is small within most of the ice stream (Fig. 5.16b), consistent with the commonly applied assumption that ice is incompressible, and high in some localized areas and within portions of the shear margin. Where divergence is high and spatially localized, we expect the ice to be damaged due to local changes in ice volume (positive values denote extension and negative values indicate compression) or to have relatively steep ice surface gradients resulting from localized uplift or downwelling caused by nonzero spatial gradients in basal shear traction or topography. Damage often appears as bright areas in radar amplitude images, because damaged areas tend to scatter more energy back to the radar than non-damaged areas, while steep surface slopes will appear in optical imagery but may be less apparent in radar images because radar penetrates to a wavelength-dependent depth of order meters below the ice surface (Ulaby et al., 1986; Rignot et al., 2001). We observe coincident areas of high divergence in the inferred velocity fields and high radar backscatter amplitude in CSK amplitude images (not shown) and the RADARSAT-1 AMM-1 mosaic (Jezek et al., 2013). Areas of modest, but non-zero, divergence spread over several ice thicknesses are present in the upstream extent of the observational domain and are coincident with hummocky features in the MODIS mosaic of Antarctica 2009 (MOA) (Haran et al., 2005; Scambos et al., 2007; Haran et al., 2014). Strong localized divergence is manifest near the eastern shear margin in the upstream extent of the observational domain where flowing ice first encounters the Filchner Promontory, the elongated high in basal topography that forms most of Rutford's eastern boundary. Approximately 40 km upstream of the grounding zone and near the center of the ice stream trunk we observe high velocity divergence localized in an area not more than a few km across. This feature is present as an isolated region of downwelling in the vertical velocity field and is coincident with localized stiff basal sediments and a prominent bathymetric ridge (King et al., 2009; Smith and Murray, 2009; Smith et al., 2015). Within the grounding zone, we observe localized high velocity divergence within the u-shaped bend, approximately 3 km southwest of the downstream extent of the grounding zone bend, and in the western ice stream margin directly across flow from the grounding zone bend where the bathymetric channel protrudes slightly into the the path of the ice flow. Along the eastern margin on the ice shelf, we see extensional strain inboard and compressional strain outboard of the curve. Divergence in this part of the shelf is beaded, a pattern that is reflected in the morphology shown in the underlying MOA imagery. This section of high divergence is located directly across flow from MG where the bathymetry is relatively flat, the shear margin is poorly defined, and, as we later show, the width of the ice stream changes at fortnightly periods more dramatically than anywhere else in the observational domain.

5.5.1.3.3 Normal strain rates

Along- and transverse-flow deviatoric strain rate components have some of the highest values in the shear margins where bathymetry is steep and where tributary glacier meet the main ice stream. But the highest deviatoric normal strain rates are located in the eastern shelf margin where strong divergence is observed. Along flow normal strain rates are oriented against the flow in this part of the shear margin while transverse flow normal stresses act outward. In both normal strain components, we note a rapid sign change in the eastern shear margin immediately downstream of MG where the bathymetry begins to shallow to a nunatak just beyond the observational domain (approximately 79.3 °S, 81.5 °W).

5.5.1.3.4 Lateral shear strain and rotation rates

Lateral shearing is strong in the ice stream margins and diminishes to near zero within the main trunk of the ice stream because of the nonlinear rheology of ice and shear heating, damage, and ice fabric reorientation in the margins (Fig. 5.16e) (e.g., Echelmeyer et al., 1994; Hudleston, 2015). Lateral shear rates are high where the ice stream is bounded by steep bathymetry, with maximum values located in areas where bathymetry is steepest along both the east and west margins. Shearing is relatively low in the upstream eastern margin, where bathymetric slopes are shallow, and in the ice shelf margins. The lowest shear rates within the margins are coincident with the suture zone where MG intersects the main flow from Rutford. Shearing increases, relative to its upstream value, as ice approaches the nunatak at 79.3 °S, 81.5 °W. The first-order thickness of the shear margins everywhere in the ice stream varies as the inverse of the shear strain rate and the thinnest shear margins are co-located with the highest secular horizontal speeds. Lateral rigid body rotation rates are highest in the shear margins and behave much like lateral shear strain (Fig. 5.16f). Due to the relatively small normal strain rates, lateral solid body rotation rates are approximately half the coincident lateral shear strain rates.

5.5.1.3.5 Vertical strain rates

Along- and transverse-flow vertical shear strain rates have lower values in general than all other strain and rotation rate components (Fig. 5.16g–h). Like lateral shear strain rates, both vertical shear strain rate components are typically near zero along the central trunk. Unlike lateral shear strain rates, the vertical shear components have high frequency features of interest. In the upstream region, along-flow vertical shearing indicates hummocky patterns similar in character to those observed in MOA. Given the broad spatial scales of velocity divergence values in this area, it is likely that they these surface features are due to roughness along the bed. Approximately 40 km upstream of the grounding zone, in the area of downwelling and strong divergence, we observe a strain doublet, which indicates compression on the upstream side of the area of rigid sediment. A complementary doublet that is rotated approximately 90° and has less than a quarter the magnitude, occurs in transverse vertical shear at the same location. In the central bend of the grounding zone, we observe a similar strain doublet. This doublet extends westward from the central grounding zone by approximately 3–5 km into the flow path of ice traversing the grounding zone through the western horn. Along the western margin immediately upstream of the grounding zone, we observe a 10-km-long stretch of strong vertical shearing whose downstream end features a multi-km-scale section of compressive along-flow vertical strain. This same area indicates high transverse vertical strain, owing to the fact that vertical velocity is concentrated in the ice stream margin in this area. High extensive-inboard, compressive-outboard transverse vertical strains are present though half of the observed western ice stream margin and are complemented by slightly higher transverse vertical strain rates in the eastern margin. A broad stretch of moderate transverse vertical strain rates is evident approximately 3 km inboard of the eastern shear margin near the downstream extent of the observational domain.

5.5.2 Periodic deformation fields

Vertical uplift caused by ocean tides drives horizontal flow variability. Because of the dependence of horizontal flow variations on vertical motion over the ice shelf, we begin with estimates of vertical periodic motion before presenting results for horizontal periodic motion.

5.5.2.1 Vertical motion

The M_2 and O_1 tidal constituents have the largest vertical amplitudes of all the tidal frequencies that are observable with CSK. In order of decreasing amplitude at approximately 20 km seaward of the Rutford grounding zone, we expect M_2, S_2, O_1, and K_1 tides (Padman et al., 2002; Padman and Fricker, 2005). Solar semi-diurnal, S_2, and solar diurnal, K_1, tides are aliased by the repeat-pass time interval of CSK. In the vertical component, M_{sf} has an amplitude that is more than two orders of magnitude smaller than M_2 and about 20 times smaller than O_1. We therefore discuss results only at M_2 and O_1 frequencies for brevity, but note that the inferred M_{sf} amplitudes are approximately equal to the value given in Table 5.2 over the ice shelf and are near-zero over grounded ice, consistent with GPS measurements from Gudmundsson (2006).

5.5.2.1.1 Lunar semi-diurnal component

Vertical M_2 amplitude and phase values are broadly consistent across the central trunk of the ice stream (Figs. 5.17a–b and 5.18a) and are in good agreement with the CATS2008a_opt regional tidal model, whose predicted tidal amplitudes fit co-located GPS observations (Padman et al., 2002; Padman and Fricker, 2005; Gudmundsson, 2006). Amplitudes decrease quickly in the vicinity of the grounding zone while the respective phase values—in areas with amplitudes high enough to give reasonable estimates of phase—lag (< 0) by approximately 20 minutes in most areas within approximately 10 km of the grounding zone. Phase lag within the grounding zone is most prevalent and has the largest areal extent within the two horns that mark the immediate downstream side of the grounding zone of Rutford. Comparing the two horns, we observe roughly symmetric phase values and asymmetric amplitudes, where amplitudes in the western horn are a factor of two larger than in the eastern horn (Fig. 5.18c). Landward of the grounding zone, we observe zero amplitude for the M_2 component. Amplitude and phase values have small standard deviations relative to their absolute values (Fig. 5.17c–d). Consistent with the results from the synthetic test, the uncertainties estimated from the posterior model covariance matrix, $\widetilde{\mathbf{C}}_m^{-1}$, are well within 5% of the inferred value over the majority of the area inferred to have significant vertical motion at M_2 periods.

5.5.2.1.2 Lunar diurnal component

Vertical O_1 amplitude and phase values have greater spatial variability than M_2 values but are in good agreement with CATS2008a_opt predictions (Figs. 5.17e–f and 5.18b). As with M_2 amplitudes, O_1 amplitudes decrease rapidly within approximately 10 km of the grounding zone and are near-zero over grounded ice (Fig. 5.18d). Over the central trunk, we observe large areas, coincident with a region of high amplitudes, where the O_1 phase leads (> 0) the rest of the ice shelf. These areas are within 50 km of the central trunk grounding zone and occupy the deepest ice shelf draft in the observed section of the shelf. (True bathymetry is unknown in this part of the shelf (Fretwell et al., 2013).) Near the northeastern margin of the ice shelf, and coincident with the area of relatively low secular horizontal velocity (Fig. 5.14a), we observe a phase lag of order one hour in the inferred O_1 vertical field. All of the features discussed here are larger than the estimated uncertainties (Fig. 5.17g–h). According to these uncertainty estimates, amplitude and phase values in areas with strong O_1 signal, are approximately 5% and rarely exceed 10% of the respective measured value.

5.5.2.2 Horizontal fields

Low-frequency variations are dominant in horizontal ice flow (Gudmundsson, 2006, 2011; Murray et al., 2007; Aðalgeirsdóttir et al., 2008). GPS observations at 40 km upstream of the grounding line show that horizontal amplitudes at M_2 and O_1 frequencies are more than an order of magnitude smaller than at M_{sf}, with both M_2 and O_1 imparting sub-centimeter-scale amplitude variations. For brevity and due to the disparity in amplitudes, we discuss only results for the horizontal component of M_{sf}-period variations. We note that inferred M_2 and O_1 amplitudes are at least an order of magnitude smaller than M_{sf} amplitudes in the areas of interest.

5.5.2.2.1 Along-flow periodic variations

Along-flow, or longitudinal, M_{sf}-period amplitude and phase values (Fig. 5.19a–b) agree with results from local GPS surveys (Fig. 5.20) (Gudmundsson, 2006; Murray et al., 2007; Aðalgeirsdóttir et al., 2008). Our inferred M_{sf}-period values indicate spatial variability in grounded and floating ice, though tidal responses landward of the grounding zone are less pronounced than over the shelf, in areas not covered by previous GPS surveys. Along-flow amplitudes increase smoothly across the grounding zone in the central flowline and are, on average, at least twice the upstream values at

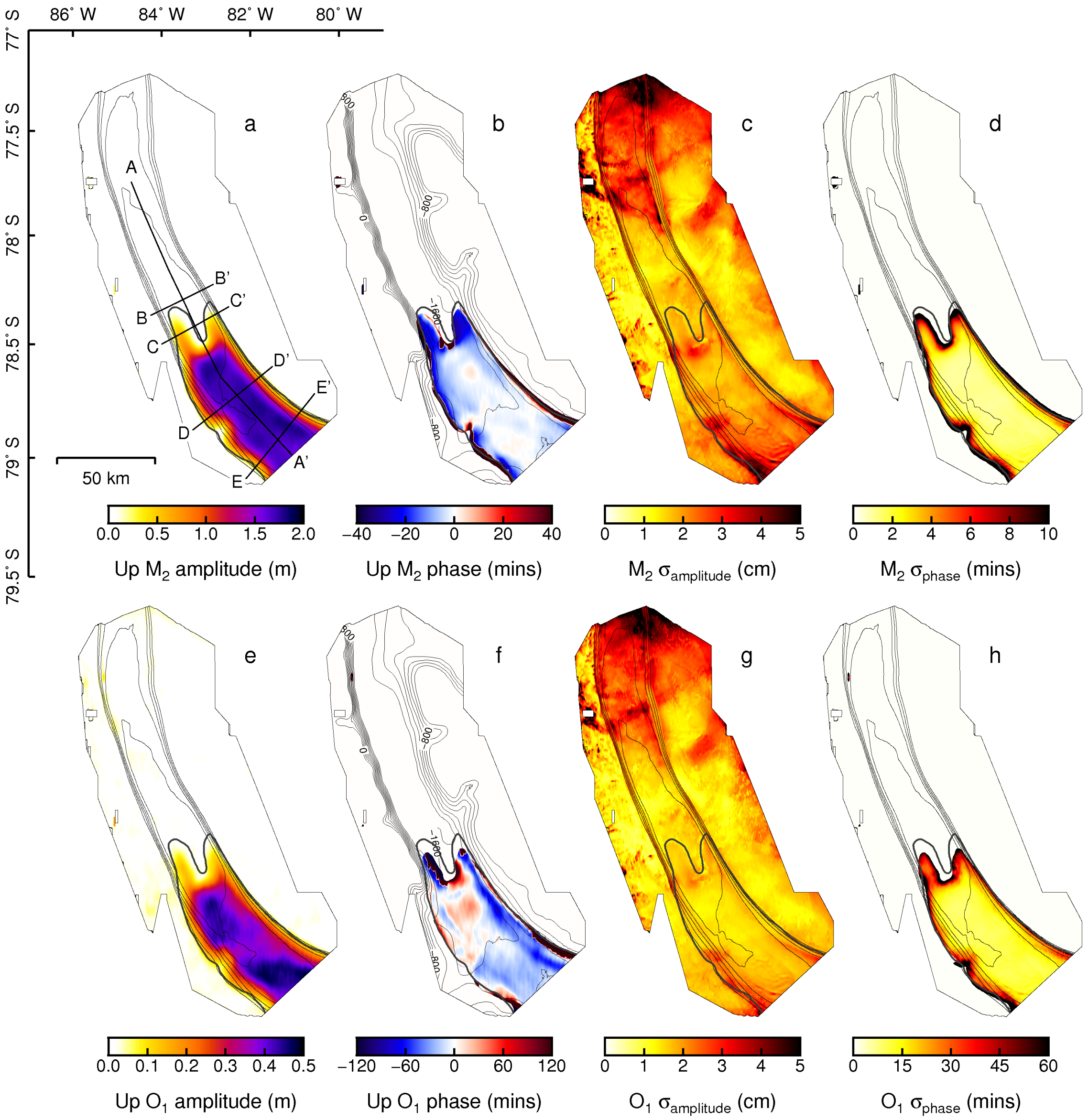

Figure 5.17: Time-dependent vertical velocity components for the (a–d) M_2 lunar semi-diurnal and (e–h) O_1 lunar diurnal tidal periods. (a) Vertical amplitude for the M_2 tide with dark, thin contour lines showing horizontal secular speed in 0.2 m/day increments. (b) Vertical M_2 phase relative to the median M_2 phase over the ice shelf. Contour lines are bathymetry from Bedmap2 in 400-m increments. Areas with amplitude < 10 cm are set to zero for clarity. (c–d) Standard deviation of vertical M_2 amplitude and phase, respectively, with contour lines as in (a). Phase errors are set to zero in the same areas as in (b). (e–h) are the same as (a–d) but for O_1 values. Grounding lines are the same as in Fig. 5.1.

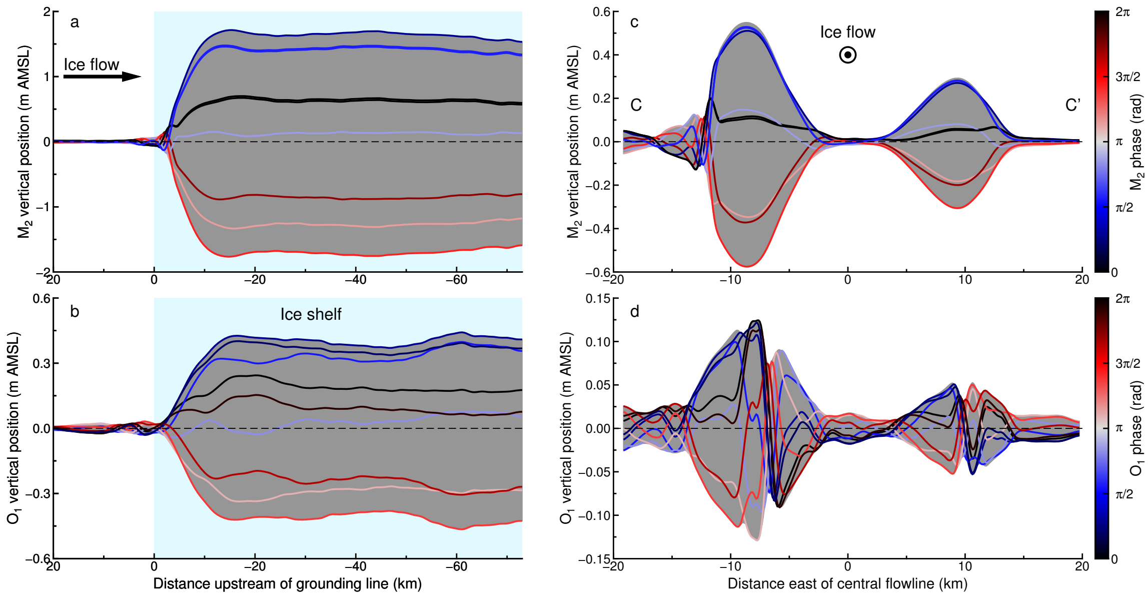

Figure 5.18: Time-dependent vertical velocity components along transects (a–b) A–A' (truncated to 20 km upstream of the grounding zone) and (c–d) C–C' for inferred (a and c) M_2 and (b and d) O_1 tidal constituents. See Fig. 5.17 for transect locations.

±20 km from the grounding zone. Beyond 85 km downstream of the grounding zone, along-flow M_{sf} amplitudes are effectively zero, meaning that inferred amplitudes are typically less than one standard deviation in estimated uncertainty (Fig. 5.19c). The largest amplitudes, by a significant margin, are along the southwest ice stream margin and are strongest where MG intersects the main ice stream flow. High amplitudes are manifest at the extreme downstream end of the observational domain in the vicinity of a known deep bathymetric trough (Fig. 5.1d).

In general, the ice shelf leads the grounded ice in tidal response. Leading (positive) phase values are present along much of the ice stream trunk. Among the first areas to accelerate is the downstream portion of the western grounding zone horn, where some of the thickest ice, supported by the deepest bed under Rutford, goes afloat. This horn provides the wider of two passages between the bathymetric channel sidewalls and the central bump that pins the grounding line at the downstream extent of the u-shaped bend and features larger vertical M_2 and O_1 period uplift than the eastern horn. Leading phase values extend downstream from the western horn into the central trunk—with the exception of a lagging (negative-valued) egg-shaped feature that, as we discuss later, is likely a pinning point—and diminish immediately downstream of the region with leading O_1 phase values (Fig. 5.17f). Leading phase values are also present in the downstream extent of the central trunk. Lagging phase values are manifest along the northeastern shelf margin, where we

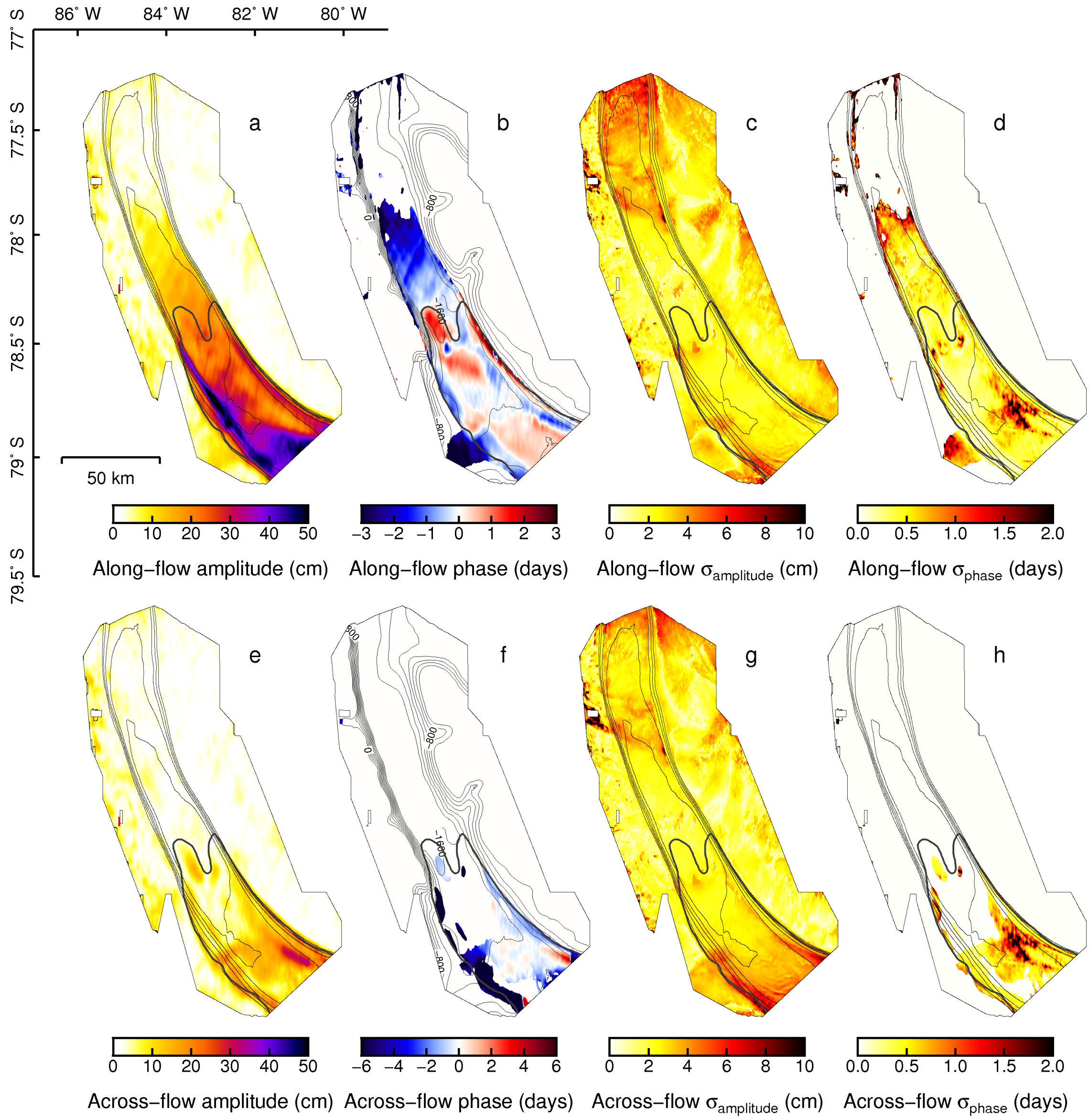

Figure 5.19: Time-dependent (a–d) along-flow and (e–h) across-flow horizontal velocity components for the M_{sf} (14.77-day) tidal period. (a) Along-flow amplitude with contour lines showing horizontal secular speed in 0.2 m/day increments. (b) Along-flow phase relative to the median along-flow M_{sf} phase over the ice shelf. Contour lines are bathymetry from Bedmap2 in 400-m increments. Areas with small amplitude and horizontal secular velocity are set to zero for clarity. (c–d) Standard deviation of along-flow amplitude and phase, respectively, with contour lines as in (a). Phase errors are set to zero in the same areas as in (b). (e–h) Same as (a–d) but for across-flow M_{sf}-period variability. Phase values in (f) are referenced to the median along-flow M_{sf} phase over the ice shelf as in (b). Grounding lines are the same as in Fig. 5.1.

observe relatively slow secular ice flow. MG experiences tidal variability with approximately the same amplitude as upstream areas on Rutford, but lags variations on the ice shelf by 3 days or more. We observe no clear spatial correlation between amplitude and phase values.

5.5.2.2.2 Cross-flow periodic variations

The margins of the ice stream and shelf are largely constrained by bathymetry, causing the flow direction to remain approximately constant, the M_{sf} cross-flow amplitude to be near zero, and the cross-flow phase to be approximately constant over most of the observational domain (Figs. 5.19e–f). Significant cross-flow variations occur on both the east and west side of the u-shaped grounding line bend, with most of the cross-flow variations occurring in the western horn. The largest cross-flow variations occur in the extreme downstream region of the observational domain. Cross-flow amplitude increases markedly coincident with the intersection of MG and the main ice stream flow. A localized region containing the highest across-flow amplitudes is manifest near the eastern shelf margin at the downstream extent of the observational domain. This feature is coincident with a relative low in along-flow amplitude, slow secular horizontal velocity, and a region of wide lateral secular shearing, strong secular velocity divergence and strong secular transverse-vertical shearing (Fig. 5.16). Taken together, these observations suggest that the ice stream grounds on this portion of the shelf during low tide.

In the downstream areas of interest where the strongest tidally induced variations in ice flow are expected, the CSK-derived velocity fields have estimated amplitude errors that are typically within 10% of the observed M_{sf} along-flow amplitude and have phase errors less than 0.5 days (Figs. 5.19c–d). Aside from an isolated patch of high phase error near the east margin of the ice shelf, phase errors in areas with amplitude values > 5 cm are relatively consistent and are much less than the spatial variance observed in the phase field. Standard deviations in M_{sf} across-flow amplitude and phase are consistent with along-flow amplitude and phase standard deviations (Figs. 5.19g–h). These relatively small uncertainties allow for a detailed analysis of the upstream propagation of M_{sf}-period flow variability and the influence of basal topography on horizontal ice flow both upstream and downstream of the grounding zone.

5.5.2.2.3 Propagation of tidal signal

Longitudinal M_{sf}-period flow variability propagates upstream of the grounding zone at a mean rate of approximately 25 km/day (0.28 m/s) within the first 30 km and at a faster mean rate of 33 km/day (0.38 m/s) between 40 and 80 km upstream of the grounding zone. Amplitudes in along-flow M_{sf} variability are damped at a near-constant mean rate of 2.6 mm/km over 80 km upstream (Figs. 5.19a–b and 5.20). Despite point-wise agreement between the SAR-derived and GPS-measured M_{sf} amplitude and phase values, propagation and damping rates are notably different. Estimates of upstream M_{sf} along-flow propagation are almost an order of magnitude slower in the CSK-inferred fields relative to speed estimated from GPS data by Gudmundsson (2006) but agree with estimates from data presented by Murray et al. (2007). Damping rates are consistent with both GPS studies, but are slightly higher than those inferred by Gudmundsson (2006) from 4 GPS stations located along the central flowline. The most likely explanation for disparities between our estimates and those of Gudmundsson (2006) is the limited duration and the season of the GPS data collection. The co-linear GPS data were collected for approximately two months during the austral 2003/2004 summer. The limited duration of the data makes it impossible to separate from the M_{sf} component contributions from the lunar fortnightly, M_f and lunar monthly, M_m, tides, which have similar periods to and whose amplitudes are within an order of magnitude of M_{sf}. Two months is also too short a time series to allow for inferences of the strong seasonal and annual variability on Rutford, which reach a minimum during the austral summer (Murray et al., 2007). CSK observations spanned approximately 9 months and though we are unable to uniquely infer annual, seasonal, M_f and M_m variability, we showed in the synthetic results that our sampling rate is sufficient to solve for accurate solutions for M_{sf} alone.

Amplitude and phase values are sensitive to ice thickness resulting from variations in bathymetry over grounded and floating ice (Figs. 5.20 and 5.21). Inland of the grounding zone, this sensitivity is most distinct in the vicinity of the prominent bump and upstream deepening of the bathymetry between 30 and 40 km inland. At and immediately downstream of the bump, M_{sf} amplitudes decrease by more than 10% and phase lags by approximately 6 hours while both increase by the approximately the same amounts upstream of the bump. These observations indicate that the tidal signal is being transmitted around the bump such that ice on the seaward side feels the perturbation first, followed by the leeward side, and last ice flow over the bump is perturbed. Phase lags by more than a day and amplitude decreases by approximately 30% landward of the bump where bathymetry is the deepest along this transect. This deep section corresponds to the region with higher M_{sf}-period propagation speeds. It is unclear whether the deeper bed, and consequently thicker ice, in this part of the ice stream leads to the observed increase in propagation speed, or if the mechanical properties of the bed or the ice stream margins in the upstream region differ from those downstream.

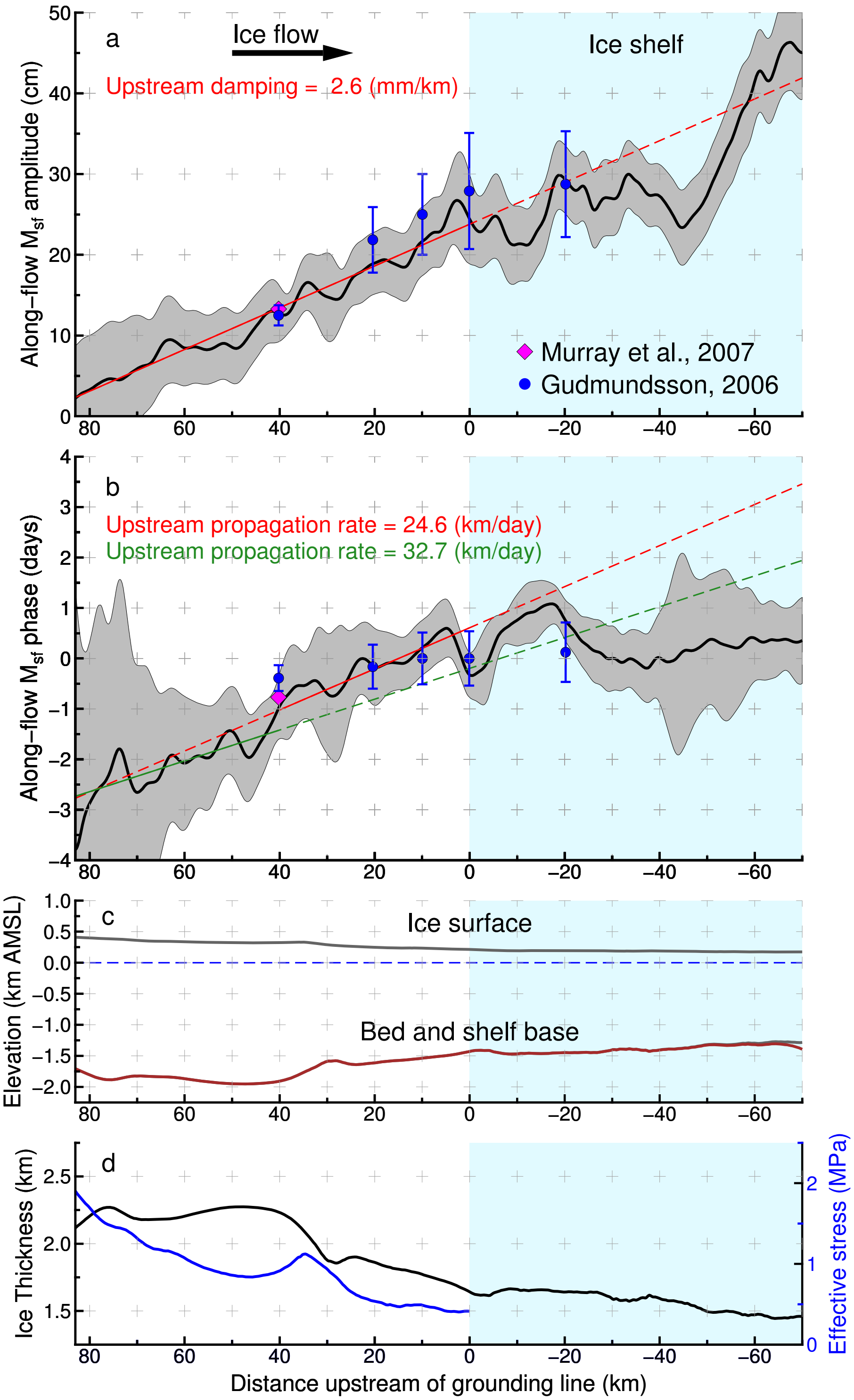

Figure 5.20: Longitudinal M_{sf} (a) amplitude and (b) phase values along transect A–A' with co-located, non-contemporaneous GPS observations from (magenta diamond) Murray et al. (2007) and (blue circles) Gudmundsson (2006). Gray-shaded region around the lines and error bars on the GPS data indicate 2 standard deviations about the measured value. (c–d) Collocated ice stream geometry from Bedmap2. Effective stress is calculated as $N = \rho g h - \rho_{sw} g s_b$, where ρ_{sw} is the density of seawater and s_b is the depth of the bed.

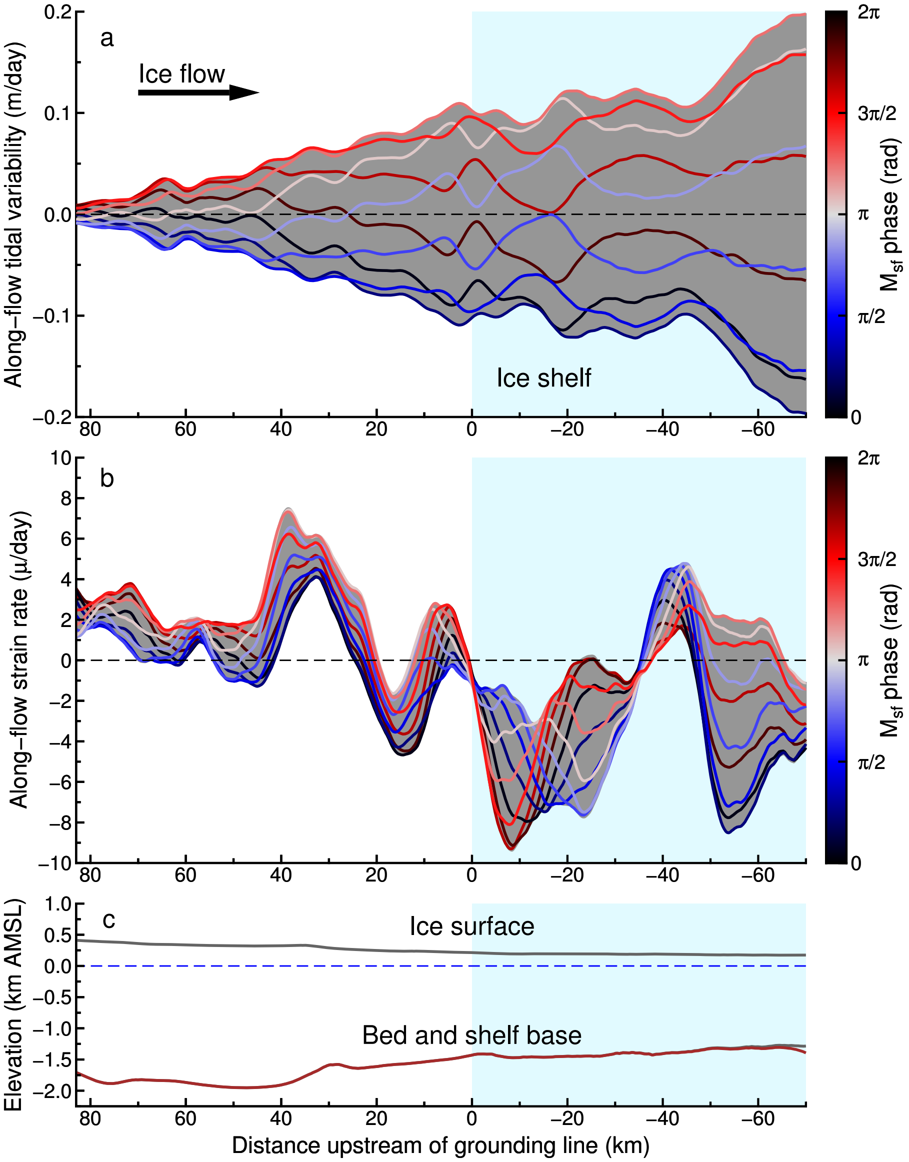

Figure 5.21: M_{sf}-period longitudinal (a) flow variability, (b) strain rates, and (c) ice stream geometry along transect A–A'. Line colors in (a) and (b) indicate time relative to the beginning of the cycle. Gray-shaded region shows the full extent of the respective value in each panel. The light-blue shaded regions in both panes indicate flowing ice. Geometric data are from Bedmap2.

Interaction of floating ice and solid features on the bed, commonly called pinning points, is of particular interest because of their potential to change the ice shelf buttressing, or back-stress. As discussed previously, we observe several areas over the ice shelf where ice grounds at low tide. These features are not initially apparent in the M_{sf} amplitude and phase values (Fig. 5.20), but are readily apparent in transects of the M_{sf}-period horizontal flow variability and total along-flow strain rate (Fig. 5.21) Over the ice shelf and in the grounding zone, we observe amplitude and phase responses at two notable bumps in basal topography: one at -2 km and the other at -32 km along the A–A' transect (see Fig. 5.17a for transect position). These same bumps manifest as nodal points in the along-flow strain rate, where strain rate remains approximately constant throughout the M_{sf} cycle and switches signs between ice upstream and downstream of the points. Phase lags at these pinning points by approximately 1 day relative to the downstream phase, an effect that is facilitated by perturbation propagating around the pinning point and that is visible in the along-flow tidal variability transect (Fig. 5.21a).

5.5.2.2.4 Profiles of tidal variability

Transverse-flow transects of the horizontal speed, along-flow M_{sf} variability, and ice stream geometry provide insight into the response of Rutford to tidal forcing, the role of ice stream geometry, and the mechanical properties of the ice (Fig. 5.22). Here we consider three transverse-flow transects denoted B–B', D–D', and E–E' in Fig. 5.17a. The former transect, B–B', is approximately 10 km upstream of the landward extent of the grounding zone while the other two transects are on the shelf. Transect D–D' is immediately upstream of MG and E–E' is near the downstream extent of the observational domain.

Broadly speaking, the shapes of horizontal flow speed in the transverse direction differ between grounded and floating ice while the shapes of along-flow M_{sf} variability are broadly similar between the three transects. Horizontal speed is asymmetric over the ice shelf and nearly symmetric upstream of the grounding zone, consistent with a classic ice stream cross-flow profile (Raymond, 1996; Joughin et al., 2004; Cuffey and Paterson, 2010). Upstream of the grounding zone where Rutford is laterally confined within a bathymetric channel, the width of the ice stream remains constant over M_{sf} periods, with effectively zero M_{sf}-period variability beyond the margins. The amplitude of M_{sf} variability is approximately constant along the width of the ice stream with a notable amplitude peak along the western margin where the ice stream abuts the Ellsworth Mountains. Downstream of the grounding zone, along transect D–D' we observe higher speeds and M_{sf}-period

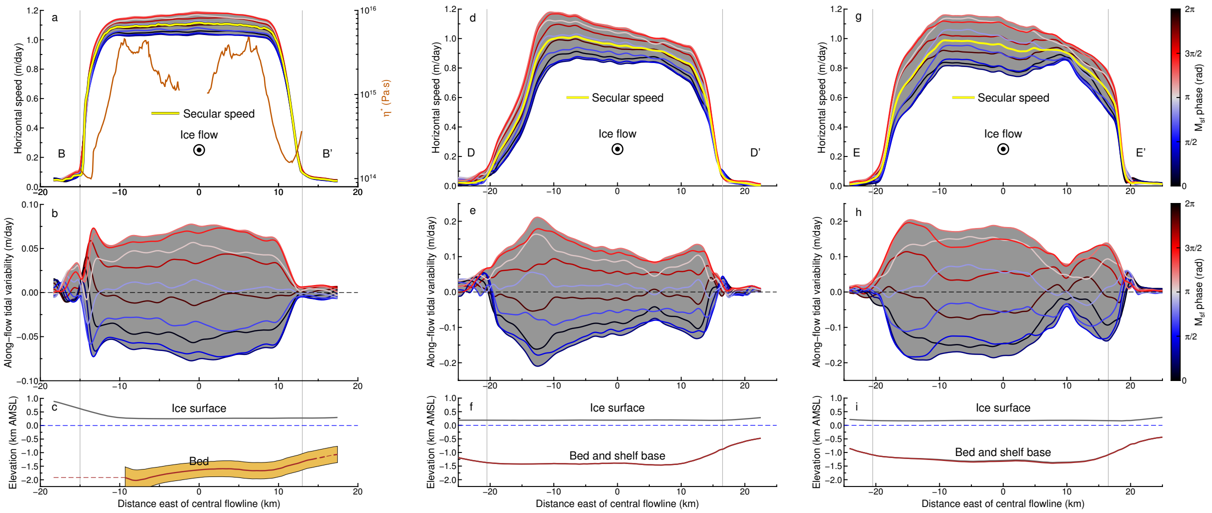

Figure 5.22: Time-dependent horizontal flow, M_{sf}-period longitudinal flow variability, and ice stream geometry along transections (a–c) B–B', (d–f) D–D', and (g–i) E–E'. In all cases, ice flow direction is out of the page. Line colors and gray shaded regions are the same as in Fig. 5.21 and geometric data are from Bedmap2. Inferred effective dynamic viscosity, η^* (Eq. 5.56), in profile B–B' is shown in (a) by the broken burnt orange line. Dashed brown line in (c) indicates that no bathymetric data are available within 3 km in any direction and light brown shaded region indicates two-standard deviation uncertainty in bathymetry.

amplitudes in the western portion of the ice shelf, both peaking at 10–12 km west of the central flowline. Westward of this peak the margin migrates transverse to the flow over the M_{sf} period due to the relatively shallow cross-flow gradient in horizontal speed. The width of the ice stream, defined as the cross-flow distance between inboard points of near-zero horizontal speed on each side, does not change outside of estimated uncertainties. The peak in M_{sf} amplitude in D–D' at 12-km west of the central flowline lies along roughly the same flowline as the peak in B–B'. Further downstream, along E–E', transverse flow is asymmetric, with an overall shape that tends more toward symmetry than the D–D' transect. We observe a slight peak in M_{sf} at 15 km west of the central flowline that lies along roughly the same flowline as the amplitude peaks in B–B' and D–D'. On the eastern half of E–E' transect we observe a notable low in M_{sf} amplitude at approximately 10 km east of the central flowline where the secular horizontal flow speed begins to decrease, there is a relatively strong cross-flow M_{sf} signal (Fig. 5.19), and the draft of the ice shelf shallows. Given these observations, the ice shelf likely grounds along the eastern margin at low tide.

5.5.2.2.5 Ice rheology

The cross-flow profile of horizontal ice flow includes information about the mechanical properties of the ice and the ice-bed interface. Landward of the grounding zone, ice is slipping along the bed at approximately the same rate as we observe at the surface (Morlighem et al., 2013). Observed along-flow and across-flow normal secular strain rates are small upstream of the grounding zone (Fig. 5.16c–d), so we can reasonably assume negligible longitudinal and transverse normal stresses. Velocity divergence is small along transect B–B', which we consider here, meaning that ice is virtually incompressible (Fig. 5.16b). From these assumptions, it can be shown that lateral shear stress in each half of the ice stream is given as (see Chapter 4, Appendix C):

$$\frac{\partial\left(h\tau_{\hat{x}\hat{y}}\right)}{\partial\hat{y}} = \tau_b - \tau_d \tag{5.54}$$

where subscripts $\hat{x}$ and $\hat{y}$ indicate along- and transverse-flow directions, respectively, and τ_b is the shear traction at the bed. The constitutive relation for ice is given as:

$$\tau_{\hat{x}\hat{y}} = 2\eta\dot{\varepsilon}_{\hat{x}\hat{y}} \tag{5.55}$$

where $2\eta = A^{-1/n_g}\dot{\varepsilon}_e^{(1-n_g)/n_g}$, η is the vertically averaged effective dynamic viscosity, and A and n_g are defined in Table 5.1. We assume the ratio τ_b/τ_d is approximately constant across the ice stream within the immediate vicinity of transect B–B'. The best evidence supporting this assumption is the lack of significant strain rates within the central ice stream trunk and results from numerical modeling studies, which also suggest that $\tau_b/\tau_d \ll 1$ (e.g., Morlighem et al., 2013). Taking τ_b/τ_d to be constant allows us to separate the unknown factors η and τ_b from those that are constrained by observations such that:

$$\eta^* = \frac{1}{2h\dot{\varepsilon}_{\hat{x}\hat{y}}}\int \tau_d \, \mathrm{d}\hat{y} \tag{5.56}$$

where $\eta^* = \eta/(1 - \tau_b/\tau_d)$ and $h = h(y)$, $\tau_d = \tau_d(y)$, and $\dot{\varepsilon}_{\hat{x}\hat{y}} = \dot{\varepsilon}_{\hat{x}\hat{y}}(y)$. We solve the indefinite integral numerically subject to the boundary condition $\tau_{\hat{x}\hat{y}} = 0$ at the centerline and use data from Bedmap2 to constrain the ice stream geometry (Fig. 5.22a). Where bathymetric data are available, we use the Bedmap2 geometry shown in Fig. 5.22c and where bathymetric data are not available we apply linear interpolation to fill gaps and extrapolate the nearest data through the western margin (dashed brown line in Fig. 5.22c).

Inferred values of η^* indicate that ice in the margins upstream of the grounding zone has up to a factor of 50 lower effective dynamic viscosity than ice located in the central ice stream trunk, which has typical values of $\eta^* \sim 4 \times 10^{15}$ Pa·s (Fig. 5.22a). Taking Young's Modulus for ice to be $E = 9.33$ GPa and assuming that ice acts as a Maxwell viscoelastic material over the M_{sf} timescale (Petrenko and Whitford, 2002), we find a Maxwell relaxation time of up to $2\eta/E \sim 9.9$ days in the central ice stream, reducing to as little as ~ 0.25 days in the margins. Ice in the western (left) margin has a lower minimum value of inferred viscosity than ice in the eastern margin, whose minimum inferred η^* is approximately a factor of two higher. Ice within a few kilometers of the ice stream centerline has lower viscosity due to the advection of damage from the prominent sticky spot located approximately 40 km upstream of the grounding line (approximately 20 km upstream of transect B–B'). We exclude inferred values of η^* within ± 2 km of the centerline because the boundary condition used to solve equation 5.56 diminishes the accuracy of η^* near the centerline.

Within the western margin, the largest amplitudes in M_{sf} along-flow variability are aligned with the smallest values of inferred effective dynamic viscosity (Fig. 5.22a–b). The peak in M_{sf} horizontal flow variability at approximately -13 km aligns with the minimum inferred viscosity along the B–B' transect and inferred viscosity increases by approximately a factor of 2 over about 100 m slightly inboard of minimum viscosity. This peak in M_{sf} along-flow amplitude is along the same flowline as the highest amplitude of M_{sf} along-flow variability over the shelf, suggesting that shear heating or excess damage driven by the higher M_{sf} along-flow variability reduces ice viscosity in the western margin.

5.6 Discussion

Inferred 4D velocity fields elucidate the complex, spatially heterogenous secular and tidally induced periodic flow variability on Rutford. Comparisons with GPS measurements and the CATS2008a_opt tidal model, formal error estimates from the posterior model covariance matrix, and synthetic tests discussed in §5.3.4.1 indicate that the 4D velocity fields inferred from the CSK observations capture variations in horizontal ice stream flow at the M_{sf} (14.77-day) period and vertical motions over the ice shelf at M_2 (12.42-hour) and O_1 (25.82-hour) periods with less than 10% error. Inferred vertical motion at M_2 and O_1 periods agree with our prior expectations of vertical motion based on tidal model results and GPS observations. We observe spatially consistent phase values for M_2 uplift over the bulk of the observed ice shelf indicating that the ice shelf rises and falls in response to the strong lunar semi-diurnal tide approximately monolithically. Delays of order 20 minutes are inferred in the two prominent grounding zone horns, which may be useful in future studies to ascertain the elastic properties of ice in the grounding zone. O_1 uplift is more spatially heterogenous than

M_2 uplift and features spatial variability in phase of order 30 minutes, and more in some localized regions. Some of the greatest lags in O_1 phase are coincident with an area of low velocity and relatively small M_{sf}-period horizontal flow variability along the eastern ice stream margin where the ice likely grounds during low tide. Though beyond the scope of this study, the differences in spatial variability in M_2 and O_1 tidal amplitudes and phase values may inform estimates of water column depth beneath the ice shelf, which are lacking in the Bedmap2 dataset (Fretwell et al., 2013).

Owing to the fine resolution of CSK data, the secular velocity and resulting strain rate fields resolve the ice stream margins, which are critical to our understanding of the mechanics of ice flow and the mechanisms underlying tidally induced horizontal flow variability. Effective and lateral shear strain rates in the margins are much greater than anywhere else in the ice stream and ice shelf. Margin thickness and secular shear strain rates vary as functions of bathymetry and the presence of intersecting tributary glaciers. Within 70 km upstream of the grounding zone, the shear margins exhibit the highest strain rates in the observational domain and are concentrated in the thinnest margins. Secular strain rate fields also indicate areas of expected damage and features of interest at the bed. Values of along-flow vertical shearing are consistent with hummocky features in optical imagery in the upstream extent of the observational domain and prominently indicate a patch of known stiff sediment 40 km upstream of the grounding zone and the stiff sediment underlying the u-shaped bend in the grounding zone. The divergence of the velocity field indicates damage concentrated in the margins upstream of the grounding zone, a feature that is important for ascertaining stress transmission mechanisms.

In better understanding stress transmission mechanisms in ice streams, the observed characteristic of greatest interest is M_{sf}-period horizontal flow variability. Our results agree with collocated GPS data, but indicate amplitudes of M_{sf} variability over the ice shelf that can exceed the maximum values observed on grounded ice by up to a factor of 3. Areas of high M_{sf} amplitudes are concentrated downstream and along the western margin of the ice shelf. These amplitudes decrease markedly in the presence of ice delivered by MG, where the phase correspondingly lags the immediately surrounding ice by more than a day. These observations show how sensitive the dynamics of the main ice stream are to the influx of cold, possibly undamaged ice from tributary glaciers. Our observations suggest that MG damps the response of ice flow in Rutford to tidal forcing and observed changes in flow speed and geometry on MG may portend longer timescale variations in Rutford's response to ocean tidal loading.

In general, the response of horizontal ice flow to ocean tidal forcing is most pronounced over the ice shelf and subsequently propagates through the grounded ice stream at a mean rate of approximately 29 km/day, decaying quasi-linearly with distance over approximately 85 km upstream of the grounding zone. These observations support the hypothesis that changes in ice shelf buttressing caused by ice lifting off of pinning points drive upstream tidal variability. We observe several areas that likely contain pinning points. One is an egg-shaped region immediately west of the u-shaped bend in the grounding zone at the downstream mouth of the west grounding zone horn. This area has several characteristics that are consistent with pinning points in that it (1) lags the surrounding area in M_{sf} horizontal flow response by approximately 5 days, (2) has lower secular horizontal flow speeds than the surrounding ice, (3) exhibits along-flow vertical shear strain rates comparable to the u-shaped grounding zone bend, and (4) has poorly fit M_2 and O_1-period vertical motion. Due to its central location in the zone of leading phase and the portion of the grounding zone with the highest flux rates, this pinning point is likely to be a one of the more important pinning points in determining the response of horizontal flow to tidal forcing. The other important pinning feature is the long zone along the eastern margin of the ice shelf. Here ice flows more slowly than surrounding areas on the shelf and features a strong cross-flow M_{sf} response. Weak lateral shear strain rates extend several kilometers into the flow at the downstream end of this feature while the upstream portion that is coincident with the central flowline transect A–A' is a nodal point in the along-flow strain rate. The centrality and spatial extent of this long region along the eastern shelf margin along with our observations of strong M_{sf}-period amplitudes downstream and along the opposite margin from this pinning zone make it a likely source of observed tidal variability.

If changes in ice shelf buttressing are driving M_{sf} along-flow variability in grounded ice, then it is necessary to explain the how stresses from the ice shelf are transmitted almost 100 kilometers inland of the grounding zone. Previous work by Thompson et al. (2014) using 2D and 3D viscoelastic models of a simplified ice stream designed to resemble Rutford shows that it is only possible to transmit stresses through ice over the observed distances if the ice is largely decoupled from the sidewalls and the bed. Several studies provide evidence that the ice stream is largely decoupled from the bed, satisfying the latter condition for upstream propagation (e.g., Smith and Murray, 2009; Gudmundsson, 2011; Morlighem et al., 2013). The restrictive necessary condition that ice in the margins be severely weakened relative to the central ice stream, which is justified by the modeled exponential decay with distance of tidal-timescale perturbations, led Thompson et al. (2014) to conclude that a mechanism external to the ice stream, such as changes in basal shear traction, is necessary to explain the observed M_{sf} along-flow variability in grounded ice. The need for such external mechanisms negates the possibility that ice shelf buttressing is the source of inland accelerations in ice flow. However, inferred values of effective dynamic viscosity upstream of the grounding zone indicate that ice in the margins has lower effective viscosity than ice in the central ice stream by as much as a factor of 50 and that the width of the lower viscosity margins is much thinner than supposed by Thompson et al. (2014). Reduced effective viscosity in the margins results from a combination of shear heating, damage and healing, and reorientation of fabrics in the ice within the margins (e.g., Echelmeyer et al., 1994; Suckale et al., 2014; Perol and Rice, 2015; Hudleston, 2015). More sophisticated models than we have applied here are warranted, but these results indicate that it may be possible to transmit stresses upstream through the ice column, meaning that changes in ice shelf buttressing at pinning points remains a viable mechanism for generating the observed tidal variability in horizontal ice flow.

While weakening in the margins may facilitate stress transmission through the grounded ice column, our observations indicate that the ice stream margins dampen stress perturbations as expected (Thompson et al., 2014). As previously noted, if we assume ice behaves as a Maxwell viscoelastic material (with Young's modulus $E = 9.33$ GPa) over the timescales of interest, the Maxwell relaxation time for the central ice is approximately 9.9 days. For the mean upstream propagation velocity of M_{sf} along-flow variability (28.7 km/day), this gives a relaxation length scale of 285 km, which is around a factor of 5 farther upstream than the observed distance of ≈ 85 km (Fig. 5.20a). Further work is needed to ascertain what fraction of this damping is due to shear traction at the bed and how much is attributable to shearing in the margins, but high values of inferred dynamic viscosity can be reasonably expected to play an important role in damping stress perturbations that generate M_{sf} along-flow variability (Thompson et al., 2014).

5.7 Conclusions

We present a method for deriving 3D velocity field time series (4D velocity fields) using continuous synthetic aperture radar observations. These first-of-their-kind observations represent an important step in the development of geodetic methods aimed at a mechanistic understanding of glacier flow. Essentially, we have combined some of the temporal benefits of GPS data with the spatial benefits of SAR to illuminate the spatiotemporal characteristics of flow in Rutford Ice Stream. Through comparison with GPS data and numerous tests on a synthetic ice stream, we show that our method, when applied to temporally continuous SAR data, can infer temporal ice flow variability to within

10% in vertical and horizontal dimensions.

Tests conducted using a synthetic ice stream whose prescribed temporal ice flow variability matches observations on Rutford showed that the posterior model that yields the overall most accurate results contains the 3D secular velocity and the M_2, O_1, and M_{sf} family of tidal constituents. We find that including the M_2 period is essential for accurate estimates of ice flow over the shelf. It is possible that this finding is unique to the Filchner-Ronne region because of the anomalously strong semi-diurnal tides in this area, but we postulate that accurately inferring vertical motion at M_2 is necessary wherever accurate velocity fields are desired over an ice shelf because M_2 has the highest tidal amplitudes of all the tidal constituents observable (non-aliased) with modern and planned spaceborne SAR systems.

We observe the strongest variability in horizontal ice flow at the M_{sf} (14.77-day) period over the ice shelf, where amplitudes exceed those of grounded ice by up to a factor of 3. Observed pinning points and an extensive pinning zone extending tens of kilometers along the eastern shelf margin may be the primary drivers of horizontal flow variability, though further studies are needed to test this hypothesis. Along-flow strain rates indicate that these pinning points are nodal features that induce buttressing, or back stress, at low tide, which is released as the shelf lifts off the point at high tide thereby driving horizontal flow primarily at the M_{sf} period. The observed M_{sf} along-flow variability propagates upstream at a mean rate of 24.6 km/day within 30 km of the grounding zone and at 32.7 km/day between 40 and 80 km upstream of the grounding zone. Along the way, the signal amplitude is damped by 2.6 mm/km on average and is almost completely damped beyond 85 km upstream of the grounding zone. Propagation rates and amplitudes of M_{sf} along-flow variability are sensitive to changes in ice thickness, with the most notable alterations in amplitude and phase occurring in the vicinity of a prominent bump in the basal topography that induces a marked increase in ice thickness.

We use a cross-flow model to infer effective dynamic viscosity along a transect located upstream of the grounding zone. Inferred values of viscosity indicate that ice within the shear margins has lower viscosity relative to undamaged ice within the central ice stream trunk by up to a factor of 50. This apparent weakening of the shear margins may facilitate propagation of buttressing stresses through the ice column to the distances observed. Higher values of inferred dynamic viscosity and the observed upstream propagation rate of M_{sf} along-flow variability in grounded ice could allow stresses to be transmitted much further upstream than observed, but damping in the shear margins and at the bed limits stress transmission to within 85 km of the grounding zone.

5.8 Acknowledgements

Coauthors for this work are Bryan Riel, Mark Simons, and Pietro Milillo. We benefitted from conversations with H. Martens, V. Tsai, and J. Thompson. SAR data were provided by ASI. B.M. was partially funded by a NASA Cyospheric Sciences Award NNX14AH80G and generous donations from the Albert Parvin and ARCS LA Chapter foundations. B.R. was partially funded by a NASA Earth and Space Sciences fellowship.

Bibliography

G. Aðalgeirsdóttir, A. M. Smith, T. Murray, M. A. King, K. Makinson, K. W. Nicholls, and A. E. Behar. Tidal influence on Rutford Ice Stream, West Antarctica: observations of surface flow and basal processes from closely spaced GPS and passive seismic stations. *Journal of Glaciology*, 54 (187):715–724, 2008.

S. Anandakrishnan, D. E. Voigt, R. B. Alley, and M. A. King. Ice Stream D flow speed is strongly modulated by the tide beneath the Ross Ice Shelf. *Geophysical Research Letters*, 30(7):n/a–n/a, 2003. doi: 10.1029/2002GL016329.

R. Bamler and M. Eineder. Accuracy of differential shift estimation by correlation and split-bandwidth interometry for wideband and Delta-k SAR systems. *IEEE Geoscience and Remote Sensing Letters*, 2(2):151–155, 2005.

N. B. D. Bechor and H. A. Zebker. Measuring two-dimensional movements using a single InSAR pair. *Geophysical Research Letters*, 33(16), 2006. doi: 10.1029/2006GL026883.

R. A. Bindschadler, M. A. King, R. B. Alley, S. Anandakrishnan, and L. Padman. Tidally controlled stick-slip discharge of a West Antarctic ice stream. *Science*, 301(5636):1087–1089, 2003a. doi: 10.1126/science.1087231.

R. A. Bindschadler, P. L. Vornberger, M. A. King, and L. Padman. Tidally driven stick-slip motion in the mouth of Whillans Ice Stream, Antarctica. *Annals of Glaciology*, 36(1):263–272, 2003b. doi: 10.3189/172756403781816284.

K. M. Cuffey and W. S. B. Paterson. *The Physics of Glaciers*. Elsevier, 4th edition, 2010.

K. A. Echelmeyer, W. D. Harrison, C. Larsen, and J. E. Mitchell. The role of the margins in the dynamics of an active ice stream. *Journal of Glaciology*, 40(136):527–538, 1994.

T. R. Emardson, M. Simons, and F. H. Webb. Neutral atmospheric delay in interferometric synthetic aperture radar applications: Statistical description and mitigation. *Journal of Geophysical Research: Solid Earth*, 108(B5):2231, 2003.

A. C. Fowler. Sliding with cavity formation. *Journal of Glaciology*, 33:255–267, 1987.

P. Fretwell, H. D. Pritchard, D. G. Vaughan, J. L. Bamber, N. E. Barrand, R. Bell, C. Bianchi, R. G. Bingham, D. D. Blankenship, G. Casassa, G. Catania, D. Callens, H. Conway, A. J. Cook, H. F. J. Corr, D. Damaske, V. Damm, F. Ferraccioli, R. Forsberg, S. Fujita, Y. Gim, P. Gogineni, J. A. Griggs, R. C. A. Hindmarsh, P. Holmlund, J. W. Holt, R. W. Jacobel, A. Jenkins, W. Jokat, T. Jordan, E. C. King, J. Kohler, W. Krabill, M. Riger-Kusk, K. A. Langley, G. Leitchenkov, C. Leuschen, B. P. Luyendyk, K. Matsuoka, J. Mouginot, F. O. Nitsche, Y. Nogi, O. A. Nost, S. V. Popov, E. Rignot, D. M. Rippin, A. Rivera, J. Roberts, N. Ross, M. J. Siegert, A. M. Smith, D. Steinhage, M. Studinger, B. Sun, B. K. Tinto, B. C. Welch, D. Wilson, D. A. Young, C. Xiangbin, and A. Zirizzotti. Bedmap2: improved ice bed, surface and thickness datasets for Antarctica. *The Cryosphere*, 7(1):375–393, 2013.

R. M. Goldstein, H. Engelhardt, B. Kamb, and R. M. Frolich. Satellite radar interferometry for monitoring ice sheet motion: Application to an Antarctic Ice Stream. *Science*, 262(5139):1525–1530, 1993. doi: 10.1126/science.262.5139.1525.

A. L. Gray, N. Short, K. E. Mattar, and K. C. Jezek. Velocities and flux of the Filchner Ice Shelf and its tributaries determined from speckle tracking interferometry. *Canadian Journal of Remote Sensing*, 27(3):193–206, 2001. doi: 10.1080/07038992.2001.10854936.

G. H. Gudmundsson. Fortnightly variations in the flow velocity of Rutford Ice Stream, West Antarctica. *Nature*, 444(7122):1063–1064, 2006. doi: 10.1038/nature05430.

G. H. Gudmundsson. Tides and the flow of Rutford Ice Stream, West Antarctica. *Journal of Geophysical Research: Earth Surface*, 112(F4):n/a–n/a, 2007. doi: 10.1029/2006JF000731.

G. H. Gudmundsson. Ice-stream response to ocean tides and the form of the basal sliding law. *The Cryosphere*, 5(1):259–270, 2011. doi: 10.5194/tc-5-259-2011.

S. C. Han, C. K. Shum, and K. Matsumoto. GRACE observations of M2 and S2 ocean tides underneath the Filchner-Ronne and Larsen ice shelves, Antarctica. *Geophysical Research Letters*, 32 (20):n/a–n/a, 2005. ISSN 1944-8007. doi: 10.1029/2005GL024296. L20311.

R. F. Hanssen. *Radar Interferometry: Data Interpretation and Error Analysis*. Springer, 1st edition, 2001.

T. Haran, J. Bohlander, T. Scambos, T. Painter, and M. Fahnestock. MODIS Mosaic of Antarctica 2003-2004 (MOA2004) Image Map. Technical report, National Snow and Ice Data Center, Boulder, Colorado USA, 2005.

T. Haran, J. Bohlander, T. Scambos, T. Painter, and M. Fahnestock. MODIS Mosaic of Antarctica 2008-2009 (MOA2009) Image Map. Technical report, National Snow and Ice Data Center, Boulder, Colorado USA, 2014.

S. Hensley, T. Michel, M. Simard, C. Jones, R. Muellerschoen, C. Le, H. Zebker, and B. Chapman. Residual motion estimation for UAVSAR: Implications of an electronically steered array. In *Proceedings 2009 IEEE Radar Conference*, Pasadena, CA, 2009a.

S. Hensley, H. Zebker, C. Jones, T. Michel, R. Muellerschoen, and B. Chapman. First demonstration results using the NASA/JPL UAVSAR instrument. In *2nd Annual Asia Pacific SAR Conference*, Xian, China, 2009b. doi: 10.1109/APSAR.2009.5374246.

E. A. Hetland, P. Musé, M. Simons, Y. N. Lin, P. S. Agram, and C. J. DiCaprio. Multiscale InSAR Time Series (MInTS) analysis of surface deformation. *Journal of Geophysical Research: Solid Earth*, 117(B2):n/a–n/a, 2012. doi: 10.1029/2011JB008731.

P. J. Hudleston. Structures and fabric in glacial ice: A review. *Journal of Structural Geology*, 2015. doi: 10.1016/j.jsg.2015.09.003.

K. C. Jezek, J. C. Curlander, F. Carsey, C. Wales, and R. G. Barry. RAMP AMM-1 SAR Image Mosaic of Antarctica. Version 2. Technical report, National Snow and Ice Data Center, Boulder, Colorado USA, 2013.

I. Joughin. Ice-sheet velocity mapping: a combined interferometric and speckle-tracking approach. *Annals of Glaciology*, 34(1):195–201, 2002. doi: doi:10.3189/172756402781817978.

I. Joughin, E. Rignot, C. E. Rosanova, B. K. Lucchitta, and J. Bohlander. Timing of recent accelerations of Pine Island Glacier, Antarctica. *Geophysical Research Letters*, 30(13):n/a–n/a, 2003. doi: 10.1029/2003GL017609.

I. Joughin, D. MacAyeal, and S. Tulaczyk. Basal shear stress of the Ross ice stream from control method inversions. *Journal of Geophysical Research*, 109(B09405):1–20, 2004. doi: 10.1029/2003JB002960.

I. Joughin, S. Tulaczyk, J. L. Bamber, D. Blankenship, J. W. Holt, T. Scambos, and D. G. Vaughan. Basal conditions for Pine Island and Thwaites Glaciers, West Antarctica, determined using satellite and airborne data. *Journal of Glaciology*, 55(190), 2009. doi: doi: 10.3189/002214309788608705.

B. Kamb. Glacier surge mechanisms based on linked cavity configuration of the basal water conduit system. *Journal of Geophysical Research*, 92(B9):9083–9100, 1987.

E. C. King, R. C. A. Hindmarsh, and C. R. Stokes. Formation of mega-scale glacial lineations observed beneath a West Antarctic ice stream. *Nature Geoscience*, 2:585–588, 2009. doi: 10.1038/ngeo581.

M. A. King, T. Murray, and A. M. Smith. Non-linear responses of Rutford Ice Stream, Antarctica, to semi-diurnal and diurnal tidal forcing. *Journal of Glaciology*, 56(195):167–176, 2010. doi: 10.3189/002214310791190848.

R. Lohman and M. Simons. Some thoughts on the use of InSAR data to constrain models of surface deformation: Noise structure and data downsampling. *Geochemistry, Geophysics, Geosystems*, 6 (1):1–12, 2005.

D. MacAyeal. The basal stress distribution of Ice Stream E, Antarctica, inferred by control methods. *Journal of Geophysical Research*, 97(B1):595–603, 1992.

D. MacAyeal. A tutorial on the use of control methods in ice-sheet modeling. *Journal of Glaciology*, 39(131):91–98, 1993.

B. M. Minchew, M. Simons, S. Hensley, H. Björnsson, and F. Pálsson. Early melt-season velocity fields of Langjökull and Hofsjökull ice caps, central Iceland. *Journal of Glaciology*, 61(226): 253–266, 2015. doi: 10.3189/2015JoG14J023.

B. M. Minchew, M. Simons, M. Morlighem, H. Björnsson, F. Pálsson, S. Hensley, and E. Larour. Plastic bed beneath Hofsjökull Ice Cap, central Iceland, and the sensitivity of ice flow to surface meltwater flux. *Journal of Glaciology*, in press, 2016.

P. Misra and P. Enge. *Global Positioning System: Signals, Measurements, and Performance*. Ganga-Jamuna Press, Lincoln, Massachusetts, 2nd edition, 2006.

M. Morlighem, E. Rignot, H. Seroussi, E. Larour, H. Ben Dhia, and D. Aubry. Spatial patterns of basal drag inferred using control methods from a full-Stokes and simpler models for Pine Island Glacier, West Antarctica. *Geophysical Research Letters*, 37(14):1–6, 2010. doi: 10.1029/2010GL043853. L14502.

M. Morlighem, H. Seroussi, E. Larour, and E. Rignot. Inversion of basal friction in Antarctica using exact and incomplete adjoints of a higher-order model. *Journal of Geophysical Research: Earth Surface*, 118(3):1746–1753, 2013. doi: 10.1002/jgrf.20125.

T. Murray, A. M. Smith, M. A. King, and G. P. Weedon. Ice flow modulated by tides at up to annual periods at Rutfurd Ice Stream, West Antarctica. *Geophysical Research Letters*, 34(18):n/a–n/a, 2007. ISSN 1944-8007. doi: 10.1029/2007GL031207. L18503.

K. W. Nicholls, S. Osterhus, K. Makinson, T. Gammelsrod, and E. Fahrbach. Ice-ocean processes over the continental shelf of the southern Weddell Sea, Antarctica: A review. *Reviews of Geophysics*, 47(3):1–23, 2009. doi: 10.1029/2007RG000250.

L. Padman and H. A. Fricker. Tides on the Ross Ice Shelf observed with ICESat. *Geophysical Research Letters*, 32(L14503):n/a–n/a, 2005. doi: 10.1029/2005GL023214.

L. Padman, H. A. Fricker, R. Coleman, S. Howard, and L. Erofeeva. A new tide model for the Antarctic ice shelves and seas. *Annals of Glaciology*, 34(1):247–254, 2002. doi: 10.3189/172756402781817752.

L. Padman, S. Y. Erofeeva, and H. A. Fricker. Improving antarctic tide models by assimilation of icesat laser altimetry over ice shelves. *Geophysical Research Letters*, 35(22):n/a–n/a, 2008. ISSN 1944-8007. doi: 10.1029/2008GL035592. L22504.

T. Perol and J. R. Rice. Shear heating and weakening of the margins of west antarctic ice streams. *Geophysical Research Letters*, 42(9):3406–3413, 2015. ISSN 1944-8007. doi: 10.1002/2015GL063638. 2015GL063638.

V. F. Petrenko and R. W. Whitford. *Physics of Ice*. Oxford University Press, Oxford, England, third edition, 2002.

H. D. Pritchard, S. R. M. Ligtenberg, H. A. Fricker, D. G. Vaughan, M. R. van den Broeke, and L. Padman. Antarctic ice-sheet loss driven by basal melting of ice shelves. *Nature*, 484:502–505, 2012.

C. Raymond. Shear margins in glaciers and ice sheets. *Journal of Glaciology*, 42(140):90–102, 1996.

E. Rignot, L. Padman, D. R. MacAyeal, and M. Schmeltz. Observation of ocean tides below the Filchner and Ronne Ice Shelves, Antarctica, using synthetic aperture radar interferometry: Comparison with tide model predictions. *Journal of Geophysical Research: Oceans*, 105(C8):19615–19630, 2000. ISSN 2156-2202. doi: 10.1029/1999JC000011.

E. Rignot, K. Echelmeyer, and W. Krabill. Penetration depth of interferometric synthetic-aperture radar signals in snow and ice. *Geophysical Research Letters*, 28(18):3501–3504, 2001. doi: 10.1029/2000GL012484.

E. Rignot, G. Casassa, P. Gogineni, W. Krabill, A. Rivera, and R. Thomas. Accelerated ice discharge from the Antarctic Peninsula following the collapse of Larsen B Ice Shelf. *Geophysical Research Letters*, 31(18):n/a–n/a, 2004. doi: 10.1029/2004GL020697.

E. Rignot, J. Mouginot, and B. Scheuchl. Ice Flow of the Antarctic Ice Sheet. *Science*, 333(6048): 1427–1430, 2011a. doi: 10.1126/science.1208336.

E. Rignot, J. Mouginot, and B. Scheuchl. Antarctic grounding line mapping from differential satellite radar interferometry. *Geophysical Research Letters*, 38(10):n/a–n/a, 2011b. doi: 10.1029/2011GL047109.

E. Rignot, S. Jacobs, J. Mouginot, and B. Scheuchl. Ice-shelf melting around Antarctica. *Science*, 341(6143):266–270, 2013. doi: 10.1126/science.1235798.

E. J. Rignot. Fast recession of a West Antarctic Glacier. *Science*, 281(5376):549–551, 1998. doi: 10.1126/science.281.5376.549.

E. Rodriguez and J.M. Martin. Theory and design of interferometric synthetic aperture radars. *Radar and Signal Processing, IEE Proceedings F*, 139(2):147 –159, 1992.

P. A. Rosen, S. Hensley, I. R. Joughin, F. K. Li, S. N. Madsen, E. Rodriguez, and R. M. Goldstein. Synthetic aperture radar interferometry. *Proceedings of the IEEE*, 88(3):333 –382, 2000. doi: 10.1109/5.838084.

P. A. Rosen, S. Hensley, G. Peltzer, and M. Simons. Updated repeat orbit interferometry package released. *Eos, Transactions American Geophysical Union*, 85(5):47–47, 2004. doi: 10.1029/2004EO050004.

P. A. Rosen, Gurrola E., G. F. Sacco, and H. Zebker. The InSAR Scientific Computing Environment. In *9th European Conference on Synthetic Aperture Radar*, 2012.

S. H. R. Rosier, G. H. Gudmundsson, and J. A. M. Green. Insights into ice stream dynamics through modelling their response to tidal forcing. *The Cryosphere*, 8(5):1763–1775, 2014. doi: 10.5194/tc-8-1763-2014.

S. H. R. Rosier, G. H. Gudmundsson, and J. A. M. Green. Temporal variations in the flow of a large Antarctic ice-stream controlled by tidally induced changes in the subglacial water system. *The Cryosphere*, 9(4):1649–1661, 2015. doi: 10.5194/tc-9-1649-2015.

H. Rott, Wolfgang Rack, P. Skvarca, and H. de Angelis. Northern Larsen Ice Shelf, Antarctica: further retreat after collapse. *Annals of glaciology*, 34:277–282, 2002.

T. A. Scambos, T. M. Haran, M. A. Fahnestock, T. H. Painter, and J. Bohlander. MODIS-based Mosaic of Antarctica (MOA) data sets: Continent-wide surface morphology and snow grain size. *Remote Sensing of Environment*, 111(2–3):242–257, 2007. doi: http://dx.doi.org/10.1016/j.rse.2006.12.020.

B. Scheuchl, J. Mouginot, and E. Rignot. Ice velocity changes in the ross and ronne sectors observed using satellite radar data from 1997 and 2009. *The Cryosphere*, 6(5):1019–1030, 2012. doi: 10.5194/tc-6-1019-2012.

C. Schoof. Ice sheet grounding line dynamics: Steady states, stability, and hysterisis. *Journal of Geophysical Research*, 112(F3):1–19, 2007. doi: 10.1029/2006JF000664. F03S28.

M. Simons and P. Rosen. Interferometric synthetic aperture radar geodesy. In G. Schubert, editor, *Treatise on Geophysics*, pages 339–385. Elsvier, Amsterdam, 2nd edition, 2015. doi: 10.1016/B978-0-444-53802-4.00061-0.

A. M. Smith and T. Murray. Bedform topography and basal conditions beneath a fast-flowing west antarctic ice stream. *Quaternary Science Reviews*, 28(7–8):584–596, 2009. doi: http://dx.doi.org/10.1016/j.quascirev.2008.05.010.

A. M. Smith, T. Murray, K. W. Nicholls, K. Makinson, G. Aðalgeirsdóttir, A. E. Behar, and D. G. Vaughan. Rapid erosion, drumlin formation, and changing hydrology beneath an Antarctic ice stream. *Geology*, 35(2):127–130, 2007. doi: 10.1130/G23036A.1.

E. C. Smith, A. M. Smith, R. S. White, A. M. Brisbourne, and H. D. Pritchard. Mapping the ice-bed interface characteristics of rutford ice stream, west antarctica, using microseismicity. *Journal of Geophysical Research: Earth Surface*, 120:1–14, 2015. doi: 10.1002/2015JF003587.

J. Suckale, J. D. Platt, T. Perol, and J. R. Rice. Deformation-induced melting in the margins of the West Antarctic ice streams. *Journal of Geophysical Research: Earth Surface*, 119(5):1004–1025, 2014. doi: 10.1002/2013JF003008.

S. Sugiyama and G. H. Gudmundsson. Short-term variations in glacial flow controlled by subglacial water pressure at Lauteraargletscher, Bernese Alps, Switzerland. *Journal of Glaciology*, 50(170): 353–362, 2004. doi: 10.3189/172756504781829846.

A. Tarantola. *Inverse problem theory and methods for model parameter estimation*. Society for Industrial and Applied Mathematics, 2005.

J. Thompson, M. Simons, and V. C. Tsai. Modeling the elastic transmission of tidal stresses to great distances inland in channelized ice streams. *The Cryosphere*, 8(6):2007–2029, 2014. doi: 10.5194/tc-8-2007-2014.

V. C. Tsai, A. L. Stewart, and A. F. Thompson. Marine ice-sheet profiles and stability under coulomb basal conditions. *Journal of Glaciology*, 61(226):205–215, 2015. doi: 10.3189/2015JoG14J221.

F. T. Ulaby, R. K. Moore, and A. K. Fung. *Microwave Remote Sensing: Active and Passive*. Artech House, Dedham, Massachusetts, 1986.

J. Weertman. On the sliding of glaciers. *Journal of Glaciology*, 3(21):33–38, 1957.

P. Wessel, W. H. F. Smith, R. Scharroo, J. F. Luis, and F. Wobbe. Generic mapping tools: Improved version released. *Eos, Transactions American Geophysical Union*, 94(45):409–410, 2013. doi: 10.1002/2013EO450001.

J. P. Winberry, S. Anandakrishnan, R. B. Alley, R. A. Bindschadler, and M. A. King. Basal mechanics of ice streams: Insights from the stick-slip motion of Whillans Ice Stream, West Antarctica. *Journal of Geophysical Research*, 114(F01016):1–11, 2009. doi: 10.1029/2008JF001035.

H. A. Zebker and J. Villasenor. Decorrelation in interferometric radar echoes. *IEEE Transactions on Geoscience and Remote Sensing*, 30(5):950–959, 1992.

H. A. Zebker, S. Hensley, P. Shanker, and C. Wortham. Geodetically accurate InSAR data processor. *IEEE Transactions on Geoscience and Remote Sensing*, 48(12):4309–4321, 2010. doi: 10.1109/TGRS.2010.2051333.

Chapter 6

Conclusions

6.1 Synopsis

Our overarching goal with this thesis is a more thorough understanding of the mechanics of deformable glacier beds and their influence on ice flow. To that end, we develop new observational methods that exploit remotely sensed synthetic aperture radar data collected from multiple vantage points and at different times to infer surface velocity fields in all three spatial dimensions and in time. We combine these observations with other geodetic and meteorological observations to validate the remotely sensed data and provide greater context for the observed changes in ice surface velocity. By constraining numerical ice flow models with our observed velocity fields, we are able to infer the mechanical properties of ice and the bed in our study areas. Based on observations and numerical modeling results, we develop new mechanistic models of ice flow over deformable beds.

Chapter 2 lays the foundation for the observational methods developed and used in this thesis. We present an original Bayesian method that we developed for the purpose of inferring 3D ice flow velocities. We apply the method to airborne InSAR data collected during the early melt season over Langjökull and Hofsjökull ice caps, central Iceland. These observations showed that changes in moisture content at the glacier surface induce erroneous offsets in the InSAR measurements. Using only the much larger horizontal surface speeds and an ice flow model that accounts only for deformation within the ice column, we conclude that more than half of the observed surface velocity in fast-moving outlet glaciers on both ice caps is due to slip within the till-mantled glacier bed.

In Chapter 3 we apply the Bayesian method developed in Chapter 2 to data collected during midwinter and the early melt season over Hofsjökull. The results indicate significant seasonal speedup in most outlet glaciers within two weeks of the onset of seasonal melt and a spatially heterogenous response in outlet glaciers to continued surface meltwater flux. We constrain numerical ice flow models in ISSM with the surface velocity fields to show that the bed of Hofsjökull deforms plastically. Assuming a Mohr-Coulomb rheology for plastically deforming till, we infer basal water pressure fields over the entire ice cap and observe that slight changes in basal water pressure, of order 2–3 percent, are sufficient to double the observed surface velocity in some outlet glaciers. We derive a new mechanistic model for basal slip over plastic beds wherein the sensitivity of ice flow to changes in basal water pressure is inversely related to the ice surface slope such that ice flow in shallower sloping glaciers is more sensitive to changes in water pressure.

We expand on this mechanistic model for basal slip over deformable beds in Chapter 4 by considering the unique case of surges in glaciers with till-covered beds. We apply a model for till shear strength that is commonly used in studies of slip on gouge-filled tectonic faults and that accounts for the influence of basal slip rate and basal slip history on the shear strength of the till. Based on our model development and a linear stability analysis, we propose four conditions for glaciers to be capable of surging. Two of these conditions involve a coupling between local climate, glacier geometry, and till shear strength. The other conditions are based solely on the mechanical and hydrological properties of the bed. Taken together, these conditions should help explain the rarity of surge-type glaciers and their geographic distribution.

In the final chapter, we extend the methods presented in Chapter 2 to the time domain to study the influence of ocean tides on ice flow tens of kilometers inland. Through a series of tests using synthetic data designed to resemble our study site, Rutford Ice Stream, West Antarctica, we demonstrate that our method is capable of capturing temporal variability in ice flow to within 10% of the true value. We apply this method to synthetic aperture radar data collected by the Italian Space Agency (ASI) using the COSMO-SkyMed four-satellite constellation over Rutford to illuminate ice flow variability at timescales ranging from semi-diurnal to fortnightly. Our results indicate that the response of horizontal ice flow to tidal motion at 14.77-day periods is stronger over the ice shelf than over grounded ice by up to a factor of 3 and that accelerations always occur over the ice shelf first and then propagate inland at ice-thickness-dependent rates. We model the cross-flow profile of horizontal flow inland of the grounding zone and show that the ice in the shear margins is significantly weaker than in the main trunk of the ice stream. Weakened shear margins may allow changes in buttressing over the ice shelf to be transmitted upstream through the ice column, potentially explaining the mechanical link between ocean tides and ice flow tens of kilometers inland.

6.2 The importance of basal and ice mechanics

Understanding how environmental changes influence glaciers and our ability to develop models that provide a plausible range of forecasts for future glacier states require a thorough understanding of the mechanical properties both within ice and at the ice-bed, ice-atmosphere, and ice-ocean interfaces. The first-order response of glaciers to environmental changes is governed by ice rheology and basal mechanics. The special case of basal mechanics in glaciers with deformable beds is the primary focus of this thesis, but our results highlight the importance of ice rheology, particularly in the shear margins, in our understanding of basal mechanics.

Basal mechanics provide an important control on ice flow. In glaciers throughout the world, much of the observed ice flow is attributable to basal slip and direct observations of glacier beds have shown that deformable beds are prevalent in nature. Observations over the past few decades have shown that environmental changes can cause significant, rapid changes in the rate of flow and the geometry of these glaciers. Traditionally, studies of basal mechanics have focused largely on glaciers with clean, rigid beds, ignoring the unique challenges posed by deformable beds. What are needed are more studies combining geodetic observations and numerical ice flow models that aim to infer the mechanical properties of a variety of glaciers throughout the world. We have shown in Chapter 3 that the commonly applied basal boundary condition, which assumes a power-law relation between basal shear traction and basal slip rate, works well for inferring basal mechanics even where the glacier is underlain by plastically deforming till. Nevertheless, applications of newer, more sophisticated approaches to inferring basal mechanics are warranted and will improve our overall understanding of the range of plausible mechanical models for the bed. When combined with synoptic-scale observations of temporal variability in ice flow, the methods should constrain the mechanical properties of the beds beneath many glaciers, including those glaciers that exhibit the greatest changes and potential for future change.

Basal shear traction and ice rheology are the two first-order mechanisms that work together to resist gravitational driving stress. As we progress in our understanding of basal mechanics, we must also consider spatially varying ice rheology. This spatial variability can be driven by damage, reorientation of fabrics within the ice, and shear heating and will be most pronounced in shear margins and in areas where basal shear traction is dramatically different from the surrounding areas. Mechanistic models are needed to understand how damage increases and is healed for given (observable) strain conditions, but deriving such models will be challenging. It may be possible to infer both ice rheology and basal shear traction simultaneously from observationally constrained numerical ice flow models. Such an approach could yield more accurate basal shear traction estimates and observational underpinnings to aid in the development of mechanistic models of ice rheology under realistic strain conditions that can account for all of the potential mechanisms driving changes in the mechanics of the ice. With the exponential growth in geodetic observations, this approach should provide challenges to and motivation for further theoretical development aimed at a more thorough understanding of the mechanics of glacier flow.

6.3 Closing thoughts

The work presented here is only the beginning of our research into the mechanics of ice and deformable glacier beds. Some of major questions, like the stability of the West Antarctic Ice Sheet, remain open and we intend to continue to pursue lines of inquiry similar to those discussed here in order to help answer a number of open questions in glaciology. With the latest generation of radar satellites that are now or will soon be in orbit, we will have a wealth of data to use to challenge and improve our models and understanding of the mechanics of glacier flow and glacier beds.

We will to continue to build upon the observational methods presented in this thesis and to develop more sophisticated ice flow models to study the basal mechanics of Rutford Ice Stream, as well as Pine Island and Thwaites Glaciers, West Antarctica. Having observations that constrain the temporal variability in ice flow is invaluable because time is critical dimension that will allow us to adequately constrain the set of viable mechanistic models glacier beds.

Though we follow a unique path in our efforts to understand the mechanics of deformable beds, we ended up where the pioneering work of Barclay Kamb and his students left off. Barclay Kamb is a legendary figure in glaciology and at Caltech and his many students have made significant advances in the field. Glaciological research largely ceased at Caltech after Barclay left and this thesis represents some of the early work in revitalizing a glaciological program at Caltech. It is fitting that we have come back to some of the same problems that Barclay and his students were working on through our own approaches and inherent curiosity.